UNIVERSIDADE ESTADUAL DE CAMPINAS

INSTITUTO DE FÍSICA GLEB WATAGHIN

GIOVANI GRISOTTI MARTINS

Obtaining Optical and Dynamical Properties of Biological Tissue with Diffuse Optical Spectroscopy Techniques

Obtenção das Propriedades Ópticas e Dinâmicas do Tecido Biológico com Técnicas de Espectrocopia Óptica de Difusão

CAMPINAS

2024

GIOVANI GRISOTTI MARTINS

Obtaining Optical and Dynamical Properties of Biological Tissue with Diffuse Optical Spectroscopy Techniques

Obtenção das Propriedades Ópticas e Dinâmicas do Tecido Biológico com Técnicas de Espectrocopia Óptica de Difusão

Thesis presented to the Institute of Physics of the University of Campinas in partial fulfillment of the requirements for the degree of Ph. D. in Science, in the area of Applied Physics.

Tese apresentada ao Instituto de Física Gleb Wataghin da Universidade Estadual de Campinas como parte dos requisitos exigidos para a obtenção do título de Doutor em Ciências, na área de Física Aplicada.

Supervisor: Rickson Coelho Mesquita

Cosupervisor: Gabriela Castellano

ESTE EXEMPLAR CORRESPONDE À VERSÃO FINAL DA TESE DEFENDIDA PELO ALUNO GIOVANI GRISOTTI MARTINS E ORIENTADA PELO PROF. DR. RICKSON COELHO MESQUITA.

CAMPINAS

2024

Ficha catalográfica
Universidade Estadual de Campinas
Biblioteca do Instituto de Física Gleb Wataghin
Lucimeire de Oliveira Silva da Rocha - CRB 8/9174

Martins, Giovani Grisotti, 1995-
M366o Obtaining optical and dynamical properties of biological tissue with diffuse optical spectroscopy techniques / Giovani Grisotti Martins. – Campinas, SP : [s.n.], 2024.

Orientador: Rickson Coelho Mesquita.
Coorientador: Gabriela Castellano.
Tese (doutorado) – Universidade Estadual de Campinas, Instituto de Física Gleb Wataghin.

1. Espectroscopia de infravermelho próximo. 2. Espectroscopia ótica de difusão. 3. Espectroscopia de correlação de difusão. 4. Curvatura. 5. Pele - Absorção. I. Mesquita, Rickson Coelho, 1982-. II. Castellano, Gabriela, 1970-. III. Universidade Estadual de Campinas. Instituto de Física Gleb Wataghin. IV. Título.

Informações Complementares

Título em outro idioma: Obtenção das propriedades ópticas e dinâmicas do tecido biológico com técnicas de espectroscopia óptica de difusão
Palavras-chave em inglês:
Near infrared spectroscopy
Diffuse optical spectroscopy
Diffuse correlation spectroscopy
Curvature
Skin absorption
Área de concentração: Física Aplicada
Titulação: Doutor em Ciências
Banca examinadora:
Gabriela Castellano [Coorientador]
André Monteiro Paschoal
Felippe Alexandre Silva Barbosa
Luciano Bachmann
Diogo Coutinho Soriano
Data de defesa: 06-06-2024
Programa de Pós-Graduação: Física

Identificação e informações acadêmicas do(a) aluno(a)
- ORCID do autor: https://orcid.org/0000-0001-6163-489X
- Currículo Lattes do autor: https://lattes.cnpq.br/6450320149057127

INSTITUTO DE FÍSICA
GLEB WATAGHIN

MEMBROS DA COMISSÃO EXAMINADORA DA TESE DE DOUTORADO DO ALUNO GIOVANI GRISOTTI MARTINS - RA 146254, APRESENTADA E APROVADA AO INSTITUTO DE FÍSICA GLEB WATAGHIN, DA UNIVERSIDADE ESTADUAL DE CAMPINAS, EM 06/06/2024.

COMISSÃO JULGADORA:

- Profa. Dra. Gabriela Castellano – Presidente da Comissão Examinadora (IFGW/ UNICAMP)

- Prof. Dr. Andre Monteiro Paschoal (IFGW/ UNICAMP)

- Prof. Dr. Felippe Alexandre Silva Barbosa (IFGW/ UNICAMP)

- Prof. Dr. Luciano Bachmann (Faculdade de Filosofia, Ciências e Letras de Ribeirão Preto – USP)

- Prof. Dr. Diogo Coutinho Soriano (Universidade Federal do ABC)

OBS.: Ata da defesa com as respectivas assinaturas dos membros encontra-se no SIGA/Sistema de Fluxo de Dissertação/Tese e na Secretaria do Programa da Unidade.

CAMPINAS

2024

ACKNOWLEDGEMENTS

I understand there is a chronological order for thanking the people (and institutions) without whom I would not have written this text. First of all, I would like to thank Unicamp. As far as I can remember, I always wanted to enter the (medical) physics undergraduate course here. While it is widely recognized that the course at Unicamp is of high quality, I would like to emphasize how much I have learned about the workings of the world through my studies here. I'm extremely grateful for that. In addition to the excellent undergraduate course and everything I learned here, Unicamp allowed me to meet Professor Rickson. And he is the first person I must thank. Thank you for all your patience and persistence in discussing my research with me and guiding me along this journey so far. I certainly wouldn't be the professional I am today without your support.

Secondly, I need to thank the version of the LOB that welcomed me when I joined. Professor Rickson introduced me to a laboratory fulfilled of brilliant students. This version of the Biomedical Optics Laboratory (LOB) supported me extensively until I acquired the foundational knowledge I hold today. I especially thank Andrés for teaching me almost everything I know about data acquisition, Rodrigo for teaching me almost everything I know about FD-DOS and DCS, and Sérgio for teaching me almost everything I know about NIRS and listening to me through various personal life issues. If I was able to see a little further, it was because I stood on the shoulders of giants. Thank you very much!

Thirdly, time has passed, and I wish to thank the people who have been collaborating closely with me every day. It includes all the people who discussed my work daily with me in my fraternity (Guilherme, Carlos, Pedross, Felipe, Rafael, Gio, Antônio, Jhow, Nathan,...), but more importantly, all the LOB members. I am immensely grateful to Lusca, Marina, Pedro, Kelvin, Carlos, Caetano, Bianca, Victor, Bruno, and Lipe. Each of you contributed in a unique way to the completion of this work. Especially you, Lipe, for being my engineer and personal assistant during this final stage of the work. And also for having the patience to listen to me think out loud about all my questions and results.

Last but certainly not least, I thank *The São Paulo Research Foundation - FAPESP* (process 2019/25281-9), the *Ministry of Science, Technology, and Innovation* and the *National Council for Scientific and Technological Development – CNPq* (process 140960/2019-8) for making all my research financially feasible, as well as the Gleb Wataghin Physics Institute for providing all the infrastructure I needed. I also thank all the groups that collaborated with us, such as the Hemocovid project and the applied kinesiology laboratory.

ABSTRACT

Early disease detection can increase the chances of successful treatment and improve the efficiency of healthcare resource use. One method to achieve early detection is through the identification of biomarkers, which are quantifiable physiological parameters that indicate the potential presence of a specific disease. Biomarkers can enhance healthcare delivery by providing valuable insights that improve diagnosis, prognosis, and therapeutic monitoring. This work focuses on Diffuse Optical (DO) techniques, which offer a potential solution for identifying biomarkers for vascular diseases. DO techniques estimate hemodynamic-related parameters such as blood volume, flow, and oxygen saturation, which can help detect physiological differences between patients and healthy individuals. Despite their potential, DO techniques have limitations due to oversimplified assumptions about tissue structure, such as homogeneity and flatness. In this context, this research aims to refine these methodologies by investigating the impact of tissue heterogeneity and curvature on DO estimations. The thesis proposes enhanced models that better represent the macroscopic structural complexities of tissues, such as heterogeneity and non-planar geometries, which could significantly improve the accuracy of physiological parameter estimations.

The thesis encompasses a comprehensive approach to validate the methodologies that consider tissue heterogeneity and curvature when analyzing DO data. Furthermore, the research explores the combined effects of tissue curvature and heterogeneity on real DO data. It also addresses the biases introduced by darker skin tones on blood oxygen saturation estimations using optical methods, offering a preliminary correction strategy to mitigate this bias. The conclusion reached is that the refined methodologies enhance the accuracy of physiological parameter estimations, which could potentially improve early diagnosis and patient care. The investigation also concluded that a crucial aspect of accurate model predictions is integrating prior knowledge about the individual anatomy. By proposing and validating methodologies that can improve parameter accuracy by incorporating tissue macroscopic complexity, the research suggests that diffuse optical techniques could potentially meet the precision required for clinical applications in the future, moving a step closer to practical healthcare implementation.

RESUMO

A detecção precoce de doenças pode aumentar as chances de que um tratamento seja bem-sucedido e melhorar a eficiência do uso dos recursos de sistemas de saúde. Uma alternativa para se obter esta detecção precoce é através da identificação de biomarcadores, ou seja, parâmetros fisiológicos quantificáveis que sugerem a presença de uma doença específica. Os biomarcadores podem melhorar os cuidados de saúde de individuos, fornecendo informações valiosas que aprimoram o diagnóstico, prognóstico e monitoramento terapêutico. Este trabalho foca em técnicas Ópticas de Difusão (OD), que são uma potencial alternativa para seleção de biomarcadores de doenças vasculares. As técnicas de OD estimam parâmetros relacionados à hemodinâmica, bem como volume, fluxo e saturação de oxigênio sanguíneos, que podem ser úteis para viabilizar a detecção de diferenças fisiológicas entre pacientes e indivíduos saudáveis. Apesar de seu potencial, estas técnicas tem limitações devido a hipóteses simplificadas sobre a estrutura dos tecidos, como homogeneidade e planicidade. Neste contexto, esta pesquisa visa refinar as metodologias usadas com técnicas de OD investigando o impacto da heterogeneidade e curvatura dos tecidos nas estimativas. Esta tese propõe metodologias aprimoradas que representam melhor as complexidades estruturais macroscópicas dos tecidos, como heterogeneidade e geometrias não planares, capaz de melhorar significativamente a precisão das estimativas dos parâmetros fisiológicos.

Este texto traz abordagens que visam validar as metodologias que consideram a heterogeneidade e a curvatura dos tecidos ao analisar dados de OD. Além disso, a pesquisa explora os efeitos combinados de curvatura e heterogeneidade em dados reais. A tese também aborda os erros introduzidos por tons de pele mais escuros nas estimativas de saturação de oxigênio no sangue usando métodos ópticos, discutindo uma estratégia preliminar de correção para mitigar esse viés. Em resumo, concluiu-se que as metodologias refinadas apresentadas neste trabalho melhoram a precisão das estimativas dos parâmetros fisiológicos, o que pode potencialmente melhorar o diagnóstico precoce e o cuidado ao paciente no futuro. A investigação também concluiu que um aspecto fundamental por trás da precisão das estimativas dos modelos é a integração do algum conhecimento prévio sobre a anatomia individual. Ao propor e validar metodologias que podem melhorar a acurácia dos parâmetros incorporando a complexidade macroscópica dos tecidos, esta pesquisa sugere que técnicas de OD podem potencialmente atender à precisão necessária para aplicações clínicas no futuro, aproximando-se de uma implementação concreta no cuidado à saúde.

List of Figures

List of Tables

ABREVIATIONS AND ACRONYMS

$2L$	Two-Layered model
$[HbO]$	Oxy-hemoglobin concentration
$[HbR]$	Deoxy-hemoglobin concentration
$[HbT]$	Total hemoglobin concentration
β	DCS coupling experimental parameter
$\langle \Delta r^2(\tau) \rangle$	Mean-square displacement
ℓ	First layer thickness
ℓ_a	Absorption mean free path
ℓ_s	Scattering mean free path
ℓ_{tr}	Transport mean free path
λ	Wavelength
μ_a	Absorption coefficient
μ_s	Scattering coefficient
$\mu_s^{'}$	Reduced scattering coefficient
ω	Frequency of light amplitude modulation
ϕ	Photon fluence rate
ρ	Source-detector distance
τ	Delay time
ε	Extinction coefficient
ABP	Arterial blood pressure
CBF	Cerebral blood flow
$CrCP$	Critical closing pressure
$CW-DOS$	Continuous-wave Diffuse Optical Spectroscopy
D	Photon diffusion coefficient
DCS	Diffuse Correlation Spectroscopy
DO	Diffuse Optics
DOS	Diffuse Optical Spectroscopy
F	Blood flow index
$FD-DOS$	Frequency-Domain Diffuse Optical Spectroscopy
g	Anisotropic factor
$G_1(\tau)$	Electric field autocorrelation function
$g_1(\tau)$	Normalized electric field autocorrelation function
$G_2(\tau)$	Intensity autocorrelation function
$g_2(\tau)$	Normalized Intensity autocorrelation function

ITA^o	Individual topologic angle
J	Photon flux
L	Light radiance
$MAPE$	Median absolute percentage error
n	Refractive index
$NIRS$	Near-Infrared Spectroscopy
OD	Optical density
SDS	Source-detector separation (channel)
SI	Semi-infinite model
SRS	Spatially-Resolved Spectroscopy
StO_2	Blood oxygen saturation
z_b	Extrapolated-zero boundary condition distance

CONTENTS

CHAPTER 1

INTRODUCTION

In clinical settings, early detection of diseases could improve healthcare delivery and patient care. This improvement is a consequence of the increased likelihood of successful treatment and more efficient use of resources in healthcare, which are made possible by detecting diseases prior to significant clinical progression. Early detection, or at least early screening, is facilitated by analyzing biological indicators that reflect the health status of tissues. In this context, *biomarkers*, defined as quantifiable physiological indicators of tissue health, provide valuable insights that can guide clinical decision-making by offering a better understanding of disease mechanisms, improving diagnosis and prognosis, and aiding in developing and monitoring therapeutics [1]. By employing biomarkers, healthcare professionals can improve traditional diagnostic methods, leading to a more effective and patient-specific approach to disease management.

Current clinical practice already comprises the use of several specific biomarkers associated with unhealthy status across well-known diseases. For example, measuring glycosylated hemoglobin levels in blood provides an efficient manner of diagnosing and monitoring diabetes, in contrast to more invasive and time-consuming glucose tolerance tests [2]. Similarly, low-density lipoprotein cholesterol levels indicate cardiovascular disease risk, serving as a simpler assessment method than imaging-based diagnostics, such as angiography, that could be used for pre-screening purposes [3, 4]. The detection of salivary alpha-amylase has been extensively used to indicate stress and certain metabolic conditions [5, 6]. Prostate-specific antigens for prostate or CA-125 for ovarian cancer have significantly improved the ability to monitor disease evolution, offering an alternative to surgical biopsies or imaging procedures [7, 8]. These examples highlight the potential of biomarkers in reducing the need for expensive and burdensome diagnostic procedures, thus enhancing the efficiency of disease detection and management at a potentially lower cost.

A particular class of diseases in which early prognostics are critical are those with vascular impact. Such diseases are a leading cause of preventable death and disability, with significant social and economic impacts [9]. Conditions such as ischemic stroke, which results from an interruption of blood supply to specific brain regions, have the potential to ideally be anticipated by hemodynamic biomarkers that can provide blood flow, blood volume, or blood oxygenation within particular brain areas. Similarly, peripheral artery

diseases are related to impaired blood delivery to extremities and might be detected early by hemodynamic-related parameters. Identifying and accurately assessing hemodynamic biomarkers that reflect vascular impact in these cases can guide treatment decisions and potentially prevent severe outcomes.

Diffuse Optics (DO) offers the possibility of estimating blood flow and blood oxygenation in deep tissue (1-2 cm), thus holding promise as a tool for providing biomarkers for vascular diseases. Broadly speaking, diffuse optical techniques, such as *Diffuse Optical Spectroscopy* (DOS) and *Diffuse Correlation Spectroscopy* (DCS), involve emitting radiation in the near-infrared region (from ~ 700 to 900 nm). As biological tissue significantly scatters such radiation, one can acquire the backscattered light on the same illumination plane, a few centimeters from the illumination point. The detected signal provides information about the optical and dynamic properties of the tissue. These properties can be related to the tissue composition and dynamics, providing estimates of local oxygenation, blood volume, and blood flow. These physiological parameters enable insights regarding the tissue's hemodynamic and metabolic states, including changes in oxygen consumption and cellular activity indicative of various disease states [10]. Additionally, diffuse optical techniques are noninvasive and portable, and the optical data can be readily analyzed to estimate physiological information.

However, the impact of any biomarker on patient outcomes is dependent on various factors, including diagnostic accuracy [11]. Imprecise estimation can lead to incorrect physiological parameters and, consequently, to data misinterpretation and erroneous conclusions. This is precisely where most diffuse optical techniques currently fall short. Despite their great potential, the accuracy of optical properties obtained for biological tissue *in vivo* has room for improvement. Previous research has indicated that the optical properties obtained with diffuse optical techniques are often significantly underestimated, resulting in lower-than-expected hemoglobin concentrations [12, 13]. Similarly, the dynamical indices derived from DCS are also underestimated [14, 15], although it remains unclear whether these discrepancies in DCS arise primarily from this technique itself or are merely a consequence of the lower optical properties on which DCS relies.

The primary reason why optical properties obtained from diffuse optical spectroscopies are underestimated relates to spatial resolution. Since these techniques sample bulk regions, they lack the resolution to distinguish between different types of tissues within the sampled volume. This bulk averaging can distort the true signal from any specific tissue components, especially in highly heterogeneous samples, leading to *partial volume effects*. In the tissue bulk, the contribution of the microvasculature (which is the main structural tissue to which diffuse optics is sensitive) to the overall signal is overshadowed by other surrounding tissues, resulting in an underestimation of the properties measured with diffuse optical methods. In addition, most mathematical models used to interpret diffuse optical data often assume homogeneous tissue properties (i.e., that the tissue has the same physio-

logical properties) throughout the entire bulk. Despite their simplicity, these models do not account for partial volume effects, thus producing underestimated or inaccurate estimates of optical properties.

One potential solution to minimize partial volume effects in diffuse optical techniques is to increase spatial resolution by using multiple light sources and detectors to sample the same volume. While high-density devices can target smaller volumes of tissue, they lead to more complex devices that restrict their use in some clinical settings, particularly in applications targeting pre-screening [16–18]. Another possibility is to utilize more sophisticated models that account for tissue heterogeneity and other macroscopic features, reflecting the measurement more reliably. This latter option also enables accounting for other geometric features of real data acquisition, such as the biological tissue's curvature. Models of optical data analysis usually assume the air-tissue as a planar interface, which is not a suitable approximation for most real applications. As previously observed, this mismatch between the real and the assumed interface of data acquisition reduces the reliability of the tissue properties estimations [19–22].

In this context, this work aimed to investigate how modeling could improve the quantification of optical properties in biological tissue using diffuse optical spectroscopy. Here, I defend the thesis that models considering the macroscopic structural complexity of tissue can mitigate partial volume effects and thereby increase the accuracy of measurements obtained with diffuse optical techniques to the level they could be used as biomarkers for vascular diseases. To test this hypothesis, I approached this problem by using more detailed models that incorporate the most well-known sources of variability affecting the estimation of optical properties, which typically lead to a lack of accuracy. Importantly, I propose new methodologies that effectively utilize these detailed models to estimate optical properties in tissue. By comparing the accuracy of the estimated properties using these novel methodologies with the homogeneous, flat models broadly used in the literature, I was able to assess the impact of each feature from actual data acquisition on the estimations through optical data.

In order to present the work, I organized this thesis into eight chapters, including this one. Chapter 2 details the foundational principles of diffuse optical techniques, introducing the models that I utilized to analyze optical data. This chapter also contains information on how tissue physiology can be readily assessed from the backscattered detected light and the instrumentation used during this work. In Chapter 3, I present a clinical study performed with one diffuse optical technique in an intensive care unit (ICU) during COVID-19. This chapter illustrates the potential of optical properties to serve as biomarkers, showing that the physiological parameters derived with diffuse optical spectroscopy can provide valuable information about the microvasculature function status in patients diagnosed with severe acute respiratory syndrome (SARS) that correlates with clinical outcome.

Chapters 4 and 5 present my main contributions to improving the accuracy of optical estimations through models that consider the macroscopic structural complexity of tissue. In Chapter 4, I investigate the performance of an algorithm proposed to estimate the optical properties using the analytical solution of a heterogeneous model. In this work, we compared this model to the homogeneous model and investigated the influence of heterogeneity on optical estimations. In Chapter 5, I targeted the influence of curvature in the interface of data acquisition when estimating the optical properties. To approach this problem, I employed a numerical model to generate a set of possible configurations that could be used to solve the inverse problem using an exhaustive approach. This chapter presents the results obtained, as well as the implications of curvature on the accuracy of the optical properties.

Chapter 6 deals with an overwhelmingly ignored problem in the scientific community regarding the influence of skin color on the estimation of optical properties with diffuse optics. As the COVID-19 pandemic highlighted the problem of poor oxygen saturation estimations in black people, we decided to investigate this effect in diffuse optics as well. To approach this problem, I employed the heterogeneous model presented in Chapter 4 to account for the presence of a thin layer representing skin.

The previous three chapters investigated different factors that could affect the accuracy of the optical properties in diffuse optics separately. In Chapter 7, I present the pilot results of an analysis that combines more than one factor simultaneously. More specifically, I introduce one last model that accounts simultaneously for tissue heterogeneity and for the curvature in the interface of data acquisition and attempts to estimate the optical properties based on a previously defined configuration set generated with an exhaustive approach for the parameters of interest. Lastly, Chapter 8 finishes this thesis with the main conclusions from the different experiments performed throughout the previous chapters and points out future directions and perspectives on the problem of absolute quantification of the optical properties with diffuse optical spectroscopies.

CHAPTER 2

REVIEW ON THE PRINCIPLES OF DIFFUSE OPTICS

Diffuse Optical (DO) techniques are a set of methods that study how the backscattered radiation can provide information about a turbid medium in which an incident wave propagates. This chapter discusses the theoretical background of such techniques and the mechanisms for estimating information regarding biological tissue used in this work. To this end, I first introduce the relevant interactions between light and such medium. Then, I present the techniques used in this research and how they can be utilized to obtain physiological information on biological tissue. Although I aimed to be as general as possible, restrictions and assumptions made throughout the text were made considering applications to biological tissue, which is the focus of this work. I decided to move most of the calculations to Appendix A, which I highly recommend reading since it discusses some assumptions in the development of important equations in this chapter.

2.1 Light interaction with a medium

There are several possible interactions between radiations of any kind and matter. For this work, we will assume that the radiation is such that the only relevant interactions with the media are the absorption and elastic scattering events. As we will further discuss, this is the case for low-power radiations in the near-infrared region (650 – 900 nm) propagating into biological tissue.

When light enters an absorbing medium, its intensity is attenuated due to absorption events. Briefly, the molecules inside the medium absorb photons and transition to a higher vibrational or rotational energetic level. The excited molecules have expanded mechanical movements and generally release this extra energy through heat when colliding with other particles. Since the collisions occur faster than the molecule's relaxation time, the absorbed photon is not re-emitted. Therefore, each absorbed photon decreases the total light intensity. Since the number of interactions increases with the traveled distance, the medium attenuates the amplitude of the light beam while it travels through. Statistically speaking, one option to characterize this phenomenon is using the **absorption coefficient**, $\mu_a(\vec{r}, \lambda, t)$,

which represents the average number of absorption events experienced by light per unit of length traveled inside the medium. Such quantity depends on the light wavelength, λ, time, t, and position, $\vec{r}$, since the medium may not be homogeneous. In other words, the higher the μ_a, the higher the probability of absorption in $\vec{r}$. Alternatively, the *absorption mean free path*, $\ell_a = 1/\mu_a$, which is the average distance traveled by the radiation between subsequent absorptions, characterizes absorption events in a medium.

When several molecules may be present in a medium, μ_a is the linear sum of the absorption contribution of each molecule:

$$\mu_a(\vec{r}, \lambda, t) = \sum_i \varepsilon_i(\lambda) C_i(\vec{r}, t), \tag{2.1}$$

where C_i is the concentration of the i-th chromophore (i.e., constituents of the medium that absorb light), and ε_i is the *extinction coefficient*, which measures the absorption power per unit mole of a specific molecule in a given λ. This formulation is, in fact, the Beer-Lambert law, proposed centuries ago [23]. It is straightforward to see that if there are m chromophores in the medium and μ_a is known (or measured) for at least m wavelengths, it is possible to solve the set of m linear equations to find the concentrations of the chromophores inside the medium.

In addition to absorption, a medium may scatter light while it travels through. Briefly, scattering arises primarily from variations in the refractive index, which results from the heterogeneity within the medium. In this case, the interaction does not change the total light intensity within the medium, but it changes the direction of propagation of the light beam. On this limit, the incoming radiation forces the charges inside the medium to oscillate with the same frequency of the light, re-emitting this same frequency in several directions. As this phenomenon may occur outside the frequency of vibration of the particles, the amplitudes of oscillation are such that there is no energy loss by collisions, making it possible for the particles to re-emit light. Additionally, the light may cross an interface inside the medium, refracting and changing its direction. To statistically characterize scattering, the **scattering coefficient**, $\mu_s(\vec{r}, \lambda, t)$, represents the average number of scattering events experienced by light per unit length traveled into the medium. Similarly to absorption, the *scattering mean free path*, $\ell_s = 1/\mu_s$, which is the average distance traveled by light between subsequent scattering events, also characterizes scattering.

2.2 Models of Light Propagation in Turbid Media

The absorption and scattering events discussed in Section 2.1 co-occur (although in an exclusive way) for a given light beam traveling through a medium. Thus, when we shine light into a medium, the detected intensity differs from the incident one due to the combination of both interactions. Therefore, comparing both signals provides information regarding μ_a

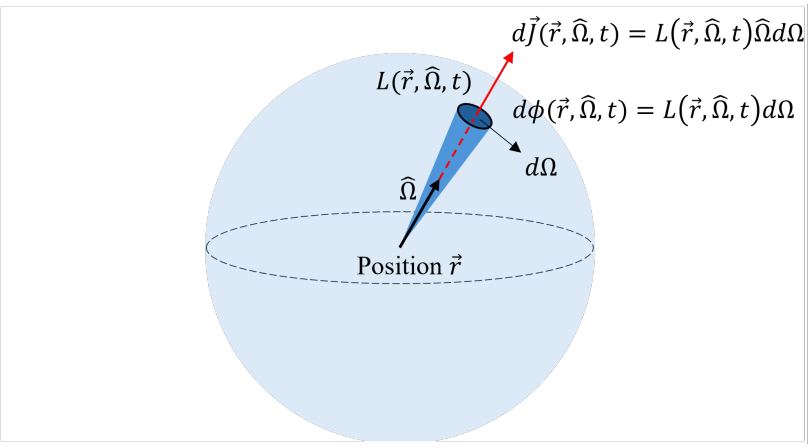

Figure 2.1: Representation of the quantities used to study light propagation in this section: the radiation (L), the photon flux ($\vec{J}$), and the photon fluence rate (ϕ).

and μ_s. This section exhibits the theory that aims to estimate these coefficients for a particular medium. First, we derive the **Radiative Transport Equation** (RTE). Then, after some manipulations, the **Photon Diffusion Model** is obtained. A representative illustration of the variables used in this chapter is in Figure 2.1. It is worth noting that this section follows the same rationale as [10, 24], which I highly recommend reading for a deeper understanding.

2.2.1 Radiative Transport Equation

Although Maxwell's equations describe light propagation in any media, including biological tissue, their complexity in handling multiple scattering/absorption motivates the search for another approach. In situations where light travels many times its wavelength, λ, between interactions, the electric field propagation is well approximated by lines, and we can use the light **radiance**, $L(\vec{r},\hat{\Omega},t)$, to quantify the power per unit area traveling in the $\hat{\Omega}$ direction outside an infinitesimal volume at position $\vec{r}$ and time t. The radiance can be used to describe light propagation through a medium in which several interactions occur. This assumption implies that $\ell_a, \ell_s >> \lambda$, and that light interference is negligible. For unpolarized light, L is proportional to the square of the electric field, $|\vec{E}(\vec{r},\hat{\Omega},t)|^2$, which is the only case we will discuss in this work. The RTE is a conservation equation that characterizes the changes in L in a specific position $\vec{r}$, in a given direction $\hat{\Omega}$ at time t (see the development in Appendix A.1):

$$\frac{1}{v}\frac{\partial L}{\partial t} + \hat{\Omega}\cdot\vec{\nabla}L = -(\mu_a+\mu_s)L + Q(\vec{r},\hat{\Omega},t) + \mu_s\int_{4\pi} L(\vec{r},\hat{\Omega}',t)f(\hat{\Omega},\hat{\Omega}')d\Omega'. \tag{2.2}$$

This equation explicitly states that the RTE represents the conservation of the radiance. The temporal and spatial changes over L are on the left side of the equation. On the right side, the first term represents the radiance losses due to scattering and absorption events. The following terms stand for the gains in L, either by sources that shine light at position $\vec{r}$ and direction $\hat{\Omega}$, or by summing all scattering events that produce photons at the same direction and position of L.

2.2.2 Photon Diffusion Model

Despite its simplicity compared to any other formulation, Equation 2.2 is still complex to solve. However, it can become simpler under some assumptions. For biological tissue, the radiance is nearly isotropic, so we can expand L using a spherical harmonics basis:

$$L(\vec{r},\hat{\Omega},t)=\sum_{l=0}^{N}\sum_{m=-l}^{l}\sqrt{\frac{2l+1}{4\pi}}\phi_{lm}(\vec{r},t)\,Y_{lm}(\hat{\Omega}).$$

By employing the steps described in Appendix A.2, we can write:

$$L(\vec{r},\hat{\Omega},t)=\frac{1}{4\pi}\phi(\vec{r},t)+\frac{3}{4\pi}\vec{J}(\vec{r},t)\cdot\hat{\Omega}\equiv L_1(\vec{r},\hat{\Omega},t), \tag{2.3}$$

where ϕ and J are defined in the Appendix terms of spherical harmonics quantities.

Equation 2.3 allows some insights about the physical interpretation of the previously defined $\phi(\vec{r},t)$ and $\vec{J}(\vec{r},t)$. By integrating the radiance over all solid angles:

$$\int L(\vec{r},\hat{\Omega},t)\,d\Omega=\frac{1}{4\pi}\int\phi(\vec{r},t)\,d\Omega+\frac{3}{4\pi}\int\vec{J}(\vec{r},t)\cdot\hat{\Omega}\,d\Omega\Rightarrow$$
$$\int L(\vec{r},\hat{\Omega},t)\,d\Omega=\frac{1}{4\pi}\phi(\vec{r},t)\int d\Omega+\frac{3}{4\pi}\vec{J}(\vec{r},t)\cdot\int\hat{\Omega}\,d\Omega.$$

As $\int d\Omega=4\pi$ and $\int\hat{\Omega}\,d\Omega=\vec{0}$:

$$\phi(\vec{r},t)=\int L(\vec{r},\hat{\Omega},t)\,d\Omega. \tag{2.4}$$

In other words, Equation 2.4 tells that $\phi(\vec{r},t)$ is the total power per unit area radially traveling outside the infinitesimal volume in $\vec{r}$ at time t. $\phi(\vec{r},t)$ is called the **photon fluence rate**, or simply *fluence*.

Now, multiplying Equation 2.3 by $\hat{\Omega}$ and integrating over all solid angles:

$$\int L(\vec{r},\hat{\Omega},t)\hat{\Omega}\,d\Omega=\frac{1}{4\pi}\phi(\vec{r},t)\int\hat{\Omega}\,d\Omega+\frac{3}{4\pi}\int(\vec{J}(\vec{r},t)\cdot\hat{\Omega})\hat{\Omega}\,d\Omega.$$

For any vector $\vec{V}$, the integral, $\int(\vec{V}\cdot\hat{\Omega})\hat{\Omega}\,d\Omega=\frac{4}{3}\pi\vec{V}$. Thus:

$$\vec{J}(\vec{r},t)=\int L(\vec{r},\hat{\Omega},t)\hat{\Omega}\,d\Omega. \tag{2.5}$$

Equation 2.5 says that $\vec{J}(\vec{r},t)$ is a vectorial sum of the radiance emerging from the infinitesimal volume in position $\vec{r}$ at time t. Moreover, $\vec{J}(\vec{r},t)\cdot\hat{\Omega}$ is the power per unit area traveling at the direction $\hat{\Omega}$ outside the infinitesimal volume in position $\vec{r}$ at time t. $\vec{J}(\vec{r},t)$ is called the **photon flux**, or simply *flux*. Note that in cases where L is perfectly isotropic $\big(L(\vec{r},\hat{\Omega},t)=L(\vec{r},t)\big)$, it comes out of the integral in Equation 2.5 and the right side vanishes, meaning $\vec{J}=\vec{0}$, i.e., there is no privileged direction. Yet, by Equation 2.4, $\phi=4\pi L(\vec{r},t)\neq 0$.

Thus, in cases where the radiance is approximately isotropic, $\phi >> |\vec{J}|$.

As $\vec{J}(\vec{r},t)$ and $\phi(\vec{r},t)$ come from L, we can employ few steps (see Appendix A.3) to obtain:

$$\vec{\nabla}\phi = -3(\mu_a+\mu_s)\vec{J}+3\mu_s g\vec{J},$$

assuming isotropic sources, $Q(\vec{r},\hat{\Omega},t) = Q(\vec{r},t)$, and slow temporal variation, $\frac{3\partial\vec{J}}{v\partial t} << 3(\mu_a+\mu_s-g\mu_s)\vec{J}$ (see next section for more details). By defining the **reduced scattering coefficient**, $\mu_s^{'} \equiv (1-g)\mu_s$, we have:

$$\vec{\nabla}\phi = -3(\mu_a+\mu_s^{'})\vec{J} \Longrightarrow \vec{J} = -\frac{1}{3(\mu_a+\mu_s^{'})}\vec{\nabla}\phi, \tag{2.6}$$

which is a Fick law between ϕ and $\vec{J}$. Using Equation 2.6 in Equation A.5:

$$-\vec{\nabla}\cdot\left(\frac{v}{3(\mu_a+\mu_s^{'})}\vec{\nabla}\phi\right)+v\mu_a\phi+\frac{\partial\phi(\vec{r},t)}{\partial t} = vS(\vec{r},t).$$

The **photon diffusion coefficient** can be defined as $D(\vec{r}) \equiv \frac{v}{3(\mu_a+\mu_s^{'})}$. Note that, in general, $D = D(\vec{r},t)$, since $\mu_a = \mu_a(\vec{r},t)$ and $\mu_s^{'} = \mu_s^{'}(\vec{r},t)$. The above equation then becomes:

$$\vec{\nabla}\cdot\Big(D(\vec{r},t)\vec{\nabla}\phi(\vec{r},t)\Big)-v\mu_a\phi(\vec{r},t)-\frac{\partial\phi(\vec{r},t)}{\partial t} = -vS(\vec{r},t). \tag{2.7}$$

Equation 2.7 is known as the *Photon Diffusion Model* since it is a diffusion equation for light fluence propagating through a medium.

Note that μ_s and g are never apart. Indeed, they always appear together, in the term we defined as $\mu_s^{'}$. Although there are estimations of g around 0.8 on biological tissue [25], using the RTE only allows the assessment of $\mu_s^{'}$. When g is closer to 1, a bias exists for scattering events oriented in the forward direction, which implies that the direction of each photon is not completely randomized after each scattering event. However, after a longer distance traveled, the number of partially biased scatterings combined randomize the direction of the photons, making it undergo a random walk step. Such distance is known as the *transport mean free path*, and it is approximately $\ell_{tr} \simeq 1/\mu_s^{'}$. An illustration of the phenomenon is in Figure 2.2. Note that as $g \approx 1$, $\mu_s >> \mu_s^{'}$ and $\ell_s << \ell_{tr}$, which means the photon experiences several scatterings over length ℓ_{tr}. The photon travels through this scheme until absorbed or leaves the medium.

The central assumption through all this algebra is that the radiance is nearly isotropic, which implies that $\phi >> |J|$. Indeed, if $\mu_s^{'} >> \mu_a$ (at least ten times, as a rule of thumb [26]) and the medium is large compared to ℓ_{tr}, this condition is fulfilled. In this context, photons travel tens of ℓ_{tr} before they are absorbed. Media whose $\mu_s{}' >> \mu_a$ are known as **turbid media**, and they are the target of this thesis, as biological tissue behaves as a turbid medium for near-infrared light.

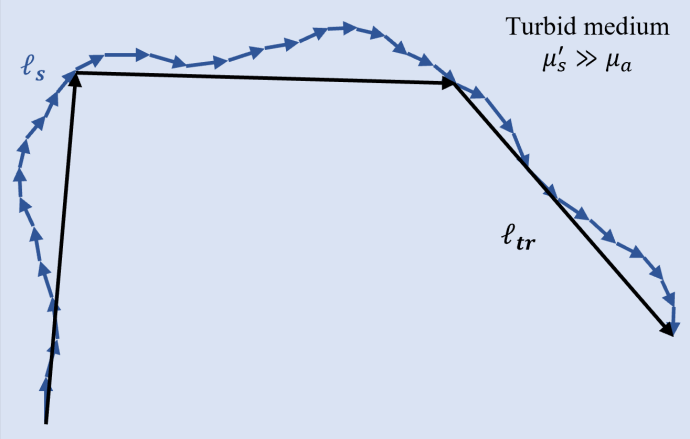

Figure 2.2: Photon path in a medium with a high anisotropic factor g and $\mu_s^{'} >> \mu_a$ (turbid medium). Note that the photon experiences several scattering events, biased in the forward direction until its macroscopic direction is randomized. The average distance traveled between scatterings is $\ell_s = 1/\mu_s$ and the randomization happens over a length of $\ell_{tr} = 1/\mu_s^{'} = 1/((1-g)\mu_s)$. Image based on [24].

2.3 Diffuse Optical Spectroscopy

Equation 2.7 rules the light fluence propagating in a turbid media with absorption coefficient μ_a, reduced scattering coefficient $\mu_s^{'}$, and refractive index n, given a source S. Solving this equation makes it possible to predict ϕ and use this prediction to adjust experimental data. As ϕ depends on the medium's optical properties, the solution that best fits the data estimates the medium's optical properties. Experimental techniques that employ this strategy are known as **Diffuse Optical Spectroscopy** (DOS) techniques.

However, since Equation 2.7 depends on the source term, the kind of information that we can obtain using DOS relates to the illumination pattern used. There are, essentially, three illumination techniques used in DOS: Frequency-Domain (FD-DOS), Time-Domain (TD-DOS), and Continuous-Wave (CW-DOS). Since we did not use TD-DOS in this work, and the analytical solutions for this method are inverse Fourier Transforms of the FD-DOS ones, we will focus only on FD-DOS and CW-DOS techniques. The temporal patterns of both methods are illustrated in Figure 2.3. For CW-DOS measurements (Figure 2.3b), a light with continuous amplitude is shined, and the detected intensity is attenuated due to scattering and absorption events. A light with intensity sinusoidal amplitude modulated over time is used for FD-DOS acquisitions (Figure 2.3c). Consequently, the detected signal is also oscillatory. TD-DOS measurements use pulsed lasers to obtain information regarding the medium.

A light source and detector used to obtain information regarding the medium is known as a *source-detector pair*, also referred to as a *channel* or *source-detector separation* (SDS, Figure 2.3a). Typically, light is irradiated using optical fibers and is detected a distance ρ away from the incidence point on the same plane. This arrangement is generally referred to as *reflection geometry*. It is worth pointing out that the directed light from the source fiber does not violate the assumption of isotropic sources discussed in the previous section within cer-

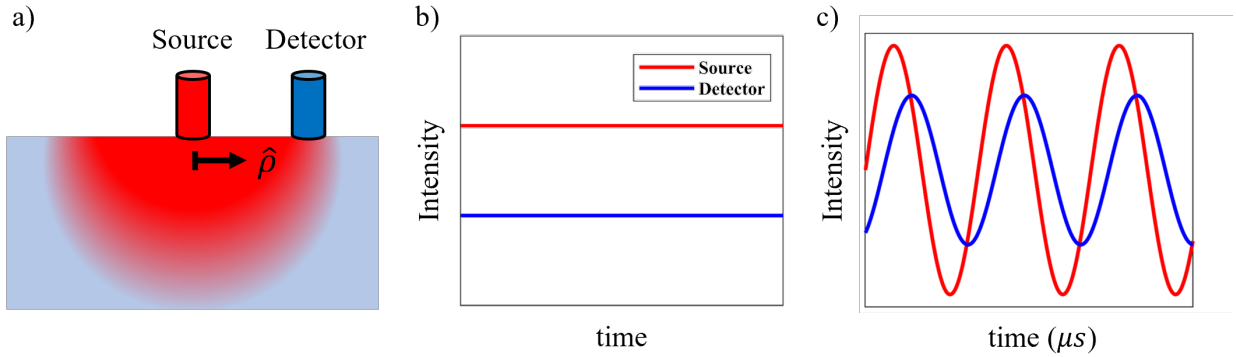

Figure 2.3: (a) Illustration of a channel (source-detector pair) used in DOS to obtain information regarding the media. (b) Illumination pattern used in CW-DOS measurements: the light intensity is constant over time. (c) Illumination pattern used in FD-DOS measurements: the light intensity is modulated sinusoidally over time.

tain restrictions. Indeed, the light source from an optical fiber is well approximated by an isotropic and point-like source at a distance ℓ_{tr} inside the medium if the source-detector separation is larger than $3\ell_{tr}$ [27]. It makes sense since the photons' direction of propagation is randomized after it travels ℓ_{tr} on average. By respecting this constraint, solutions to the photon diffusion model can estimate the medium's optical properties through an inversion procedure. The following sections deduce solutions for ϕ for some media under certain assumptions.

2.3.1 Frequency-Domain Diffuse Optical Spectroscopy

Within the scope of this work, FD-DOS is the most complex DOS technique in terms of illumination pattern. The main idea behind this method is to shine an intensity-modulated light at a point source, $S(\vec{r},t) = (S_{DC} + S_{AC}e^{i\omega t})\delta(\vec{r}-\vec{r}_s)$, and use both the attenuation and the time delay between the input and output signals to estimate the optical properties of the medium. Here, $\omega = 2\pi f$, where f is the modulation frequency, $\vec{r}_s$ is the position of the source, and δ is the Dirac delta function. Since the goal is to obtain information from the amplitude and the phase shift, the period of oscillation of the light source must "experience the medium" *at the same time*. In practice, this means that the period of oscillation of S must be small compared to the time spent by light in the medium between leaving the source and reaching the detector. As a rough estimate, if we assume the source-detector separation is 1 cm, that light travels approximately six times the distance between the source and the detector, and the refractive index of tissue is 1.4, the time spent by the light is $\sim (6\cdot 1)/v = (1.4\cdot 6)/(3\cdot 10^8) \sim 2.8\cdot 10^{-8} s$. Thus, f must be greater than $1/(2.8\cdot 10^{-8}) \sim 35MHz$ for detecting photons at 1 cm source-detector separation. Considering that we are interested in distances longer than 1 cm for probing deep tissue, commercial FD-DOS systems usually have $f \sim 100MHz$ or more.

Modulating S at hundreds of MHz suggests that the flux J will vary quickly, and it would violate the hypothesis of slow temporal variation. To hold the assumption true, we must have:

$$\frac{3\partial\vec{J}}{v\partial t} << 3(\mu_a + \mu_s^{'})\vec{J},$$

or, more precisely, as previously discussed,

$$\frac{3\partial\vec{J}}{v\partial t} + 3(\mu_a + \mu_s^{'})\vec{J} \approx 3(\mu_a + \mu_s^{'})\vec{J}.$$

Rewriting the left side, we have:

$$\frac{3\partial\vec{J}}{v\partial t} + 3(\mu_a + \mu_s^{'})\vec{J} \approx 3(\mu_a + \mu_s^{'})\left(\frac{\ell_{tr}}{v}\frac{\partial\vec{J}}{\partial t} + \vec{J}\right).$$

Let's consider that light spends t_{tr} time to travel ℓ_{tr}. Additionally, if we consider that the flux oscillates with the same frequency as S, $\vec{J} \approx \vec{J}e^{i\omega t}$, then:

$$\frac{3\partial\vec{J}}{v\partial t} + 3(\mu_a + \mu_s^{'})\vec{J} = 3(\mu_a + \mu_s^{'})(t_{tr}\, i\omega\vec{J} + \vec{J}) = 3(\mu_a + \mu_s^{'})(i\omega t_{tr} + 1)\vec{J}.$$

In other words, we must have:

$$3(\mu_a + \mu_s^{'})(i\omega t_{tr} + 1)\vec{J} \approx 3(\mu_a + \mu_s^{'})\vec{J},$$

which is true if $\omega t_{tr} << 1$. Again assuming $n = 1.4$ and typical values for optical properties of tissue ($\mu_a = 0.1cm^{-1}$ and $\mu_s^{'} = 10cm^{-1}$), we must have $f << 34GHz$. Then, assuming that we shine a light modulated with a frequency higher than tens of MHz and much smaller than tens of GHz, FD-DOS can estimate the medium's optical properties by using analytical solutions of the photon diffusion model.

Considering a source that can be represented as $S(\vec{r}, t) = (S_{DC} + S_{AC}e^{i\omega t})\delta(\vec{r} - \vec{r}_s)$, it is reasonable to find solutions to two terms: one related to the continuous component (DC component), and another associated with the oscillating (AC) component of the source. More specifically, it makes sense to expect the fluence to oscillate with the same frequency ω. In other words, we are searching for solutions with the form:

$$\phi(\vec{r}, t) = \phi_{DC}(\vec{r}) + \phi_{AC}(\vec{r})e^{i\omega t}.$$

Substituting this expression into Equation 2.7 results in a set of two equations:

$$\vec{\nabla}\cdot(D(\vec{r})\vec{\nabla}\phi_{DC}) - v\mu_a\phi_{DC} = -vS_{DC}\delta(\vec{r} - \vec{r}_s);$$

$$\vec{\nabla}\cdot(D(\vec{r})\vec{\nabla}\phi_{AC}) - (v\mu_a + i\omega)\phi_{AC} = -vS_{AC}\delta(\vec{r} - \vec{r}_s),$$

since complex exponentials of different arguments are linearly independent. If we assume the medium is homogeneous, i.e., $D(\vec{r}) = D$, the equations become:

$$(\nabla^2 - k_0^2)\phi_{DC} = -\frac{vS_{DC}}{D}\delta(\vec{r} - \vec{r}_s); \tag{2.8}$$

$$(\nabla^2 - k^2)\phi_{AC} = -\frac{\upsilon S_{AC}}{D}\delta(\vec{r} - \vec{r}_s), \tag{2.9}$$

where $k_0^2 = \upsilon\mu_a/D$ and $k^2 = (\upsilon\mu_a + i\omega)/D$. Note that the Equation 2.8 is Equation 2.9 with $\omega \to 0$ and $S_{AC} \to S_{DC}$. In other words, if we find a solution for one of these equations, we would have solved both. Additionally, S_{AC}, S_{DC} is usually taken as 1, and ϕ is calculated as a ratio of the source amplitude.

In summary, the equation for the fluence in turbid media is a Helmholtz equation in the frequency domain; its solution depends on the geometry and the boundary conditions assumed. The following subsections present the solutions for some geometries of interest. It is also important to consider that one can use fluence expressions to fit data; however, when using the reflection geometry (Figure 2.3a), the reflected intensity might be assumed as the flux expression using Fick's Law aiming a better agreement with experimental data.

Homogeneous, infinite media

Although this medium does not realistically represent tissue, finding the analytical solution of Equation 2.9 for this medium provides a physical intuition regarding the behavior expected for light propagation inside any turbid media. Since the medium is infinite, let's assume the source is centered at $\vec{r}_s = \vec{0}$ and the boundary condition is such that $\phi(\vec{r}) \to 0$ when $r \to \infty$. Note that assuming $S_{AC} = 1$ and omitting the sub-index AC, we can write Equation 2.9 as:

$$-(\nabla^2 - k^2)\frac{D\phi(\vec{r})}{\upsilon} = \delta(\vec{r}) \Rightarrow (\nabla^2 - k^2)\psi(\vec{r}) = \delta(\vec{r}),$$

where $\psi(\vec{r}) \equiv -D\phi(\vec{r})/\upsilon$. As this is a case of spherical symmetry, it is reasonable to suppose that $\psi(\vec{r}) = \psi(r)$, which reduces the equation to:

$$\frac{1}{r}\frac{d^2(r\psi(r))}{dr^2} + k^2\psi(r) = \delta(\vec{r}).$$

It is possible to verify that the solution of the above equation is

$$\psi(r) = -\frac{e^{-kr}}{4\pi r},$$

by remembering that $\nabla^2(FG) = \nabla^2 F + 2\vec{\nabla}F\cdot\vec{\nabla}G + \nabla^2 G$ and $\nabla^2(1/r) = -4\pi\delta(\vec{r})$. Thus:

$$\phi(\vec{r}) = \frac{\upsilon}{4\pi D}\frac{e^{-kr}}{r}.$$

Since k is a complex number, this solution means that the fluence through the medium is an overdamped wave. Including the temporal part (usually omitted since the reference is always the incident wave, $e^{i\omega t}$), the full solution is:

$$\phi(\vec{r},\omega) = \frac{\upsilon}{4\pi Dr}e^{-k_r r}e^{i(\omega t - k_i r)} \equiv A(r)e^{i(\omega t - \theta(r))},$$

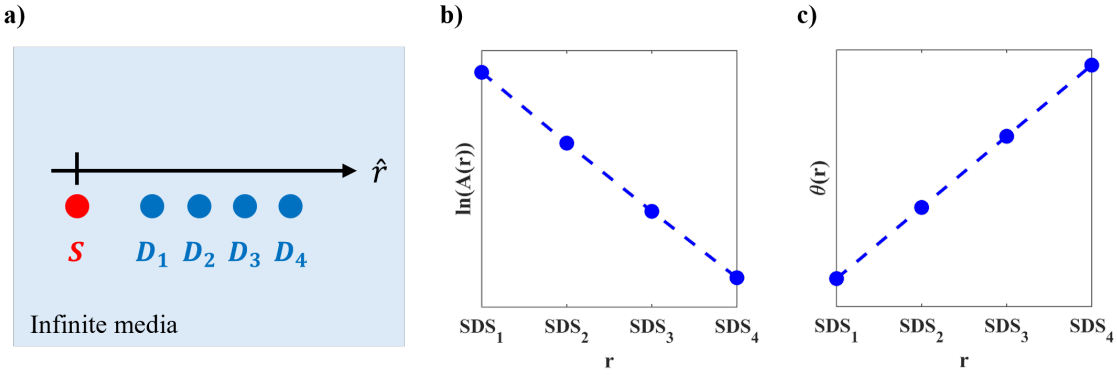

Figure 2.4: Illustration of an FD-DOS measurement in an infinite media. a) Infinite media, represented in blue, with one light source (red, S) and four detectors (blue, D_1 up to D_4). b) Behaviour of $ln(A(r))$ against the SDSs for the channels SDS_n (between source and detector D_n), $n = 1,...4$. Dots represent "experimental" data. c) Same as (b), but for $\theta(r)$.

where k_r and k_i are the real and imaginary parts of the complex wave-vector, k, $A(r) = v\,exp(-k_r r)/(4\pi D r)$, and $\theta(r) = k_i r$. Ideally, it would be possible to determine μ_a and $\mu_s^{'}$ (implicit dependencies on D and k) with just one channel using the previous expression. However, since we cannot be sure of the magnitude of S_{AC} that penetrates the medium, DOS usually employs more than one source-detector distance. A simple experimental setup (Figure 2.4a) measures the amplitude, A, and the phase shift, θ, of ϕ at several distances (usually three or more), and k_r and k_i can be obtained by calculating the slopes of $ln(A(r))$ vs r and $\theta(r)$ vs r (Figure 2.4b and 2.4c, respectively). After taking the square root of k, we can find that:

$$k_r = \sqrt{\frac{v\mu_a}{2D}}\sqrt{\sqrt{1+\left(\frac{\omega}{v\mu_a}\right)^2}+1};$$

$$k_i = \sqrt{\frac{v\mu_a}{2D}}\sqrt{\sqrt{1+\left(\frac{\omega}{v\mu_a}\right)^2}-1},$$

or, conversely,

$$\mu_a = \frac{\omega}{2v}\left(\frac{k_r}{k_i}-\frac{k_i}{k_r}\right);$$

$$\mu_s^{'} = \frac{2v}{3\omega}k_r k_i - \mu_a.$$

Thus, using multiple source-detector separations, one can readily assess k_r and k_i from the experimental data, which can be used to estimate μ_a and $\mu_s^{'}$. Although the expressions for more realistic media are not as simple, this solution provides a general framework to readily obtain optical information using FD-DOS measurements. Additionally, the experimental curves measured using FD-DOS resemble Figure 2.4.

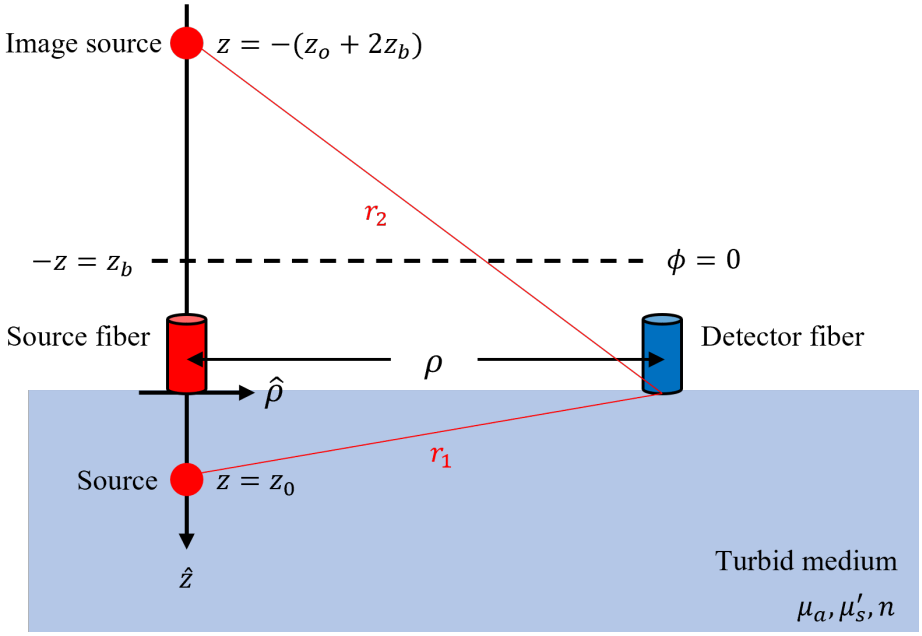

Figure 2.5: Illustration of the semi-infinite media. The turbid media is assumed as infinite in any direction perpendicular to the $\hat{z}$ axis. The air-tissue interface is positioned at $z = 0$ for convenience. Also, the figure exhibits important lengths in the algebra of the model.

Homogeneous, semi-infinite media (SI)

A more realistic approach for biological applications is the semi-infinite (SI) approach. In this geometry, we approximate the medium as infinite in two directions (e.g., the xy plane) and finite in the remaining one, where the interface with the outside medium is located (Figure 2.5). Although the SI medium is still a simplified model, this approach produces robust, average results in practice.

We must first set a boundary condition to find the analytical expression for this geometry. There are some choices, but the most common is the *extrapolated-zero boundary condition*, which assumes that the fluence decreases linearly outside the turbid medium and goes to zero at a distance z_b (see Equation B.4 in Appendix B).

The solution to this geometry can be obtained using the method of images [28]. The goal is to find a plane where $\phi = 0$ at a distance z_b outside the medium (see Figure 2.5), and since the point source alone is not able to achieve that, we add another fictional source (or *image source*) on the other side of the plane. To make sure the fluence is zero at the plane, this new source must have the opposite sign of the real one and must be at the same distance from the plane (i.e., $z_o + z_b$, where $z_o = \ell_{tr} = 1/\mu_s'$ by the point source approximation). The fluence produced on the detector is the sum of the (infinite media) fluences of both sources:

$$\phi(\rho) = \frac{v}{4\pi D}\left(\frac{e^{-kr_1}}{r_1} - \frac{e^{-kr_2}}{r_2}\right), \tag{2.10}$$

where $r_1 = \sqrt{(z-\ell_{tr})^2 + \rho^2}$ and $r_2 = \sqrt{(z+z_b+\ell_{tr})^2 + \rho^2}$, being z the detector position.

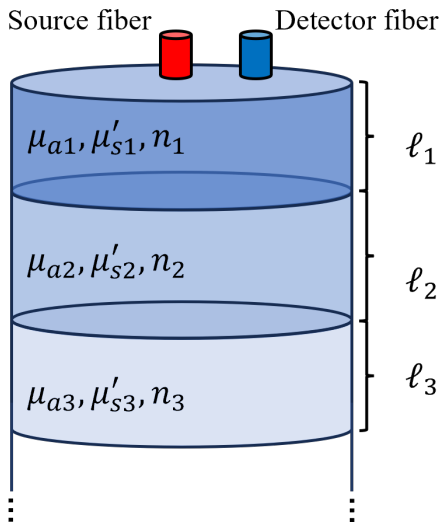

Figure 2.6: Illustration of a layered media. Note that, in this picture, the turbid medium is assumed to be a composition of several layers with different optical properties

If we assume that $\rho >> 2z_b + \ell_{tr}$, Equation 2.10 simplifies to:

$$\phi(\rho) = \frac{\upsilon e^{-k_r \rho}}{4\pi D \rho^2}[2k(z_b \ell_{tr} + z_b^2)]e^{-ik_i\rho} \equiv \tilde{A}(\rho)e^{-i\tilde{\theta}(\rho)},$$

and the slopes of $ln\left(\rho^2 \tilde{A}(\rho)\right)$ vs ρ and $\tilde{\theta}(\rho)$ vs ρ are k_r and $-k_i$, respectively. From this point, one can estimate the optical properties using the same approach presented before for the infinite medium (Figure 2.4).

Alternatively, one can use Equation 2.10 as a model to predict the fluence at a point on the interface where the detector is located and define a cost function that compares the predicted and measured fluences. The minimization of this cost function with respect to the model parameters (μ_a and $\mu_s^{'}$ in this case) provides an optimal solution that approximates the optical properties of the medium. This approach can be formalized as an inverse problem discussed in Section 2.5.

Layered media

A sophistication of the SI model is to consider a turbid media as a composition of several homogeneous slices of different optical properties (Figure 2.6). Although it increases the complexity of the model, it captures more nuances in realistic situations. When used *in vivo* experiments, such as on acquisitions on the head, the different layers can mimic the scalp, skull, cerebrospinal fluid, and cortex. Since there is no further gain of physical intuition regarding this geometry, I will only present the main results below. For more information, I suggest reading the deduction of this solution for two layers in a cylinder of radius a that is available in the literature [29]. In my opinion, the only step that is not clear enough is the calculation of the z function, $G_k(s_n, z, \omega)$, so you can find a more detailed development in Appendix C.

Briefly, Equation 2.9 is solved for each layer as a homogeneous medium, with the source located in the first layer. Then, the extrapolated-zero boundary condition is imposed at all interfaces with the external medium, as well as continuity of ϕ and J through each layer:

$$n_{k+1}^2(\phi_k)|_{k;k+1} = n_k^2(\phi_{k+1})|_{k;k+1};$$

$$D_k(J_k^{\perp})|_{k;k+1} = D_{k+1}(J_{k+1}^{\perp})|_{k;k+1},$$

where A_k is a notation denoting quantity A of layer k, $A|_{k;k+1}$ indicates the quantity A evaluated at the interface between layers k and $k+1$, and $J^{\perp}$ is the component of $\vec{J}$ perpendicular to the interface between two layers. For a point source located at the center of the first layer:

$$\phi_k(\rho) = \frac{1}{\pi a'^2}\sum_{n=1}^{\infty} G_k(s_n, z, \omega) J_0(s_n\rho) J_1^{-2}(a' s_n), \tag{2.11}$$

where J_m is the Bessel function of order m, $a' = a + z_{bk}$, s_n are such that $J_m(a' s_n) = 0, n = 1,2,3...$, and:

$$G_1(s_n, z, \omega) = \frac{e^{-k_1|z-z_0|} - e^{-k_1(z+z_0+2z_{b1})}}{2D_1k_1} + \frac{sinh(k_1(z_0+z_{b1}))sinh(k_1(z+z_{b1}))}{D_1k_1e^{k_1(\ell_1+z_{b1})}} \times \frac{D_1k_1n_1^2\beta_3 - D_2k_2n_2^2\gamma_3}{D_1k_1n_1^2\beta_3 cosh(k_1(\ell_1+z_{b1})) + D_2k_2n_2^2\gamma_3 sinh(k_1(\ell_1+z_{b1}))},$$

where $\beta_3 = sinh(k_2(\ell_2+z_{b2}))$ and $\gamma_3 = cosh(k_2(\ell_2+z_{b2}))$. Since DOS methods acquire the fluence on the first layer in a reflective geometry (as in Figure 2.6), only G_1 is needed. Using these equations, the only possibility to estimate μ_a and μ_s' of each layer is through an optimization approach. The more layers considered in the model, the greater the number of variables to estimate. Thus, DOS studies usually use two-layer (2L) or three-layer (3L) models, and even in these cases, problems with accuracy and numerical stability are common [13, 29–32].

Alternative Geometries

The analytical solutions obtained when using the symmetries and boundary conditions I exhibited so far yield numerically stable solutions that closely resemble experimental DO measurements (i.e., Figure 2.4). However, those geometries lack characteristics of real data acquisition. For instance, both the SI and 2L models do not consider the curvature at the acquisition data interface. One alternative to this problem I investigated is to change the position of the source at the Liemert's 2L model [29] to the side of the cylinder, so that the cylinder curvature may mimic the biological tissue curvature. However, this new analytical solution only resembles DO measuremets for small cylinder radius (around 2 cm), which is

not reliable for real cases.

Aiming to obtain an analytical solution that takes into account more macroscopic features of real data acquisition, I solved the Photon Diffusion Model for a homogeneous sphere and for a heterogeneous cylinder (which I refer to as the two-layered concentric cylinder). The highlights of the solutions are in Appendix D. However, my analytical solutions fail to produce reliable curves that match experimental observations. I hypothesize that those discrepancies are primarily due to numerical instabilities that arise during the computation process, as when dealing with exponential functions of large numbers or other mathematically complex functions related to these geometries. The exponential growth or rapid oscillations in the functions can lead to computational errors or the breakdown of numerical methods, resulting in unreliable results. Thus, to address this problem, I decided to use numerical models to solve the Photon Diffusion Model, which I will further discuss in Section 2.3.3.

2.3.2 Continuous-Wave Diffuse Optical Spectroscopy

In CW-DOS, only the amplitude of light intensity is available as a measurement. From a theoretical perspective, one can analyze the behavior of photon transport by taking $\omega \to 0$ in the solutions to Equation 2.9 derived above. Thus, for an infinite, homogeneous medium, the CW solution is:

$$\phi(\rho) = \frac{v}{4\pi D}\frac{e^{-k_0\rho}}{\rho},$$

where $k_0^2 = v\mu_a/D$. It is straightforward to note that it is not possible to separate μ_a and $\mu_s^{'}$ using this single expression [33]. Therefore, most CW-light approaches estimate μ_a considering some assumptions regarding D or $\mu_s^{'}$. Despite this intrinsic limitation compared to FD or TD techniques, CW approaches have the advantage of using simpler instrumentation, which is more affordable than its FD and TD counterparts.

Spatially-Resolved Spectroscopy (SRS)

Considering the SI approximation for the medium and making the large ρ approximation, the fluence for the CW case can be derived from Equation 2.10 in the limit $\omega \to 0$:

$$\phi(\rho) = \frac{v}{4\pi D}(2k_0(z_b\ell_{tr} + z_b^2))\frac{e^{-k_0\rho}}{\rho^2}.$$

The **optical density**[1], defined as $OD(\rho) = -ln(\phi(\rho)/S_{DC})$, is (since we assumed $S_{DC} = 1$):

[1] It is also common to define the *absorbance*, which represents the same as the optical density, but the $\log_{10}$ is used instead of the natural logarithm.

$$OD(\rho) = -ln\left(\frac{v}{4\pi D}(2k_0(z_b\ell_{tr} + z_b^2))\right) + k_0\rho + 2ln(\rho),$$

thus

$$\frac{\partial OD(\rho)}{\partial \rho} = k_0 + \frac{2}{\rho}.$$

As $\mu_s^{'} >> \mu_a$, $D \approx v/(3\mu_s^{'})$ and the expression becomes:

$$\frac{\partial OD(\rho)}{\partial \rho} = \sqrt{3\mu_a\mu_s^{'}} + \frac{2}{\rho}.$$

Since we can measure $OD(\rho)$, and the goal is to estimate the optical properties, the best that the above equation can provide is:

$$\mu_a\mu_s^{'} = \frac{1}{3}\left(\frac{\partial OD(\rho)}{\partial \rho} - \frac{2}{\rho}\right)^2.$$

In other words, this approach can only estimate the product $\mu_a\mu_s^{'}$, which is not of great help in obtaining physiological information regarding the tissue. As previously discussed, μ_a is related to the concentration of absorbers inside the medium. Thus, in exchange of properly determining $\mu_s^{'}$, it is preferred to estimate μ_a. Assuming all the particles inside the medium are spherical and of a size similar to the λ of the light, the scattering can be modeled as $\mu_s^{'} = a\lambda^{-b}$ [34,35]. Considering near-infrared radiation $(650-900nm)$, this expression is well approximated for biological tissue by $\mu_s^{'} = \alpha(1-\beta\lambda)$ [36,37]. Thus:

$$\alpha\mu_a = \frac{1}{3(1-\beta\lambda)}\left(\frac{\partial OD(\rho)}{\partial \rho} - \frac{2}{\rho}\right)^2.$$

Usually, data acquisition involves collecting data with a few source-detector separations, making it impossible to calculate a numerical derivative. To adjust for real measurements, we write:

$$\alpha\mu_a = \frac{1}{3(1-\beta\lambda)}\left(\frac{\Delta OD(\rho)}{\Delta \rho} - \frac{2}{\rho}\right)^2.$$

An illustration of how to estimate the term between parenthesis is the following: let's say we have a source at the origin and two detectors, one at the position $\rho_1 = 1cm$ and the other at $\rho_2 = 2cm$. In this situation, the term in parenthesis is:

$$\frac{OD(\rho_2) - OD(\rho_1)}{\rho_2 - \rho_1} - \frac{2}{1.5},$$

assuming $(\rho_2 + \rho_1)/2 = 1.5cm$.

One can calibrate the device and estimate α and β using phantoms that mimic the medium under study. By assuming these constants would not change in real situations, this

technique provides estimates of μ_a for each λ. Since fluence measurements may be subject to different coupling factors under different media (see section 2.3.4), the most accurate estimation of SRS is $\alpha\mu_a$. This approach is known as *spatially-resolved spectroscopy* (SRS).

Modified Beer-Lambert approach

Although SRS is a robust method for estimating optical properties, it depends on appropriately calibrating the acquisitions for $\mu_s^{'}$. Considering that $\mu_s^{'} >> \mu_a$, the fluence for infinite media is:

$$\phi(\rho) = \frac{v}{4\pi D}\frac{e^{-\sqrt{3\mu_s^{'}\mu_a}\rho}}{\rho} \equiv \frac{v}{4\pi D\rho}e^{-\mu_{eff}\rho},$$

where $\mu_{eff} = \sqrt{3\mu_s^{'}\mu_a}$. This expression is similar to the Beer-Lambert law for purely absorbing media, $I(\rho) = I_0 exp(-\mu_a\rho)$, but with the attenuation coefficient depending additionally on scattering. On purely absorbing media, μ_a is estimated through the optical density, $OD(\mu_a) \equiv -ln(I(\rho)/I_0) = \mu_a\rho$.

In some circumstances, we are interested in the changes in absorption coefficient in a short period of time (i.e., from seconds to minutes). For these cases, there is an implicit dependence on time t, i.e., $\mu_a = \mu_a(t)$. However, in scattering media, $OD = OD(\mu_{eff}) = OD(\mu_a, \mu_s^{'})$. Thus, we can relate **temporal changes** in OD in a small timestamp from $t = 0$ to t to changes in the optical properties by [28]:

$$OD(t) = OD(0) + \left(\frac{\partial OD}{\partial \mu_a}\right)\Big|_0 (\mu_a(t) - \mu_a(0)) + \left(\frac{\partial OD}{\partial \mu_s^{'}}\right)\Big|_0 (\mu_s^{'}(t) - \mu_s^{'}(0)) \Rightarrow$$

$$\Delta OD = L(\rho)\Delta\mu_a + \frac{\mu_a(0)}{\mu_s^{'}(0)}L(\rho)\Delta\mu_s^{'},$$

where $L(\rho) \equiv (\partial OD/\partial\mu_a)|_0$ is the *differential pathlength*, which is an estimation of the distance traveled by the light between the source and the detector when they are ρ apart. The second term on the right side is small when compared to the first since $\mu_s^{'} >> \mu_a$. Additionally, in biological tissues, scattering changes are negligible in the time scale considered. Under these conditions, $\Delta OD = L(\rho)\Delta\mu_a$ is an approximation that relates the changes in the optical density, measured in an experiment, with changes in μ_a. In turn, changes in μ_a relate to changes in the concentrations of the absorbers inside the medium. Although it is out of the scope of this work, it is worth mentioning that tracking changes in μ_a is the pillar of functional neuroimaging.

2.3.3 Numerical Models

Light fluence can also be estimated through numerical models. Methods such as the **Finite Element Method** (FEM) are suitable to simulate outcomes at irregular geometries or in media with a highly varying range of optical properties [38, 39]. Essentially, this method subdivides the entire domain into smaller parts (the so-called *finite elements*). In practice, one defines a domain under analysis through a **mesh**, i.e., a set of K tetrahedrons (elements) joined at U vertices, organized side-by-side to build a specific volume. Each element is taken as a finite element in the FEM. The light transport equation (2.9) is then numerically solved within each element, resulting in a detailed representation of light propagation.

Since the FEM might be used for heterogeneous media, it can deal with the Photon Diffusion Model originally written for FD-DOS as:

$$\left(\vec{\nabla}\cdot D(\vec{r})\vec{\nabla} - v\mu_a(\vec{r}) - i\omega\right)\phi(\vec{r}) = -S(\vec{r}).$$

A solution of this equation for $\phi(\vec{r})$ is also a solution of:

$$\int_V \psi(\vec{r})\left(\vec{\nabla}\cdot D(\vec{r})\vec{\nabla} - v\mu_a(\vec{r}) - i\omega\right)\phi(\vec{r})dV = -\int_V \psi(\vec{r})S(\vec{r})dV,$$

where V is the entire domain under analysis, and $\psi(\vec{r})$ is a test function attending the same boundary conditions as $\phi(\vec{r})$. Integrating by parts the first term on the left-hand side, we obtain:

$$\int_V \psi(\vec{r})\vec{\nabla}\cdot D(\vec{r})\vec{\nabla}\phi(\vec{r})dV = \oint_A \psi(\vec{r})D(\vec{r})\vec{\nabla}\psi(\vec{r})\cdot d\vec{A} - \int_V D(\vec{r})\vec{\nabla}\phi(\vec{r})\cdot\vec{\nabla}\psi(\vec{r})dV,$$

where A is the surface that encloses the volume V. Thus:

$$\int_V \left(D(\vec{r})\vec{\nabla}\psi(\vec{r})\cdot\vec{\nabla}\phi(\vec{r}) + v\mu_a\psi(\vec{r})\phi(\vec{r}) + i\omega\psi(\vec{r})\phi(\vec{r})\right)dV = \int_V \psi(\vec{r})S(\vec{r})dV + \oint_A \psi(\vec{r})D(\vec{r})\vec{\nabla}\psi(\vec{r})\cdot d\vec{A}.$$

Thus, solving the Photon Diffusion Model is the same as solving the previous equation for $\forall\psi(\vec{r})$. For the purpose of the method, the choice is to expand $\psi(\vec{r})$ in a basis $\psi_i \in \{\psi_i\}$, $i = 1,...,U$, and if ϕ satisfies the equation $\forall\psi_i$, than it is the optimal solution of this FEM problem with U nodes. In practice, since $\psi(\vec{r})$ is expanded, the formulation finds $\phi(\vec{r}) = \sum_{i=1}^{U}\phi_i\psi_i(\vec{r})$ [40, 41]. Using this expansion choices for ϕ and ψ, the Photon Diffusion Model becomes a matrix expression:

$$\left(A(D) + B(v\mu_a + i\omega)\right)\phi = C + \beta,$$

$$A_{ij} = \int_V D(\vec{r})\vec{\nabla}\psi_j(\vec{r}) \cdot \vec{\nabla}\psi_i(\vec{r}) dV,$$

$$B_{ij} = \int_V (v\mu_a(\vec{r}) + i\omega)\psi_j(\vec{r})\psi_i(\vec{r}) dV,$$

$$C_j = \int_V \psi_j(\vec{r}) S(\vec{r}) dV,$$

$$\beta_j = \oint_A \psi_j(\vec{r}) D(\vec{r}) \vec{\nabla}\psi(\vec{r}) \cdot d\vec{A}.$$

Thus, the problem is to find the nodal fluence, ϕ_i, for each vertex. In other words, it becomes a problem of inverting a sparse matrix. In diffuse optics, a popular choice to simulate light transport using FEM is NIRFASTer [39, 42]. This software employs a piecewise continuous polynomial function as the expansion basis choice and uses a bi-conjugate gradient stabilized iterative solver to solve this matrix problem. Additionally, the source term is treated as a Gaussian source to match the profile at the end of the optical fiber.

Usually, FD-DOS (i.e., $|\phi|$ and $arg(\phi)$) and DCS ($G_1(\tau)$, refer to Section 2.4) are estimated using a mesh by setting a position for the light source and the detectors and solving the set of equations for each vertex. Meshes can reproduce the assumed geometry of the SI and 2L models. However, as one can build any mesh, this method is particularly useful for situations in which a more realistic model of the medium is required, and there is no analytical expression for the geometric model. Also, FEM can be used together with high-quality volume meshes generated from medical images, improving the mesh quality and the reliability of optical simulations through the forward problem [42].

2.3.4 Coupling factors between optical fibers and turbid media

Previous sections discussed how light fluence, ϕ, can be readily estimated in turbid media from a theoretical perspective (using either analytical or numerical approaches). Experimentally, however, diffuse optical spectroscopy measures the backscattered light *intensity*, which is proportional to ϕ. The proportionality coefficient depends on the details of the optical fibers used and how they are coupled with tissue (see Appendix E). In practice, the fluence measured through intensity, ϕ^m, is related to the theoretical fluence by:

$$\phi^m = C\phi,$$

where C is the *coupling factor* between the optical fiber and the turbid medium. C depends on the detector's sensitivity, the fiber material, the physical coupling between the fiber and the medium, the surface properties, and other factors [43–45]. In systems where optical fibers guide light in both ends (sources and detectors), $C = C_S C_D$, where C_S and C_D are the

coupling factors of the source and the detector, respectively.

For a source-detector pair, C is an additional unknown. Since ϕ is a complex quantity, it is expected that $C = C_A e^{-iC_\theta}$. Thus, there are at least four parameters to be determined in a real problem: $C_A, C_\theta, \mu_a, \mu_s^{'}$. Adding more source-detector pairs would not necessarily solve the problem since it would introduce more unknowns (amplitude and phase of the coupling factor for each pair introduced).

One possible solution is to use *calibrating phantoms*, i.e., blocks large enough to be considered semi-infinite media. Considering that the optical properties of these phantoms are known, μ_a^{ref} and $\mu_s^{'ref}$, it is possible to use this information to find the coupling factors. Since we know the source-detector separation, the λ of the radiation, ω, and n, the expected fluence can be estimated using Equation 2.10: $\phi(\mu_a^{ref}, \mu_s^{'ref}) = A_{teo} exp(-i\theta_{teo})$. By collecting experimental data on the phantoms, we obtain $\phi^m = A_m exp(-i\theta_m)$. Thereby:

$$C = \frac{\phi^m}{\phi} \Rightarrow C_A e^{-iC_\theta} = \frac{A_m}{A_{teo}} e^{-i(\theta_m - \theta_{teo})}.$$

Consequently, $C_A = A_m / A_{teo}$ and $C_\theta = \theta_m - \theta_{teo}$. Performing this process for every source-detector separation and light wavelength, one can estimate the calibration factors that must be used to compare experimental measurements with their predicted values. This method, however, relies on the assumption that the coupling factors between the turbid medium and the optical fibers are the same as in the phantom. Hairy regions, for example, compromise the coupling between the fibers and the tissue, so the calibration method does not work well in these regions.

Given that the coupling factors for a specific source-detector pair can change throughout an experiment due to uncontrolled circumstances (e.g., motion artifacts), it is common to rely on several SDSs and normalize the intensity of each channel by the intensity measured at the shortest separation (or any channel with a good signal-to-noise ratio).

2.4 Diffuse Correlation Spectroscopy (DCS)

So far, I have discussed how the DOS techniques involved in this work obtain information about a turbid medium from the backscattered light. Another technique to obtain information about a medium is *Diffuse Correlation Spectroscopy* (DCS). In DCS, fluctuations of the detected light intensity are quantified and related to the movement of the scatterers inside the medium. As DCS is not the main focus of this work, this section will focus more on presenting the general idea of the technique. Please refer to [24, 46] for a more detailed development and discussion.

Consider a continuous-wave light beam propagating through a turbid medium. Suppose the intensity of the incident light is constant, and the configuration of the medium does not change over time. In that case, the detected intensity is expected to be constant for

a time interval Δt long enough so that any statistical fluctuations of photon arrivals are averaged out. At short time scales $t \ll \Delta t$, however, the stochastic nature of scattering will give rise to small fluctuations in the detected light. The fact that particles are constantly moving, either by Brownian motion or due to directed motion (as is the case of cells in blood vessels), changes the spatial configuration of the scatterers, which produces a different intensity on the detector and increases the intensity fluctuations at short time scales. Thus, the fluctuations in the recorded intensity (Figure 2.7b) carry information regarding the motion of the scatterers.

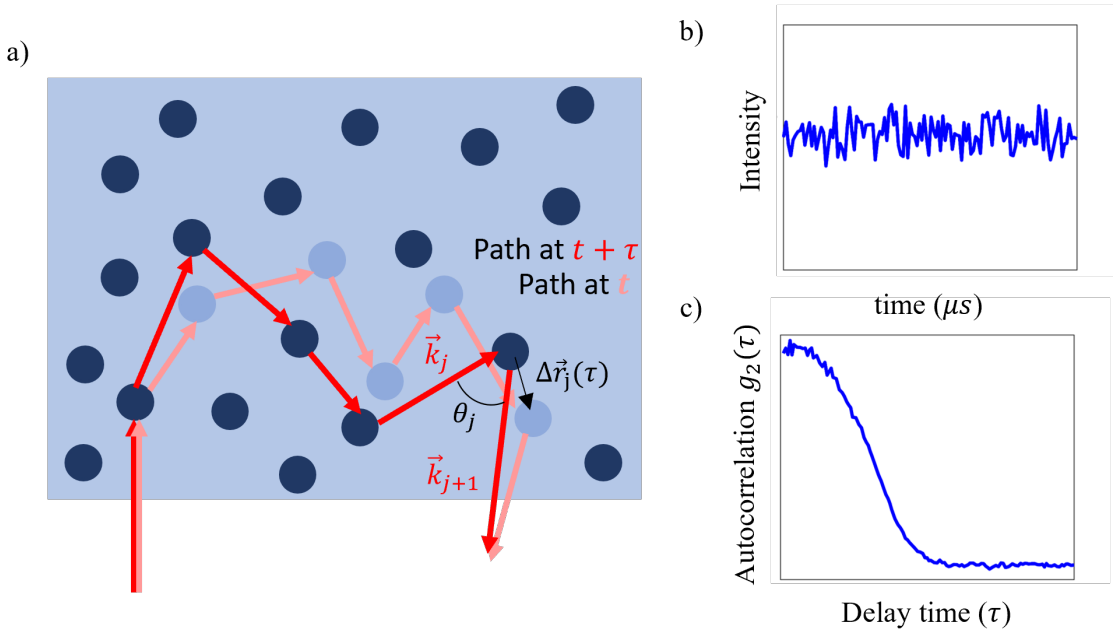

Figure 2.7: a) Set of scatterings that produce the path traveled by the light at time t (red) and at a posterior time, $t+\tau$ (rose). The dark blue circles represent the scatterers at time $t+\tau$, while the blue ones represent some of them at time t. The wave vector before the j-th scattering is $\vec{k}_j$, and it becomes $\vec{k}_{j+1}$ after the interaction, rotating at an angle θ_j. As an example, a particle moves $\Delta\vec{r}_j(\tau)$ from t to $t+\tau$. b) Intensity recorded at a scale of μs. c) Autocorrelation function of the intensity at b).

In the event of light traveling through a dilute medium, where it will be scattered at maximum once before leaving the medium, the detected electric field, $\vec{E}(t)$, is a superposition of all the contributions from each scatterer. Since the particles are in motion, the phases of the scattered fields change and the recorded light also changes as a consequence. One can extract information from the detected fluctuations through a *temporal autocorrelation function*. The temporal autocorrelation function of some quantity $A(t)$ is defined as:

$$g(\tau) \equiv \frac{\langle A^*(t)A(t+\tau)\rangle}{\langle |A(t)|^2\rangle},$$

where $\langle\cdot\rangle$ represents an *ensemble* average and τ is known as *delay time*. Note that $g(\tau) = 1$ if $A(t)$ is constant. Additionally, $A(t) \neq A(t+\tau)$ unless τ is much smaller than the typical time of fluctuation in A. Thus, $A(t+\tau)$ is similar (or correlated) with $A(t)$ if τ is small. However,

the similarity between $A(t+\tau)$ and $A(t)$ is lost as τ increases. Therefore, the autocorrelation function is a metric of how much $A(t)$ is getting different from itself through a time translation, and it decreases with increasing τ (Figure 2.7c). The denominator, $\langle|A(t)|^2\rangle$, normalizes the fraction since the maximum value of $\langle A^*(t)A(t+\tau)\rangle$ occurs when $\tau = 0$.

For independent particles with isotropic dynamics, the electric field autocorrelation function is [46]:

$$g_1(\tau) \equiv \frac{\langle \vec{E}^*(t)\vec{E}(t+\tau)\rangle}{\langle|\vec{E}(t)|^2\rangle} \Rightarrow g_1^s(\tau) = e^{2\pi i f \tau} e^{-q^2\langle \Delta r^2(\tau)\rangle/6}, \tag{2.12}$$

where f is the light frequency, and $\vec{q} \equiv \vec{k}_f - \vec{k}_i$, where $\vec{k}_f$ and $\vec{k}_i$ are the wave vector after and before the scattering event, respectively. $\langle \Delta r^2(\tau)\rangle$ is the *mean-square displacement* of the scatterers at τ. Note that the greater the motion of the scatterers (greater $\langle \Delta r^2(\tau)\rangle$), the faster the decay in $g_1(\tau)$. This is expected since the motion of the particles changes the spatial configuration that produced the measured signal, and this change in intensity becomes faster when scatterers move quickly.

However, obtaining $g_1(\tau)$ directly in experiments is hard. In turn, the intensity autocorrelation function, $g_2(\tau) = \langle I(t)I(t+\tau)\rangle/\langle I(t)^2\rangle$ can be measured, and $g_1(\tau)$ is estimated through the *Siegert's relation* [47],

$$g_2(\tau) = 1 + \beta|g_1(\tau)|^2, \tag{2.13}$$

where β is a constant related to the experimental setup. Typically, $\beta = 0.5$ for highly scattering media with single-mode fibers and unpolarized light (see Appendix F).

Equation 2.12 results from a model for single scattering. In turbid media (Figure 2.7a), each scattering event contributes to the fluctuations in the detected intensity. Although there are methods to treat this problem, there is a more interesting approach through the same formalism of the radiative transport equation (Equation 2.2). The idea is that the radiance could be written as

$$L(\vec{r},\hat{\Omega},t) = \langle I(\vec{r},\hat{\Omega},t)\rangle \propto \langle \vec{E}^*(\vec{r},\hat{\Omega},t)\cdot\vec{E}(\vec{r},\hat{\Omega},t)\rangle = G_1(\vec{r},\hat{\Omega},t,\tau=0),$$

where $G_1(\vec{r},\hat{\Omega},t,\tau) \equiv \langle \vec{E}^*(\vec{r},\hat{\Omega},t)\cdot\vec{E}(\vec{r},\hat{\Omega},t+\tau)\rangle$ is the unnormalized temporal autocorrelation function for the electric field. With this modification, a *Correlation Transport Equation* for turbid media can be derived [48]:

$$\frac{1}{v}\frac{\partial G_1(\vec{r},\hat{\Omega},t,\tau)}{\partial t} + \hat{\Omega}\cdot\vec{\nabla}G_1(\vec{r},\hat{\Omega},t,\tau) = (\mu_a+\mu_s)G_1(\vec{r},\hat{\Omega},t,\tau) + Q(\vec{r},\hat{\Omega},t) + \mu_s\int_{4\pi} G_1(\vec{r},\hat{\Omega},t,\tau)g_1^s(\hat{\Omega},\hat{\Omega}',\tau)f(\hat{\Omega},\hat{\Omega}')d\Omega', \tag{2.14}$$

where g_1^s is the single scattering function defined in Equation 2.12. For $\tau = 0$, Equation 2.14

reduces to Equation 2.2. To write Equation 2.14, it is assumed that the speed of light is greater than the speed of the particles, which means that the autocorrelation function is calculated instantaneously for each τ, i.e., the particles may be considered static for a given (small) τ. A more detailed discussion can be found on [48], but the general idea is that the electric field autocorrelation is not conserved in scattering events (as energy and radiance are). For each scattering and each increase in τ, less G_1 should be transported. Thus, we must analyze carefully the terms $\mu_s L$ and the last term of Equation 2.2 to change to Equation 2.14.

It is easy to see that the first term should be only switched to $\mu_s G_1$, since scattering out of $\hat{\Omega}$ decreases the radiance in that direction but also decreases the G_1 function due to the scattering outward $\hat{\Omega}$. In Equation 2.2, however, the scatterings that resulted in a photon propagating in the $\hat{\Omega}$ direction increase the radiance due to energy conservation. However, since it comes from a scattering event, the amount of G_1 transferred into the $\hat{\Omega}$ direction depends also on the correlation after a single scattering event, given by g_1^s. So, we must account not only for the probability of the scattering results in $\hat{\Omega}$ but also for the amount of correlation lost on the scattering by including g_1^s inside the integral.

The advantage of using Equation 2.14 is that it is identical to Equation 2.2. Thus, we can implement similar steps as the one previously exhibited to obtain a diffusion model for the autocorrelation function [49]:

$$\left(\vec{\nabla}\cdot(D(r)\vec{\nabla}) - v\mu_a(r) - \frac{\alpha}{3}v\mu_s^{'}K_0^2\langle\Delta r^2(\tau)\rangle\right)G_1(r,\tau) = -vS(r),$$

where $G_1(r,\tau) = \int G_1(r,\hat{\Omega},\tau)\,d\Omega = \langle\vec{E}^*(r,t)\cdot\vec{E}(r,t+\tau)\rangle$, $S(r) = \int Q(r,\hat{\Omega})\,d\Omega$, $K_0 = 2\pi/\lambda$, and α is the fraction of scattering events due to moving (i.e., not static) particles. For homogeneous media, the equation becomes:

$$(\nabla^2 - K^2(\tau))G_1(\vec{r},\tau) = \frac{-vS_{DCS}}{D}\delta(\vec{r}-\vec{r}_s), \tag{2.15}$$

where $K^2(\tau) \equiv v(3\mu_a + \alpha\mu_s^{'}K_0^2\langle\Delta r^2(\tau)\rangle)/(3D)$; we usually assume $S_{DCS} = 1$. Note that Equation 2.15 is the same as Equation 2.9 with $\phi \to G_1$ and $k \to K$. Thus, G_1 and ϕ must have the same solutions (with $k \to K$) for the same geometries and boundary conditions, including the SI and 2L geometries calculated in Section 2.3.

As in DOS measurements, the temporal autocorrelation function can also be estimated with numerical models, such as the FEM using volumetric domains through meshes [39,42]. Thus, by normalizing the predicted G_1 and using Siegert's relation, one can predict $g_2(\tau)$ to compare with experimental measurements. At this step, β must be assumed as it is an experimental parameter.

In experiments, a photon counter records the light intensity through single-mode optical fibers and feeds a correlator that computes $g_2(\tau)$. A long-coherence light source must be used to maximize speckle contrast in acquisitions. Siegert's relation allows the estimation of $g_1(\tau)$ from experimental data, from which $\langle\Delta r^2(\tau)\rangle$ can be inferred. Since DCS also

depends on the optical properties μ_a and μ_s', ideally DOS and DCS are performed together. When DCS is used alone, typical values of optical properties must be assumed, unless DCS is performed with at least two wavelengths [50, 51]. Additionally, the type of the scatterers' motion must be considered. Two theoretical models fit experimental evidence: Brownian motion and random flow [52–54]. In the first one, $\langle \Delta r^2(\tau) \rangle = 6 D_B \tau$, where D_B is an effective Brownian diffusion coefficient, but orders of magnitude greater than Einstein's. In the second model, $\langle \Delta r^2(\tau) \rangle = \langle V^2 \rangle \tau^2$, where $\langle V^2 \rangle$ is the second moment of the distribution of particles' speed.

2.5 Solving the Inverse Problem

The models presented in Section 2.3 can be used to solve the so-called *forward problem*: given the geometry (which defines the model) and its optical properties, one can predict the optical measurements (i.e., the fluence in DOS or the autocorrelation function in DCS) at any location. Both analytical and numerical models are suited for this purpose. Analytical expressions are generally faster and more general to work with. On the other hand, numerical models are able to deal with more complex geometries at the cost of more computational time and memory.

However, in practice, real experiments involve the *inverse problem*. Here, one acquires experimental data (DOS and/or DCS) using a predefined array of sources and detectors in a given geometry, while the optical properties (μ_a, μ_s' in DOS, and $\langle \Delta r^2(\tau) \rangle$ in DCS) are unknown. This problem can be mathematically formulated as a *combinatorial optimization problem*, i.e., it requires minimizing an *objective function*[2] $H(w)$ with respect to a set of all possible configurations, $\mathcal{W}$:

$$w^\star = \underset{w' \in \mathcal{W}}{\arg\min}\, H(w'), \tag{2.16}$$

so that $w^\star$ is the *optimal* configuration solution. Any combinatorial optimization problem can always be solved exhaustively by computing $H(w')$ for all $w' \in \mathcal{W}$, and then selecting the optimal solution. While this method is exact (i.e., it's guaranteed to find the *global* optimal solution), it is intractable for most real-world problems due to combinatorial explosion.

When the set $\mathcal{W}$ is infinite (e.g., if w can assume any real value), it is possible to find an optimal solution by discretizing the configuration set ($\mathcal{W}'$) and creating a **look-up table** which contains a list of every value of the input, $w' \in \mathcal{W}'$, and its associated output, $H(w')$. This approach, however, is only exact within the reduced configuration space, which is dependent on the discretization resolution.

In the specific problem involving DO techniques, the configuration set $\mathcal{W}$ is the Euclidean space $\mathbb{R}^D$, where D is the number of parameter dimensions. Typically, the objective

[2] The objective function can also be called cost function, loss function, or error function, depending on the context.

function $H(w)$ is not convex and has many local optima, so the method to solve 2.16 does not necessarily seek to find the global optima. In this case, one of the most widely used methods for solving problem 2.16 is the *sequential gradient descent*. In this approach, the optimal configuration is found through an iterative process guided by the gradient of the objective function:

$$w_{n+1} = w_n - \alpha H_w(w),$$

with $w_0 \in \mathbb{R}^D$ being an *initial guess*. Here, H_w is the gradient of $H(w)$ with respect to the parameters w, and $\alpha > 0$ is a constant that determines how quickly the minimum is reached. It is clear from the formulation above that this approach requires the objective function to be differentiable.

A common objective function employed in this situation is the *square loss function*, which is the square of the difference between the prediction of the model, denoted as $f(w, x_i)$, and the corresponding output, y_i:[3]

$$H(w) = \sum_{i=1}^{N} \big(f(w, x_i) - y_i\big)^2, \tag{2.18}$$

Here, we assume the model is a function of the parameters to be optimized, w, and N independent variables, x_i. For example, considering the DOS problem in a semi-infinite geometry, x represents the different source-detector separations, y_i is the fluence measured by the detector at the i-th source-detector separation, $w = [\mu_a, \mu_s^{'}]^T \in \mathbb{R}^2$, and $f(w, x_i)$ is the fluence predicted by the SI model at each source-detector separation considered in the problem (Equation 2.10).

When the model is linear, so that $f(w, x) = w_1 x_1 + w_2 x_2 + ... + w_k x_k$, the optimization problem with the square loss function is the so-called *least squares regression*. For this problem, the gradient can be analytically computed, and the expression can be used within the gradient descent approach to find the approximate optimal solution. For nonlinear models, computing the gradient can be quite complex, although there are methods available to approximate the gradient, such as the Levenberg–Marquardt or Newton-Raphson. In this work, I used an algorithm based on the interior-point method [55] implemented in MATLAB (*fmincon* function), which allows for the definition of boundaries and constraints on the parameters. Briefly, this method adds barrier functions to the original problem, penalizing any parameter that violates the constraints of the problem, ensuring that the subsequent interactions remain within the feasible region.

[3] It is worth noting that the most general form of the square loss function should be given by

$$H(w) = \alpha \sum_{i=1}^{N} \big(f(w, x_i) - y_i\big)^2, \tag{2.17}$$

where α is a constant. On several occasions, it is common to define the *mean squared error* (MSE) function, which represents the square loss function with $\alpha = 1/N$.

When the forward problem uses a numerical model (Section 2.3.3), the iterative nature of the gradient descent approach requires the reevaluation of the model at each step, which involves performing the simulation with the new set of parameters. This is a slow process that requires a high computational cost. For this reason, when dealing with numerical models in the forward problem, I opted to use a look-up table solution. Although this approach is even slower than computing the gradient descent steps, it can provide a more reliable (global) solution within a certain parameter resolution. In addition, the range of optical properties for actual tissue can be greatly reduced based on previous experimental data. In this work, we constrained μ_a from 0.05 to 0.3 cm^{-1} in steps of $0.005cm^{-1}$, and $\mu_s^{'}$ from 5 to 15 cm^{-1} in steps of 0.1 cm^{-1} (unless stated otherwise). This choice led to a resolution of 1.5 $\mu molar$ in $[HbO]$, 0.9 $\mu molar$ in $[HbR]$ and approximately 0.4% in StO_2. Considering the noise observed in FD-DOS brain data, those resolutions were enough for our research.

2.6 Diffuse Optical Techniques and the Biological Tissue: Near-Infrared Spectroscopy (NIRS)

Once the optimal solution for the optical properties is found through the inverse problem, we can use them to estimate physiological parameters of biomedical interest. As it has been implied since the beginning of this chapter, biological tissue behaves as a turbid media for radiations between $\sim 650-900nm$, which means that all the discussion above holds for it. Because of this specific window in the electromagnetic spectra, DOS (which, historically, was the first DO technique attempted in biological tissue) is often referred to as *Near-Infrared Spectroscopy (NIRS)*. This section discusses specifically how μ_a (obtained from DOS) and $\langle \Delta r^2(\tau) \rangle$ (obtained from DCS) carry physiological information.

Typical values of μ_a in tissue are around $0.1cm^{-1}$, while $\mu_s^{'} \sim 10cm^{-1}$ [56–58], validating the main assumption that $\mu_s^{'} >> \mu_a$. To make sure that the point source approximation holds, the separation between source and detector should exceed $3\ell_{tr} \approx 0.6cm$ since it is not hard to find tissues with $\mu_s^{'} \sim 5cm^{-1}$. In this context, ℓ_{tr} is far greater than λ, validating the approximation $\ell_{tr} >> \lambda$. Additionally, g is close to 1 (typically 0.8), so the photon path inside biological tissue is as illustrated in Figure 2.2. However, it is worth noting that the photon diffusion model is not perfect. The rotational assumption may fail close to the more superficial axon fiber bundles in the cortex [59].

In biological tissue, scattering is mainly due to spatial changes in the refractive index, such as when light travels in and out of some tissue, cell, or organelle, or simply because light travels through regions of different densities so that the refractive index changes on the scale of λ. Thus, light scattering can be seen as a rough estimation of tissue heterogeneity. Since light interacts with particles of size comparable to λ, scattering in biological tissue can be well modeled with Mie scattering [60], which is not isotropic, to reinforce the bias toward

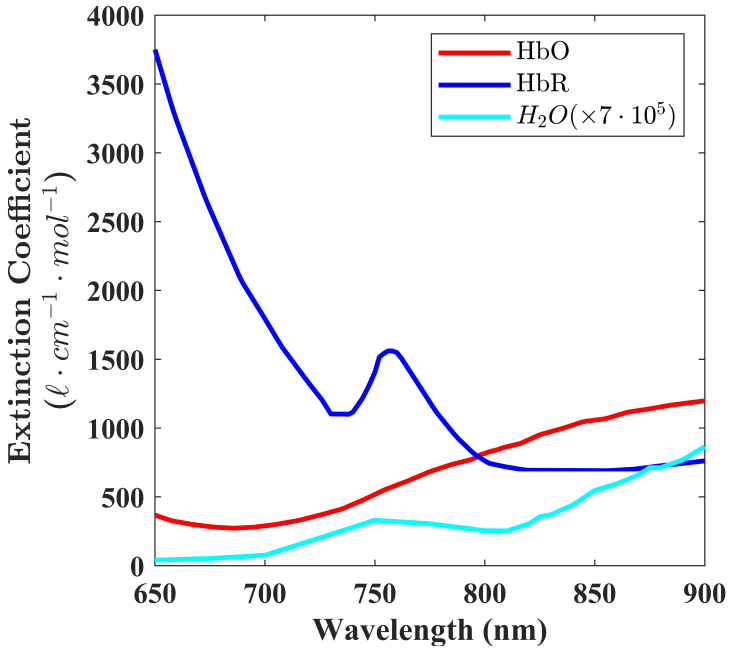

Figure 2.8: Extinction coefficient of the main absorbers of NIRS light. Note that we multiplied the water values by 10^6 since it is roughly the ratio of how much it is more concentrated than oxyhemoglobin. Data available on https://omlc.org/spectra/index.html.

forward scatterings.

A small fraction ($\sim$ 10%) of all scatterers in tissue come from red blood cells, which are moving within the blood and carry hemoglobin [61, 62]. Red blood cells are a major component of biological tissue that interacts with NIR light. Despite their directed motion within blood vessels, it has been found that DCS data are better adjusted by considering a diffusive model ($\langle \Delta r^2(\tau) \rangle = 6 D_B \tau$, where D_B is an effective diffusion constant) [63]. Since α can not be directly measured, a **Blood Flow Index** (F) is commonly defined as $F \equiv \alpha D_B$. Thus, although F is not a direct measurement of blood flow, it has been shown that this quantity is proportionally related to blood flow [64].

Lastly, recalling Equation 2.1, μ_a brings information about the composition of biological tissue that absorbs near-infrared light. Figure 2.8 illustrates the extinction coefficients, ε, of the main tissue absorbers, which are essentially oxyhemoglobin (HbO) and deoxyhemoglobin (HbR). Lipids are absorbers below $600nm$, while H_2O is a main absorber beyond $900nm$.[4] Thus, NIRS brings information regarding tissue oxygenation through hemodynamics. Metabolic information can also be inferred in certain cases since the hemoglobin carries oxygen (HbO) and delivers it (becoming HbR) to tissues around the body.

Considering the above, Equation 2.1 can be written as:

[4] To estimate the ε of water (H_2O) in Figure 2.8, I divided the tabulated absorption coefficient by 55 mol/ℓ, its molar concentration. To graph it, I multiplied by $7 \cdot 10^5$ since it is roughly the ratio between water and hemoglobin concentration in biological tissue.

$$\mu_a(\lambda) = \varepsilon_{HbO}(\lambda)[HbO] + \varepsilon_{HbR}(\lambda)[HbR] + \varepsilon_{H_2O}(\lambda)[H_2O],$$

where $[HbO]$ and $[HbR]$ are the concentrations of oxy and deoxy-hemoglobin, respectively. Since the absorption coefficient of H_2O, $\mu_a^{H_2O}$, is tabulated, it is more useful to write the previous equation as:

$$\mu_a(\lambda) = \varepsilon_{HbO}(\lambda)[HbO] + \varepsilon_{HbR}(\lambda)[HbR] + f_{H_2O}\mu_a^{H_2O}(\lambda),$$

where $0 \leq f_{H_2O} \leq 1$ is the fraction of water in tissue. Thus, at least three wavelengths must be used to properly account for all chromophores. An often-used alternative to decrease experimental complexity is to assume a value for f_{H_2O} and use only two wavelengths to estimate $[HbO]$ and $[HbR]$, or simply (but less desirable) neglect that water term since it is smaller than the other two terms, especially in cases where the exact absolute value is not so important (e.g., comparisons between groups). Of course, using more wavelengths than the minimum necessary is positive since it reduces the systematic errors in the estimations of $[HbO]$ and $[HbR]$.

The concentrations of HbO and HbR allow the assessment of other two relevant parameters for clinical applications. The first one is the **total hemoglobin concentration**, $[HbT] = [HbO] + [HbR]$, which is proportional to local blood volume. The second one is the blood **oxygen saturation**, $StO_2 = (100\%) \times [HbO]/[HbT]$, which provides a picture of the local oxygenation $1-2cm$ depth in the biological tissue. Together with F, these parameters are often suggested as indicators of the physiological health of tissues in general. Clinical problems that lead to vascular impacts, such as stroke, disturb these values from a physiological healthy range.

To close this section, two final comments are worth making. First, source-detector separations (SDSs) must be chosen wisely. Typically, DO techniques estimate information from approximately one-third to half the SDS depth. This means that smaller channels, $1-2cm$, with a high signal-to-noise ratio (SNR), bring very little information of deep tissues. As the SDS increases, DO techniques probe deeper tissues but with a worse SNR. From my experience, SDSs way above $3.5cm$ are too noisy to obtain information in most applications (forehead acquisitions, for example, are exceptions). Techniques that use several SDSs, such as FD-DOS and SRS, must ideally spread the channels in the range of $1.5-3.5$ or 4 cm at most. Second, specifically for SRS, what is estimated is $k\mu_a$, which allows estimations for $k[HbO]$ and $k[HbR]$ (see section 2.3.2). Despite the k factor, the technique still estimates absolute values of StO_2 since k cancels out in the division.

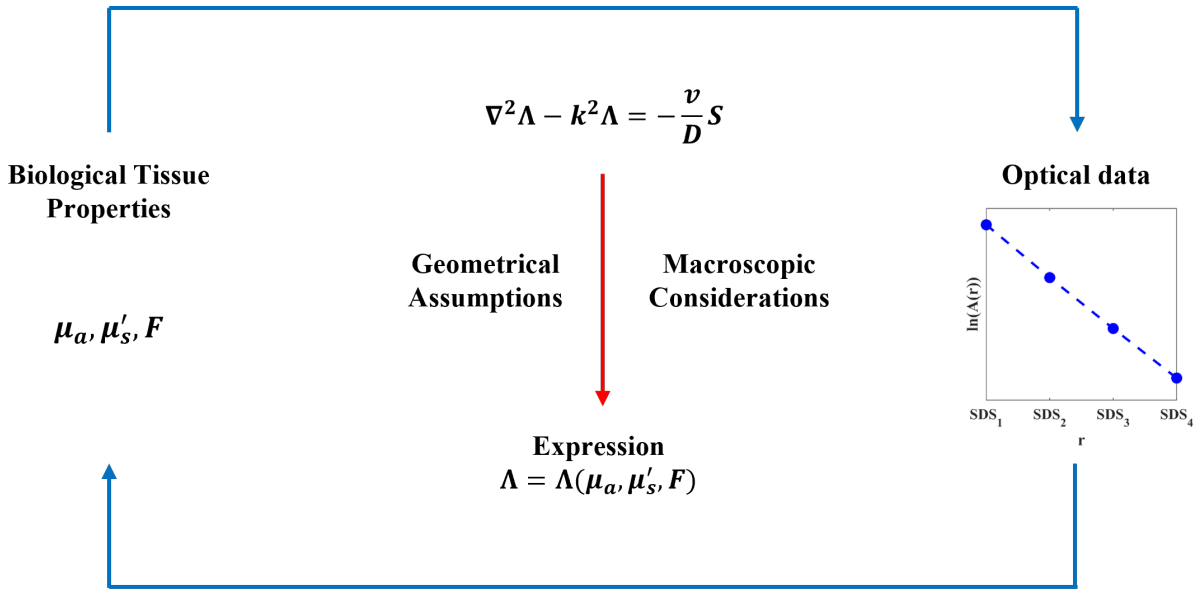

Figure 2.9: General framework of obtaining biological tissue information through DO techniques.

2.7 Brief Overview of Optical Estimations Framework

The general expression to describe the light propagation in a turbid media is written in Figure 2.9. There, Λ is either ϕ when considering the FD-DOS technique or G_1 when considering the DCS technique (in this case, $k \rightarrow K$). Solving the diffusion model means finding a model for Λ, relating experimental measurements with the properties DO techniques aim to estimate regarding biological tissue (i.e., μ_a, $\mu_s^{'}$, and F). For a specific Λ expression obtained, this issue can be split into the forward and the inverse problems. The model at last must satisfy the forward problem, i.e., given the tissue properties, $\Lambda = \Lambda(\mu_a, \mu_s^{'}, F)$ must generate curves that resemble experimental optical data, illustrated by $ln(A(r))$ versus r in Figure 2.9. However, the main interest is solving the inverse problem. In other words, the goal is to find a model that estimates μ_a and F from experimental data with high accuracy since these quantities are related to physiological parameters.

As in the solution of any differential equation, finding Λ involves making assumptions for the macroscopic and geometrical features of the medium (i.e., the biological tissue). Currently, the SI model is the most used approach in the area. Although it estimates optical properties with high accuracy on homogeneous phantoms [65], the accuracy decreases in heterogeneous media that mimic tissues stratified into layers [13], such as in cortical investigations using DO. This suggests that the accuracy of the SI model has room for improvement in real scenarios. An available model to better incorporate the macroscopic complexity of biological tissue in the estimations is the 2L model. Although research suggests that it increases the accuracy when compared to the SI model in heterogeneous phantoms (errors reducing from 5-20% to 5-7%) [13], the accuracy in estimating parameters is still not ideal due to the cross-talk between the numerous parameters to be assessed [32]. Thus, develop-

ing a method that increases the numerical stability of estimations when solving the inverse problem is relevant in achieving high accuracy.

I aim to list two other macroscopic biological tissue features that influence estimations' accuracy when solving the inverse problem: curvature and superficial layers. Both have not been extensively investigated in DO literature. The former is because available analytical models do not deal with the forward problem since they do not reproduce experimental acquisitions. The few investigations use non-reasonable assumptions, such as a huge curvature or $\mu_a = 0$ [21]. The latter is probably because the issues when estimating StO_2 in people with darker skin tones became more evident during the COVID-19 pandemic. Since pulse oxymeters were the most used technique, research using DO techniques (as described in this work) has yet to be made.

This work aims to increase the accuracy when solving the inverse problem using DO techniques. I approached the heterogeneity feature by developing methodologies that improve the stability of 2L estimations. Additionally, I proposed methods to incorporate the curvature and the influence of the superficial layers, such as skin, in optical estimations. The following chapters aim to further elucidate these issues and introduce the approaches I developed.

2.8 Diffuse Optical Systems used in this work

This research comprised experiments involving FD-DOS, DCS, and SRS acquisitions. Figure 2.10 shows a photo of the optical devices used: a commercial SRS device (Portamon, Artinis Medical Systems, The Netherlands), a commercial FD-DOS device (Imagent, ISS Inc., USA), and a homemade continuous-wave DCS device.

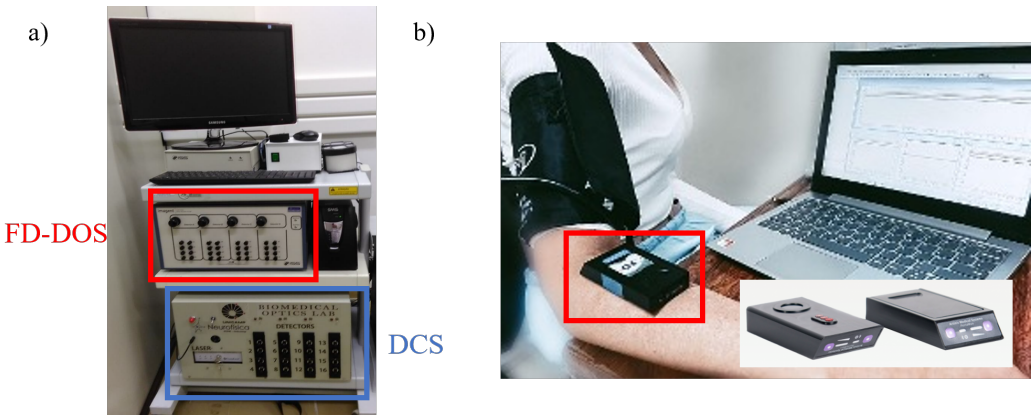

Figure 2.10: Optical systems used in this research. a) A combined system with DOS (red) and DCS (blue). b) A commercial SRS system (Portamon, Artinis). Right-corner image from: https://neurolite.ch/en/products/nirs/portamon.

The Portamon was used in the investigation of patients with severe acute respiratory syndrome (Chapter 3). Considering the situation in which this study was performed (mostly

during the COVID-19 pandemic), we needed a simple and portable instrument that was easy to use by healthcare personnel without much experience in NIRS. This device is small (its dimensions are $8.4 \times 4.3 \times 1.7 cm^3$) and operates via Bluethooth, powered by a Li-polymer battery, with a sampling rate of 10 Hz. It was designed specifically for muscle research, making it easy to use inside the ICU. The optical probe comprised three light sources, each containing two LEDs centered at 760 and 850 nm, and one photodiode as a detector, forming three SDSs of 3.0, 3.5, and 4 cm that can be analyzed together to provide one single channel of absolute oxygen saturation. To estimate scattering, the system uses the approximation $\mu_s^{'} = \alpha(1-\beta\lambda)$, with $\alpha = 1.1 mm^{-1}$ and $\beta = 4.6 \times 10^{-4} nm^{-1}$ [66].

The FD-DOS system was used in the remainder of this work. It contains 32 laser diode sources (eight on each wavelength of 690, 705, 750, and 850 nm) with amplitude modulated at 110 MHz, and four photomultiplier tubes (PMTs) as detectors. The detectors use a heterodyne scheme to demodulate the detected light and provide information on its amplitude and phase shift with respect to the incident light. The system can operate with sampling rates as fast as 50 Hz. It is easy to note that the system is less portable than the Portamon one and depends on optical fibers as waveguides for delivering/collecting light to/from tissue, making it portable but not wearable.

For the study presented in Chapter 7, the FD-DOS system was combined with a homemade DCS system developed in our laboratory [67]. The DCS comprises one long-coherent continuous-wave laser source (785 nm) and 16 single photon-counting detectors (APDs) that feed a correlator to provide a measurement of $g_2(\tau)$. The FD-DOS and DCS measurements described in Chapter 7 were performed sequentially, with a cycle of 10 s of FD-DOS (acquisition rate of 4.5 Hz) followed by a cycle of 50 s of DCS (2.8 Hz).

2.9 Conclusion and Next Chapters

In this chapter, I reviewed the physical principles of diffuse optical techniques and discussed how they can be used to obtain information on tissue. In the process, I also discussed the analytical and numerical forward models that are commonly used to predict FD-DOS and DCS measurements and introduced how the inverse problem can be solved to find the optical properties based on DOS/DCS measurements. Once the optical properties are estimated, one can readily infer physiological information about hemoglobin concentration and the blood flow index. In the end, I presented the systems used throughout this work. In the next chapter, I will demonstrate how the measurements performed with DOS can be used as biomarkers of vascular diseases through an application in the intensive care unit (ICU).

CHAPTER 3

MICROREACTIVITY ASSESSMENT OF PATIENTS USING DIFFUSE OPTICAL SPECTROSCOPY

As discussed in the previous chapter, DO techniques provide estimations regarding local oxygenation and hemodynamics. These parameters hold the potential to serve as biomarkers of diseases with vascular impact as they relate to tissue physiology. The original plan was to test this hypothesis at the end of my project using FD-DOS and DCS techniques in patients with carotid artery stenosis. However, the unexpected COVID-19 pandemic forced a change in the schedule. Aiming to take advantage of this unfortunate situation, I explored how DO techniques could help in the prognosis of patients diagnosed with Severe Acute Respiratory Syndrome (SARS). Considering the restrictions imposed by the pandemic, including social distance, the only possibility to make measurements in the ICU was with a portable, fiberless, and ready-to-use device that could be readily used by healthcare workers in ICU environments.

In this chapter, I discuss part of the results obtained during a multicenter study that started during the pandemic (Hemocovid project) with the goal of investigating microvascular reactivity in severe cases of COVID-19. Section 3.1 introduces the research question and its rationale. Section 3.2 presents the experimental methods of the clinical study. In Section 3.3, I present the results obtained, while Section 3.4 discusses their implications for the problem investigated. Lastly, Section 3.5 brings the main conclusions of this investigation.

3.1 Introduction

COVID-19, caused by the SARS-CoV-2 virus, has spread globally in recent years [68]. Its clinical symptoms vary from asymptomatic cases to severe pneumonia [69], often requiring mechanical ventilation in acute cases [70]. A primary complication is severe acute respiratory syndrome (SARS), a pulmonary inflammatory process that often results in hypoxia (i.e., low arterial blood oxygen concentration) [71, 72]. For severe COVID-19 patients, there is a high mortality rate and long-term sequels [73–76] despite the use of strategies aimed at increasing

oxygenation during hospitalization.

Another consequence of SARS is the alveolar diffuse damage. Those damages lead to endothelial dysfunction and changes in the microcirculation, usually correlated with the severity of the case and its outcome [77–79]. Thus, information about oxygenation and circulatory disturbance can lead to better understanding and predict the severity and outcome of blue in ICU environments.

DOS techniques can estimate local oxygenation in deep tissue, as discussed in the previous chapter. Indeed, DO monitoring during a Vascular Occlusion Test (VOT) can bring valuable information regarding the microvascular reactivity of healthy individuals and patients, including SARS [80–84]. During a VOT, the blood supply to a specific region is temporarily interrupted, being re-established after some time. The StO_2 desaturation and resaturation rates reflect the local oxygen consumption and the microvascular hyperemic capacity, respectively [85, 86]. Microvascular tests have shown that blood microcirculation evaluated in muscle regions is disturbed in several clinical contexts [80, 82, 83]. Still, there is little data on patients with SARS, even though the monitoring of tissue oxygen saturation with DO techniques has been shown to hold the potential to predict clinical outcomes [83].

Moreover, COVID patients who survived the disease have presented medium- to long-term sequelae due to alveolar damage regardless of their severity [87]. The mechanisms underlying long COVID are not fully understood due to their relatively new emergence. In severe cases, it is known that, after the acute phase of SARS, the subsequent clinical evolution in survivors has been associated with functional sequelae due to pulmonary limitations, thus affecting their quality of life [68]. Furthermore, survivors of acute respiratory distress syndrome, which is one complication of COVID-19 pneumonia, have been shown to have a decrease in strength and mobility [88, 89], as well as cognitive damage and psychiatric dysfunction [90, 91], up to five years after the acute phase.

In this context, this study aimed to assess the microvascular condition of patients diagnosed with SARS in ICU environments, correlating this information with clinical outcomes. Additionally, a secondary goal was to evaluate the medium- to long-term sequelae after ICU discharge, correlating it with the patients' physical improvement. For that purpose, we acquired diffuse optical data during a VOT and analyzed the parameters that might be extracted from the protocol. For longitudinal analysis, we also analyzed the patients' performance during a physical test to track their recovery over time.

3.2 Materials and Methods

3.2.1 Study Design

We investigated four groups of distinct participants in this study (demographics are in Table 3.1). Two of them consisted of patients admitted to the ICU of the Hospital of Clinics

Table 3.1: Enrolled patient's demographics.

	ICU Groups		non-ICU Groups	
	COVID	non-COVID	post-COVID	Controls
Total	36	40	69	79
Excluded	2	7	16	13
Females	17	10	8	50
Age(std) [years]	63 ± 13	58 ± 10	56 ± 17	39 ± 14

Table 3.2: Time (in months) between the ICU discharge and the data acquisition for the non-excluded participants within the post-COVID group.

Months after discharge	0	1	2	3	4	5	6	7	8
N	5	2	0	8	11	11	10	4	2

(University of Campinas). The *COVID group* consisted of patients who tested positive for COVID-19 infection. To identify possible correlations of oxygenation with other conditions in the ICU, we also acquired data from patients admitted with other diagnostic hypotheses, such as stroke, neoplasm, and others. We refer to this group as *non-COVID group*. To understand the remaining effects of COVID-19 infection after the acute clinical phase, we recruited patients from a few days to nine months after their ICU discharge Ideally, each participant should have undergone an acquisition within three, six, and nine months after discharge. Unfortunately, due to the difficulty in guaranteeing the participants' return, we could acquire data on 69 participants, with only nine of them returning just one more time. We called this group the *post-COVID* group. The time (in months) between the ICU discharge and the data acquisition is exhibited in Table 3.2. Lastly, to have a comparison basis of the values estimated in COVID, non-COVID, and post-COVID groups, we also included a control group consisting of participants who did not test positive for COVID-19 infection within the 21 days prior to data acquisition. We call this group the *Control* group.

The main goal of this investigation is to assess the microvascular condition of COVID-19 patients. To this end, we submitted the participants to the VOT. This test consisted of laying the participant supine with the optical sensor above the brachioradialis muscle, aligned with a sphygmomanometer (Figure 3.1a). We used a commercial SRS-NIRS system (Portamon, Artinis, see Figure 2.10b). After acquiring three minutes of data in a resting condition, the pressure on the sphygmomanometer was inflated to 50 mmHg above the (previously measured) systolic pressure of the participant. The occlusion was held for three minutes. After this period, the pressure on the sphygmomanometer was suddenly released, while optical data was collected for three more minutes.

Figure 3.1b exhibits a typical StO_2 VOT curve. From the curve, we obtained the baseline oxygen saturation (St_o), the desaturation slope (DS), the minimum of oxygen saturation (St_{min}), the resaturation slope (RS), the maximum saturation after the occlusion (St_{max}) and the hyperemic area (AUC). DS and St_{min} are parameters related to the patient's oxygen consumption at the microvascular level. DS reflects the speed of the consumption, while St_{min}

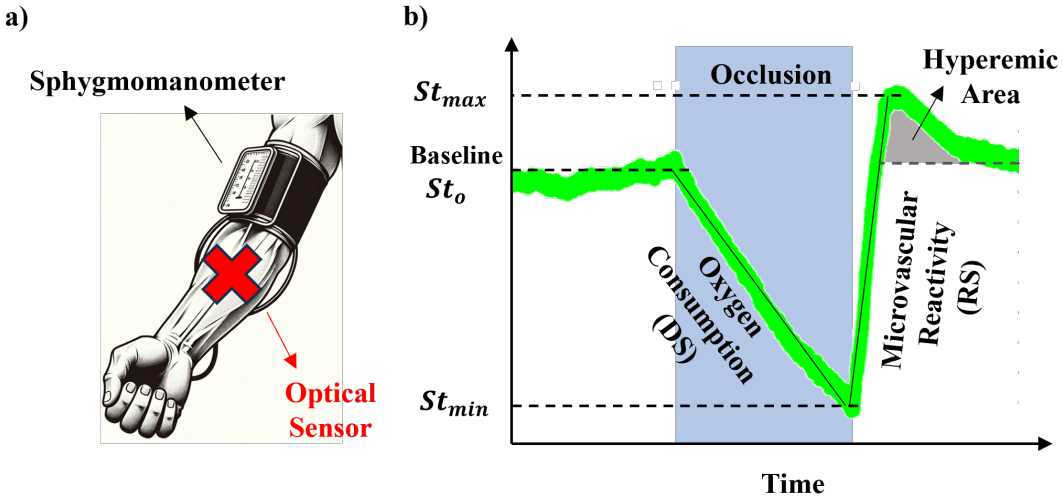

Figure 3.1: Illustration of (a) the probe placement for VOT protocol and (b) a typical StO_2 curve extracted from a VOT protocol, with the parameters extracted from the curve. Of note, we obtained the baseline oxygen saturation (St_o), the desaturation slope (DS, related to oxygen consumption), the minimum of oxygen saturation (St_{min}), the resaturation slope (RS, related to the microvascular reactivity), the maximum saturation after the occlusion (St_{max}) and the hyperemic area (AUC).

is related to the ability to sustain a smaller oxygenation condition. Conversely, RS and AUC are related to the patient's microvascular reactivity. RS reflects the speed at which blood fulfills the vasculature, while AUC is related to the overshoot of excess blood inside the vascular system after the occlusion. Additionally, the system estimates the total hemoglobin concentration, $[HbT]$. We discarded data where the StO_2 curve did not resemble Figure 3.1b (see Table 3.1).

To further correlate oxygenation levels with physical recovery in post-COVID patients, we also conducted a *walking test* to evaluate their performance. This test required participants to walk as much as they could for six minutes. For each participant, we calculated the expected walking distance using the Enright and Sherrill Equation [92] and assessed the performance by comparing the actual distance walked to the expected distance. Results were expressed as a percentage of the predicted distance (WD, ranging from 0 to 100%). This protocol was approved by the local Ethics Committee at the University of Campinas (CAAE 34454920.7.0000.5404). Participants were instructed concerning the experiment protocol before signing an informed consent form prior to participation (Appendix H for controls and I for patient enrollment).

3.2.2 Statistical Analysis

For each parameter extracted from the VOT curve, we compared the distributions between the patient groups and the Control group. Additionally, we compared the distributions obtained among ICU groups (i.e., COVID and non-COVID). To this end, we tested the normality of the distributions with a Lilliefors test. Then, we compared two distributions using a T-test

if both parameters were normal and using a Wilcoxon test otherwise. We considered a significant difference between the two groups if the p-value was smaller than 0.05.

To better highlight the potential of optical estimation in clinical scenarios, we also related them to clinical outcomes (i.e. obit or not) for ICU measurements. For that purpose, we used a generalized linear mixed effects approach [66, 93–95], initially through the following expression:

$$O = \sum_{i=1}^{N} \left(X_i + \sum_{j>i} X_i X_j \right) + (1|participant) + (1|covid) \tag{3.1}$$

as a complete model. Here, O is the clinical outcome (1 if obit; 0 if surviving), and $X_i, i = 1, ..., N$ are the VOT variables. Note that we included random, specific intercepts for each patient, as well as for the presence of COVID-19, denoted by $(1|participant)$ and $(1|covid)$. We also included first-order interactions between the VOT parameters through the products $X_i X_j$. We adjusted Equation 3.1 by assuming a binomial distribution for O and using a *logit* link function. We subtracted X_i by its mean and divided it by its standard deviation before adjusting the model.

To reduce the model, we followed a reduction procedure of the whole equation [96–100]. To this end, we adjusted the expression, obtaining the first model, M_1. Then, we identified the independent variable with the greatest p-value. If this variable is an interaction variable (i.e., of the $X_i X_j$ kind), we remove this variable and fit the remaining model, obtaining the second model, M_2. Otherwise, we remove the variable X_i and all their interactions (i.e., $X_i X_j, \forall j$) and fit the remaining model to obtain M_2. To decide which model is better, M_1 or M_2, we used the Aikake Information Criterion (AIC), Bayesian Information Criterion (BIC), and the logarithm of the likelihood function (Log-Likelihood). If M_2 has a smaller AIC, a smaller BIC, and a greater (or statistically similar) Log-Likelihood, we repeated the previously described variable removal procedure with the new-largest p-value. We repeated this interaction until removing a new variable worsened the model. If the variable on occasion is an interaction variable ($X_i X_j$), we stopped. If it was a first-order variable (of the X_i kind), we removed the interaction variable with the greatest p-value to improve the model even more. Then, we stop if the model worsens or when the highest p-value of the $X_i X_j$ variables is smaller than 0.1, which we understand is a robust significance cutoff.

Additionally, we used a linear mixed-effects approach to track trends of VOT parameters regarding the time after ICU discharge. We started with the following relation:

$$T_D = \sum_{i=1}^{N} \left(X_i + \sum_{j>i} X_i X_j \right) + (1|participant), \tag{3.2}$$

where T_D is the time (in days) between the ICU discharge and the VOT protocol. As the output is not binary in this situation, we were able to include age as an independent variable together with the VOT parameters. The reduction process followed the same methodology

Table 3.3: Parameters obtained from the VOT curve (Figure 3.1b) for the ICU groups with a positive test for COVID-19 infection (COVID), without a positive test for COVID-19 infection (non-COVID) and for the control group. The results are exhibited in median(first quantile; third quantile) pattern.

	COVID	non-COVID	Controls
$St_o(\%)$	$69(64;74)^{b,c}$	$62(57;67)^{a,c}$	$67(64;70)^{a,b}$
$[HbT](\mu molar)$	35(29;47)	43(30;58)	39(32;46)
$DS(\%/s)$	$-0.08(-0.10;-0.06)^{b,c}$	$-0.11(-0.14;-0.08)^{a}$	$-0.12(-0.15;-0.10)^{a}$
$St_{min}(\%)$	$56(47;60)^{b,c}$	$43(36;50)^{a}$	$47(40;53)^{a}$
$RS(\%/s)$	1.1(0.7;1.4)	1.3(0.7;1.8)	1.2(0.9;1.9)
$St_{max}(\%)$	$75(72;78)^{b}$	$72(66;76)^{a,c}$	$76(73;80)^{b}$
$AUC(\% \cdot min)$	$5.0(3.0;7.5)^{c}$	$5.2(3.2;9.9)^{c}$	$8.4(6.1;12.0)^{a,b}$

a - Significative difference in relation to the COVID group
b - Significative difference in relation to the non-COVID group
c - Significative difference in relation to the Control group

previously described. In addition, to analyze more individualized clinical evolutions, we also investigated the subgroup of participants that have returned to one more protocol acquisition by correlating changes in WD and VOT parameters between the two acquisitions as a preliminary approach.

3.3 Results

3.3.1 ICU Parameters Analysis

Group Comparisons

The comparisons of VOT parameters among the COVID, non-COVID, and Control groups are exhibited in Table 3.3. We can see that VOT parameters are sensitive to the presence of COVID-19 infection and other clinical hypotheses induced by respiratory syndromes or by worsening the clinical condition and/or intensive use of pharmaceuticals and other external supports. This fact is especially noticeable for parameters directly induced by occlusion, except for RS. The evoked AUC seems to be similar in both COVID and non-COVID groups, although different from the control group. On the other hand, DS and St_{min}, parameters more related to oxygen consumption and tissue metabolism, distinguish COVID and non-COVID groups from the control group.

Relationship between VOT parameters and clinical outcome

To investigate the correlation between VOT parameters and clinical outcomes, we performed a reduction in a linear mixed-effects model to relate obit cases to VOT variables (Equation 3.1). After the reduction, we obtained the final model:

Table 3.4: Parameters obtained from the VOT curve (Figure 3.1b) for the post-COVID and the Control group. The results are exhibited in median(first quantile; third quantile) pattern.

	post-COVID	Controls
$St_o(\%)^*$	61(58;65)	67(64;70)
$[HbT](\mu molar)$	40(34;50)	39(32;46)
$DS(\%/s)^*$	$-0.14(-0.17;-0.11)$	$-0.12(-0.15;-0.10)$
$St_{min}(\%)^*$	43(36;46)	47(40;53)
$RS(\%/min)^*$	1.6(1.3;2.3)	1.2(0.9;1.9)
$St_{max}(\%)^*$	73(70;76)	76(73;80)
$AUC(\% \cdot min)$	10.0(6.4;13.2)	8.4(6.1;12.0)

* - p<0.05

$$O = DS + RS + St_{max} + AUC + St_o \cdot AUC + (1|subject) + (1|covid).$$

Only two parcels were significant: DS (estimate(95% confidence interval) $\beta = -0.87(-1.68;-0.06)$, p=0.035, T=2.2) and AUC ($\beta = -1.32(-2.29;-0.37)$, p=0.008, T=2.8). This suggests that these parameters are more related to obit outcomes than those extracted from the VOT curve. Moreover, as $\beta < 0$, the higher the AUC and the steeper DS, the less likely the obit outcome.

3.3.2 Post-discharge Parameters Analysis

Group Comparisons

As in the ICU data, we first compared the post-COVID VOT parameters with those of the Control group. The results are in Table 3.4. Data suggest that the optical parameters measured during the VOT protocol can distinguish even between a control group and a previously infected group in recovery. More specifically, St_o (p<0.00001), DS (p=0.0134), St_{min} (p=0.0130), RS (p=0.0015), and St_{max} (p=00010) are statistically different between those two groups. These results are independent of the lag time between the ICU discharge and the VOT protocol.

Individual Trends with 6-minute Walking Distance Score

We investigated the subgroup of participants that have returned to one more acquisition of the protocol. They all have increased the WD compared to the first acquisition (an average increase of 11%), suggesting a physical improvement between the two sessions. This change might reflect an attenuation of COVID-19 sequelae. To investigate which VOT variables may reflect this attenuation (if any), we correlated the changes in WD to the changes in the hemodynamic variables. The greatest correlations found were 0.91 for RS (p = 0.033) and 0.90 for St_o (p = 0.039), both statistically significant. In sequence, 0.89 for St_{max} (p = 0.052), and 0.86 for DS (p = 0.060) and $[HbT]$ (p = 0.064). The remaining variables presented correlations

with $p > 0.1$. Although these results do not have enough statistical power, they encourage us to investigate trends in VOT parameters concerning the lag time between ICU discharge and data acquisition since these changes might be correlated to physical improvements.

Trends of VOT Parameters After Discharge

To investigate changes in VOT parameters over time after the ICU discharge, we used the same approach as in ICU data with the Equation 3.2. However, in this situation, there were not many steps to reduce the model. Of the 34 remaining parcels, 16 were statistically significant, suggesting that most variables were related to the dependent variable T_D. Among those 16, only four first-order variables: DS ($\beta = 0.93(0.40;1.47)$,p=0.0018, T=3.7), RS ($\beta = -0.42(-0.82;-0.02)$, p=0.039, T=2.2), St_{max} ($\beta = 1.06(0.51;1.61)$, p=0.0007, T=4.1), and AUC ($\beta = -0.56(-0.92;-0.19)$, p=0.0048, T=3.2). Additionally, there are seven interactions with high estimates (i.e., $\beta > 0.8$ on the relation between the normalized $X_i X_j$ and T_D): $DS \cdot St_{min}$ ($\beta = -2.10(-3.24,-0.96)$, p=0.0011, T=3.9), $St_o \cdot DS$ ($\beta = 1.51(0.47,2.54)$, p=0.0067, T=3.1), $St_{max} \cdot age$ ($\beta = 1.27(0.35,2.19)$, p=0.0098, T=2.9), $St_o \cdot St_{min}$ ($\beta = -1.12(-2.01,-0.16)$, p=0.249, T=2.5), $St_{min} \cdot St_{max}$ ($\beta = 1.10(0.16,2.05)$, p=0.0245, T=2.5), $RS \cdot St_{max}$ ($\beta = 0.97(0.10,1.85)$, p=0.3112, T=2.3), and $RS \cdot AUC$ ($\beta = -0.82(-1.41,-0.23)$, p=0.0090, T=2.9).

3.4 Discussion

In this work, we used SRS-NIRS to evaluate StO_2 during a VOT in patients who tested positive for COVID-19 infection to investigate the impact of the disease on microvascular reactivity. To this end, we performed the VOT protocol inside the ICU in two groups: one that tested positive for the infection (the COVID group) and another group with other disabilities (the non-COVID group). Additionally, we acquired data from a group outside the ICU that had not tested positive for COVID-19 infection in the previous 21 days, which we called the Control group. Our goal was to compare the VOT parameters obtained in the ICU groups with those of the Control group, taken as a cohort that does not suffer any influence of the infection.

The main limitation of our study is related to the data acquisition period. We started the acquisition of the Control group a few months after the beginning of the pandemic when there were few people infected with COVID-19. However, as we kept data acquisition for years, there came a time when the new acquisitions of this group were people who probably already had COVID-19 once and, therefore, had their microvascular parameters compromised, as we can see by our post-COVID study. Although we tried to control this influence by asking if they tested positive (or had some symptoms) in the previous 21 days, now we know the recovery time is far beyond that period.

A second limitation of this study was the age difference between the Control and ICU

groups (39 years on average versus 58 and 63 for the non-COVID and COVID groups, respectively). Aging influences optical estimations of physiological parameters [12, 101, 102] (see also Chapter 5). To estimate the aging effect in the Control group of this work, I adjusted a linear fit (also refer to Chapter 5) and calculated the Pearson correlation between VOT parameters and age. Only St_{max} yielded a significant slope ($-0.08 \pm 0.04\%/year$, p=0.05), while only DS yielded a correlation close to 0.2, but with no significance (r=0.17, p=0.16). It might suggest that the aging effect over the VOT variables is less pronounced than the effect due to the presence of the diagnostic hypotheses of ICU participants. Nevertheless, since we cannot untangle age from COVID-19 effects within this cohort, further investigations matching age between groups are necessary.

This work reinforces previous research that found alterations in microcirculation in COVID patients, evidencing the relation between endothelial dysfunction and the disease [103–105]. In particular, St_o, DS, and St_{min} statistically differ between the COVID and Control and non-COVID groups. The less steep DS and higher St_{min} indicate a smaller oxygen consumption in the COVID group [106]. Additionally, ICU patients have, in general, smaller AUC and RS compared to the Control group. It suggests that a late ischemic condition due to a high ICU period added to the severity of the disease, and the use of vasoactive drugs makes the resaturation process slower [103, 107–110]. The statistical difference among VOT parameters between non-COVID and Control groups highlights that endothelial dysfunction results from several diseases such as hypertension, stroke, and diabetes [111–114]. In this protocol, we also assessed the pulse oxygen saturation through pulse oxymeters for the ICU patients, aiming to correlate low values of this parameter, especially in the COVID group, with low StO_2 values (data not shown). However, all measurements were above 92%, a regular saturation value. We understand those normal values are due to the ICU ventilatory support, which makes it hard to correlate low saturation values.

Since clinical practice aims to predict which cases are more likely to become an obit outcome to put more effort into it, we investigated which VOT variable is more sensitive to the outcome. With that purpose, we reduced a complete linear mixed-effects model with binary output, including the VOT variables and their first-order interactions as independent variables and random intercepts regarding the subject and the COVID-19 infection. Our results show that DS and AUC are related to clinical outcomes, with a more pronounced effect on AUC (β estimations of 1.32 versus 0.87 in the obit outcome model). The higher the AUC and the steeper the DS, the less likely the obit outcome. Note that this result also suggests that AUC and DS parameters closer to the Control group values are less likely to become an obit output. Although further investigation with higher cohorts is necessary, this result suggests that these parameters, estimated with a fast VOT protocol with DOS, can be used as prognostics of ICU disease severity in the future.

We also acquired data on a group of previously infected COVID-19 patients after their ICU discharge. The first comment regarding this group is that their VOT parameters are

statistically different from those of the Control group. This suggests that DO techniques can separate post-discharge COVID patients from healthy ones. Ideally, we aimed to acquire data for every participant three times (i.e., 3, 6, and 9 months after the discharge). However, the difficulty in making them return with no clinical necessity forced us to conduct this study as a transversal study.

With the small subgroup of 9 participants that returned to one more acquisition, we correlated the changes in WD, taken as a surrogate of the physical and physiological condition of the participant, with the changes in VOT parameters to investigate if there is a relation between both. We found a strong and significant correlation between changes in WD and changes in RS and St_o, but also strong correlations with St_{max}, DS, and $[HbT]$. This result suggests that changes in VOT parameters, related to changes in the microvascular condition of the participants, could be related to changes in the physical condition. It motivates the investigation of trends of VOT parameters with time after ICU discharge. However, based on Table 3.2, it is hard to make an even split regarding the months after discharge since there is a high concentration of participants between the third and the sixth month. Thus, we decided one more time to use a linear mixed-effects model to correlate the time (T_D, in days) after ICU discharge and VOT parameters. As we have a continuous variable as output at this time, we were able to add age and its first-order interactions as independent variables. Our data revealed several variables with a statistically significant relation to T_D, which suggests that most parameters are correlated. This is reinforced by the fact that several first-order interactions remain significant after the reduction of the model. Among the VOT variables, we found that DS gets steeper, RS gets less steep, and there is an increase in St_{max} and a decrease in AUC with T_D. This result suggests that the VOT parameters and the microvascular condition of post-COVID patients change for at least eight months after the ICU discharge.

3.5 Conclusions and Next Chapters

In this research, we investigated parameters associated with microvascular health and reactivity of ICU patients who tested positive for COVID-19 infection and post-discharge COVID-19 patients and compared them with a control group. Our results suggest that DO techniques parameters during a VOT protocol are sensitive to diseases with vascular impact so that they can separate the COVID group from the non-COVID and Control groups. Additionally, the parameters distinguish the post-COVID group from the Control group. These results highlight the potential of DO techniques to achieve biomarkers of diseases with vascular impact. On top of that, this research also indicates that DS and AUC are related to clinical outcomes, and the microvascular parameters are still changing eight months after the ICU discharge. These results further highlight the potential of DO techniques in clinical scenarios.

From a methodological perspective, it is worth noting that this analysis was performed assuming the SI model. This model assumes that tissue is homogeneous, i.e., it has the same

optical properties throughout its bulk and, therefore, the same physiological properties everywhere. Additionally, it assumes the interface of data acquisition (the surface where the optical sensor is coupled) is planar. All those assumptions suggest that estimations through this model might not be useful for studying biological tissue due to the inaccuracies arising from the hypothesis. However, this model estimates parameters that can distinguish between healthy and unhealthy groups. It is probably because acquisitions targeting muscle tissues are performed in regions reasonably homogeneous. Beyond that, the surface is so that the coupling between the optical sensor and the tissue might be manipulated so that the influence of the curvature of the region does not harm optical estimations.

However, this approximation is not robust for biological tissues in general. For example, when the target is the brain, the sources and detectors lie on curved surfaces (e.g., the forehead). Additionally, light travels through tissues with different physiological properties, such as skin, skull, and cerebrospinal fluid. This non-flat and local heterogeneity jeopardizes optical estimations with DOS. In this context, the following two chapters of this thesis investigate these influences in optical estimations. In these chapters, I also propose and test methodologies to incorporate such features of real data acquisition in optical estimations.

CHAPTER 4

INFLUENCE OF TISSUE HETEROGENEITY ON DIFFUSE OPTICAL TECHNIQUES ESTIMATIONS

This chapter is the first of a series of methodologies I am proposing to increase the accuracy of optical and physiological estimations through DO techniques. As previously discussed, the use of layered models, especially the 2L model (Equation 2.11), is not an innovation in the diffuse optics field. However, since the model depends on several variables (i.e., the optical and dynamical properties of each layer and its thicknesses), it is subject to numerical instability when solving the inverse problem. Thus, developing a method to accurately estimate the absorption coefficient (μ_{a2}) and the blood flow index (F_2) of the second layer with high stability is useful for DOS/DCS applications. In this chapter, I propose an algorithm to use the 2L model with higher reliability. By restricting the parameter space from $\mathbb{R}^8$ (absorption/scattering coefficients, blood flow, and thicknesses of the first/second layer) to $\mathbb{R}^5$ (absorption coefficient and blood flow of first/second layer and scattering coefficient), the inverse problem becomes more stable. In this context, Section 4.1. introduces the problem through further clarifications of the issues of using a homogeneous model. In Section 4.2, I describe the methods I used to generate FD-DOS and DCS data and the proposed algorithm to solve the inverse problem. I exhibit the results of the investigation in Section 4.3, while Section 4.4 is the discussion of such results. Finally, Section 4.5 summarizes the main conclusions of this investigation. It is worth noting that the results and development of this chapter are part of a bigger work, already published [15].

4.1 Introduction

The use of DO techniques *in vivo* over the human head through FD-DOS and DCS is a promising approach to estimate cerebral blood flow (CBF) and parameters which provide estimations of blood oxygenation and oxygen metabolism [10, 115, 116]. However, the validation studies with pediatric populations and animals use the SI model to analyze optical data. Since the SI model assumes the biological tissue as a homogeneous media, the model

averages the optical and dynamical properties of all tissues where light has gone through. It means that there are significant extracerebral tissue (scalp and skull) contributions to the cerebral estimated values, and neglecting such contributions can result in large errors, especially in adults [13, 14, 117, 118].

To overcome this issue and increase sensitivity to brain tissue, analytical layered tissue models have been investigated in the literature for both FD-DOS and DCS estimations [13, 14, 30, 32, 118–121]. However, as the layered model depends on several parameters (optical properties, blood flow, and thickness of each layer), the inverse problem is usually ill-posed, which leads to high variability and potentially large errors when estimating physiological parameters [32, 120, 121]. When constraining the inverse problem (e.g., assuming known optical properties to adjust blood flow or assuming known thicknesses), layered estimations are usually higher than SI estimations [13,14,119], even though still subject to errors. However, layered estimations are still below the simulated or expected values [13]. Additionally, errors in the assumed parameters also lead to inaccuracies in estimations [13, 14, 30].

In this context, we investigated the accuracy of CBF and μ_a measurements derived from a constrained two-layer (2L) model algorithm to FD-DOS and DCS simulated data. To my knowledge, the simultaneous use of layered models to fit both DCS and FD-DOS data in combination has not yet been demonstrated. Such an approach is particularly relevant for CBF estimations since this quantity also depends on the optical properties. The proposed method uses the 2L model exhibited in 2.11, assuming the first layer is infinitely thin compared to the second one. A cylindrical geometry is used instead of a slab one because the numeric approximation of the solution for 2.9 is more robust [13]. The method further incorporates the constraint of homogeneous $\mu_s^{'}$, i.e., $\mu_{sk}^{'} = \mu_s^{'}, \forall k$, which I justify below, to reduce the risk of crosstalk between unknown fitting parameters. Finally, the method fits multidistance FD-DOS (eight distances; 0.8 to 4 cm) and DCS (0.8 and 2.5 cm distances) data in sequential steps to constrain the recovery of μ_a, $\mu_s^{'}$ and F. Note that, as I used a 2L model, the second layer properties represent cerebral information. To test the method, I characterized its errors across a wide range of tissue optical properties and blood flows in forward-model simulations, simulations in a 2L cube, and simulations using a realistic head geometry. I also characterized the approach's sensitivity to extracerebral layer thickness.

4.2 Materials and Methods

This section explains the methods of data generation and data analysis. Briefly, I generated FD-DOS and DCS data using both the forward 2L model and software that generates optical measurements numerically (NIRFASter). I analyzed this data with the SI model and with an algorithm that uses the 2L model in steps to estimate the optical properties and flow.

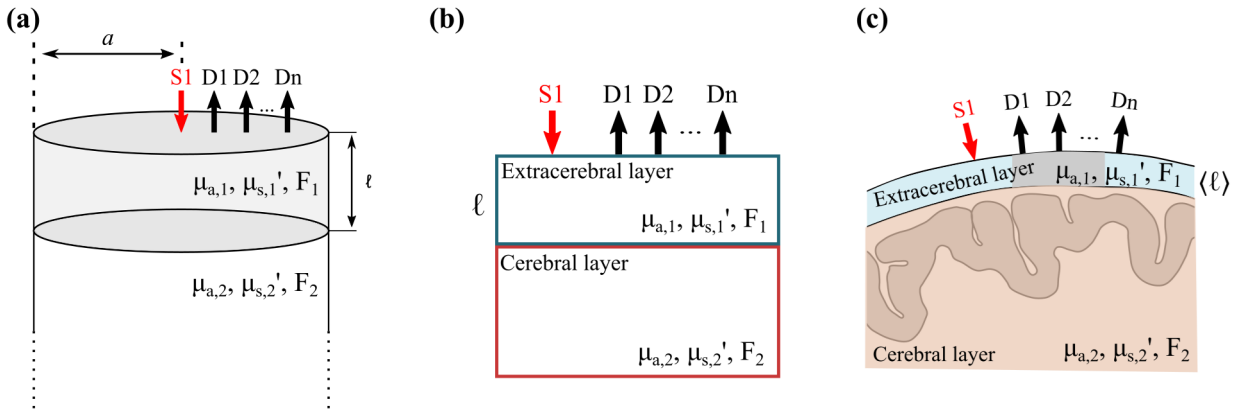

Figure 4.1: Geometry used for the 2L model and the simulations. (a) Our 2L model comprised a homogeneous cylindrical extracerebral layer of thickness ℓ and radius a (corresponding to the extracerebral scalp and skull tissue) above an infinitely thick homogeneous cylindrical cerebral layer (corresponding to the brain cortex). The tissue absorption coefficient, reduced scattering coefficient, and blood flow index of the extracerebral layer are μ_{a1}, $\mu_{s1}^{'}$, and F_1, respectively. The corresponding properties of the cerebral layer are μ_{a2}, $\mu_{s2}^{'}$, and F_2. A point source (S1) is incident on the middle of the cylinder top, and multiple point detectors D1, D2, ..., Dn are positioned at different distances from the source. (b) Using the NIRFASTer package, we generated synthetic data for a $10 \times 10 \times 10$ cm^3 2L cube, with an extracerebral layer thickness of $\ell = 1.2cm$. (c) We additionally used NIRFASTer to generate synthetic data for a realistic adult head geometry, wherein the scalp and skull were combined to form a homogeneous extracerebral layer, and the CSF, white matter, and gray matter were combined to form a homogeneous cerebral layer. The source and detectors were positioned on the right side of the head, and we used the average skin-to-brain distance under the middle portion of the optical probe (i.e., the average thickness of the 2-cm long gray line in (c)), as ℓ. Figure taken from [15]

4.2.1 Forward Models

Two-Layer Head Model

The 2L model consists of modeling the head as a cylinder with radius a. In this approximation, the top layer represents a homogeneous extracerebral layer of thickness ℓ, which is located above an infinitely thick homogeneous cerebral layer (Figure 4.1a). The tissue absorption coefficient, reduced scattering coefficient, and blood flow index of the extracerebral layer are μ_{a1}, $\mu_{s1}^{'}$ and F_1, respectively. The corresponding properties of the cerebral layer are μ_{a2}, $\mu_{s2}^{'}$ and F_2. I assumed the refractive index to be the same for both tissue layers. In this model, a point source was located at the center of the top of the cylinder, and multiple detectors were positioned on the same plane at different distances from the source. The distance between the source and the i-th detector is ρ_i.

To evaluate the 2L fitting algorithm, we simulated data for 8 FD-DOS SDSs (ρ_i = {0.9, 1.2, 1.6, 2.0, 2.8, 3.2, 3.6, 4} cm) and 2 DCS SDSs ($\rho_i = 0.8$ and $2.5cm$) across a wide range of values for the optical properties and blood flow indices. At each detector position, the fluence's amplitude and phase were computed, i.e., $AC_{meas}(\rho_i)$ and $\theta_{meas}(\rho_i)$. Also, for each detector, the normalized intensity temporal autocorrelation function, $g_2^{meas}(\rho_i, \tau)$ was computed at multiple delay times, τ.

Analytical Model Simulations

I employed the analytical solution of the photon diffusion model for the 2L geometry (Equation 2.11) to generate FD-DOS and DCS data. Of note, I opted to use a cylindrical geometry since it provides analytical solutions more numerically stable than a rectangular one. For FD-DOS, data were obtained using $f = 110MHz$, $a = 30cm$, and $n = 1.4$. Note that 110 MHz is a commonly used modulation frequency in FD-DOS instrumentation (e.g., Imagent, ISS), and a was sufficiently large such that the solution for FD-DOS and DCS at the detector positions was not affected by the cylindrical boundary.

For each of the eight ρ_i's (see previous section), data were obtained across a wide range of optical properties for four evenly spaced ℓ between 1.0 and 1.6 cm, since this range approximates the range of thicknesses for adult humans [122, 123]. Specifically, at each thickness, Equation 2.11 was computed for 2,030 different combinations of optical properties. To mimic the range of properties observed in adult humans in the NIR spectral range, μ_{a1} and μ_{a2} were randomly selected between 0.08 and 0.18 cm^{-1}, and $\mu_{s1}^{'}$ and $\mu_{s2}^{'}$ were randomly selected between 6 and 15 cm^{-1}, subjected to the constraint that the fractional difference between $\mu_{s1}^{'}$ and $\mu_{s2}^{'}$ was lower than 20 % [56–58]. This latter constraint is justified by a recent study that observed considerable variations in overall scattering across the NIR range but small scattering differences between skin, skull, and brain tissue [57].

Random amplitude and phase noise were derived from a Gaussian noise model with zero mean and then added to each SDS for every combination of optical properties. For the amplitude, I generated data with a signal-to-noise ratio (SNR)[1] of 100. For the phase, I added noise with a standard deviation equal to 0.1 degrees. These amplitude and phase noise levels were chosen based on previously published *in vivo* data in adults [124]. I assumed that noise was independent of λ and SDS. This roughly resembles the case in practice wherein the detected intensities at short SDSs are attenuated to approximately the same scale as the intensities at longer SDSs (i.e., to reduce the dynamic range of detection across separations).

For DCS, we used $\lambda = 785nm$ and evaluated the solution at two ρ_i (0.8 and 2.5 cm) and 100 different τs (spanning from 0.6 μs to 3.7 ms in a multitau scheme [125]). Specifically, for each FD-DOS optical properties combination, I evaluated the correlation diffusion solution for a randomly selected F_1 and F_2 combination. To mimic adult humans, F_1 was selected between 10^{-9} and $2 \times 10^{-8} cm^2/s$, and F_2 was selected between 10^{-9} and $10^{-7} cm^2/s$. The normalized intensity autocorrelation function, $g_2^{theo,2L}$, was then obtained via the Siegert relation (Equation 2.13), where $\beta = 0.5$ was assumed. Intensity autocorrelation noise was independently added to each $g_2^{theo,2L}$. The autocorrelation noise was derived using a correlation noise model [126] evaluated with DCS photon count rates of 200 and 40 kHz for the short and long SDSs, respectively. Note that 40 kHz is on the high end for the 2.5-cm SDS, but it is still within the range observed in previously published in vivo measurements

[1] The signal-to-noise ratio, SNR, is defined as $SNR \equiv \mu/\sigma$, where where μ and σ are, respectively, the mean and the standard deviation of the time series.

on adults [127]. I added random Gaussian noise (with zero mean and a standard deviation based on the correlation noise model described above) independently for each delay-time and SDS and independently for each combination of optical properties and flow indices.

NIRFASTer Simulations

I used the open-source finite-element software package NIRFASTer [39,42] to generate additional synthetic datasets for the same set of eight FD-DOS and two DCS SDSs placed in two different geometries. The first geometry was a $10 \times 10 \times 10\ cm^3$ 2L cube (Figure 4.1b) with a node size of 0.07 cm, which provided a final mesh containing 482,460 nodes. The extracerebral layer thickness and absorption coefficient were set to $\ell = 1.2cm$ and $\mu_{a1} = 0.1cm^{-1}$, respectively. The reduced scattering coefficients of both layers in the cube were set to the same value, i.e., $\mu_{s1}^{'} = \mu_{s2}^{'} = 10cm^{-1} = \mu_s^{'}$, and held constant. NIRFASTer was then used to simulate $AC(\rho_i)$ and $\theta(\rho_i)$ via a finite-element method for 11 evenly spaced cerebral layer absorption coefficients (μ_{a2}) between 0.08 and 0.18 cm^{-1}. Similar to the analytical simulations, I added Gaussian noise to AC and θ to obtain 20 different pairs of $AC_{meas}(\rho_i)$ and $\theta_{meas}(\rho_i)$ synthetic data for each value of μ_{a2} (amplitude SNR = 100; phase σ= 0.1 degrees).

For each combination of optical properties, NIRFASTer was also used to generate $G_1^{theo,2L}(\rho_i,\tau)$ via a finite-element method for 16 different CBF indices between 10^{-9} and $10^{-7}cm^2/s$ (the extracerebral flow index was held constant at $F_1 = 10^{-8}cm^2/s$). Then, correlation noise was added to $G_1^{theo,2L}$ to obtain a synthetic DCS measurement (i.e., $g_2^{meas}(\rho_i,\tau)$) independently for each SDS. For each combination of optical properties, flow indices, and noise additions from FD-DOS, 15 synthetic DCS measurements were generated (in total, we generated 300 autocorrelation curves for each SDS at each combination of optical property and flow).

The second geometry was a realistic adult head mesh created using an open-source library (brain2mesh, with a Delaunay sphere radius of 0.11 cm, radius-to-edge ratio of 1.24, and maximum element volume of 4 mm^3) [128]. The head was segmented into the scalp, skull, cerebral spinal fluid (CSF), white matter, and gray matter, containing ~ 1.4 million nodes. I removed the nodes further than 10 cm from the simulated source, reducing the final mesh to 663,470 nodes. For these simulations, the scalp and skull were merged to form one homogeneous tissue type (i.e., the extracerebral layer), whereas the CSF, gray matter, and white matter were merged to form a second homogeneous tissue type (i.e., the cerebral layer). The synthetic data for this geometry were generated with NIRFASTer in the same manner as the cube simulations (including the same combinations of extracerebral and cerebral tissue properties and noise additions). Note that although the scalp and skull blood flow indices are quite different under normal conditions, the concatenation of the scalp and skull into one layer is closer to reality for applications wherein a transient high probe pressure can be applied against the scalp to reduce the scalp flow closer to levels in the skull [118]. The results are thus most relevant for these conditions.

We did, however, conduct a pilot test of the algorithm under conditions of the scalp flow being higher than the skull flow. This test used simulated data for the same realistic head geometry, except that the scalp and skull tissues were assigned distinct optical properties and flow indices (i.e., a three-layer realistic head geometry). Specifically, we simulated data in which the absorption coefficients for the scalp and skull were $\mu_{scalp} = 0.1cm^{-1}$ and $\mu_{skull} = 0.15cm^{-1}$ [57], respectively, and the blood flow indices were equal to $F_{scalp} = 10^{-8}cm^2/s$ and $F_{skull} = 10^{-9}cm^2/s$, respectively. Here, we varied the true cerebral absorption coefficient $\mu_{a2,act}$ between 0.08 and 0.16 cm^{-1} (in steps of 0.02 cm^{-1}). For each change in cerebral absorption, we also varied the cerebral flow, $F_{2,act}$, between 4×10^{-8} and 10^{-7} (in steps of $10^{-8}cm^2/s$). As with the other simulations, homogeneous scattering was assumed, and we fixed $\mu_s^{'} = 10cm^{-1}$. We added random Gaussian noise to generate multiple datasets from each simulation.

4.2.2 Two-Layer Fitting Algorithm

The 2L fitting scheme is depicted in Figure 4.2. The scheme assumes homogeneous tissue reduced scattering (i.e., $\mu_{s1}^{'} = \mu_{s2}^{'} = \mu_s^{'}$; see Section 4.3.2); it also assumes that the extracerebral layer thickness is known *a priori*. We first used a nonlinear constrained global optimizer implemented in MATLAB R2020a (*fmincon*, Mathworks, Natick, Massachusetts, United States) to obtain estimates of μ_{a1}, μ_{a2}, and $\mu_s^{'}$ by fitting multidistance FD-DOS data (i.e., $AC_{meas}(\rho_i), \theta_{meas}(\rho_i)$) to the 2L analytical solution (i.e., $AC_{theo,2L}(\rho_i)$ and $\theta_{theo,2L}(\rho_i)$). Specifically, I used fmincon to find the set of parameters that minimize the cost function $H_{FD} = \sqrt{H_{AC}} + \sqrt{H_\theta}$, where:

$$H_{AC} = \sum_{i=1}^{N} \left(ln\left(\frac{AC_{meas}(\rho_i)}{AC_{meas}(\rho_1)}\right) - ln\left(\frac{AC_{theo,2L}(\rho_i)}{AC_{theo,2L}(\rho_1)}\right)\right)^2,$$

$$H_\theta = \sum_{i=1}^{N} \left(\left(\theta_{meas}(\rho_i) - \theta_{meas}(\rho_1)\right) - \left(\theta_{theo,2L}(\rho_i) - \theta_{theo,2L}(\rho_1)\right)\right)^2.$$

Here, N = 8 is the total number of SDSs. The minimization was also subject to the following constraints: $0.005 \leq \mu_{a1} \leq 0.6$, $0.005 \leq \mu_{a2} \leq 0.6$, and $4 \leq \mu_s^{'} \leq 20$. These constraints were based on an adult head's expected ranges of optical properties [56, 57]. The extracerebral layer thickness ($\ell = 1.22cm$), refractive index ($n = 1.4$), and cylindrical radius ($a = 30cm$) were used as inputs in the minimization, and the initial guesses used for μ_{a1}, μ_{a2}, and $\mu_s^{'}$ in the minimization were 0.1, 0.1, and 10 cm^{-1}, respectively. In the cost function, the normalization of the amplitude and phase by the shortest SDS removes the need to fit for additional amplitude and phase scaling factors since the global factor cancels out (see Section 2.3.4). Additionally, because the amplitude decreases exponentially with increasing the SDS, I used the logarithm of the amplitude to minimize bias to the shorter distances (i.e., such that fitting errors at each distance are weighted approximately evenly in the cost function).

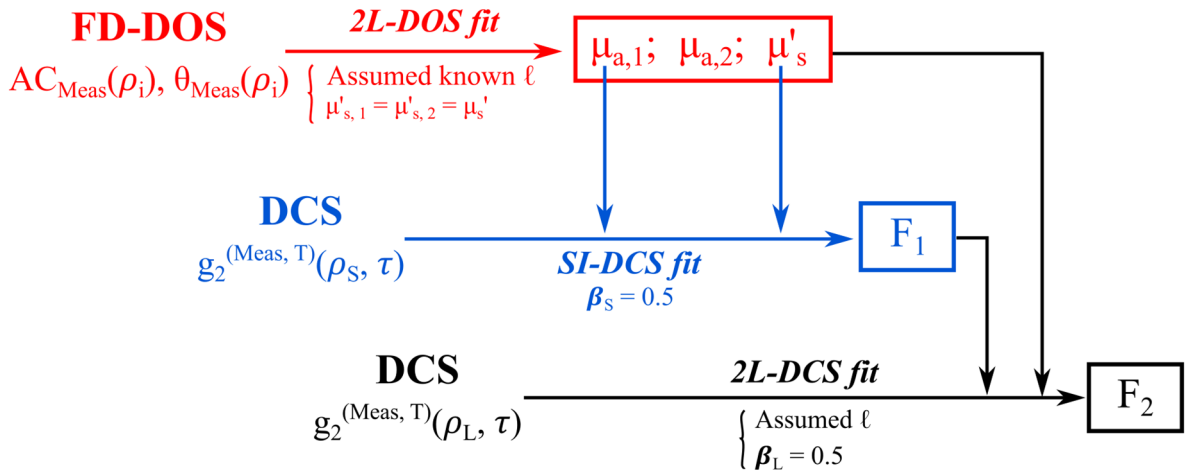

Figure 4.2: 2L fitting scheme. The scheme assumes a priori knowledge of the extracerebral layer thickness (ℓ). First, we fit the multidistance FD-DOS amplitude ($AC_{meas}(\rho_i)$) and phase ($\theta_{meas}(\rho_i)$) data to the two-layer (2L) cylindrical solution to recover the intracerebral and cerebral layer absorption coefficients (μ_{a1}, μ_{a2}), and the reduced scattering coefficient ($\mu_s^{'}$, assuming $\mu_{s1}^{'} = \mu_{s2}^{'} = \mu_s^{'}$). Next, using the recovered μ_{a1} and $\mu_s^{'}$ as inputs, we fit the DCS measurement at the short SDS ($g_2^{meas}(\rho_s,\tau)$) to the SI solution (Equation 2.10) to recover the extracerebral flow index (F_1), assuming knowledge of the β factor from Siegert's relation ($\beta_s = 0.5$). Finally, using μ_{a1}, μ_{a2}, $\mu_s^{'}$, and F_1 as inputs, we fit the DCS measurements at a long SDS ($g_2^{meas}(\rho_L,\tau)$) to the 2L cylindrical solution to recover the cerebral flow index (F_2), assuming $\beta_L = 0.5$. Figure taken from [15]

From μ_{a1} and $\mu_s^{'}$ estimated by the procedure above, I fit the short-separation DCS data, $g_2^{meas}(\rho_s,\tau)$, to the SI correlation solution to obtain the extracerebral flow index, F_1. The short separation ($\rho_s = 0.8cm$) was chosen such that the detected light is predominantly confined to the extracerebral layer for the adult head geometry [129, 130]. The use of a homogeneous SI model for the short-separation data is thus reasonable. I employed the same nonlinear optimizer (*fmincon*) to find an F_1 value that minimizes the cost function H_{DCS,ρ_s}:

$$H_{DCS,\rho_s} = \sum_{\tau_i}\left(g_2^{meas}(\rho_s,\tau_i) - \left(1+\beta_s\left|\frac{G_1^{theo,SI}(\rho_s,\tau_i)}{G_1^{theo,SI}(\rho_s,\tau_0)}\right|^2\right)\right)^2,$$

where τ_i was summed over values satisfying the limit $g_2^{meas}(\rho_s,\tau) \geq 1$, $G_1^{theo,SI}(\rho_s,\tau)$ is the analytical solution to the correlation diffusion equation for the SI homogeneous geometry (Equation 2.10), and β_s is the Siegert relation coefficient for the short separation, assumed to be 0.5. The minimization was constrained within $10^{-11} \leq F_1 \leq 10^{-5}cm^2/s$, and the initial guess for F_1 in the minimization was $10^{-8}cm^2/s$.

In the third and final step, I fit the long-separation DCS data, $g_2^{meas}(\rho_L,\tau)$, to the 2L correlation solution to obtain the cerebral flow index, F_2, given the inputs of μ_{a1}, μ_{a2}, $\mu_s^{'}$, and F_1 from the previous two steps. Additional inputs in the fit were the extracerebral layer thickness, ℓ, refractive index, n, DCS wavelength ($\lambda = 785nm$), the cylindrical radius ($a = 30cm$), and $\beta_L = 0.5$. I used *fmincon* to find the F_2 value that minimizes the cost function H_{DCS,ρ_l}:

$$H_{DCS,\rho_l} = \sum_{\tau_i} \left(g_2^{meas}(\rho_L, \tau_i) - \left(1 + \beta_L \left| \frac{G_1^{theo,2L}(\rho_L, \tau_i)}{G_1^{theo,2L}(\rho_L, \tau_0)} \right|^2 \right) \right)^2,$$

where τ_i was summed over values satisfying the limit $g_2^{meas}(\rho_L, \tau) \geq 1$, $G_1^{theo,2L}(\rho_s, \tau)$ is the analytical solution to the correlation diffusion equation for the 2L geometry (Equation 2.11), and β_L is the Siegert relation coefficient for the short separation, assumed to be 0.5. The minimization was constrained within $10^{-11} \leq F_2 \leq 10^{-5} cm^2/s$, and the initial guess for F_2 in the minimization was $10^{-8} cm^2/s$.

4.2.3 Data Analysis

Accuracy of the two-layer and homogeneous approaches

To compare the results of the 2L scheme with the commonly used SI model, I used the SI solution of the diffusion equation to recover F_{SI}, $\mu_{a,SI}$, and $\mu'_{s,SI}$. For this analysis, we focused on the longer SDSs: for FD-DOS, we used $\rho = 2.8, 3.2, 3.6$, and $4.0cm$; for DCS $\rho = 2.5cm$, and we also assumed $\beta_L = 0.5$ for Siegert's relation. In addition, we restricted our analysis to $g_2^{meas}(\rho_L, \tau) \geq 1.25$ to increase the sensitivity to cerebral tissue [129, 131].

I applied the homogeneous SI analysis described above and the scheme described in Section 4.2.2 and Figure 4.2 to the synthetic datasets generated with the 2L forward model, NIRFASTer in the 2L cube geometry, and NIRFASTer in the 2L realistic adult head geometry. Of note, for the realistic adult head geometry, I used the average skin-to-brain distance under the middle portion of the probe ($\ell = 1.22cm$, see Figure 4.1) as the extracerebral thickness. All DCS estimations were obtained with an integration time of $T = 10s$, corresponding to an acquisition rate of $f = 0.1Hz$.

By defining the absolute percent error as (100%)× |actual - recovered|/actual, I computed the median absolute percent error (MAPE) and the interquartile range (IQR) of the absolute percent errors of the recovered parameters obtained with the constrained 2L and homogeneous fitting algorithms across all simulations in each synthetic dataset. I used paired Wilcoxon sign-rank tests to compare the MAPE between the 2L and homogeneous reconstructions of the cerebral tissue absorption coefficient and the CBF index. All statistical tests were two-sided, and $p < 0.05$ was considered to indicate significance.

I also plotted the medians and IQRs of the recovered parameters as a function of the actual values in each synthetic dataset (i.e., $F_{i,act}$, $\mu_{ai,act}$, and $\mu'_{s,act}$). The IQRs represent the robustness of the recovered parameters in the presence of noise. They are also a measure of the stability of the recovered flow indices with varying optical properties. I further used linear regression to investigate the agreement between the recovered 2L cerebral tissue absorption coefficient (μ_{a2}) and the actual cerebral tissue absorption coefficient ($\mu_{a2,act}$), as well as between the recovered SI tissue absorption coefficient ($\mu_{a,SI}$) and $\mu_{a2,act}$. Additionally, I investigated the agreement between the recovered 2L cerebral flow index (F_2) and the

actual cerebral flow index ($F_{2,act}$), and between the recovered SI flow index (F_{SI}) and $F_{2,act}$.

Sensitivity of the FD-DOS two-layer solution to changes in tissue optical properties

In a secondary analysis, I sought to justify the homogeneous reduced scattering coefficient assumption ($\mu_{s1}^{'} = \mu_{s2}^{'} \equiv \mu_{s}^{'}$) by evaluating the sensitivity of the 2L FD-DOS amplitude, $AC_{theo,2L}$ and phase, $\theta_{theo,2L}$, to changes in μ_{a1}, μ_{a2}, $\mu_{s1}^{'}$ and $\mu_{s2}^{'}$. If the amplitude and phase values are minimally sensitive to changes in $\mu_{s2}^{'}$, I argue that the extraction of all four optical properties from fitting the FD-DOS data to the 2L model will be inaccurate because of high crosstalk between $\mu_{s2}^{'}$ and the other fitting parameters. Instead, it is better to assume homogenous reduced scattering, especially given the evidence from a recent study that found small scattering differences between skin, skull, and brain [57]. To assess the sensitivities, I computed the partial derivatives $\partial ln(AC_{theo,2L}(\rho_i))/\partial x_i$ and $\partial \theta_{theo,2L}(\rho_i)/\partial x_i$, where x_i refers to μ_{a1}, μ_{a2}, $\mu_{s1}^{'}$ and $\mu_{s2}^{'}$. The derivatives for each parameter were evaluated at SDS between 0.8 and 5 cm for the tissue properties at the midpoints of the ranges used for the forward simulations ($\mu_{a1} = \mu_{a2} = 0.13cm^{-1}$, $\mu_{s1}^{'} = \mu_{s2}^{'} = 10.5cm^{-1}$, and $\ell = 1.2cm$).

Errors arising from inaccurate extracerebral thickness

The final secondary analysis estimated the sensitivities of the recovered F_2 and μ_{a2} to the extracerebral layer thickness ℓ in the 2L realistic adult head geometry. I applied the 2L fitting algorithm using nine evenly spaced ℓ between 1.0 and 1.4 cm. For each ℓ, the algorithm was applied to the same subset of the synthetic data with $F_{2,act} > F_{1,act}$. We focused on this subset to mimic the typical case of CBF greater than extracerebral blood flow [132]. The MAPE (IQR) of the recovered F_2 and μ_{a2} was determined for each ℓ.

4.3 Results

4.3.1 Accuracy of the two-layer and homogeneous approaches

The first step of the 2L fitting algorithm was the recovery of the optical properties of each layer from the FD-DOS measures of AC_{meas} and θ_{meas}. With the algorithm, I recovered the tissue absorption and reduced scattering coefficients with excellent agreement between the recovered and actual values for the analytical model, 2L cube, and 2L realistic head simulations (see Figure 4.3 and Table 4.1). In these geometries, median errors were < 8%. The best-fit linear regression lines for the comparison of μ_{a2} and $\mu_{a2,act}$ approached the unity line. However, the agreement for the SI analysis was not as good. The slope of the linear best-fit line between $\mu_{a,SI}$ and $\mu_{a2,act}$ (0.5) deviated from the unity line.

Regarding the fit of F_1 and F_2 from DCS, the forward-model and 2L cube simulations were able to accurately recover F_1 with median errors below 3% (Table 4.1, Figure 4.4a and

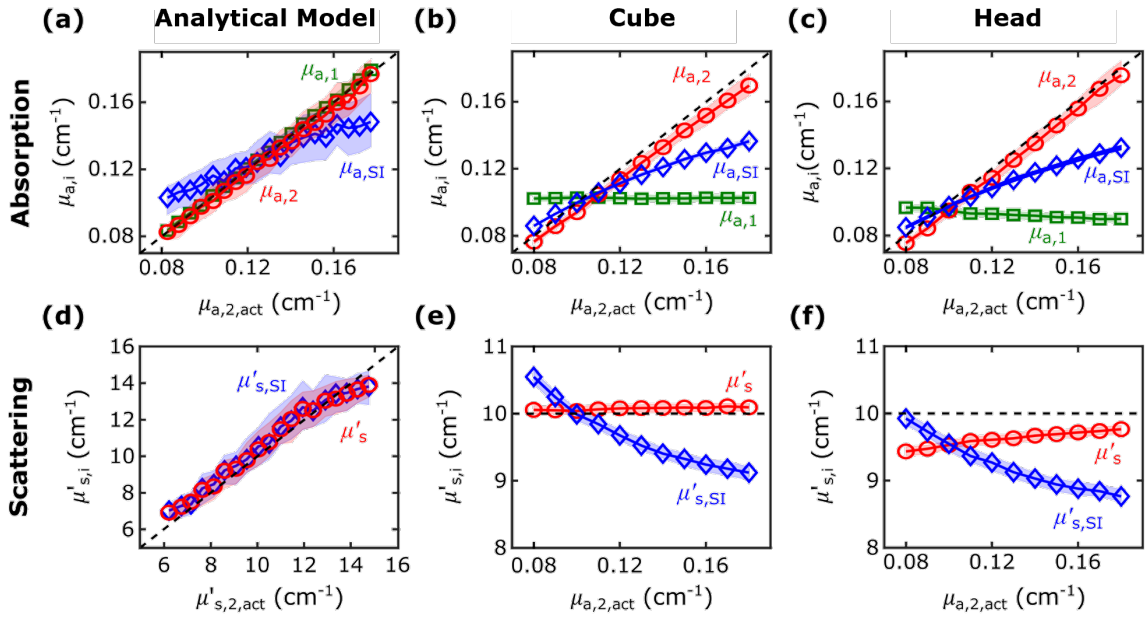

Figure 4.3: Recovered versus actual tissue optical properties. (a)–(c) The recovered tissue absorption (μ_{ai}) and reduced scattering coefficient (μ'_{si}) for the extracerebral (green lines) and cerebral (red lines) layers are plotted against the actual values of the second-layer absorption ($\mu_{a2,act}$) for the (a), (d) forward-model, (b), (e) cube, and (c), (f) realistic head simulations (circles denote the medians of the recovered values across all simulations run for each actual value; shaded areas represent the IQR). The corresponding recovered tissue absorption ($\mu_{a,SI}$) and reduced scattering coefficients from the SI model are also plotted against the actual cerebral absorption values (blue diamonds). Dashed lines represent the actual relationships between each parameter and the cerebral absorption coefficient. Figure taken from [15]

Figure 4.4b). For the 2L realistic head simulations, the method of using an SI model to recover F_1 from a short DCS SDS was modestly less accurate, with errors around 13% (Table 4.1 and Figure 4.4c).

I observed excellent agreement between the recovered and actual F_2 for the forward-model and 2L cube simulations (Table 4.1 and Figures 4.4d and 4.4e). For both datasets, the errors were < 10% on average, and the best-fit linear regression lines approached the unity line (Table 4.1). In the 2L realistic head simulations, however, the recovered F_2 systematically underestimated the true value by a median error of 34% (Table 4.1 and Figure 4.4f). The small IQRs of the recovered flow values demonstrate robustness against noise and optical absorption changes.

When neglecting the extracerebral layer using an SI model to estimate $F_{2,act}$, the systematic errors (i.e., MAPE > 69%) were larger than the errors recovered with our 2L approach in all simulated datasets ($p < 0.001$). The SI homogeneous model recovered the correct directional trends for the 2L cube and realistic head simulations, where the first-layer flow was held constant. However, for the forward-model simulations, the recovered F_{SI} values were highly sensitive to variations in first-layer flow ($F_{1,act}$, Figure 4.4a). Note that the small IQRs for F_2 across variations in extracerebral blood flow indicate minimal cross-talk between extracerebral and CBF (Figure 4.4d).

Table 4.1: MAPE of the optical properties (μ_{a1}, μ_{a2}, and $\mu_s^{'}$) and flow indices (F_1 and F_2) recovered with the 2L approach and with the SI approach ($\mu_{a,SI}$, $\mu_{s,SI}^{'}$, and F_{SI}) for all datasets generated. The linear best-fit relations between the recovered and actual values for the second layer are also reported.

			MAPE(IQR) (%)	Linear regression
Analytical model	Absorption	μ_{a1}	2.4(1.1,4.5)	–
		μ_{a2}	7(3,12)	$1.011\mu_{a2,act} - 0.002$
		$\mu_{a,SI}$	11(5,19)	$0.51\mu_{a2,act} + 0.06$
	Scattering	$\mu_s^{'}$	8(4,13)	–
		$\mu_{s,SI}^{'}$	9(5,15)	–
	Flow	F_1	2.4(1.0, 4.1)	–
		F_2	7(3,13)	$0.098F_{2,act} + 0.05$
		F_{SI}	79(65,88)	$0.004F_{2,act} + 0.95$
2L Cube	Absorption	μ_{a1}	2.7(1.4,4.3)	–
		μ_{a2}	5.0(3.0,7.9)	$0.841\mu_{a2,act} + 0.001$
		$\mu_{a,SI}$	10(5,19)	$0.50\mu_{a2,act} + 0.05$
	Scattering	$\mu_s^{'}$	0.8(0.3,1.4)	–
		$\mu_{s,SI}^{'}$	5.3(2.8,7.3)	–
	Flow	F_1	1.7(0.8,2.8)	–
		F_2	6(3,13)	$1.02F_{2,act} + 0.08$
		F_{SI}	69(35,90)	$0.008F_{2,act} + 1.03$
Realistic head (2L)	Absorption	μ_{a1}	7.7(4.7,9.8)	–
		μ_{a2}	4.6(2.4,7.2)	$1.020\mu_{a2,act} - 0.007$
		$\mu_{a,SI}$	12(6,21)	$0.47\mu_{a2,act} + 0.05$
	Scattering	$\mu_s^{'}$	3.6(2.8,4.8)	–
		$\mu_{s,SI}^{'}$	9(5,11)	–
	Flow	F_1	13(11,16)	–
		F_2	34(30,42)	$0.70F_{2,act} - 0.09$
		F_{SI}	69(33,80)	$0.06F_{2,act} + 1.14$

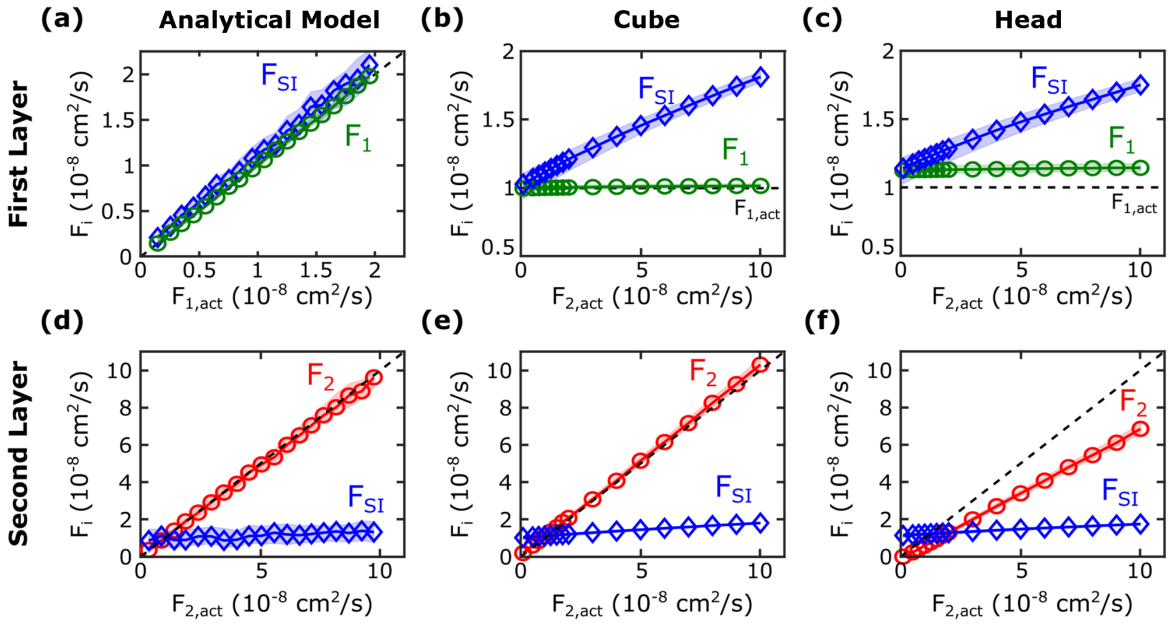

Figure 4.4: Recovered versus actual flow indices. The (a)–(c) recovered extracerebral flow (F_1, green lines) and (d)–(f) cerebral flow (F_2, red lines) indices are plotted against the actual values of the second-layer flow ($F_{2,act}$) for the (b) and (e) (cube) and for (c) and (f) (realistic head simulations). For the forward-model simulations (a) and (d), we plot the extracerebral and CBF values against their actual values. The corresponding recovered flow indexes (F_{SI}) from the SI model are also plotted against the actual values (blue diamonds). Dashed lines represent the actual relationships between each parameter and the x-axis. In all cases, circles denote the medians of the recovered values across all simulations (with varying noise, flow indices, and varying absorption), and shaded areas represent the IQR. Figure taken from [15]

4.3.2 Sensitivity of the FD-DOS two-layer solution to changes in tissue optical properties

I found that the 2L cylindrical FD-DOS solution was minimally sensitive to changes in $\mu_{s2}^{'}$ for SDSs (ρ) up to 5 cm (Figure 4.5). Variations in the solutions for FD-DOS amplitude ($AC_{theo,2L}$) and phase ($\theta_{theo,2L}$) by variations in $\mu_{s2}^{'}$ from 5 to 15 cm^{-1} were smaller or on the same order of the expected noise (Figures 4.5a and 4.3d). Here, I fixed the other tissue parameters at ℓ = 1.2 cm, μ_{a1} = 0.13 cm^{-1}, μ_{a2} = 0.13 cm^{-1}, and $\mu_{s1}^{'}$ = 10.5 cm^{-1}. The sensitivities of the FD-DOS amplitude and phase to extracerebral and cerebral layer optical properties are also plotted vs. SDS in Figure 4.5. The sensitivities are defined by the evaluation of the derivatives $\partial log(AC_{theo,2L})/\partial x_i$ and $\partial \theta_{theo,2L}/\partial x_i$ at $\mu_{a1} = \mu_{a2}$ = 0.13 cm^{-1}, $\mu_{s1}^{'} = \mu_{s2}^{'}$ = 10.5 cm^{-1}, and ℓ = 1.2 cm (x_i denotes μ_{a1}, $\mu_{s1}^{'}$, μ_{a2}, and $\mu_{s2}^{'}$). Note that the sensitivities to $\mu_{s2}^{'}$ are lower than those for the other optical properties. For example, at ρ = 4 cm, the sensitivities of the FD-DOS amplitude and phase to $\mu_{s2}^{'}$ are 5% and −3% of the corresponding sensitivities to $\mu_{s1}^{'}$, and < 0.5% of the sensitivities to μ_{a1} and μ_{a2}. Given its minimal sensitivity to the FD-DOS measurements, $\mu_{s2}^{'}$ is not a good fitting parameter. These results justify the need to assume homogeneous tissue reduced scattering.

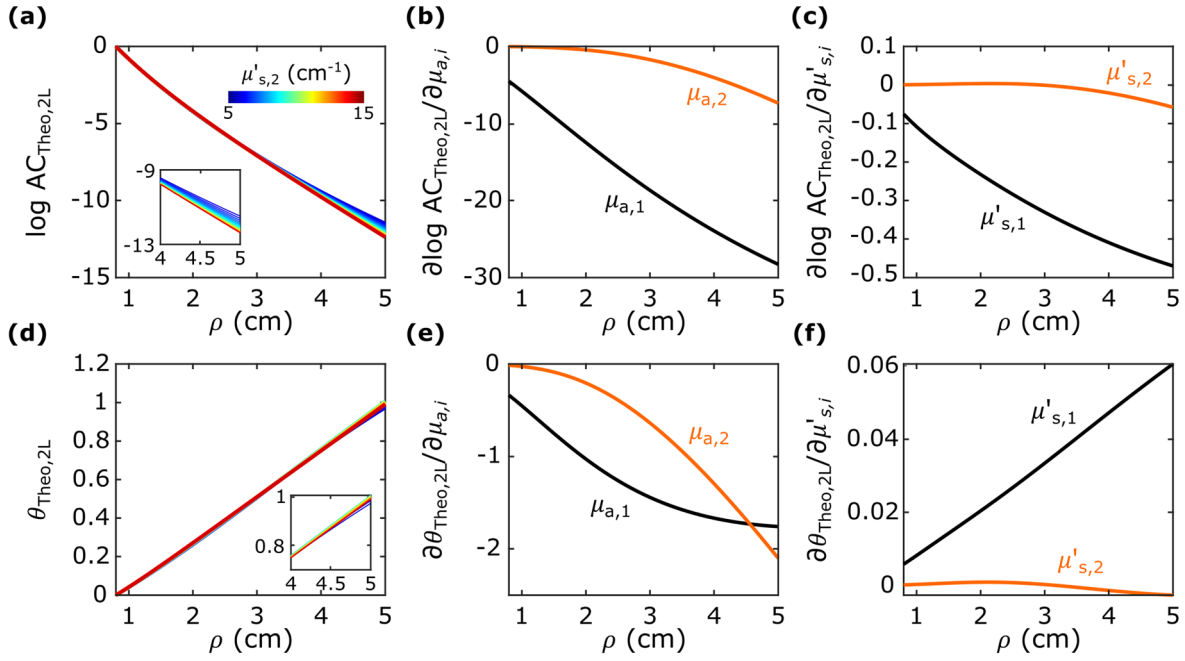

Figure 4.5: Sensitivity of the 2L FD-DOS solution to changes in tissue optical properties. The (a) amplitude logarithm ($log(AC_{theo,2L})$) and (d) phase $\theta_{theo,2L}$ of the cylindrical 2L FD-DOS solution are plotted against SDS (ρ) for a wide range of cerebral tissue reduced scattering coefficients ($\mu_{s2}^{'}$ between 5 (blue) and 15 cm^{-1} (red)). For each $\mu_{s2}^{'}$ evaluation, the extracerebral and cerebral tissue absorption coefficients (μ_{a1} and μ_{a2}) were both fixed at 0.13 cm^{-1}, the extracerebral tissue reduced scattering coefficient ($\mu_{s1}^{'}$) was fixed at 10.5 cm^{-1}, and the extracerebral layer thickness was fixed at 1.2 cm. The sensitivities of the amplitude logarithm ($\partial log(AC_{theo,2L})/\partial x_i$) in (b) and (c) and phase ($\partial \theta_{theo,2L}/\partial x_i$, (d) and (e)) to tissue optical property changes are also plotted against ρ; x_i refers to μ_{a1}, $\mu_{s1}^{'}$, μ_{a2}, and $\mu_{s2}^{'}$. All derivatives were evaluated at the same optical properties used for (a) and (d) with $\mu_{s2}^{'}$ fixed at 10.5 cm^{-1}. Figure taken from [15].

4.3.3 Errors arising from inaccurate extracerebral thickness

I also used realistic head simulations to investigate the influence of errors in the extracerebral layer thickness on the recovery of F_2 and μ_{a2}. The influence was significant for the F_2 recovery but more modest for the μ_{a2} recovery (Figure 4.6). For example, ± 0.2 cm errors in ℓ resulted in median errors of up to 15% in μ_{a2} and up to 60% in F_2. Surprisingly, the minimum error for the recovery of F_2 occurred when the extracerebral layer thickness was overestimated by $\Delta\ell \approx 0.1$ cm.

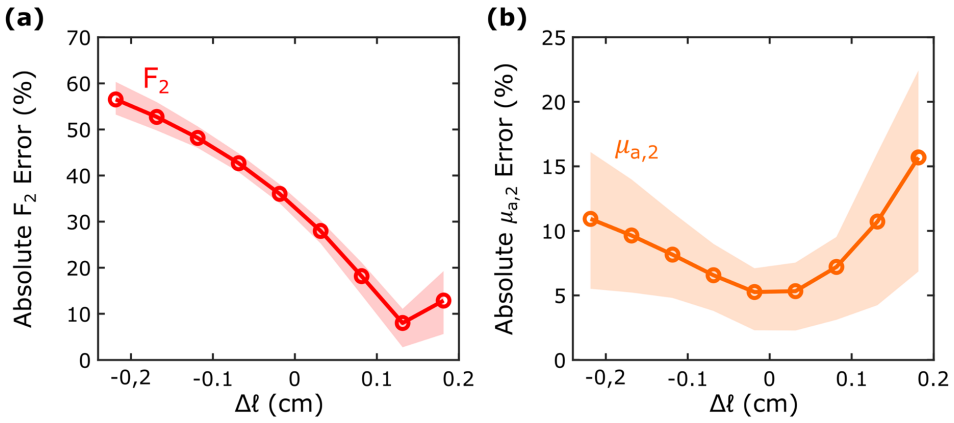

Figure 4.6: Reconstruction errors in CBF and tissue absorption arising from inaccurate extracerebral layer thickness (ℓ). Errors in the recovered (a) CBF (F_2) and (b) cerebral tissue absorption coefficient (μ_{a2}) plotted against errors in the extracerebral layer thickness used for the 2L fits of the realistic head synthetic data. $\Delta\ell$ is the difference between the extracerebral layer thickness used in the fits and the actual extracerebral layer thickness (1.22 cm). The circles and dashed lines denote the median and IQR of the absolute percent errors across all simulations with actual CBF larger than actual extracerebral blood flow.

4.4 Discussion

Using multilayer tissue models is an effective strategy for separating cerebral signals from extracerebral artifacts. Their implementation, however, is often confounded by noise-induced cross-talk in the fitting parameters. To mitigate cross-talk between each parameter, here I used a constrained 2L model in which, instead of fitting for all unknowns simultaneously, the algorithm fits the multidistance FD-DOS and DCS data in sequential steps (Figure 4.2). Other constraints are *a priori* knowledge of the extracerebral layer thickness and homogeneous tissue reduced scattering coefficient. I used hybrid FD-DOS and DCS simulations with noise to characterize the algorithm's accuracy and stability. The simulations were carried out in slab and realistic head geometries and featured typical SDSs for cerebral hemodynamic monitoring with DCS (0.8 and 2.5 cm distances) and FD-DOS (0.8 to 4 cm). I found that the constrained 2L algorithm recovered CBF and tissue absorption with higher accuracy than the conventional SI approach. The small IQRs of the parameters recovered across multiple distinct simulations also demonstrate robustness to noise. The comparable IQR between the

SI and the 2L models also suggests that the numerical stability of both models is similar.

The homogeneous reduced scattering assumption is justified by the minimal sensitivity of the FD-DOS signals to changes in cerebral tissue reduced scattering (Figure 4.5). Note that this minimal sensitivity was also previously reported for time-domain DOS [133]. Fitting for a parameter when a signal is minimally sensitive to it leads to increased recovery errors due to increased numerical instability, which might explain the low cerebral reduced scattering coefficients (e.g., 2 cm^{-1} at 830 nm) reported in previous studies that employed multilayer models to analyze DOS data [13, 58]. One mitigating strategy is to assume the same cerebral tissue scattering coefficient for every subject based on literature values (e.g., from *ex vivo* measurements). Instead, I opted to fit for a homogeneous reduced scattering coefficient based on a prior study that observed similar skin, skull, and brain tissue reduced scattering coefficients [57]. Note that the minimal sensitivity of FD-DOS signals to changes in cerebral tissue reduced scattering reported herein is valid for adult geometries sampled with SDSs $\leq$ 5 cm. For applications wherein thinner extracerebral layers are expected (e.g., in children) or larger SDSs are used, alternative methodologies that separately recover the reduced scattering coefficient from the first and second layers could be feasible and should be investigated.

Surprisingly, the minimum error for the recovery of F_2 in the realistic head geometry occurred when the extracerebral layer thickness was $\Delta\ell \approx 0.1$ cm higher than the estimation of the "actual" thickness (Figure 4.6). This suggests that the method of estimating the actual extracerebral layer thickness was suboptimal. In the realistic head geometry simulation, the skin-to-brain distance varied between 1.09 and 1.33 cm across the length of the optical probe. Recall from Figure 4.1 that the estimated actual thickness of $\ell = 1.22$ cm for the 2L fitting algorithm was obtained by averaging the skin-to-brain distance across the 2-cm-long middle portion of the optical probe. However, if we average the thickness across the 1-cm-long middle portion of the DCS SDS instead, the resulting extracerebral thickness is larger, i.e., $\ell = 1.30$ cm. Note that this larger thickness is equivalent to the thickness that minimizes the error in the recovery of F_2 in Figure 4.6. These findings, as well as prior studies [134, 135], show the importance of the method used for estimating the extracerebral layer thicknesses in multilayer tissue models. Future work is needed to test and optimize estimation methods such as the recently proposed pressure modulation paradigm (which derives an effective layer thickness that differs from direct MRI anatomical measurements) [119] and the direct fitting of the extracerebral layer thickness [121].

One concern for the use of multilayer models is regarding the procedure to solve the inverse problem. Indeed, one of the troublesome issues is the sensitivity of the recovered fitting parameters to the initial guesses for these parameters in the fitting since the method is subjected to converge to local minima. To evaluate this, I reanalyzed a subset of our realistic head simulations using 20 different random initial guesses for each fit (we used the *MultiStart* function implemented in MATLAB 2020a to this end). Specifically, I reanalyzed the data

from all cerebral flow and absorption changes for five of the different noise additions for FD-DOS and DCS. With this approach, the recovered optical properties and flow indices differed by $\sim 10^{-5}$% when compared with the approach of using a fixed initial guess. This reanalysis suggests that the algorithm is numerically stable (i.e., independent of the initial guess used in the fitting procedure).

4.5 Conclusion and Next Chapters

In this work, I used high-fidelity simulations of FD-DOS and DCS data at commonly used SDSs to demonstrate that the proposed constrained 2L approach improves the accuracy of cerebral measurements compared with the conventional SI approach, thus mitigating the inversion procedure problems. The 2L approach takes into account the head's heterogeneity – or at least part of it – separating cortical from extracortical contributions. On the other hand, the SI approach assumes the head is a homogeneous medium.

Importantly, I observed that the numerical stability of the reconstructions with the constrained 2L and SI approaches were comparable. One of the constraints used is homogeneous tissue reduced scattering, which is necessary because the FD-DOS signals are minimally influenced by the cerebral tissue reduced scattering coefficient (at SDSs up to 5 cm). Compared with cerebral absorption, the recovery of CBF was less sensitive to inhomogeneous tissue scattering but more sensitive to errors in the extracerebral layer thickness. The impact of the extracerebral layer thickness errors on FD-DOS and DCS measurements can be mitigated with future strategies that boost their brain sensitivity.

In summary, the 2L approach increases the accuracy of the estimations when compared to the SI approach. However, the results exhibited in Figures 4.3 and 4.4 suggest that the estimations with the proposed 2L algorithm still underestimate the real properties, especially in realistic head simulations. I hypothesize that this remaining lack of accuracy might be coming from the assumption of a planar interface, still present in the 2L approach. In this context, the next chapter introduces the investigation I performed regarding the influence of curvature in the interface of optical data acquisition in estimations through DO techniques.

CHAPTER 5

INFLUENCE OF TISSUE CURVATURE ON THE ABSOLUTE QUANTIFICATION IN FREQUENCY-DOMAIN DIFFUSE OPTICAL SPECTROSCOPY

As I previously discussed, there are two assumptions behind the SI model for which I aimed to develop methods to better deal with. In the last chapter, I discussed an algorithm to better incorporate the heterogeneity of biological tissue over optical estimations. There, I concluded that there is still room for improvement even when considering this feature in the analysis model. In this chapter, I aimed to deal with the second assumption: the flatness at the acquisition interface. This assumption is present even in heterogeneous models (such as the 2L model). Although it is common sense that it also jeopardizes the accuracy of optical estimations, there is little research available aiming to deal with this issue. In this chapter, Section 5.1 introduces the problem within DOS. In Section 5.2, I describe the methods of data generation, acquisition, and analysis. Section 5.3 exhibits the results, while I discuss them in Section 5.4. Lastly, in Section 5.5, I summarize the conclusions of this investigation.

5.1 Introduction

Over the past three decades, DO techniques have emerged as a powerful noninvasive technique for studying human brain function [10, 115, 136–138]. However, to obtain reliable cerebral physiology parameters for clinical use, accurate estimation of tissue optical properties is crucial. This problem is directly dependent on the reliability of the model used for data analysis. The most common approach, the SI model, only partially captures the complexity of actual biological tissues due to assumptions of homogeneity and flatness. As discussed in Chapter 4, although layered models improve accuracy in recovering optical parameters, their estimated optical coefficients are still underestimated, indicating that more factors other than extracerebral contributions should be accounted for achieving accurate and precise quantification [13–15, 29, 139–143]

In addition to the inner geometry of the medium in which light propagates, the acquisition interface can also influence the estimation of optical properties with DOS. Although

not so numerous, previous studies have highlighted the impact of interface assumptions on various DOS techniques. For instance, assuming a planar interface has been shown to cause spatial misregistration of functional magnetic resonance imaging and diffuse optical imaging [19]. Additionally, removing data points obtained in poor optode coupling conditions due to interface curvature has effectively reduced image artifacts in diffuse optical tomography [20]. When working with optical data acquired from a curved interface, errors in the blood flow index measured with diffuse correlation spectroscopy were estimated to be approximately 25% [22]. Furthermore, Monte Carlo simulations in time-domain DOS (TD-DOS) have demonstrated that accounting for the interface geometry results in more accurate assessments of the optical properties [21]. These findings emphasize the importance of considering interface characteristics in optical property estimations with DOS techniques.

In this work, I aimed to reassess the influence of local curvatures at the acquisition interface on the optical properties estimated with FD-DOS and propose a numerical method to account for curved surfaces, improving the absolute quantification of optical properties with FD-DOS. I approached this problem by performing numerical simulations of light propagation in homogeneous media with curved interfaces and using the results to build a lookup table, which is then used to search for the closest solution to the inverse problem. The proposed methodology was initially tested in planar and curved phantom surfaces and head simulations, and we compared the results using our lookup table approach to the standard SI approach. Subsequently, I evaluated the performance of the algorithm using human data.

5.2 Materials and Methods

5.2.1 Methods to Solve the Inverse Problem

I compared the performance of three different models to fit the simulated and experimental FD-DOS data (Figure 5.1). For simplicity, all models were assumed to be homogeneous, so I could only investigate the effects of the curvature and the proposed nonlinear optimization procedures without adding any cofactors to the analysis of the methodology.

Analytical Semi-Infinite Approach

The first model I tested was the analytical solution of the photon diffusion equation to the semi-infinite (SI) geometry with the extrapolated boundary condition (Equation 2.10). The SI approach is widely used in the literature due to its simplicity and low computational cost. It assumes the biological tissue as a homogeneous media, infinite in the x and y directions and with a single air-tissue boundary in the z-direction (Figure 5.1a).

Since the SI model provides an analytical solution to the diffusion equation, we used Equation 2.10 to fit any collected FD-DOS data by minimizing the following cost function, H, using the *fmincon* function in MatLab (The MathWorks Inc., Natick, MA, USA):

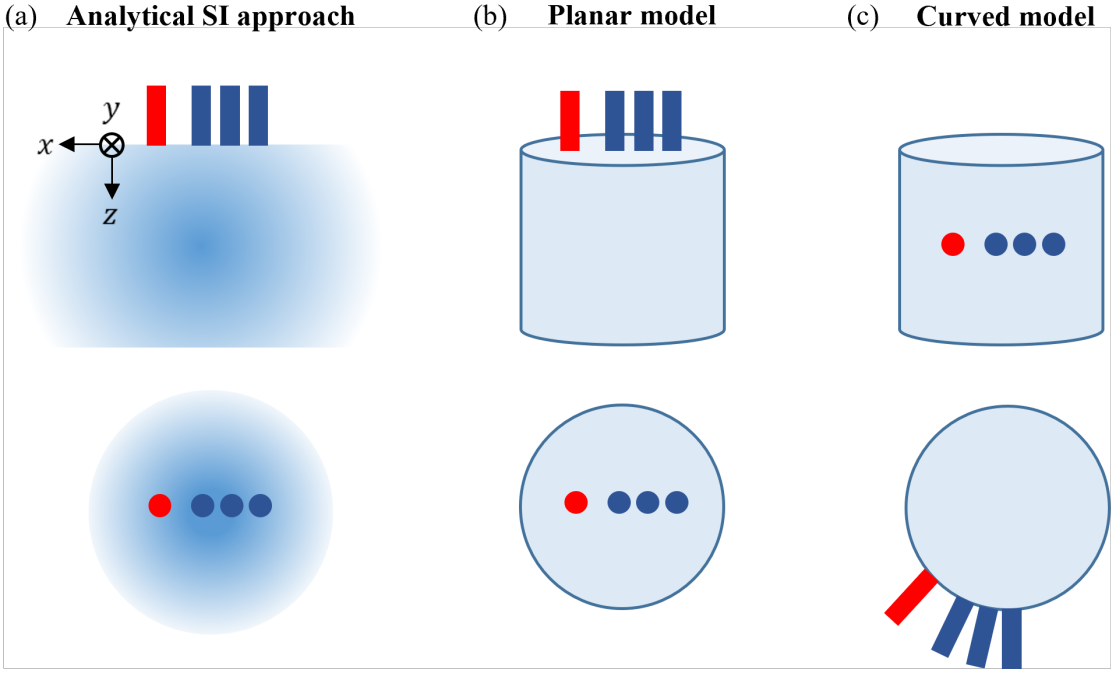

Figure 5.1: Representation of the three models used to estimate the optical properties, shown from the side (top row) and top (bottom row) views for illustrative purposes. (a) Semi-infinite (SI) model, in which the medium is infinite in any direction parallel to the acquisition interface; (b) planar model, in which the sources and detectors were positioned at the top of the cylinder; and (c) curved model, where the optodes were positioned on the side of a cylinder to add non-planarity to the acquisition interface. In all cases, the source and the detectors are represented in red and blue, respectively.

$$H = H_A + H_\theta, \tag{5.1}$$

where

$$H_A = \sum_{i=1}^{N} \left(ln\left(\frac{A^{theo}(\rho_i)}{A^{theo}(\rho_1)}\right) - ln\left(\frac{A^{exp}(\rho_i)}{A^{exp}(\rho_1)}\right)\right)^2$$

$$H_\theta = \sum_{i=1}^{N} \left((\theta^{theo}(\rho_i) - \theta^{theo}(\rho_1)) - (\theta^{exp}(\rho_i) - \theta^{exp}(\rho_1))\right)^2.$$

Here, i is the i-th source-detector separation (SDS), N is the total number of SDSs, $A(\rho_i)$ is the fluence amplitude of ρ_i, and $\theta(\rho_i)$ is the phase shift measured at ρ_i. The superscripts $theo$ and exp denote theoretical (predicted) and experimental (measured) quantities, respectively. The minimization of Equation 5.1 was used to estimate μ_a and $\mu_s^{'}$ in the SI approach without further assumptions.

Numerical Models

In addition to the SI approach, I used a finite-element method to solve the inverse problem. I simulated the expected amplitude and phase of FD-DOS data for two specific geometries using the open-source software NIRFASTer [39, 42] with a node size of 0.065 cm, which pro-

vided final meshes containing approximately 610,001 nodes. For each geometry, I varied μ_a from 0.05 to 0.30 in steps of 0.005 cm^{-1}, and $\mu_s^{'}$ from 5 to 15 in steps of 0.1 cm^{-1}. I used SDSs of 1.5, 2.0, 2.5, and 3.0 cm. The amplitude and phase for each cross combination were stored as a lookup table that was used to estimate the absolute optical properties from the FD-DOS data. For solving the inverse problem, the combination of μ_a and $\mu_s^{'}$ that minimizes the cost function described by Equation 5.1 was chosen as the optimal solution to the problem. This approach guarantees that the global minimum is selected. Of note, the theoretical amplitude and phase described in Equation 5.1 consisted of the simulated amplitude and phase obtained for each combination of μ_a and $\mu_s^{'}$ when we use lookup tables.

The first geometry consisted of a homogeneous cylinder (radius and height of 9 cm) with the source and detectors positioned on the top planar surface (Figure 5.1b). The planar model aimed to confirm the reliability of the numerical solution compared to the analytical approach since the findings should closely match those of the SI method.

In the second geometry, I simulated the same medium as before. Still, the sources and detectors were positioned on the curved side of the cylinder, on a plane parallel to the cylinder basis, to account for local curvature effects (Figure 5.1c). With this approach, the side of the cylinder can mimic biological tissue curvatures, as the cylinder radius, R, determines the curvature (i.e., $\kappa = 1/R$). To investigate how different curvatures influence the simulated data, we simulated two curved models with cylinders with radii of 9 and 7 cm ($\kappa = 0.111 cm^{-1}$ and $\kappa = 0.143 cm^{-1}$, respectively), which we will refer to as *Curved Model 1* and *Curved Model 2*, respectively. I chose these values because they are close to our estimations of different forehead curvature regions of adults.

5.2.2 Datasets for Methods Validation

The four methods above were tested with three distinct datasets generated for validation: numerical simulations mimicking standard optical phantoms in diffuse optics, experimental data collected on two homogeneous optical phantoms with known optical properties, and numerical simulations performed on an adult human head.

Numerical Simulations Mimicking Phantoms

The first step to validate the proposed methodology involved performing numerical simulations on media that mimicked optical phantoms. I created meshes consisting of homogeneous cylinders with two different radii and positioned the sources and detectors at different locations along the interface. For the cylinder with low curvature (11 cm radius, curvature $\kappa = 0.091 cm^{-1}$; mesh node size of 0.9 cm, comprising 645,643 nodes), I placed the sources and detectors on both the curved and planar sides. For the cylinder with high curvature (5 cm radius, curvature $\kappa = 0.200 cm^{-1}$; mesh node size of 0.9 cm with 148,836 nodes), I positioned the optodes exclusively on the curved side. These simulations were performed with

the same range of optical properties previously described using SDSs of 1.5, 2.0, 2.5, and 3.0 cm.

To each simulation, I added random amplitude and phase noise independently, similarly to Chapter 4. The noise was based on a Gaussian model with zero mean for each simulation independently. For the phase, the standard deviation was set at 0.1 degrees; for amplitude, the noise was incorporated such that the signal-to-noise ratio of the resulting curve reached 100, similar to the previous chapter. Then, I fitted the resulting data using the methods previously outlined for each combination of optical properties and curvature. The performance of each fitting method was assessed by the median of the absolute percentage error (MAPE), as in the previous chapter.

Phantom Measurements

In addition to the phantom simulations described in the section above, I obtained experimental FD-DOS data from phantoms (Figure 5.2). Acquisitions were performed with the commercial FD-DOS system exhibited in Figure 2.10. We used two wavelengths (690 and 847 nm), and SDS were 1.5, 2.0, 2.5, and 3.0 cm. The temporal resolution of the data acquisition was 18.4 Hz. I used two solid phantoms with known optical properties (phantom 1: $\mu_a(690nm) = 0.113cm^{-1}$, $\mu_a(847nm) = 0.113cm^{-1}$, $\mu_s^{'}(690nm) = 10.1cm^{-1}$, $\mu_s^{'}(847nm) = 9.0cm^{-1}$; phantom 2: $\mu_a(690nm) = 0.108cm^{-1}$, $\mu_a(847nm) = 0.110cm^{-1}$, $\mu_s^{'}(690nm) = 11.1cm^{-1}$, $\mu_s^{'}(847nm) = 9.9cm^{-1}$). Each phantom has three different interfaces for data acquisition: the planar top of the block and two curved sides with the same radius as the simulations (i.e., one with a 5 cm radius and the other with an 11 cm radius). I collected data at all interfaces in both phantoms for 2 minutes and fitted the data to the different models separately. To assess the stability of each method in situations with real noise, I evaluated the 95th percentile of MAPE distribution for phantom real data. Before every measurement, I calibrated the device using a standard procedure (Section 2.3.4) to ensure the accuracy of the measured amplitude and phase against the flat surface reference.

Numerical Simulations on a Human Head

The last validation of the curved model consisted of testing it in data obtained from numerical simulations employing a mesh of an adult human head created with the same open-source library previously described in the last chapter (brain2mesh, with a Delaunay sphere radius of 0.11 cm, radius-to-edge ratio of 1.24, and maximum element volume of 4 cubic voxels). This head mesh was used as input into NIRFASTer, yielding FD-DOS simulations at two locations with distinct curvatures: a 7 cm and a 20 cm radius location, which I refer to as *high* and *low* curvatures ($\kappa = 0.143cm^{-1}$ and $0.050\ cm^{-1}$), respectively. At each location, I estimated the curvature by computing the radius of the circumcenter that passes through the boundary vertices located between the source and the farthest detector. In both cases, I

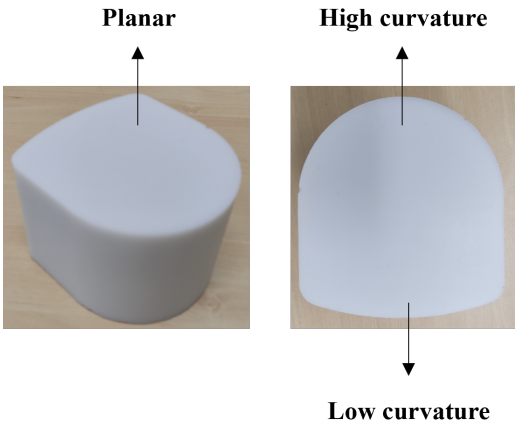

Figure 5.2: One exemplar of the phantoms used to investigate the accuracy of the models under comparison. Note that the phantom has a planar side, one surface with a slight curvature (11 cm radius) and other with a high curvature (5 cm radius).

used the same SDSs of the experimental probe (i.e., 1.5, 2.0, 2.5, and 3.0 cm) and performed simulations varying μ_a from 0.1 to 0.25 cm^{-1} in steps of 0.05 cm^{-1}, and $\mu_s^{'}$ from 6 to 12 cm^{-1} in steps of 2 cm^{-1}, always assuming the head to be homogeneous. These parameter ranges cover all the values we previously measured in human studies. Then, I applied the same noise model previously described to the simulations before attempting to recover the optical parameters by the different models.

5.2.3 Datasets for Methods Exploration

Diffuse Correlation Spectroscopy Simulations

Considering that the estimation of blood flow in Diffuse Correlation Spectroscopy (DCS) relies on absolute optical properties, I explored the impact of curvature on the accuracy of blood flow determination. For that purpose, I created a cylindrical mesh with a 7 cm radius (node size of 0.065 cm, 610,001 nodes), positioned one source and one detector on the curved side of the cylinder, and used NIRFASTer to simulate the temporal electric field autocorrelation functions.

I examined all permutations of μ_a set at 0.10, 0.17, and 0.25 cm^{-1}, and $\mu_s^{'}$ set at 6, 9, and 12 cm^{-1}. For each pair of optical properties, I simulated ten Blood Flow Indices (F) values spaced evenly at a log scale: 0.056, 0.100, 0.178, 0.316, 0.562, 1.00, 1.78, 3.16, 5.62, and 10.0×10^{-8} cm^2/s, at 100 lag times ranging from 0.6 μs up to 3.7 ms, using the same multitau scheme as last chapter. I fixed the wavelength at 785 nm and the source-detector separation at 2.5 cm. DCS data was fitted using the planar, homogeneous model (G_1), minimizing the following cost function:

$$H_{DCS} = \sum_{\tau} \left| \frac{G_1^{theo}(\tau)}{G_1^{theo}(0)} \right|^2 - \left| \frac{G_1^{exp}(\tau)}{G_1^{exp}(0)} \right|^2,$$

Table 5.1: Demographic data of all participants separated by the cofactors analyzed in this work. The values in parenthese represent the standard deviation across the distribution.

	Total	Biological Sex		Skin Color	
		Men	Women	White	Non-White
Participants	152	55	97	99	53
Age[years]	39(17)	39(18)	38(17)	37(17)	41(17)

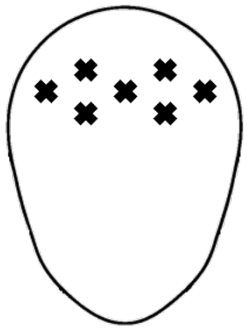

Figure 5.3: Regions of the PFC where optical data was acquired: right and left lateral frontal areas, right and left inferior frontal areas, right and left superior frontal regions, and the central frontal area.

where the sum was performed over all lag times, τ. Since the goal was to isolate the influence of curvature on F estimations, I used the simulated optical properties as inputs for G_1 instead of fitting the FD-DOS simulated data. In addition, I opted not to add noise to the simulated DCS curves since our aim was not to assess a method for fitting F in the presence of curvature. Analyzing the simulations without noise allowed us to gain intuition regarding the impact of curvature on the DCS planar fit with no additional confounders.

Characterization of Human Brain Data in the Presence of Curvature

Last, I employed the proposed curved model to analyze FD-DOS data previously obtained from 152 healthy participants [144], whose demographic data is presented in Table 5.1. Acquisitions were performed with the commercial FD-DOS system exhibited in Figure 2.10 at two wavelengths (690 and 847 nm) and SDS of 1.5, 2.0, 2.5, and 3.0 cm. The temporal resolution of the data acquisition was 18.4 Hz. Before every participant session, I calibrated the FD-DOS device as we did for phantom acquisitions. All participants were instructed to sit in a comfortable chair, stay relaxed, and not move. The optical probe was then placed on seven regions of interest (ROIs) around the prefrontal cortex (PFC), illustrated through 'X' in Figure 5.3, using adhesive tape. For every participant, we collected a two-minute data segment for each ROI. All experimental procedures were reviewed and approved by the local ethics committee at the University of Campinas.

For data analysis, I discarded time points where (1) amplitude did not decrease, or phase did not increase, with an increase of SDS, and (2) data whose $\mu_s^{'}$ at 690 nm was higher than at 847 nm. Both conditions do not match the expected response and likely result from experimental errors due to poor probe contact. From the estimation of the optical prop-

erties, we used the modified Beer-Lambert law to calculate $[HbO]$ and $[HbR]$, directly from μ_a. As we acquired data only at two wavelengths, I assumed a water fraction of 75% to obtain chromophore concentrations with more reliability. From $[HbO]$ and $[HbR]$, we calculated $[HbT]$ and StO_2.

After fitting the experimental data using curved and planar models, I conducted tests to determine whether the distributions and their moments differed significantly between the approaches. Initially, I assessed the normality of the distributions using the Lilliefors goodness-of-fit test. Subsequently, if the distributions were found to be normal, I performed comparisons using a Student's T-test; otherwise, a Wilcoxon rank sum test was applied. For the statistical moments, I calculated the mean, standard deviation (STD), skewness (s), and kurtosis (k) values of the distributions.

5.3 Results

5.3.1 Phantom Validations

Figure 5.4 presents the MAPEs for the recovered absorption coefficients when applying the four different fitting methods to both planar and curved interfaces over the range of optical properties tested.

When the sources and detectors were positioned on the planar surface (Figure 5.4a), the errors of the recovered optical properties were consistently low regardless of the fitting model; in this condition, MAPEs were less than 10% when compared to the ground truth, with the lowest MAPEs obtained when fitting the data with planar models (i.e., analytical SI and numerical planar model). Across all optical properties simulated, the average MAPE (95th percentile) for the SI model was 2.8 (0.5, 4.6)%, while the planar simulation achieved 0.2 (0.0, 3.2)%. The Curved Models 1 and 2 resulted in slightly higher MAPEs of 4.5 (2.2, 8.0)% and 6.5 (4.3, 9.5)%, respectively. These differences were statistically significant when I compared the MAPE distributions ($p< 0.001$, Wilcoxon test). Additionally, the robust Cohen's D effect size between planar and curved models (2.4 on average) is larger than the one computed between the planar models and among the curved models (1.2 on average). It is also worth noting the lower errors achieved by the planar simulation when compared to the standard SI approach ($p<0.001$, Wilcoxon test), suggesting that the numerical approach is robust and can yield precise results.

For the highly curved surface (Figure 5.4c), curved models significantly outperformed planar models. The lowest error rate was obtained when the mismatch between the curvature of the interface and the simulated model was minimal (Curved Model 2, MAPE: 5.6 (2.8, 8.7)%). However, the error was small even when the curvature of the curved model was distant from the actual interface curvature (Curved Model 1, MAPE: 6.8 (4.2, 10.3)%). On the other hand, the use of planar models resulted in errors as high as 25%, with average MAPEs

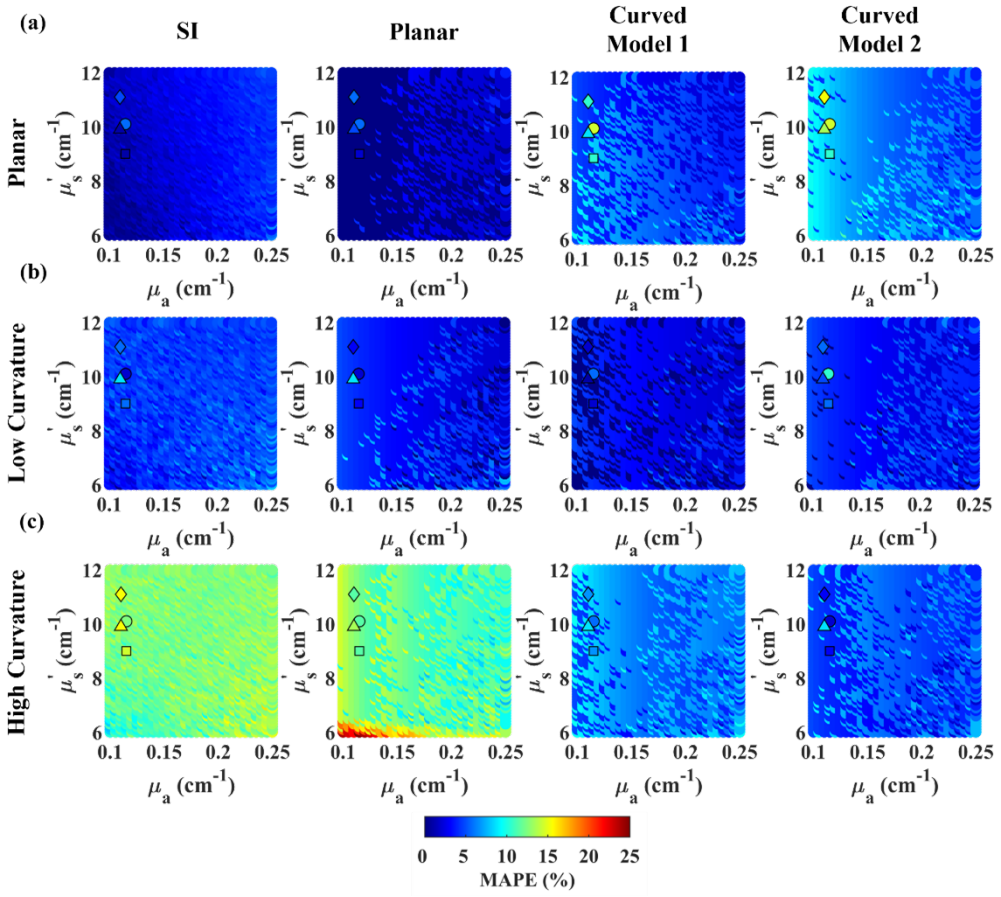

Figure 5.4: Median Absolute Percentage Errors (MAPE) of each fitting method in simulations that mimic (a) planar, (b) 11 cm, and (c) 5 cm phantom sides. Additionally, for each fitting method and curvature condition, the MAPE obtained when fitting real data in phantoms are exhibited (circle markers for Phantom 1, 690 nm; square markers for Phantom 1, 850 nm; diamond markers for Phantom 2, 690 nm and triangle markers for Phantom 2, 850 nm).

of 13.3 (10.3, 16)% for the SI model and 12.3 (9.1, 25)% for the planar simulations. A Wilcoxon test yielded statistically significant differences among all distributions ($p < 0.001$), and D values between curved and planar models (4.9 on average) are larger than the ones between models that assume curvature or not (0.7 on average).

For the interface with a less pronounced curvature (Figure 5.4b), all models showed statistically different yet comparably modest MAPEs ($p < 0.001$, Wilcoxon test). Unlike other surfaces, D values between curved and planar models (0.8 on average) are similar to the ones between both planar and both curved models (0.9 on average). Across all optical properties, the curved model which closely matched the actual interface curvature achieved a smaller error of 2.2 (0, 5.3)%, slightly better than the Curved Model 1 model's MAPE of 3.8 (0, 7.7)%. The use of planar models in this low curvature interface resulted in comparable MAPEs of 4.8 (2.5, 6.8)% and 3.6 (0, 9.1)% for the SI model and planar simulation, respectively. Note, once more, that in addition to the small error obtained with Curved Model 2 (2.6%), the additional error of Curved Model 1 is 0.7% on average, which suggests that a mismatch in the assumed curvature introduces a smaller error than not considering it at all (2.2% additional error on average).

Real phantom experimental data revealed higher errors than the simulated data, indicating that simulations may not fully capture the nuances of actual data acquisition, even after the addition of noise models. I observed that phantom data MAPEs were about 5% higher than simulation MAPEs when the model curvature matched the interface curvature of data simulation, and approximately 8% higher when there was a curvature mismatch.

Despite the larger errors than the simulations, the experimental data followed the same trends observed for the mimicking phantom simulations. The highest errors were obtained when using planar models to fit data of a highly curved interface, yielding an average MAPE of 12(7,18)% (planar numerical) and 15(13,19)% (analytical SI) across wavelengths and phantoms. Conversely, curved models achieved MAPEs as low as 3–7%. When fitting planar interfaces, curved models yielded average MAPEs of 14(9,19)% across wavelengths and phantoms, substantially higher than the 4(0,7)% obtained with planar models for this condition across all wavelengths and both phantoms for the planar numerical and the analytical SI models, respectively. However, as the measurement surface exhibited a nonzero curvature (11 cm radius side), the MAPEs obtained with planar models significantly increased (5(2,9)% across all phantoms and wavelengths), and the errors of curved models decreased (6(0,11)%) up to the conditions of high curvature.

Lastly, I assessed the stability of the models using the 95th percentile of MAPE distribution over the 2-minute data acquisition in real data. Simulation methods and SI model yielded a 95th percentile around 5% (Table 5.2), which indicated that the stability of our simulations is similar to the analytical model. Additionally, real phantom data suggests that the results obtained with the planar numerical model are essentially the same as those obtained through the SI model, given the overlapping of its 95th percentiles.

Table 5.2: Mean absolute percentage error (MAPE) of each fitting algorithm for estimating the absorption coefficient of the optical phantoms collected at different sides of the phantom. The values in parenthesis represent the boundaries of the 95th percentile across time points collected over 2 minutes of data acquisition.

	Phantom 1				Phantom 2			
	Curved Models		Planar Models		Curved Models		Planar Models	
λ (nm)	Model 1	Model 2	Simulations	SI	Model 1	Model 2	Simulations	SI
	Planar surface of the phantom							
690	15(15,19)	15(11,15)	6(6,10)	6(5,9)	16(11,16)	11(11,16)	6(2,6)	5(3,7)
847	11(11,15)	11(11,11)	2(2,2)	1(0,2)	14(9,14)	9(9,14)	5(0,5)	1(0,2)
	Curved side ($R = 11$ cm, $\kappa = 0.09 cm^{-1}$)							
690	11(6,11)	6(6,11)	2(2,3)	2(1,4)	6(2,6)	2(2,6)	3(3,7)	6(4,8)
847	6(6,6)	2(2,6)	3(3,7)	6(5,6)	5(0,5)	1(0,1)	9(5,9)	9(8,9)
	Curved side ($R = 5$ cm, $\kappa = 0.20 cm^{-1}$)							
690	2(2,3)	3(3,3)	12(7,12)	13(12,15)	3(3,7)	7(3,7)	12(12,12)	16(15,17)
847	3(3,3)	7(3,7)	12(12,12)	15(15,16)	9(5,9)	9(9,9)	14(14,18)	16(16,17)

5.3.2 Numerical Simulations on a Realistic Head

To comprehensively examine the influence of curvature on recovering the absolute optical properties in realistic brain geometries, I also evaluated the performance of the proposed models in fitting simulated data in an adult homogeneous head with added noise. Given the similarity in performance between the numerical planar model and the analytical SI model in the previous results, I focused the comparison on curved models paired with the SI model to enhance visualization clarity.

Figure 5.5 shows the MAPE of the recovered absorption coefficient (μ_a^{fit}) relative to the simulated absorption coefficient (μ_a^{sim}) for simulations with four different reduced scattering coefficients for the two curvatures examined. In regions of the head with low curvature (Figure 5.5a), the behavior of the curved models closely paralleled that of the SI model. The average MAPE across all tested values of μ_a and $\mu_s^{'}$ was approximately 4(0,16)%, 5(0,18)%, and 6(1,19)% for the Curved Model 2, Curved Model 1, and SI models, respectively. The stability of the models was also similar: the 95th percentile range was around 4.1% for the SI model on average, close to the 5.5% measured for the curved models. A Wilcoxon test was not able to distinguish between Curved Models 1 and 2 MAPEs (p=0.10) nor between curved and the SI models (p=0.28). When analyzed as a function of the optical properties, errors tended to increase with higher values of μ_a, and decrease with higher values of $\mu_s^{'}$.

However, in regions of the head with high curvature (Figure 5.5b), the planar approach yielded significantly higher errors than the curved models. The average MAPE for recovering μ_a over all the simulations was 10(3,22)% for the analytical SI model, which is larger than the 5(0,15)% and 5(0,10)% average MAPE obtained for both Curved Model 2 and Curved Model 1, respectively. The 95th percentile range obtained for the curved and SI models were 3.3% and 2.8%, respectively. A Wilcoxon test distinguished curved from planar models (p<0.001), but

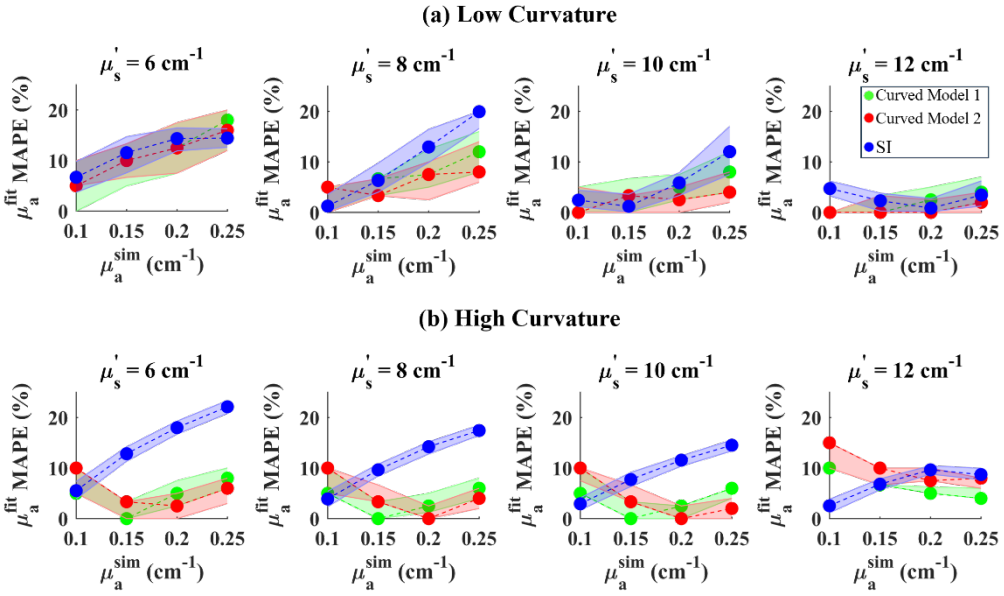

Figure 5.5: Mean absolute percentage error (MAPE) of the estimated absorption coefficient (μ_a^{fit}) when using the analytical SI approach (blue) and the two curved models with curvatures of 0.11 (green) and 0.14 (red) cm^{-1} to fit simulated data in a head model. We simulated data in head regions with (a) low curvature and (b) high curvature for varying values of μ_a and μ_s' with added experimental noise. The simulated μ_s' is displayed at the top of the graphs, while the simulated absorption coefficient (μ_a^{sim}) is along the horizontal axis. Error bars represent the 95th percentile of MAPE distributions. Of note, for lookup table methods (i.e., Curved Models 1 and 2), the median MAPE usually coincides with a border of the shaded error bar. It suggests that the noise makes the fitted values oscillate between two specific values.

did not find statistical differences between Curved Models 1 and 2 (p=0.11). The influence of curvature was particularly high in regions with high μ_a and low μ_s' values, wherein the planar models consistently yielded higher MAPE values. Similar to what I found with the optical phantoms, I did not observe any substantial differences in MAPE between the two curvature values investigated, suggesting that small discrepancies in curvature do not inherently lead to a significant increase in MAPE.

5.3.3 Diffuse Correlation Spectroscopy Simulations

To preliminary investigate the effect of the curvature on blood flow estimations, I simulated DCS data on a 7-cm radius mesh for F = 0.056, 0.100, 0.178, 0.316, 0.562, 1.00, 1.78, 3.16, 5.62 and 10.0×10^{-8} cm^2/s using all the combinations between μ_a = 0.10, 0.17, and 0.25 cm^{-1} and μ_s' = 6, 9, and 12 cm^{-1}. I adjusted the simulated data using the planar G_1 model and the actual simulated optical properties. Across all pairs of simulated optical properties, the MAPEs obtained was 1.3(0.5,3.2)%. This value, smaller than the 5-15% errors obtained in FD-DOS data, suggests that F estimations are less affected by the presence of curvature. Additionally, MAPEs from F estimations are approximately constant despite the simulated flow in this range (amplitude variation, i.e., the difference between the maximum and minimum MAPE, of 0.03(0.01,0.08)%).

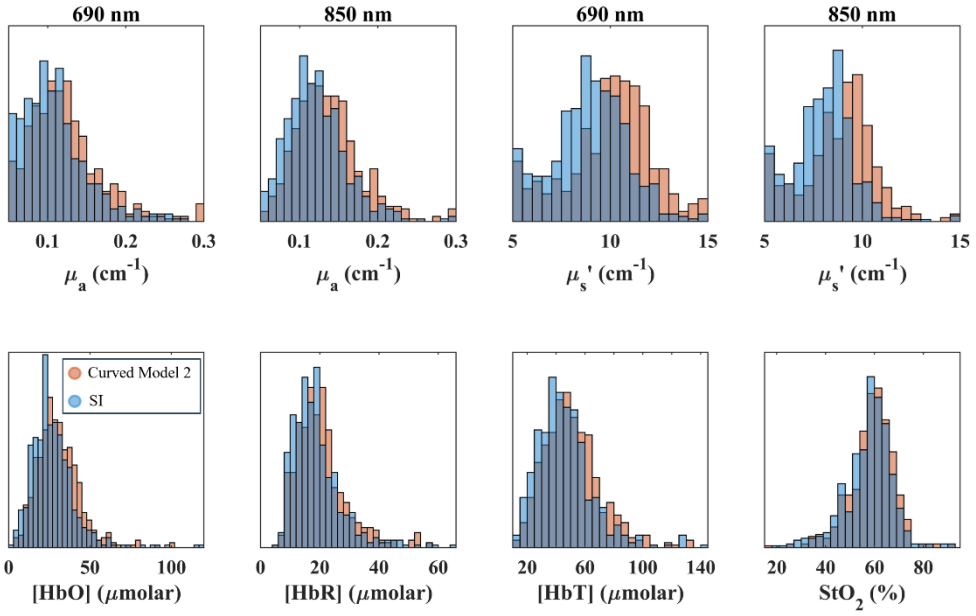

Figure 5.6: Quantities estimated by planar (SI, blue) and curved (Curved Model 2, orange) models. The first row shows the optical properties (i.e., μ_a and $\mu_s^{'}$) for both same wavelengths (690 and 850 nm). The second row shows the hemodynamic parameters derived from the absorption coefficient (i.e., $[HbO]$, $[HbR]$, $[HbT]$, and StO_2) estimated by both models.

5.3.4 Human Brain Data

To better understand how accounting for curvature can affect the estimation of the optical properties of actual brain FD-DOS data, I compared the distributions of μ_a and $\mu_s^{'}$ at both wavelengths across all participants and ROIs, as well as the derived hemodynamic parameters $[HbO]$, $[HbR]$, $[HbT]$, and StO_2, estimated using both SI and curved models (Figure 5.6).

Considering the similar performance observed for both curvatures in the previous head simulations, I opted to simplify the comparison by exclusively contrasting the SI model (represented in blue) with the higher curvature model (depicted in red). Across all subjects, the addition of curvature increased the optical properties estimates by 10(5)% when compared to the SI approach at both wavelengths (10(5)% increase for μ_a and 1(6)% increase for $\mu_s^{'}$). The variability of the estimates across the population, as measured by the standard deviation, was slightly larger for the curved model (2% increase in μ_a standard deviation and 17% in $\mu_s^{'}$ across all wavelengths). As expected, the disparities in absorption coefficients extended to the estimations of HbO, HbR, and HbT concentrations, which were 15(10), 9(8), and 12(5)% higher for the curved model when contrasted with planar models. Across all hemodynamic properties, it is worth noting that StO_2 exhibited the least sensitivity to curvature; we observed a nonsignificant increase of 2(6) in StO_2 when considering the effects of curvature.

The higher statistical moments related to the shape of the distributions are exhibited

Table 5.3: Median, standard deviation (STD), kurtosis (k), and skewness (s) for the distributions of the optical properties and physiological parameters estimated by SI and Curved Model 2

Optical properties

	$\mu_a\ (cm^{-1})$				$\mu_s'\ (cm^{-1})$			
	690 nm		850 nm		690 nm		850 nm	
	Curved Model 2	SI	Curved Model 2	SI	Curved Model 2	SI	Curved Model 2	SI
Median	0.115	0.103	0.130	0.117	10.2	9.0	9.1	8.1
STD	0.047	0.045	0.042	0.042	2.2	1.9	1.9	1.6
k	5.2	7.0	4.8	7.6	2.9	3.1	3.4	4.8
s	1.2	1.6	1.0	1.5	-0.4	0.0	-0.1	0.4

Physiological Parameters

	$[HbO]\ (\mu molar)$		$[HbR]\ (\mu molar)$		$[HbT]\ (\mu molar)$		StO_2 (%)	
	Curved Model 2	SI	Curved Model 2	SI	Curved Model 2	SI	Curved Model 2	SI
Median	29	25	19	17	48	43	60	59
STD	13	14	9	9	20	20	9	10
k	6.7	12.1	5.6	7.7	4.5	6.7	4.8	4.7
s	1.3	2.1	1.4	1.8	0.9	1.4	-0.5	-0.5

in Table 5.3. Across all cases, the skewness values, s, remained consistently close to zero, indicating that the inclusion of curvature, while increasing the variance, did not affect the symmetry of the distributions. Furthermore, I observed that the kurtosis values, k, for the curved model estimates were consistently lower than the planar estimates. This suggests that the distributions associated with the curved model had a slightly flatter profile. In addition, the kurtosis values for the curved model tended to approach a value of 3, implying that the inclusion of curvature made the distributions more closely resemble a Gaussian (normal) distribution. Additionally, all the distributions in Figure 5.6 exhibited significant differences ($p < 0.05$) when compared, except for StO_2 (p=0.052).

Relationship Between Optical Estimates and Demographic Factors

Given that the curved model yielded optical-based hemodynamic estimates with distributions that are wider and more even than the standard SI approach based on k and s values, I posited that this model might be better equipped to discern fluctuations in population demographic factors, which are often entangled with optical property estimations using FD-DOS. As this dataset encompasses a substantial cohort, I also sought to explore the variations in properties concerning age, biological sex, and skin color.

First, I investigated the dependence of the distribution of the hemodynamic parameters on the categorical cofactors (i.e., sex and skin color) independently (Figure 5.7). I found no significant difference between the distributions neither in terms of sex (male vs. female) or skin color (white vs. non-white). The median and standard deviations for these cofactors were within the same range (Table 5.4). This finding was also true for kurtosis and skewness of the paired distributions.

In addition, I quantitatively compared the pair of frequency histograms for each cofactor using the scaled robust estimator for Cohen's D to account for non-parametric distribu-

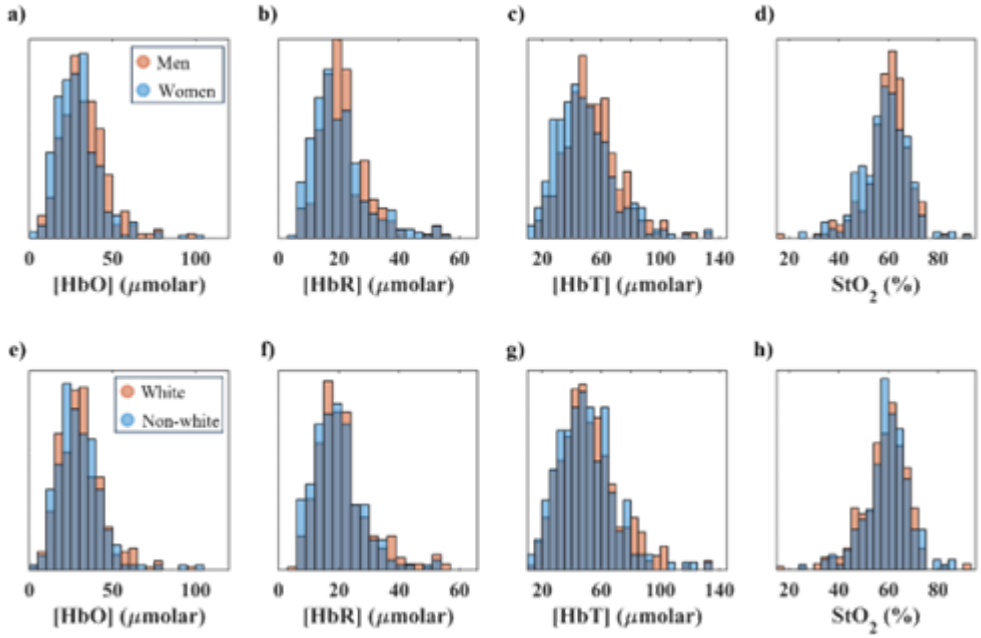

Figure 5.7: The first row shows the men (orange) and women (blue) distribution of (a) [HbO], (b) [HbR], (c) [HbT], and (d) StO_2 estimated by Curved Model 2. The second row shows the white (orange) and black and brown, described as non-white (blue), distribution of (e) [HbO], (f) [HbR], (g) [HbT] and (h) StO_2 estimated by the same model.

	[HbO] ($\mu molar$)		[HbR] ($\mu molar$)		[HbT] ($\mu molar$)		StO_2 (%)	
Physiological parameters according to biological sex								
	Men	Women	Men	Women	Men	Women	Men	Women
Median	31	27	20	18	53	46	60	59
STD	14	13	8	9	19	20	9	9
s	1.1	1.5	1.5	1.4	0.9	1.0	-0.9	-0.3
k	5.8	7.9	6.6	5.2	4.6	4.8	6.2	4.2
D	0.34		0.23		0.33		0.19	
Physiological parameters according to skin color								
	White	NW	White	NW	White	NW	White	NW
Median	29	28	20	19	49	47	60	60
STD	13	14	9	8	20	19	9	9
s	1.1	1.5	1.4	1.2	0.9	1.0	-0.6	-0.4
k	5.8	8.2	5.4	5.7	4.3	5.2	5.0	4.5
D	0.05		0.15		0.11		0.09	

Table 5.4: Median, standard deviation (STD), skewness (s), and kurtosis (k) for the distributions of [HbO], [HbR], [HbT], and StO_2 estimated by Curved Model 2 according to biological sex and skin color. For each case, the comparison between each cofactor was assessed with the robust Cohen's D (D).

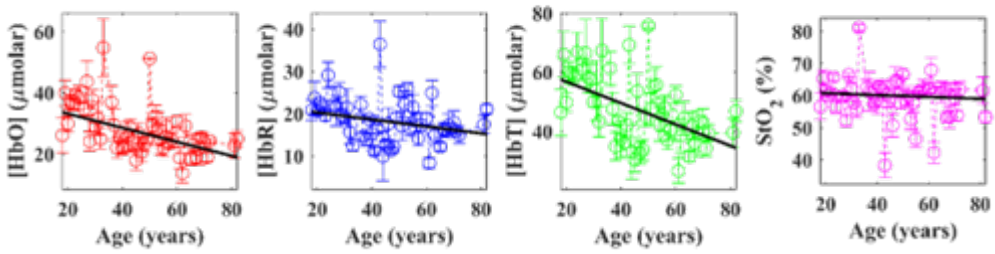

Figure 5.8: Parameters estimated by the curved model as a function of age and its linear regression (black solid line).

tions. Despite no observed differences in the distributions, the effect size of D suggests that the influence of sex on the physiological parameters, although small (D = 0.34 for HbO and D = 0.33 for HbT), may not be negligible in a cohort larger than ours.

As age is a numerical cofactor, I examined the relationship between the hemodynamic parameters and age as a continuous variable. (Note, I used the median value for analysis for ages with multiple data points.) Across all different types of hemoglobin concentrations, I observed a consistent decrease in chromophore concentration with increasing age (Figure 5.8). Pearson correlation coefficients, r, indicated strong negative correlations of 0.5 (p=0.00005) for both $[HbO]$ and $[HbT]$ and 0.3 (p=0.03) for $[HbR]$ concerning age. Linear regression analysis of the data from Figure 5.8 revealed the following relationships: $[HbO] = (38 \pm 2) - (0.23 \pm 0.05) \times Age$ (slope p=0.00001), $[HbR] = (22 \pm 2) - (0.08 \pm 0.04) \times Age$ (slope p=0.03), and $[HbT] = (64 \pm 4) - (0.36 \pm 0.08) \times Age$ (slope p=0.00007). However, I did not observe a significant correlation between oxygen saturation and age ($r = 0.2$, p=0.2). The linear relationship between oxygen saturation and age was measured as $StO_2 = (62 \pm 2) - (0.03 \pm 0.04) \times Age$ (slope p=0.46).

5.4 Discussion

This work aimed to quantitatively assess how curvature at tissue interfaces impacts the estimation of optical properties and their derived hemodynamic quantities as measured using FD-DOS. It is worth noting that the majority of previous investigations have been performed under the simplifying assumption of flat tissue surfaces, thus ignoring their curvature. Although it is possible to place optical probes in head regions with low curvature to minimize these effects in some cases, specific scenarios necessitate dealing with curved tissues. For instance, curvature cannot be avoided when measuring small heads, such as infants', or when targeting inherently curved regions like the occipital lobe or specific upper limb muscles. Therefore, understanding the implications of curvature on FD-DOS results and proposing strategies to account for its effect within experimental protocols can yield substantial improvements in the accuracy of the optical properties estimation.

One might initially assume curvature primarily affects the distance between the light source and detector, a well-known critical factor for quantification in diffuse optical techniques since it also affects the optical pathlength between the source and the detector. However, even in regions with relatively high curvature, the change in SDS is rather small; for example, a curvature of 0.2 cm^{-1} changes SDS by 3% at a 4 cm distance, which is insufficient to account for MAPEs higher than the 10–20% observed in this work. The primary challenge posed by curved interfaces lies in the change of symmetry and boundary conditions for the photon diffusion model.

To approach this challenge, I employed lookup tables based on numerical models to estimate optical properties by minimizing the difference between predicted and measured amplitude and phase data using multi-distance FD-DOS. The analytical solution for light transport in curved interfaces presents challenges to its computational implementation due to its inherent nonlinearities, which limits its practical utility. In contrast, lookup tables can significantly reduce computational time once generated, albeit at the cost of memory requirements to create and store the precomputed solutions. The similar performance of the planar model and the analytic SI model underscores the accuracy of our lookup table methodology. If enhanced resolution is needed, an alternative approach would interpolate simulated values [145]. Alternatively, machine learning methods such as deep learning can be used to extract the optical properties. However, this approach would not necessarily converge to the optimal global solution (as is the case of any machine learning algorithm).

In the presented analysis, I purposely constrained the local curvature, R, to two values to explore the effects of its presence under specific limits. While I recognize that expanding flexibility in curvature choices could enhance the resolution of the parameter space, the findings indicate that when R values of curvature are close enough to the actual curvature of the interface, adding this feature to the model of data analysis exerts a more substantial influence on the accuracy of optical properties estimates than fine-tuning its specific value within the explored range for this parameter (7-20 cm). For future applications, this parameter can be effectively held constant by measuring the local curvature of the sampled tissue. Despite the challenge, the measurement can be accomplished by collecting a few reference points along the tissue using digital tracking systems (e.g., a digitizer) and subsequently fitting these points to estimate R. In cases where the exact local curvature cannot be determined but falls within the analyzed range, data suggests that the error associated with a slight deviation in curvature falls within the range of (5±2)% (see Figure 5.4, Figure 5.5, and Table 5.2), which is smaller than the error when using the planar approximation.

Overall, the validation of the proposed methodology for addressing curvature revealed that, in most investigated scenarios, curved models outperform planar models. The only exception was the ideal flat surface case, as found in the calibration of optical phantoms. In this scenario, curved models exhibited an error in optical properties estimation within the range of (11 ± 5)%. However, this scenario does not reflect reality, as all tissue surfaces have

some degree of curvature.

In cases where curvature is present, even if slight, the validation experiments indicated that incorporating curved models does not harm the estimation of the optical properties. Both optical phantoms and head simulations demonstrated that fitting the data acquired from regions with low curvature using curved models produced results similar to those obtained with planar models. In both cases, the MAPEs were relatively small and within the experimental uncertainty due to noise, ranging from 2 to 13%, depending on the optical properties of the medium.

However, as the curvature of the tissue surface increases, curved models consistently outperformed planar models across nearly all circumstances. Not accounting for curvature in these scenarios resulted in errors of up to 20%, particularly in media characterized by low scattering and high absorption (Figure 5.5). Considering curvature reduced these errors to less than 10% in most cases. This result is consistent with earlier findings, which also reported a 15–20% inaccuracy in estimating μ_a due to a mismatch between the model and the actual interface [21]. Of note, I addressed the analysis in surfaces of a minimum radius of 5 cm for practical purposes. For smaller radius (i.e., greater curvatures), the fine-tuning of the actual curvature might be crucial to obtain high accuracy.

It is worth noting that using curved models in the inverse problem, while effective, is not the only way of addressing curvature in FD-DOS. An alternative approach would involve calibrating the FD-DOS device on an optical phantom with known optical properties and a curved surface. In fact, when the curvature of the calibration surface matches the measured surface, MAPEs decreased to an average (standard deviation) of 3(1)% (result not shown). While this fact reinforces the relevance of considering the curvature of the data acquisition interface, calibration using appropriately matched phantoms represents a more intricate solution than considering curvature in fitting models. In addition, this approach would require a curvature match between the calibration phantom and the measured tissue. Using both curved sides of our phantom, I noticed that in cases where there is a mismatch between the curvature of the calibration phantom and the measured surface, the MAPEs obtained were on the order of 10(1)%, slightly higher than the MAPEs obtained with the proposed curved model.

Additionally, the stability of the models, assessed using the 95th percentile of MAPE distribution over the 2-minute data acquisition on phantoms, are similar between simulations and the analytical SI model (Table 5.2). In spite of the lookup table methods (i.e., planar simulations, Curved Model 1, and Curved Model 2) estimating discrete values due to the 0.005 cm^{-1} step over μ_a in simulations, its 95th MAPE percentile are similar to the one obtained with the continuous estimations of SI model, which reinforces the choice of step in simulated optical properties. Moreover, the 95th percentile of the SI model and the planar simulations overlap, which suggests that the accuracy using the lookup tables is similar to the analytical SI model.

As a secondary investigation, I also quantified the MAPEs from the DCS fit of F in curved surfaces using the planar, homogeneous model G_1. To make the lookup tables for FD-DOS used in this work, I performed 5151 simulations for each curvature. Thus, for building up a lookup table for DCS fitting, I should have performed simulations covering the desired range of F (i.e., from $F \sim 10^{-10}\ cm^2/s$ to $F \sim 10^{-6}\ cm^2/s$) for each one of the 5151 simulations of each curvature, which, in addition to the computational cost, is out of the scope of this work. However, I performed a preliminary approach to better understand the error due to the curvature. Data revealed that MAPEs in the 7-cm radius region are 1.3(0.5;3.2)%, which suggests that the impact of curvature is less pronounced in DCS than in FD-DOS estimations, potentially eliminating the need for accounting for this factor. These MAPEs are smaller than previously reported ones with $\mu_a = 0.5\ cm^{-1}$ (around 8% [22]). A potentially great source of error over F estimations is using the wrong optical properties in the G_1 model, as it is known in literature [15, 146]. Indeed, when I used the estimated μ_a and $\mu_s^{'}$ through the SI model, the mismatch in the actual optical properties led to a MAPE of 9.1(1.0,17.4)% across all the simulations (data not shown). Additionally, the errors for a given condition (i.e., optical properties and curvature) are approximately constant despite the F value over our simulated range. This suggests that the curvature does not influence the relative F changes, as well as errors in optical properties [146]. It is worth noting that these results are based on preliminary observations, and further investigations are required.

In our final analysis, I attempted to quantify the impact of incorporating curvature into the study of human data. To this end, I utilized a comprehensive dataset comprising measurements from a large number of healthy subjects sampled at seven locations on the forehead. When compared to the standard SI approach, the introduction of assumed curvature resulted in an average 10(5)% increase in the estimation of the absorption coefficient. This increase translated into a 15(10)% increase in $[HbO]$, a 9(8)% increase in $[HbR]$ and a 12(5)% increase in $[HbT]$ (Table 5.3). The hemodynamic parameter least affected by curvature was StO_2, showing only a 2% increase. This is due to the fact that changes in $[HbT]$ mirror changes in $[HbO]$, and they compensate for each other when calculating StO_2.

Furthermore, not only did the median values increase with curved models, but their distributions also displayed a more uniform spread across the estimated range, more closely resembling a normal distribution. This pattern aligns with what one would expect from a relatively large sample drawn from a random cohort of healthy participants.

While few studies have explored adult cohorts as extensive as the one in this work, the findings are consistent with prior reports [12, 101, 102, 119, 147–152]. Previous FD-DOS measurements in cohorts of at least tens of individuals have reported total hemoglobin concentration and StO_2 values mainly within the 40 – 50 $\mu molar$ and 50 – 60% range, respectively, when using homogeneous models [12, 102, 150–152]. These values align with those obtained in this study using the same SI model. However, even after correcting for curvature, estimates remained slightly lower than those acquired through TD-DOS measurements using

the same models. TD-DOS has reported averages (standard deviations) for HbT and StO_2 of 57(16) $\mu molar$ and 58(4)%, respectively [101].

At least part of the difference between our curvature-corrected estimations and TD-DOS results can be attributed to assumptions about tissue composition. Despite the improvements achieved by accounting for curvature, it is important to acknowledge that the estimations should still be underestimated as the curved model relies on a homogeneous assumption. Research has indicated that incorporating tissue heterogeneity through layered models improves accuracy [13–15, 30, 120, 134, 139, 140, 153]. Typically, errors associated with recovering μ_a in layered models decrease from 20–30% to 10% or less in phantoms and head simulations, depending on the mismatch between the absorption of the layers. Correcting for tissue heterogeneity also leads to increased estimates of μ_a and hemoglobin concentrations, similar to the effects observed with curvature.

Notably, FD-DOS studies with large cohorts that considered the influence of layers reported parameters higher than those I obtained by only adding the curvature. When incorporating water content, as we did in this work, cortical values estimated with layered models were around 44 $\mu molar$, 20 $\mu molar$, 64 $\mu molar$ for HbO, HbR, HbT, respectively, and 65% for StO_2 [119, 148]. Unfortunately, the appropriate use of layered models requires a more extensive setup with additional sources and detectors beyond what the optical probe used contained [13, 15]. Future investigations incorporating both layered models and curvature in human data will likely provide even more accurate results.

Nevertheless, given the large number of subjects and the potential of the curved model to provide estimates that can be used as biomarkers more effectively, I also explored how the optical-based hemodynamic properties vary with the primary demographics of the subjects. Although I found no significant differences in hemodynamic parameters related to sex, the data hinted at a minor difference concerning this cofactor that could have been observed in a larger cohort. Differences related to sex have been reported in the literature for neonates [149]. Additionally, although prior studies reported differences in estimated physiological parameters regarding skin color in cerebral and pulse oxymeters [154–157], we have not found differences in our FD-DOS estimations due to this cofactor. This might be due to uneven distributions when comparing whites to non-whites or even the softening of the effect due to the fact I brought together blacks and browns.

The large sample size available allowed the visualization of the physiological parameters continuously with age. Although this relationship might not be strictly linear, linear regression analysis demonstrated a notable and consistent decrease in hemoglobin concentrations with increasing age, similar to what has been previously reported [12, 101, 102]. The equations outlined of physiological parameters regarding age can be readily applied to any age, offering utility in studies adopting the SI assumption. This applicability extends to investigations seeking to infer absolute optical properties for assessing oxygen saturation changes, particularly in functional experiments with CW-DOS.

Due to small sample sizes, previous studies have often grouped participants into young and elderly categories, with average ages around 30 years for the young and 78 years for the elderly group. For young individuals, FD-DOS studies have reported parameter values around [30,22,52,58], whereas elderly individuals typically exhibited values of [20,18,38,52] for [HbO, HbR, HbT, StO2]. In our dataset, employing a 55-year cutoff, as in [101], resulted in values of [31,20,52,60] for the young group and [29,18,47,59] for the elderly group. When considering the average ages from previous FD-DOS studies, the predicted values for the elderly at age 78 were [20,16,36,60], with no significant change in the values for the young group compared to the cutoff approach. These values are closer to previous reports using FD-DOS, reinforcing the robustness of the regression models. In contrast, TD-DOS studies reported notably higher values: [39,27,66,59] for young participants and [31,23,54,57] for elderly participants. This discrepancy may be attributed, at least in part, to the heterogeneity accounted for by TD-DOS models, as mentioned previously.

5.5 Conclusion and Next Chapters

In conclusion, this study has provided valuable insights into the impact of incorporating tissue curvature on the estimation of optical properties and associated hemodynamic parameters using FD-DOS. This work demonstrated that considering tissue curvature in FD-DOS analysis is crucial for accurate results. The curved model proposed in this work consistently outperformed standard planar models in all realistic scenarios, reducing errors significantly from 20% to less than 10%. Importantly, in surfaces with slight curvature, introducing a curvature does not result in an increased error compared to standard planar models. Interestingly, I found that accounting for the presence of curvature close to the actual one with a curved model is more relevant than fine-tuning its specific value within the range I investigated.

I also explored the impact of curvature in human data, revealing substantial increases of approximately 12% in the estimation of optical properties and hemoglobin concentrations when curvature was considered. The analysis of demographics revealed significant decreasing trends in hemoglobin concentrations with age, emphasizing the potential of FD-DOS as a tool for studying brain physiology.

While the approach significantly improved accuracy, it is important to acknowledge that this model relies on a homogeneous tissue assumption, which still leads to underestimations. Future studies could enhance accuracy by also incorporating tissue heterogeneity through layered models. This is the investigation exhibited in Chapter 7, where I preliminary introduced a model that accounts for tissue curvature and heterogeneity simultaneously.

A final interesting result of this investigation is regarding the lack of statistical difference between estimations in whites and non-whites. Especially after the Coronavirus pandemic, it is well known that StO_2 estimations might be jeopardized by the presence of skin

with darker tones. Thus, I better investigated the influence of skin tissue on FD-DOS estimations and exhibited the results in the next chapter.

CHAPTER 6

INFLUENCE OF SKIN TISSUE IN FREQUENCY-DOMAIN DIFFUSE OPTICAL SPECTROSCOPY ESTIMATIONS

The COVID-19 pandemic highlighted a long-ignored bias when using near-infrared light to estimate pulse oxygen saturation in people with dark skin tones. Although this problem has been known for decades [158], it has become more troublesome since it started affecting a large number of clinical decisions worldwide. As this issue is well-characterized for pulse oximeters, my goal was to investigate how skin color affects the optical properties estimated with FD-DOS. Section 6.1 introduces the problem of *occult hypoxemia*. In Section 6.2, I discuss the methods of data generation under the skin's influence. In Section 6.3, I present the results obtained from our approach, while I discuss them in Section 6.4. Finally, Section 6.5 summarizes the conclusions of this investigation.

6.1 Introduction

During the COVID-19 pandemic, pulse oxygen saturation (SpO_2) measurements guided clinical protocols. Usually, SpO_2 was measured using pulse oxymeters and taken as surrogates of the oxygenation level at the arterial blood, SaO_2. To maintain the survival chances high, cases with a low SaO_2 should receive special treatment over those with normal levels of such quantity, highlighting the importance of pulse oxymeters SpO_2 levels at that time [159, 160].

However, a severe problem during pandemic times was *occult hypoxemia*, i.e., cases where actual SaO_2 was smaller than 88% when readings of SpO_2 were equal or greater than 92%. By protocol, the patient is submitted to a specific treatment under the necessities of its clinical case. A recent 2022 study showed that racial and ethnic factors biased occult hypoxemia cases [161]. Indeed, the occurrence of this discrepancy was 30.2% in Asians, 28.5% in Blacks, 39.8% in non-Black Hispanics, and only in 17.2% in White patients. In addition to that, StO_2 overestimated SaO_2 by 1.7% on Asians, 1.2% on Blacks, and 1.1% on non-Black Hispanics, on average, when compared to Whites. Moreover, Black patients had a 29%, and

non-Black Hispanics had a 23%, lower hazard of treatment eligibility recognition, and 54.8% of the patients that never had treatment eligibility recognized were Black. The Blacks that eventually had their recognition of eligibility were 1 hour delayed on average compared to Whites. Additionally, Whites who do not show occult hypoxemia on a given measurement of a day are unlikely to exhibit it in another measurement. In contrast, Blacks show a less regular pattern beyond measurements [162]. The bias due to dark skin was confirmed by several reviews [163, 164].

Apart from physiological differences due to racial characteristics, a significant factor contributing to this disparity was the low accuracy of SpO_2 estimations in the presence of non-white skin, especially with darker tones. The calibration of optical systems in oximetry has traditionally been conducted in media that do not accurately replicate biological tissue covered by the skin when it is far different from the underlying biological tissue or in a pool of subjects with lighter skin tones [165, 166]. This discrepancy introduces biases in determining optical properties under these conditions, given that melanin and bilirubin, more abundant in darker and yellowish skins, absorb light differently than in the calibration and test conditions.

Although the bias is characterized for SpO_2 measurements through pulse oximeters based on clinical occurrences, the presence of skin biases the physiological estimations of every light-based technique. Previous research has attempted to better characterize such bias using phantoms or tasks [154–156, 161, 162]. Still, to the best of my knowledge, there is no research investigating such bias in FD-DOS. The blood oxygen saturation (StO_2) estimated from deep tissues could also be affected by skin absorbance, not included in the model of data analysis. Thus, I aimed to investigate the errors due to the skin layer on FD-DOS measurements. For that, I first studied the relationship between the optical properties of the skin and the skin tone. Then, I quantified the errors in the optical properties of FD-DOS data in the presence of the skin. Lastly, I proposed a preliminary correction on FD-DOS data to account for skin and evaluated the impact of such correction in real data.

6.2 Materials and Methods

I followed a three-step approach to account for the influence of skin tissue on FD-DOS estimations. First, I built a relationship between the skin's optical properties and skin tone. Then, I used the 2L model to generate FD-DOS data with the skin as the first layer to quantify the errors introduced by this tissue. Lastly, I compared the FD-DOS outputs of the 2L model in the presence and absence of skin tissue to investigate a potential correction factor.

6.2.1 Skin Tone Classification

There are several comparative and subjective scales for determining tones, but few objective parameters have been consolidated. Although the Fitzpatrick scale is the most popular in the dermatologic context, more objective scales are available. The trichromatic theory (RGB, for Red, Green, and Blue, CIE1931) might be the most popular. Still, the most objective and recent basis for characterizing tones is based on the opponent process theory (LAB, CIE1976). In this theory, a specific tone is described by a trio of parameters: L, which determines the grayscale of the tone (from white, 0, to black, 100); a^* (from -50 to 50), which determines whether the tone is more greenish or reddish; and b^* (also from -50 to 50), which determines whether the tone is more yellowish or bluish. Although there is a conversion between a trio (L, a^*, b^*) and a trio (R,G,B), the LAB space is more interesting in the context of the epidermis' tone classification because L is related to the level of melanin pigmentation and b^* to the presence of carotenoids or bilirubin, which gives the skin a yellowish coloration. In this sense, the individual topology angle, $ITA^o \equiv atan((L-50)/b^*)$, is a robust parameter used to determine skin tones, being able to separate different ranges of epidermal pigmentation [167]. Colorimeters often estimate ITA^o between -60^o and 60^o for the population in general.

6.2.2 Relationship Between Skin's Optical Properties and Skin Tone

To estimate the optical properties (i.e., the absorption coefficient, μ_a, and the reduced scattering coefficient, $\mu_s^{'}$) of the skin, I used data previously published with the Spatial Frequency-Domain Spectrometry method [168–170]. The system (OxImager RS^{TM} - Modulim, Inc., Irvine, California), which also provides estimations of (L, a^*, b^*), was used to acquire optical data on ten body regions (forehead, cheek, ventral forearm, palm, back, ventral upper arm, dorsal forearm, shin, neck, and chest) in a pool of 15 subjects. Demographic data and protocol were described elsewhere [171, 172].

To build a relationship between the skin's absorption coefficient, μ_a^{skin}, and ITA, I fitted the data of all the body regions of the participants according to the expression $ln(\mu_a^{skin}) = \alpha \cdot ITA^o + \beta$ for each wavelength separately. This expression is based on previous research that established this linear expression in *ex-vivo* measurements [173, 174]. I also adjusted this expression to two specific regions to understand if there is variability between the body regions: the forehead, since it is the region where most DO techniques applications are focused, and the ventral upper arm since it is a muscle region, thus more homogeneous.

6.2.3 Influence of the Skin Tissue on Frequency-Domain Diffuse Optical Spectroscopy Estimations

I used the analytical 2L model (Equation 2.11) to generate FD-DOS amplitude and phase data with the first layer mimicking the skin tissue to quantify the changes and errors due to superficial absorption. To this end, I used three values for the first layer thickness: 1.00, 1.25, and 1.5 mm, since it is expected to find melanin in the basal layer of the epidermis, i.e., from 0.5 to 1.5 mm depth [175–178], and thicknesses lower than 1.0 mm cause numerical instability in the 2L model. I varied ITA^o between -50^o and 50^o and selected the absorption coefficient of the skin based on the equations described in the previous section for 691 and 851 nm. I used a homogeneous scattering coefficient of 8.8 and 7.3 cm^{-1} for those wavelengths and varied the absorption coefficient of the second layer (that mimics the tissue under the skin) from 0.05 to 0.45 in steps of 0.005 cm^{-1}. I also generated amplitude and phase curves through the analytical 2L model using homogeneous absorption (i.e., the same first and second layers absorption coefficient) as ground truth for measurements without skin tissue. SDSs were 1.0, 1.5, 2.0, 2.5, 3.0, 3.5 and 4.0 cm. Of note, this section is entirely oriented to forehead data since it is the main goal of my thesis. To quantify the differences between FD-DOS curves due to skin influence, I computed the complex ratio $K = K_o exp(i\theta_o) \equiv R_{ideal}/R_{real}$, where R_{ideal} and R_{real} are the generated reflected intensities in the absence and the presence of skin tissue, respectively.

To investigate the error of the estimated optical parameters due to skin influence, I analyzed R_{real} and computed the MAPE of μ_a estimations. I also investigated the propagated errors from μ_a to the physiological parameters $[HbO]$, $[HbR]$, and StO_2. To this end, I evaluated the MAPE of the physiological properties using the estimated μ_a in the presence of skin tissue for all the combinations of 691 and 851 nm. I excluded data where $[HbO] > 5\mu molar$, $[HbR] > 5\mu molar$, and $StO_2 > 40\%$. As these values are not physiologically expected, they might be coming from unrealistic combinations of μ_a in 691 and 851 nm.

6.2.4 Methods to Solve the Inverse Problem and Correction Factors

I fitted each FD-DOS amplitude and phase generated using the SI model since it is the standard approach to analyzing DO data. As this model averages the optical properties of the biological tissue, skin presence is expected to introduce a bias in estimations. To mitigate this bias, I investigated whether the median of the K factors across all simulated optical properties would be a good correction factor to be applied to FD-DOS amplitude and phase. To this end, I fitted $K \cdot R_{real}$ for each ITA^o and wavelength and compared the MAPEs obtained when estimating μ_a, $[HbO]$, $[HbR]$, and StO_2 before and after such correction.

6.2.5 Impact of Correction Factors in Real FD-DOS Data

As a final step, I aimed to investigate the change in real FD-DOS data introduced by applying the previously established K factors at the 690-nm wavelength. To this end, I acquired 2 minutes of data on the ventral upper arm of 15 subjects (8 males, average (standard deviation) age of 35(12) years) with ITA^o ranging from -38^o to 46^o. ITA was measured with a ColorMeter Pro (VINCKOLOR) system, and FD-DOS measurements were performed with the system described in Figure 2.10 (SDSs of 2.0, 2.5, 3.0, and 3.5 cm). Optical properties at 690 and 847 nm and physiological parameters were estimated using the SI model before and after applying the correction factor. I evaluated the percentual change induced by the correction by:

$$\Delta P = \frac{|P_{corrected} - P_{uncorrected}|}{P_{uncorrected}} \times 100\%,$$

where P is μ_a, $[HbO]$, $[HbR]$, or StO_2. This protocol was approved by the local Ethics Committee at the University of Campinas (CAAE 50436921.3.0000.5404). Participants were instructed concerning the experiment protocol before signing an informed consent form prior to participation (Appendix J).

6.3 Results

6.3.1 Relationship Between Skin's Optical Properties and Skin Tone

I fitted the estimated slope and intercept coefficients for the expression $ln(\mu_a^{skin}) = \alpha \cdot ITA^o + \beta$ for each wavelength considering (1) all data points and (2) only the data points available for the forehead and forearm. Constants are on Table 6.1 with the standard error of the fit. The first thing to be noted is that the coefficients are dependent on the wavelength used, as expected. Additionally, the influence of the skin is more pronounced on smaller wavelengths, as β decreases with λ. The negative sign on α suggests that μ_a^{skin} decreases with ITA^o, i.e., with lighter tones. In the NIR region, μ_a^{skin} reaches values as high as 4 cm^{-1} for small ITA^o, which is way above the expected range for deeper biological tissue (under 0.5 cm^{-1}). However, for higher ITA^o, μ_a^{skin} is as low as 0.2 cm^{-1}. Additionally, although α values are similar across all the groups analyzed when considering its error, there is almost no overlap between the β values of the three groups.

6.3.2 Influence of the Skin on Optical Properties Estimations with FD-DOS

To investigate the influence of skin tissue on FD-DOS, I generated data using the 2L model both considering the skin tissue (i.e., using the optical coefficient of the first layer equal to

Table 6.1: Angular and linear coefficients of the expression $ln(\mu_a^{skin}) = \alpha \cdot ITA^o + \beta$ for all acquired data and for forehead data.

	α			β		
Wavelength (nm)	Forearm	Forehead	All data	Forearm	Forehead	All data
471	-0.017 ± 0.002	-0.016 ± 0.002	-0.0146 ± 0.0005	1.90 ± 0.06	2.05 ± 0.05	1.82 ± 0.02
526	-0.017 ± 0.001	-0.017 ± 0.002	-0.0159 ± 0.0005	1.49 ± 0.05	1.62 ± 0.05	1.40 ± 0.02
591	-0.019 ± 0.001	-0.022 ± 0.002	-0.0191 ± 0.0005	0.72 ± 0.04	0.78 ± 0.05	0.62 ± 0.02
621	-0.024 ± 0.002	-0.029 ± 0.002	-0.0252 ± 0.0007	0.09 ± 0.07	0.05 ± 0.07	-0.05 ± 0.03
659	-0.024 ± 0.002	-0.029 ± 0.002	-0.0259 ± 0.0008	-0.18 ± 0.07	-0.24 ± 0.07	-0.35 ± 0.03
691	-0.023 ± 0.002	-0.029 ± 0.003	-0.0258 ± 0.0009	-0.48 ± 0.08	-0.55 ± 0.07	-0.67 ± 0.03
731	-0.020 ± 0.002	-0.028 ± 0.003	-0.0249 ± 0.0009	-0.74 ± 0.06	-0.85 ± 0.07	-0.99 ± 0.03
851	-0.013 ± 0.002	-0.017 ± 0.002	-0.016 ± 0.001	-1.36 ± 0.09	-1.30 ± 0.06	-1.55 ± 0.04

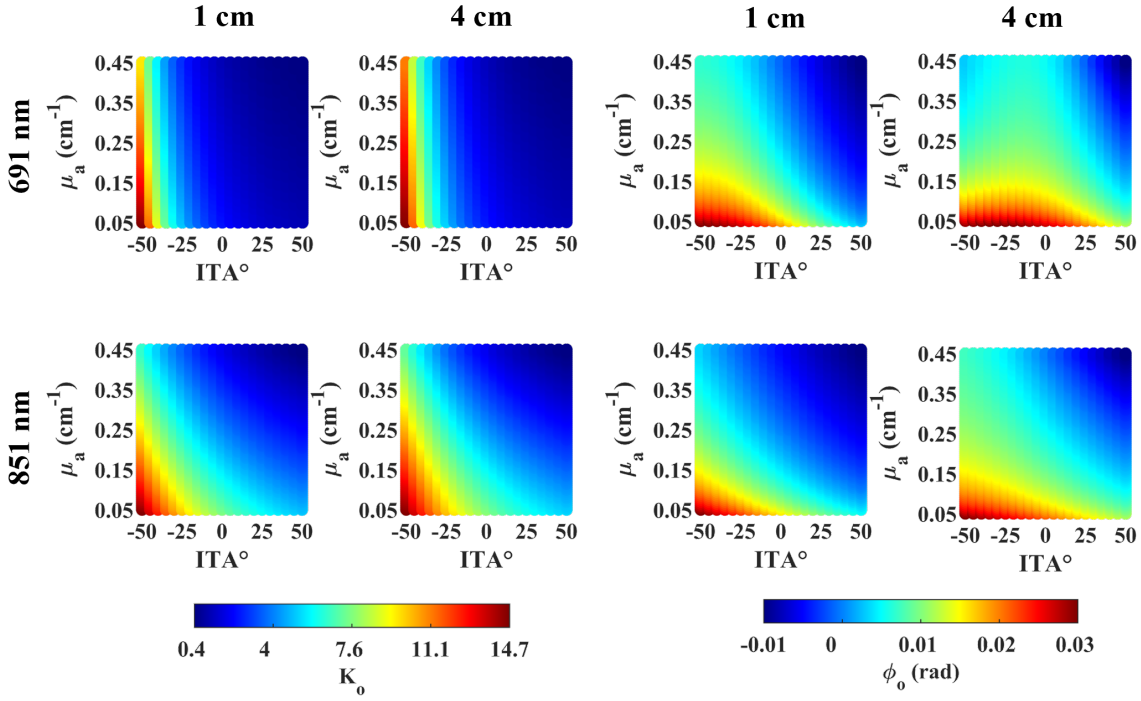

Figure 6.1: Amplitude (K_o) and phase (ϕ_o) of the ratio K between the reflected intensity in the absence and in the presence of skin tissue for two wavelengths (691 nm in the first and 851 nm in the second row) and SDSs (1 cm in the first and 4 cm in the second column of each quantity). Skin thickness was assumed as 1.5 mm.

μ_a^{skin} and assuming a thickness of 1.00, 1.25, or 1.5 mm) and not considering it (i.e., using the first layer equal the second one, taken as the depth tissue).

For each combination of skin tissue, ITA^o and simulated depth tissue absorption coefficient, μ_a, I computed the complex ratio $K = R_{ideal}/R_{real}$. Figure 6.1 exhibits the amplitude and the phase of K, i.e., K_o and ϕ_o, for two wavelengths (691 and 851 nm), all generated μ_a and ITA^o ranging from -50^o and 50^o for two different SDSs (1 and 4 cm) and skin thickness of 1.5 mm. For the other thicknesses, the trends on K_o and ϕ_o are essentially the same. Note that, although ϕ_o is dependent on both SDS and μ_a, its values are around 0.02 radians, which are negligible compared to the values of phases usually measured, R_{real}. Amplitude ratios, on the other hand, are less SDS and μ_a dependent. Both K_o and ϕ_o decrease with ITA^o, as expected.

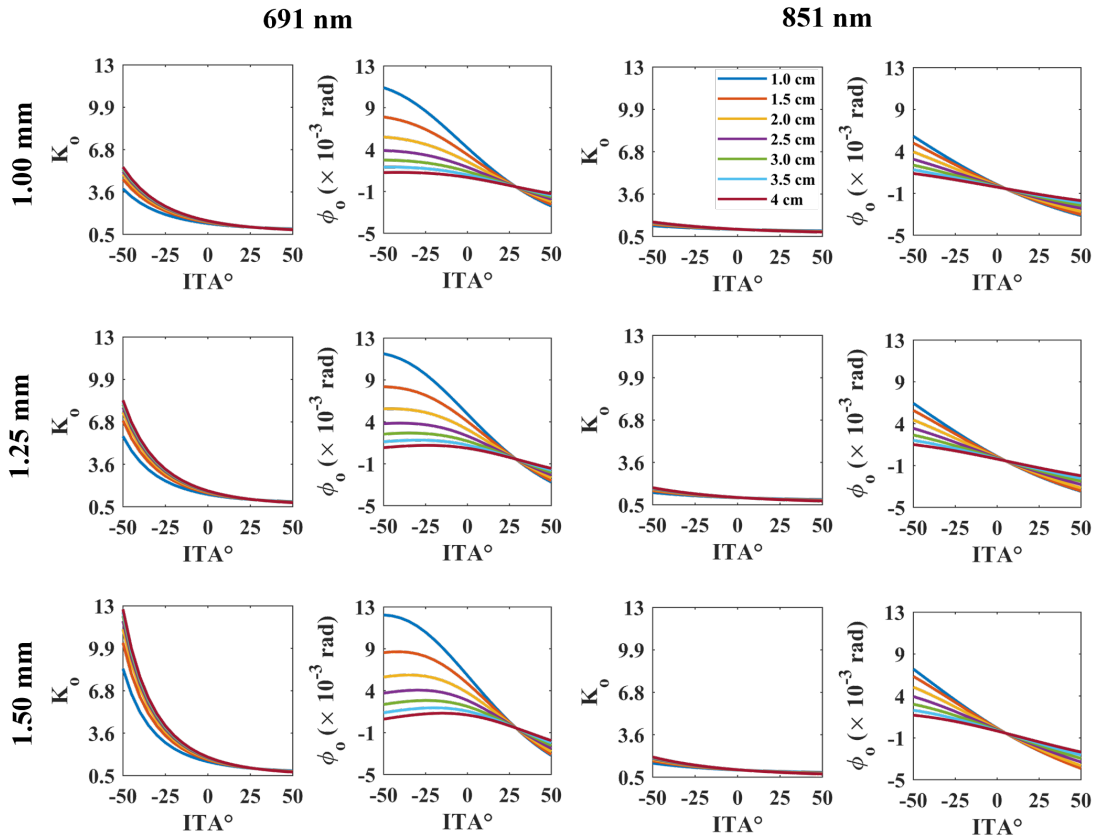

Figure 6.2: Median amplitude and phase of K factors among all the simulated optical properties for all wavelengths, skin thicknesses, and SDS used.

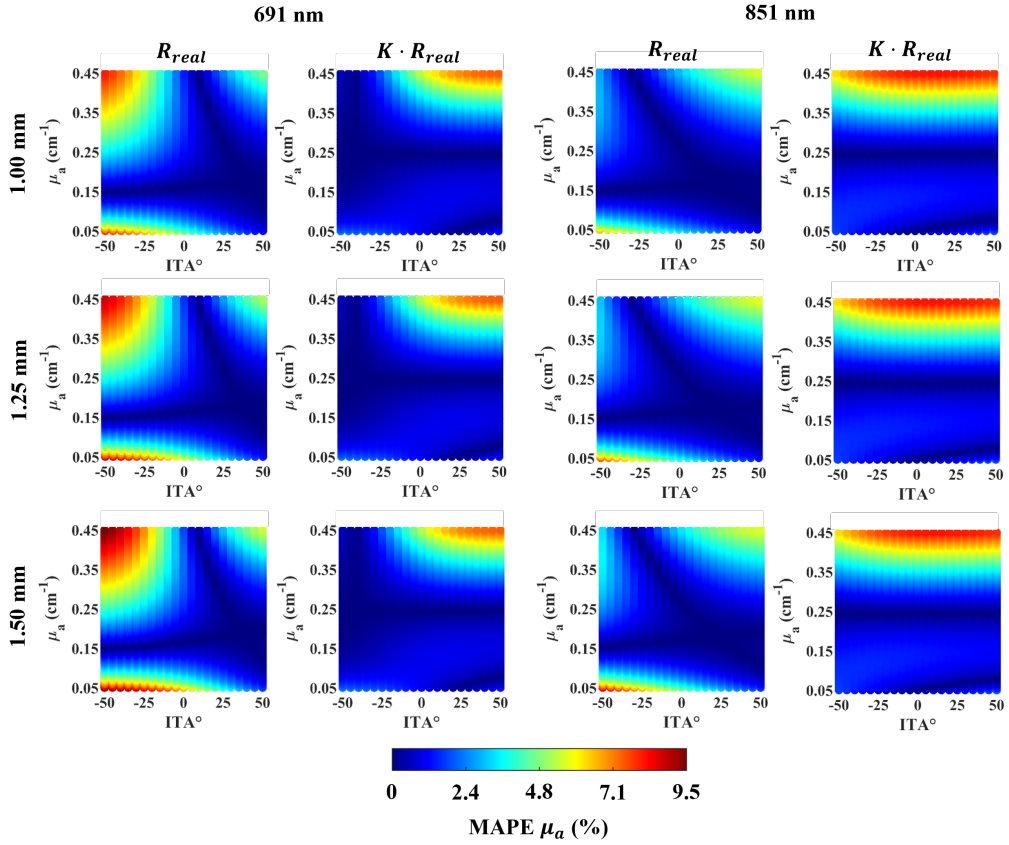

Figure 6.3: MAPEs obtained when estimating μ_a through the SI model when fitting the reflected intensity generated in the presence of skin tissue (R_{real}) and after applying the ratio K at the generated data for all skin thicknesses (1.00, 1.25 and 1.50 mm) and both wavelengths used (691 and 851 nm).

In real situations, μ_a is unknown. Thus, I took the median of K_o and ϕ_o among all the simulated μ_a values to estimate the amplitude ratio and phase shift introduced due to skin tissue. Figure 6.2 shows the results for all generated SDSs, ITA^o, and skin thicknesses. Although negligible, median ϕ_o values are slightly dependent on skin thickness but are sensitive to SDS. Median K_o, on the other hand, are sensitive to skin thickness for the smaller wavelength but are less sensitive to SDS in both wavelengths. Interestingly, K_o assumes values smaller than 1 for high ITA^o, which suggests that for $\mu_a^{skin} < \mu_a$, the reflected intensity is more intense than the ideal one. These values are the best estimation of changes in amplitude and phase of reflected intensity due to skin presence in the range of expected μ_a values.

The next step was translating the changes introduced due to skin presence to deviations in the estimated absorption coefficient. To this end, I adjusted the reflected intensities generated with skin presence, R_{real}, with the SI model and computed the MAPE for each combination of μ_a, ITA^o, and skin thickness. The results, exhibited in Figure 6.3, show that errors are as high as 9.5 % for low ITA^o at 691 nm. Additionally, errors across all generated ITA^o, μ_a, and skin thickness at 691 nm (median and boundaries of the 95th percentile of 1.6 (0.1;6.7)%) are significantly larger than the errors at 851 nm (1.0(0.0;4.2)%, p<0.00001 in a T-test). The effect size between both is 0.4, measured with Robust Cohen's D. The 95th

percentile of MAPEs at skin thickness of 1.00, 1.25, and 1.50 mm are 1.4(0.0,5.9), 1.6(0.0,6.6), and 1.8(0.0,7.3)% at 691 nm and 0.9(0.0,3.9), 1.0(0.0,4.1), and 1.1(0.0,4.4)% at 851 nm. Although all differences between the distributions are statistically significant, their effect size is small, ranging between 0.1 and 0.2 among MAPEs distributions of the same wavelength and different skin thicknesses. This result suggests that the effect of thickness is smaller than the effect of the wavelength used on the correct estimation of μ_a. To investigate the dependence of the errors regarding ITA^o, I compared the 95th inter-percentile range of the MAPEs at $ITA^o = -50^o$ to the ones at $ITA^o = 50^o$ across all generated μ_a, skin thickness, and wavelength. For $ITA^o = -50^o$, errors are 3.0(0.4;8.0)%, statistically different from the 0.8(0.0;4.8)% of $ITA^o = 50^o$, which evidences the influence of ITA^o over optical estimations. Moreover, the effect size of this difference is $D = 1.0$, which suggests that ITA^o is more relevant for MAPEs when estimating μ_a than skin thickness.

To preliminarily investigate a method of accounting for the skin absorbance when estimating μ_a, I fitted the multiplication of the reflected intensity generated with skin tissue, R_{real}, for the median of the K ratios between the intensity generated in the absence and the presence of skin tissue. In this sense, the median K is used as a correction factor to R_{real}. Since skin thickness is the less relevant factor over μ_a MAPEs, I only applied the median K factor calculated at 1.00 mm as a correction factor. Results are also in Figure 6.3. After the correction, μ_a MAPEs are 0.6(0.0,4.6)% for $ITA^o = -50^o$ and 1.0(0.1,6.7)% for $ITA^o = 50^o$ and, although the difference between both is still statistically significant, the effect size decreases to $D = 0.5$, suggesting a mitigation of skin tone effect. At skin thickness of 1.0 mm, the errors statistically decrease from 1.4(0.2,5.6)% to 0.9(0.2,1.6)% ($D = 0.7$) at 691 nm and increase from 0.9(0.1,4.2)% to 1.2(0.2,1.6)% at 851 nm, but with no statistically significant difference (p=0.32, T-test).

6.3.3 Influence of the Skin on Physiological Parameters Estimated by FD-DOS

After characterizing the errors introduced on μ_a recovery due to the presence of skin, I quantified how these errors translated to $[HbO]$, $[HbR]$, and StO_2. To this end, I used all the combinations of the previously generated FD-DOS data (R_{real}) at both wavelengths to mimic a real data acquisition. In other words, I estimated $[HbO]$, $[HbR]$, and StO_2 of all combinations of the estimated μ_a in the presence of skin for 691 and 851 nm assuming a water fraction of 0.7. I excluded combinations that yielded $[HbO] \leq 5\mu molar$, $[HbR] \leq 5\mu molar$, and $StO_2 \leq 40\%$ since they are not physiologically expected. The MAPEs of the estimations for skin thickness of 1.00 mm are in Figure 6.4 for three situations: straightly converting μ_a estimated from R_{real} (Figure 6.4a), converting μ_a estimated from $K \cdot R_{real}$ (Figure 6.4b), and using μ_a estimated from $K \cdot R_{real}$ for 691 nm and from R_{real} for 851 nm.

For $[HbO]$, the MAPEs (95th percentile) due to the presence of skin were 1.6(0.1,5.6)%.

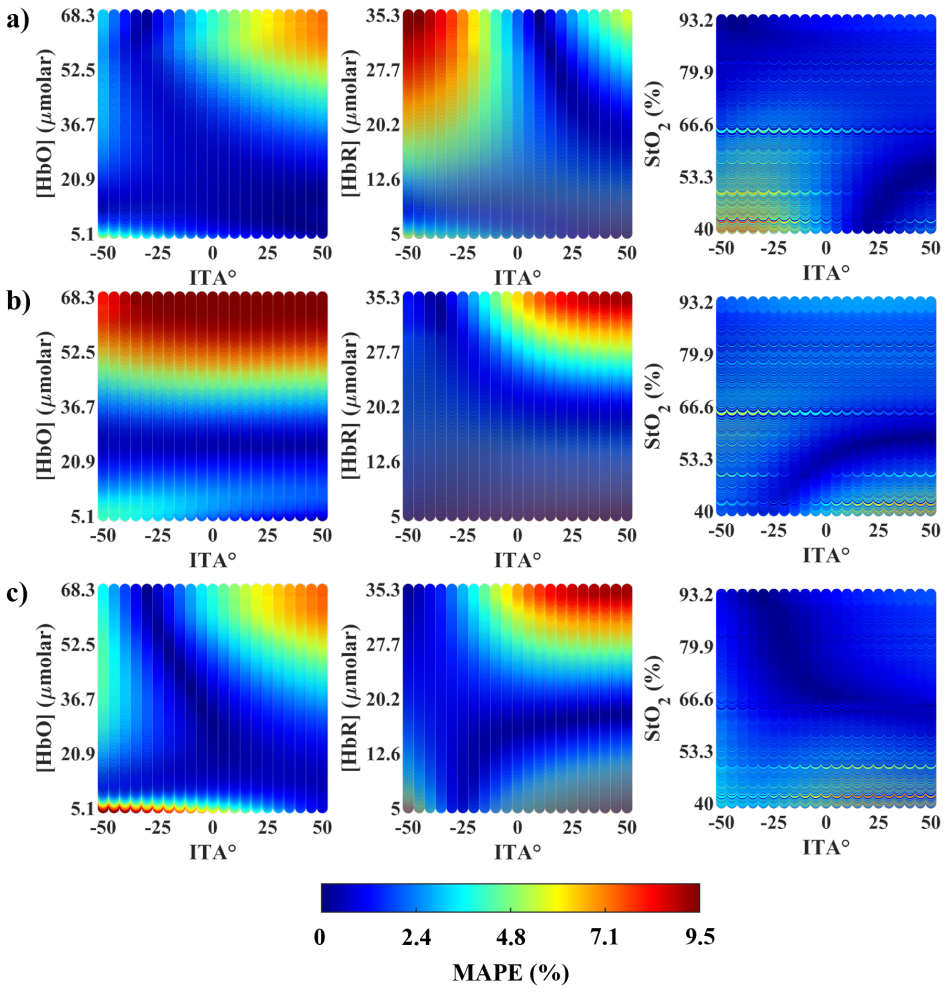

Figure 6.4: MAPEs of the estimations of $[HbO]$ (first column), $[HbR]$ (second column), and StO_2 (third column) for skin thickness of 1.00 mm. a) Errors when using μ_a estimated straightly from the generated data in skin presence, R_{real}. b) Errors when using μ_a estimated from the generated data in skin presence after applying the correction factor, $K \cdot R_{real}$, for both wavelengths. c) Errors when using μ_a estimated from the generated data in skin presence after applying the correction factor, $K \cdot R_{real}$, for 691 nm but not 851 nm. Errors above 9.5% were painted with red.

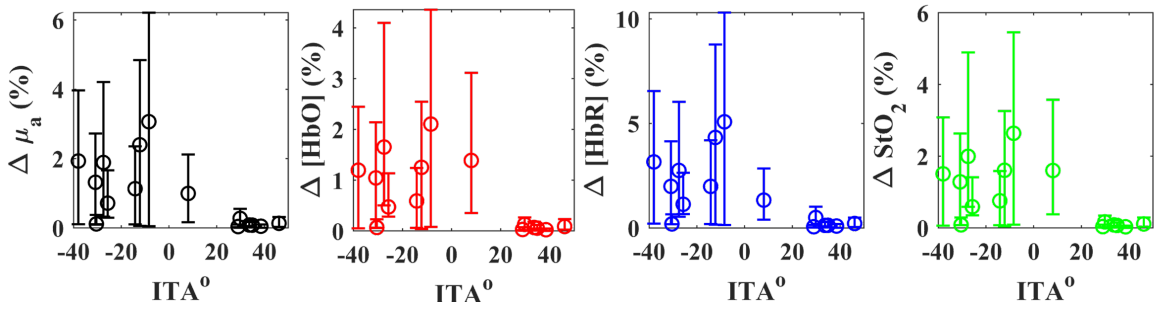

Figure 6.5: Percentage change due to the correction of skin influence through the proposed method. The error bar indicated the 95th percentile across all the estimations during the 2-minute acquisition.

When the correction factor was applied to both wavelengths, the errors increased to 2.9(0.3,10.1)% ($D = 0.6$). When using the correction factor only at the smaller wavelength, however, errors were 1.8(0.2,5.2)%. The median error increases, but the larger errors decrease ($D = 0.1$). For $[HbR]$, errors decreased from 2.4(0.1,8.3)% to 1.6(0.1,10.4)% when correcting both wavelengths ($D = 0.2$). When applying the correction factor only on the smallest wavelength, errors further decreased to 1.5(0.2,7.0)% with an effect size of $D = 0.4$. The smallest MAPEs were obtained when estimating StO_2: 1.1(0.1,4.3)%. These errors increased to 1.3(0.1,3.6)% when applying the correction on both wavelengths ($D = 0.1$), but decreased to 0.9(0.1,3.4)% correcting 691 nm only ($D = 0.2$). It is worth noting that although StO_2 MAPEs distribution is mostly smaller than 4%, outliers are as high as 9% in generated data, which is above the occult hypoxia problem.

6.3.4 Impact of Correction Factors in Real FD-DOS Data

In a cohort of 15 subjects, I used the SI model to obtain the optical properties and physiological parameters of 2 minutes of data acquisition in the biceps. After that, I used the ITA^o of each participant to compute the average K factors for the 690-nm wavelength in the ventral upper arm. Then, I applied this factor to the acquired data and once more used the SI model to estimate the optical properties and physiological parameters, similarly as performed in Section 6.3.3. The percentage change induced by the correction is exhibited in Figure 6.5 for the 690-nm wavelength μ_a and for the physiological parameters.

Changes are around 1% on average for all parameters: (0.67(0.04,3.04)% for μ_a, 0.44(0.02,2.10)% for $[HbO]$, 1.05(0.06,4.99)% for $[HbR]$, and 0.55(0.03,2.62)% for StO_2). Wilcoxon tests were unable to distinguish between the analyzed optical properties and physiological parameters prior to and after correction (D values around 0.03). However, as expected, percentage changes were greater for low ITA^o. Indeed, comparing percentage changes for $ITA^o \leq 0$ with those for $ITA^o > 0$ yielded distinctions with effect size D of 1.8 (1.41 versus 0.10% on average, p=0.004, Wilcoxon test) for μ_a, 1.7 (1.10 versus 0.06% on average, p=0.029, Wilcoxon test) for $[HbO]$, 1.6 for $[HbR]$ (2.18 versus 0.14% on average, p=0.004, Wilcoxon test) and 1.7 for StO_2 (1.35 versus 0.08% on average, p=0.014, Wilcoxon test), high-

lighting the impact of skin tissue for low ITA^o values. Of note, some percentage changes in StO_2 after correction reach up to 6.0%, which is the scale of the occult hypoxia problem.

6.4 Discussion

In this work, I investigated the impacts of the skin tissue layer on FD-DOS data. To this end, I used previously acquired data to build a phenomenological relationship between the skin's absorption coefficient, μ_a^{skin}, and the skin tone, as quantified by ITA^o. Using a 2L model and considering skin as a very thin first layer, I was able to generate FD-DOS data to compare how skin affected the fluency detected and, therefore, the recovery of the optical properties. I was not concerned about DCS estimations at this point. Still, I hypothesize it is a minor problem with this technique since minimal blood flow is expected at this depth. Thus, any impact on estimating F would arise from errors in the optical properties.

I decided to use ITA^o to quantify skin tone since it provides an objective and continuous scale for classification. Although the most known graduation for classifying skin tone is the Fitzpatrick scale, it provides a discrete classification (i.e., types I to VI) based on how each group responds to sun exposure. Since I aimed to build a relationship with a continuous parameter (μ_a^{skin}), using ITA^o enables more precision in quantifying each skin absorbance based on its tone.

One alternative method to investigate skin absorbance is by estimating its chromophore concentrations, such as melanin and bilirubin. However, it is an experimentally challenging solution to implement *in vivo* through optical techniques in general since the skin depth ranges from 0.5 to 1.5 mm. It gets even harder using most DO techniques since the penetration depth is roughly half of SDS, and there is a breakdown of diffusive approximation for SDSs smaller than ~0.6 cm. The Frequency-Domain Spectrometry method, on the other hand, allows the estimation of optical properties up to 2.5 mm depth, making the concern regarding the skin's constituents pointless. Thus, I used the absorption coefficient estimated through this technique as an estimation of μ_a^{skin}.

Based on previous research [173, 174], I used an expression of the form $ln(\mu_a^{skin}) = \alpha \cdot ITA^o + \beta$ for all acquired data and oriented specifically for forehead measurements. I found a good agreement between experimental data and the linear fits: $R^2 = 0.83$ on average for all data and $R^2 = 0.89$ on average for forehead data, with the smallest value around 0.7. However, I can see from Table 6.1 that the forehead's parameters of the linear trends differ from the fit of all data. It suggests that the relationship between μ_a^{skin} and ITA^o obtained with the Frequency-Domain Spectrometry method is sensitive not only to skin characteristics (i.e., ITA^o) but to the tissue underneath the skin. This might be due to the depth at which the technique obtains information regarding biological tissue, which is slightly greater than the skin depth, making the estimated optical properties carry some information regarding the deep biological tissue. Thus, any correction method must be developed using a relation-

ship between μ_a^{skin} and ITA^o oriented to the target body region. Previous research [174] also suggests a linear relationship between the constants of the fit, α, and β, with the wavelength used. These expressions would eliminate the necessity of matching wavelengths between different techniques (i.e., Frequency-Domain Spectrometry and FD-DOS in this case). However, when using this approach, I noticed a smaller agreement with our experimental data (i.e., R^2 around 0.5 or less, data now shown). Thus, I decided to use α and β adjusted according to Table 6.1 instead of constraining them to the wavelength.

After establishing relationships between μ_a^{skin} and ITA^o, I aimed to investigate the impact of skin on FD-DOS data. To this end, I used the 2L model, assuming skin as the first layer. I used only two wavelengths (691 and 851 nm) and three skin thicknesses (1.00, 1.25, and 1.50 mm). This approach gives rise to two main limitations of this work. The first concerns the reduced scattering coefficient, $\mu_s^{'}$. Since the first layer is thin compared to the second, and the mismatch between the scattering coefficients of skin and the underneath biological tissue is smaller than between their absorption coefficients [171, 172], I hypothesize that the analytical 2L model would not be able to properly distinguish between scattering of both layers. Thus, I decided to assume homogeneous scattering and focus only on the impacts due to the skin's absorption coefficient. Although the main interest is the light attenuation due to skin, there is cross-talk between the effects of μ_a and $\mu_s^{'}$ on FD-DOS data, so further investigations are needed. The second is related to the first layer thickness. The 2L model assumes that the FD-DOS source might be approximated by a point-like source at a depth of $1/\mu_s^{'}$ and relies on the first layer. For the $\mu_s^{'}$ assumed in this work, the first layer thickness would be at least 1.37 mm, which is not the case for our methodology. However, the general trends of the results would possibly remain the same, given the similarity of the results between skin thicknesses of 1.00, 1.25 (where this assumption is violated), and 1.50 mm. Additionally, skin $\mu_s^{'}$ is usually higher than the underneath biological tissue [171, 172], which also mitigates this issue by decreasing the point-like source depth. Nevertheless, further validation with simulation methods such as through NIRFASTer is required.

By looking at the FD-DOS curves generated including skin tissue and not including it, I hypothesized that the difference between R_{real} and R_{ideal} was a multiplicative complex constant (i.e., a multiplicative constant at $|R_{real}|$ and an additive constant at $arg(R_{real})$ to match R_{ideal}), which I denoted as $K = K_o exp(i\theta_o)$ (Figure 6.1 for all the generated μ_a and 6.2 for the median value). The generated data suggests that ϕ_o values are negligible since they are around 0.02 rad, which means that skin tissue does not introduce significant phase shifts at the reflected intensity. However, this might result from assuming homogeneous scattering at the 2L model since phase shifts are more related to scattering events. K_o, on the other hand, ranges from 0.4 to 14.7, which indicates a wide range of attenuation due to skin tissue. It is worth noting that K_o values also do not include the effect of mismatch between the scattering of skin and deep tissue.

I also investigated the errors in estimating μ_a of deep tissue due to the presence of

a skin layer by using the SI model to fit for R_{real}. Errors range up to 9.5% and are smaller at 851 than at 691 nm. As expected, ITA^o is the more relevant variable regarding errors when estimating μ_a. Additionally, the small dependence on skin thickness ($D = 0.1 \sim 0.2$) suggests that the presence of skin tissue at the correct ITA^o is more relevant to the lack of accuracy when determining the optical properties than fine-tuning other parameters. This is a promising result since, to my knowledge, no method exists to estimate the depth in which melanin can be found in each subject.

Errors arising from μ_a estimations translate to errors up to 8% in $[HbO]$, 19% in $[HbR]$, and 9% in StO_2. Errors are greater in $[HbR]$ as it is more related to the smaller wavelength, where the larger errors at μ_a occur. Note that, although the median errors of the physiological properties are not huge (1.6, 2.4, and 1.1% respectively for $[HbO]$, $[HbR]$, and StO_2), an error of 4.3% in $StO_2 = 92\%$ is enough to generate occult hypoxia. However, FD-DOS seems less sensitive to inaccuracies due to the skin layer than pulse oxymeters, as this issue happens only with a small percentage of the generated data. I hypothesized that FD-DOS is less sensitive to skin influence since it relies on several SDSs to estimate optical properties. As skin influence is similar among all tested SDSs, this impact is mitigated when estimating μ_a. This also might explain the minimal differences observed between whites and non-whites described in Chapter 5. Nevertheless, deeper investigations are necessary.

One preliminarily endeavor to minimize skin effects was to multiply R_{real} for the median of K factors to correct the skin influence, since $K = R_{ideal}/R_{real}$. By looking at Figure 6.2, we might be led to think that we must first adjust for skin thickness since K_o depends on it. However, as a global complex multiplicative constant on FD-DOS data does not alter the adjusted optical properties, the dependence of K_o on skin thickness would not be a problem if it is a global constant along the several SDSs. Indeed, K_o ranges from 5 to 13 between skin thicknesses for $ITA^o = -50^o$ in SDS of 4 cm but ranges from 1.4 to 1.5 if normalized by the shortest SDS K_o, and this pattern is also true for other SDSs (data not shown). Thus, added to the fact the errors on μ_a estimations are slightly dependent on skin thickness, this dependence of K_o should not significantly alter the corrections performed at R_{real}.

I investigated the effect of this correction (i.e., multiplying by K) over the estimated μ_a at 691 and 851 nm. Errors slightly decrease at 691 nm after the correction but slightly increase at 851 nm. This might be because errors were already smaller and more evenly spread across all generated μ_a and ITA^o before the correction for the greater wavelength. Thus, the uncertainty of taking the median of K among all the simulated μ_a potentially worsens the estimations at 851 nm. Based on this result, I investigated the change at $[HbO]$, $[HbR]$, and StO_2 errors due to both wavelengths and the correction of 691 only. Of course, there are other possibilities for correcting FD-DOS data using these K factors, such as performing the correction up to a certain ITA^o value. Indeed, it is reasonable to expect that when K_o approaches unity, the correction is meaningless. In this sense, $K_o \geq 1.1$ up to $ITA^o = 20^o$ for 691 and up to $ITA^o = -15^o$ for 851 nm. In the future, fine-tuning the correction based on

ITA^o ranges would improve the accuracy even further. Still, for the exploratory purpose of this investigation, I chose to apply the correction for all ITA^o at 691 nm.

Data suggests that correcting only 691 nm slightly reduces the MAPEs when estimating the physiological parameters from 1.7 to 1.4% on average, while correcting both wavelengths potentially worsens the estimations. At first glance, this might be taken as a negligible correction. However, MAPEs obtained when estimating StO_2 reduce from 1.1(0.1,4.3) to 0.9(0.1,3.4)%. It suggests that there is a reduction in the number of StO_2 estimations with errors above 4%. Indeed, 6.25% of the generated data has StO_2 MAPEs above 4% before the correction. After the correction, this fraction reduces to 3.21%. Recalling that an error of 4.3% on StO_2 = 92% is enough to create occult hypoxia, this correction, even preliminarily, is potentially effective in reducing the incidence of such clinical complication.

Lastly, I investigated the impact of the correction in real data. To this end, I acquired data in the ventral arm of a small number of participants. I decided to conduct this investigation in the arm (over the biceps) since it is a more homogeneous region regarding tissue stratification than the forehead. Thus, the changes due to the correction procedure are less subject to other confounders. A methodological limitation in this exploration in that the colorimeter used in this acquisition is different from the one used to tabulate skin's optical properties. Thus, the ITA^o measured for the participants might not be the same as the ones accounted in the relationship between $ln(\mu_a)$ and ITA^o. Nevertheless, the conclusions regarding groups of participants with low versus high ITA^o stand. Data suggest that the correction is smaller for high (0.10% across all optical properties and physiological parameters) than for low ITA^o (1.51% on average), which highlights the importance of accounting for skin tissue when acquiring data on darker skin tones. Additionally, changes range up to 6% on StO_2, suggesting that correcting for skin absorption might reduce the incidence of the occult hypoxia situation.

6.5 Conclusion and Next Chapters

In summary, this work investigated the effects of skin tissue on FD-DOS data and its estimations. I concluded that errors in the absorption coefficient are around 1-7%, while errors in the physiological parameters range within 1-9%. At the NIR spectral region, errors are higher for 691 nm than for 851 nm. I computed the complex ratio between the reflected intensity in the ideal situation and including the skin tissue (through the 2L model) and used it as a correction factor applied to FD-DOS data generated in skin presence. Data suggest that correcting only the smaller wavelength is the best approach to reduce the errors to 1-4% for the absorption coefficient and 1-7% for the physiological parameters. In real data, this correction is enough for introducing a change up to 6% on StO_2, suggesting a reduction of the occult hypoxia incidence. Additionally, FD-DOS might be less sensitive to skin influence as it relies on several SDSs, which are jeopardized similarly, to estimate optical parameters.

The next chapter of this text discusses the other loose ends from Chapter 5. In Chapter 7, I aimed to introduce a model that accounts for analyzing DO techniques acquisitions accounting for tissue curvature and heterogeneity simultaneously.

CHAPTER 7

ASSESSING CRITICAL CLOSING PRESSURE WITH DIFFUSE OPTICAL TECHNIQUES THROUGH IMPROVED MODELS

In the previous chapters, I discussed the hypothesis assumed when using the SI model (the standard approach in DO techniques applications) and how those assumptions jeopardize optical and physiological estimations. More specifically, I investigated the influence of tissue heterogeneity and curvature in optical estimations and proposed methods to consider these features in data analysis. In this chapter, I introduce a methodology that simultaneously accounts for both influences in real data acquisitions. The primary aim of this chapter is the assessment of the Critical Closing Pressure (CrCP) through this enhanced model. Having acquired both FD-DOS and DCS data concurrently with a systemic physiological monitor, I could also estimate this parameter. CrCP is an important parameter in clinical scenarios, as it is compromised by various diseases, making it a potential biomarker. Thus, accurately estimating CrCP is relevant to the future clinical applications of DO techniques. In Section 7.1, I introduce this parameter and the problem of analyzing optical data considering both tissue curvature and heterogeneity. In Section 7.2, I present the protocol and acquisitions I performed in this new pool of participants. Section 7.3 exhibits the pilot results I obtained, together with the discussion they led to. Finally, in Section 7.4, I summarize the main conclusions of this investigation.

7.1 Introduction

The human brain is an organ with high metabolic demands and limited capacity to store energy. Thus, Cerebral blood flow (CBF) is a clinically relevant parameter, as proper CBF values ensure that the delivery of nutrients and oxygen matches the metabolic needs [179]. Altered CBF values may lead to ischemic cell or parenchymal damage [180], potentially leading to hypoxia, ischemia, and brain tissue damage [181, 182].

An important parameter in CBF management is cerebral perfusion pressure (CPP), the pressure gradient that drives the blood to flow through the brain capillaries [183]. Of note,

the primary concern for blood delivery throughout the brain occurs in the small vessels, as this is where molecular exchange occurs. CPP is the difference between the arterial blood pressure (ABP), which pumps blood to the brain, and the opposing pressures to the flow on small vessels. One common approach to estimating CPP is to use the intracranial pressure (ICP) as a proxy of CBF resistive pressure, i.e., $CPP = ABP - ICP$. ABP can be assessed invasively through the arterial line method or noninvasively through physiological monitors using photoplethysmography [184]. On the other hand, gold standards for ICP assessment are invasive measurements (e.g., assessed with a ventricular catheter), and estimates are often around 5-15 mmHg [185]. Non-invasive techniques, such as transcranial Doppler ultrasonography (TCD), have emerged as alternatives to ICP estimations. Although their estimations usually correlate well with invasive assessments, they may lack accuracy in absolute estimations [186].

Although CPP is usually taken as $ABP - ICP$, this definition is not aligned to the actual meaning of CPP. ICP is not directly associated with the resistive pressure at the microscopic level, as it is a macroscopic quantity. Thus, it does not consider the vasomotor tone (i.e., the wall tension of vessels exerting pressure on the blood) [187, 188]. This *local resulting pressure* over the small vessels is known as **Critical Closing Pressure** (CrCP) [189]. Thus, a more accurate definition for CPP is through $ABP - CrCP$. In other words, CrCP is the value at which intraluminal pressure is insufficient to keep the vessel open, resulting in its collapse and cessation of CBF. Despite the fact that it can be estimated through physiological parameters, note that CrCP is rather a conceptual quantity (ABP - CPP) than a physiological quantity, which makes it hard to obtain a gold standard for this value. Moreover, the estimation of CrCP also reflects other features of brain vessels, such as its capacity to adjust to a greater CBF [190].

Unlike ICP, CrCP cannot be invasively assessed in humans as it is local information. Thus, non-invasive CrCP estimation methods are gaining popularity due to their reduced risk and ease of use [191, 192]. TCD is a common non-invasive method to estimate CrCP through cerebral blood flow velocity. However, TCD is still sensitive to large vessels instead of the capillaries. One alternative is to use laser-Doppler fluxmetry (LDF). Even so, the penetration depth of the technique is so that it requires a burr hole [193]. In this context, DCS provides an alternative to estimating CrCP since F estimations are sensitive to small vessels, and the penetration depth provided by this optical technique is around 1-2 cm. Previous research found high correlations between CrCP estimations of DCS with TCD [116, 127, 194, 195].

However, DCS-based CrCP estimations are usually between 20-30 mmHg, while estimations based on invasive measurements are spread around 45 mmHg [191]. In this work, I hypothesized that this difference is due to two main sources. The first one is that most investigations using DCS do not simultaneously use another optical technique to estimate μ_a and $\mu_s^{'}$. Usually, optical properties are assumed instead of assessed, which introduces errors in F estimations. The second is that prior research has used the SI model, which jeopardizes

F estimations through the previously discussed heterogeneity and planarity issues.

Since I discussed methods to analyze optical data considering those influences separately in Chapters 4 and 5, I aimed to investigate the impact of adding both corrections together in CrCP and other physiological estimations. To the best of my knowledge, both effects were not simultaneously considered when analysing DO data so far. For this purpose, I acquired both FD-DOS and DCS data from a healthy cohort and analyzed it with a novel numerical model I aim to test in this dataset. Additionally, I acquired ABP data using a commercial system, which allowed CrCP estimations.

7.2 Materials and Methods

7.2.1 Measurement Systems

7.2.2 Participants and Experimental Protocol

I acquired data on 44 participants (19 female), with an average (standard deviation) age of 41(17) years and no clinical diagnosis of neurological disorders. I acquired FD-DOS and DCS simultaneously with the system exhibited in Figure 2.10. FD-DOS measurements contained one detector and eight sources at 705, 750, and 850 nm, providing SDSs of 0.7, 1.2, 1.6, 2.1, 2.6, 3.0, 3.5, and 4.0 cm at a sampling frequency of 4.5 Hz. DCS acquisition data was performed with one source (785 nm) and two detectors positioned 0.8 and 2.5 cm away from the source at a sampling frequency of 2.8 Hz. For detection, I used three independent single-photon counting detectors at each detection position to improve SNR. Additionally, I acquired simultaneous arterial blood pressure (ABP) data with a commercial system (Finometer, Finapress) at a sampling frequency of 200 Hz.

The experimental protocol consisted of laying the participant in a hospital bed for 10 minutes to stabilize their heartbeat while the measurement systems were positioned. I positioned the optical probe (FD-DOS and DCS acquisitions) on the participant's forehead laterally to avoid the central sagittal plane. The finometer's arm and finger cuffs were positioned on the participants' left arm. After synchronizing FD-DOS, DCS, and Finometer systems through a trigger, the protocol started with five minutes of resting data, while the participants were lying motionless and with their eyes closed. Each minute of data acquisition consisted of 10 seconds of FD-DOS data followed by 50 seconds of DCS data acquisition. The FD-DOS readings were previously calibrated using the phantom calibrating method (Section 2.3.4). This protocol was approved by the local Ethics Committee at the University of Campinas (CAAE 50436921.3.0000.5404). Participants were instructed concerning the experiment protocol before signing an informed consent form prior to participation (Appendix J).

7.2.3 Models of Optical Data Analysis

I analyzed FD-DOS data using four different approaches described below (the SI model, the 2L model, simulations in a curved medium, and simulations in a two-layered curved medium). I used these pipelines to analyze the average curve of each 10 seconds of FD-DOS data acquisition, which provides five sets of optical properties. I discarded sets where $\mu_s^{'}$ did not decrease as a function of wavelength and assumed the fit as the median values of the remaining sets. DCS data were also analyzed through the four approaches using the optical properties estimated by FD-DOS as inputs. F values were estimated for each point of the DCS time series to calculate CrCP (see next section) and for the average 50-second curve of data acquisition to estimate the average blood flow value.

Semi-Infinite Model (SI)

This analysis followed the previously discussed SI model as described in Chapter 5 for FD-DOS data. DCS estimations were also based on this model, using the optical properties estimated through FD-DOS.

Curved Model (CM)

In the absence of an analytical forward model to consider the curvature at the acquisition data interface, I used the lookup table method described in Chapter 5 to analyze FD-DOS data. However, I decided to use a 9-cm radius mesh because it would better match the actual curvature of the forehead of most participants. DCS estimations relied once more upon the SI model using the optical properties estimated considering curvature. I referred to this model as the Curved Model (CM).

Two-Layered Model (2L)

The pipeline of FD-DOS analysis through the 2L model followed the same procedure of Chapter 4 with a few modifications based on the lack of knowledge of the first layer thickness ℓ. Since there was no anatomical information from the participants available to estimate ℓ, I first used FD-DOS data to estimate this parameter. To this end, I analyzed the data of the three smallest SDSs (0.7, 1.2, and 1.6 cm) with the SI model to estimate the optical properties of the first layer (μ_{a1}^0 and $\mu_{s1}^{'0}$). As the depth penetration of a regular FD-DOS channel is half the SDS rounded up, using SDSs smaller than 2 cm allows robust estimation of the first layer properties since ℓ is expected to be 1 cm or more. Next, I used the 2L model (assuming homogeneous scattering) to analyze all SDSs, allowing a variation of 20% over μ_{a1}^0 and $\mu_{s1}^{'0}$ to estimate the first layer thickness on 705, 750 and 830 nm. I assumed ℓ as the median value of those three. Then, I fixed ℓ and fitted the data once more. This time, I allowed a variation of 40% downwards and 20% upwards in μ_{a1}^0 and $\mu_{s1}^{'0}$, since the previous research using layered

models reported an underestimation of the optical properties obtained using the SI model when compared to layered models. At the end of this procedure, I estimated ℓ, and the first and second layer optical properties (μ_{a1}, μ_{a2} and $\mu_s^{'}$). DCS data analysis followed the same algorithm described in Chapter 4 using the previously estimated ℓ and optical parameters. Since β is not known *a priori* but it is expected to be around 0.5, I averaged the first 50 seconds of DCS data and adjusted the resulting autocorrelation curve (subjected to $g_2(\tau) \geq 1.25$) to estimate the β of each curve using the SI model before analyzing data using the 2L model.

Curved, Layered Model (CLM)

Aiming to consider both influences of tissue curvature and heterogeneity together, I used the same mesh as in the CM to build a numerical forward model for DOS analysis. To this end, I assumed a thickness of $\ell = 1.1cm$ and homogeneous scattering, and created a lookup table varying $\mu_s^{'}$ from 5 to 15 in steps of 0.1 cm^{-1}, and the absorption of the first and second layers (μ_{a1} and μ_{a2}) from 0.05 to 0.3 cm^{-1} in steps of $0.005cm^{-1}$. In this model, I estimated F using the 2L model through the algorithm described in Chapter 4. I used the previously estimated optical properties and fixed $\ell = 1.1cm$. I referred to this model as the Curved, Layered Model (CLM).

7.2.4 Estimation of Physiological Parameters

Once the absorption coefficient was estimated, I used Equation 2.1 to compute $[HbO]$ and $[HbR]$ assuming a water fraction of 70%. Then, I calculated the total hemoglobin concentration $[HbT] = [HbO]+[HbR]$ and the blood oxygen saturation $StO_2 = (100\%)\times[HbO]/[HbT]$.

To estimate CrCP, I used a two-compartment Windkessel model [163, 196, 197] for modeling the cerebral arterial compartment between arteries and capillaries. In this approach, the vascular bed is modeled through a parallel RC circuit, and CrCP may be estimated through the phase shift between ABP and F time series [127]:

$$CrCP = \gamma\langle ABP\rangle\left(1 - \frac{|ABP(f_{hr})|\,\langle F\rangle}{|F(f_{hr})|\,\langle ABP\rangle}\sqrt{1+(2\pi f_{hr}\tau)^2}\right), \tag{7.1}$$

where f_{hr} is the heartbeat frequency, $\langle\cdot\rangle$ denotes the temporal average value, $|\cdot|$ denotes the amplitude of the Fourier transform, γ is the ratio between the arterial pressure at the beginning of the arteriole compartment and ABP (taken as 0.6 based on animal studies [164]), and $\tau = -tan(\varphi_{hr})/(2\pi f_{hr})$. Here, φ_{hr} is the phase shift between ABP and F at the heartbeat frequency (f_{hr}). A brief deduction of Equation 7.1 may be found in Appendix G. Thus, I first estimated f_{hr} by finding the cardiac peak at the power spectrum (maximum value between 0.7 Hz and 2.2 Hz) of the entire time series of ABP data. Then, I downsampled ABP data to the same frequency acquisition of DCS data. For each 50-second segment of F data, I estimated φ_{hr} using transfer functions based on the Welch's method (*tfestimate*, MATLAB) and

a CrCP value. I took the CrCP estimation as the median of the values from each one of the five segments.

7.2.5 Data exclusion criteria

I discarded participants where the average of the 10 seconds FD-DOS acquisition resulted in $R^2 < 0.99$ for $log(\rho^2|\phi(\rho)|)\ vs\ \rho$ or $arg(\phi(\rho))\ vs\ \rho$. I also discarded participants where $\mu_s^{'}$ did not decrease in terms of λ. Based on DCS data, I discarded participants where $|\beta - 0.5| \geq 0.12$ and the cardiac frequency is greater than $1.4Hz = 84bpm$ as it would not allow the cardiac frequency at DCS data. Lastly, I discarded participants where $[HbO] \leq 5\mu molar$, $[HbR] \leq 5\mu molar$ and $StO_2 \leq 20\%$ since it might result from acquisition with poor coupling with biological tissue.

7.3 Results and Discussion

In this work, I acquired FD-DOS, DCS, and ABP data with a set of sources and detectors that enable estimations through homogeneous models (SI and CM) and layered models (2L and CLM). All methods considering curvature on the data acquisition interface (CM and CLM) were lookup table-based. On the other hand, planar models (SI and 2L) were analytical. Also, I decided not to correct for skin absorbance through the methodology discussed in Chapter 6. In that chapter, I tested a preliminary methodology to increase the accuracy of physiological estimations accounting for darker skin presence through the SI model. As I did not test if that correction is a confounder in the accuracy of the first layer estimation through layered models, I only compared estimations of SI, Curved, 2L, and CL models.

Figure 7.1 shows the physiological parameters estimated using the four models described in the previous section. The ABP estimation for all participants was 95 (86; 103) mmHg. I tested the significance of the differences between the four approaches using a Wilcoxon test or a T-test, depending on the parametricity of the distributions, assessed through a Lilliefors test. As discussed in previous chapters, I expected an increase in the μ_a as well as a reduction in the variability (e.g., the interquartile range) estimated through the layered models (i.e., 2L and CLM) when compared to homogeneous models since this methodology is supposed to improve the accuracy when solving the inverse problem. However, results suggest that there is no statistical difference between the μ_a estimations of the four models. This result is reflected in physiological estimations. There is no statistical difference between $[HbO]$, $[HbT]$, and StO_2 among the tested models. Differences were found between $[HbR]$ of CM and CLM (median(interquartile range) of 20(15;21) against 13(9;18) $\mu molar$, p=0.0035) and among 2L and CLM (17(13;22) against 13(9;18) $\mu molar$, p=0.0094).

A possible cause of this unexpected similarity between the models is the lack of accuracy of ℓ as the 2L model algorithm I validated in Chapter 4 relies on the knowledge of

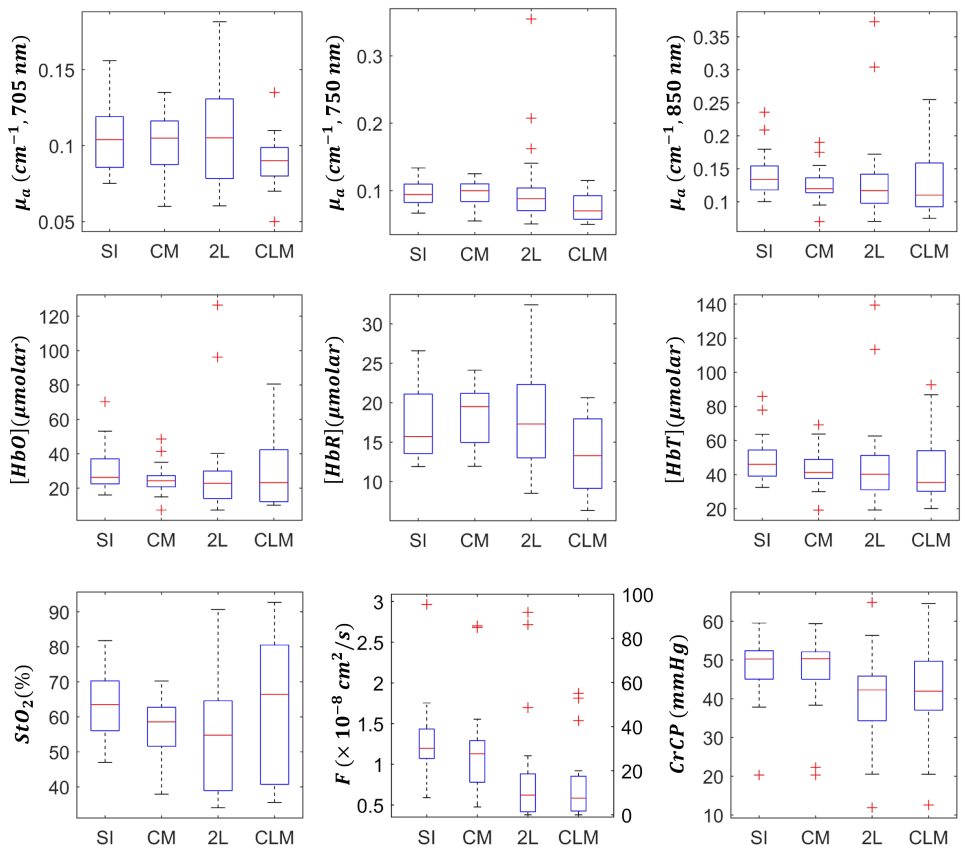

Figure 7.1: Absorption coefficient and physiological parameters estimated using the SI, CM, 2L, and CLM models. The right y-axis in F estimations relates to layered estimations (i.e., 2L and CLM boxplots).

this parameter. I tried to mitigate this issue using the smallest SDSs first and then fitting ℓ through the 2L model. Still, there is a cross-talk between ℓ and other parameters that might influence 2L estimations. Indeed, in Chapter 4, I discussed that an error of ~ 15% on ℓ is enough to introduce errors of ~ 20% or more in estimations through DO techniques. Thus, the lack of increase in estimations when comparing layered to homogeneous models might result from poor ℓ estimations. In this sense, the errors introduced by this issue should be even more pronounced in the CLM, where I fixed ℓ = 1.1 cm. Although potentially far from the real value, the 2L approach used here provides some flexibility in terms of dealing with ℓ. Thus, it is reasonable to expect that the estimated thicknesses are closer to the real value than the fixed 1.1 cm. To investigate this issue, I assessed the percentage differences between the estimated values and the fixed $\ell = 1.1cm$ value of the CLM. This deviation is 32(10;33)%, potentially jeopardizing CLM estimations even further. It is noteworthy that including the curvature in the CLM is insufficient to provide the expected increase in estimations faced with this error in ℓ. This suggests that properly adjusting the heterogeneity of the tissue through layered models and fine-tuning ℓ (using a Magnetic Resonance Image, for example) is more relevant to estimations than considering the curvature in the acquisition interface.

On the other hand, the errors introduced due to the lack of knowledge about ℓ seem insufficient to undo the expected trends for F estimations. F values are statistically different between SI (1.2(1.1;1.4) cm^2/s) and layered models (9.4(2.2;16) cm^2/s for the 2L model (note the right y-xis for layered models), p=0.0074; 7.6(1.7;18) cm^2/s for the CLM model, p = 0.0081) and between CM (1.1(0.8;1.3) cm^2/s) and layered models (p=0.0018 between CM and 2L; p = 0.0024 between CM and CLM). Estimations are almost ten times greater for layered models than for homogeneous models. Additionally, curvature seems not to influence blood flow estimations as F values are similar between SI and CM, and between 2L and CLM. This result suggests that the preliminary investigation of the influence of tissue curvature on F exhibited in Chapter 5 points in the right direction. Still, further investigations are needed.

Lastly, the main goal of this investigation was to investigate CrCP estimations since they are relevant non-invasive measurements in clinical scenarios. A reliable estimation of CrCP depends on an accurate estimation of F (Equation 7.1), which, in turn, depends on the optical properties estimation. Thus, CrCP should pile up all the previous errors. Previous research aiming to estimate CrCP relied on DCS acquisitions only (assuming optical properties), providing estimations from 5 to 30 mmHg in healthy participants using the SI model [127, 195]. Using this same model, the values estimated in this work (ranging from 40 to 60 mmHg) are considerably higher than previous estimations. These estimations are closer to previous research using invasive measurements and TCD/LDF methods (around 45 mmHg [191, 193]), which suggests that properly accounting for the optical properties in F estimations improves CrCP assessment. This result is not aligned with previous reports that claim the optical properties do not alter CrCP estimations due to the maintenance of F pulsatile pattern [146].

I also found that layered models estimate statistically smaller CrCP values than homogeneous models in this pool of participants. Indeed, CrCP estimated through homogeneous models (50(45;52) mmHg for both the SI and CM models) are statistically different from the 2L estimations (41(24;46) mmHg; p=0.0289 between SI and 2L, and p=0.0227 between CM and 2L). Thus, considering tissue heterogeneity through layered models also impacts CrCP estimations. Additionally, as in F estimations, curvature seems not to influence CrCP estimations, as planar and curved model estimations are similar. This result is aligned with the minimal influence of the tissue curvature on F estimations I preliminarily discussed in Chapter 5. It also reinforces the conclusion that adjusting for tissue heterogeneity is more relevant than considering the curvature in the data acquisition interface.

In addition to that, the average estimations through 2L and CLM (40-50 mmHg) are similar to previous research using invasive measurements and TCD/LDF methods [191,193], suggesting that accounting for layered structure is relevant in terms of increasing the accuracy of CrCP estimations. Although there is no statistical difference between the CLM and 2L models in the estimation of CrCP, several factors indicate the superior potential of the CLM model. First, the CLM model integrates both layered structure and curvature considerations, potentially making it more versatile in facing anatomical variability across participants. As discussed for physiological and optical estimations, errors in ℓ estimations might be overshadowing the improvements related to considering curvature. Interestingly, the fixed ℓ value in CLM seems to not harm CrCP estimations as it jeopardizes optical estimations. When fine-tuned, this model could lead to even more consistent and reliable estimations. Ultimately, while both models perform comparably in this study, the CLM range is closer to gold-standard measurements, which suggests that an appropriate adjustment of this model would lead to more accurate estimations when compared to other models.

7.4 Conclusions

In this work, I analyzed FD-DOS and DCS data through four models (homogeneous or not; planar or not) and compared the differences between the physiological estimations of $[HbO]$, $[HbR]$, $[HbT]$, StO_2, F, and CrCP. The main conclusion is that the prior knowledge of the thickness of the first layer is crucial for an accurate estimation of optical data since heterogeneity plays a more important role than curvature. Additionally, layered models estimate substantially higher F values and more accurate CrCP values.

CHAPTER 8

OVERALL CONCLUSIONS AND FUTURE DIRECTIONS

8.1 Overview

In this work, I explored the hypothesis that parameters estimated through diffuse optics hold the potential to serve as biomarkers of diseases with vascular impact since the estimations are hemodynamic-related. The hypothesis seems to hold for muscle applications, as discussed in Chapter 3. Muscle tissue is homogeneous, and the coupling between the optical sensor and the interface is so that curvature might not harm optical estimations through the homogeneous, planar SI model. Unfortunately, the accuracy of this model is not enough for clinical environments. Acquisitions aiming to obtain information about the brain cortex struggle with tissue heterogeneity and curvature problems.

In this context, the thesis I defended is that models considering the macroscopic structural complexity of tissue can increase the accuracy of measurements obtained with diffuse optical techniques to the level they could be used as biomarkers for vascular diseases. To this end, I investigated the effects of tissue heterogeneity (Chapter 4) and curvature (Chapter 5), primarily in FD-DOS estimations and in DCS estimations as a consequence. In both cases, I proposed and validated methods to analyze DO data, taking those features into account. In Chapter 7, I aimed to combine both corrections. Additionally, in Chapter 6, I investigated an ignored problem regarding the influence of skin on optical estimations. Overall, I conclude that those modifications in the SI model are actually improvements since they increase the accuracy of estimations. This chapter summarizes the key findings and outlines potential future directions for further research.

8.2 Main Messages

One of the central topics of this thesis was the impact of tissue heterogeneity on DO data. I discussed that the literature suggests that the SI model often underestimates optical estimations due to the contribution of extracerebral tissue to measurements. Available layered models increase the sensitivity to the deep layer, often taken as the cortical tissue, but strug-

gle with numerical stability when solving the inverse problem. Thus, I proposed an algorithm to use the 2L model in steps, improving accuracy in optical estimations. At this point, I decided to assume ℓ as a known quantity as it might be estimated through a Magnetic Resonance image. I also found that the model is not sensitive to second-layer scattering. Thus, assuming homogeneous scattering reduces the number of adjusted parameters, increasing the model's stability. However, in the exhibited investigations, there is still a lack of accuracy when analyzing simulations in templates of a realistic head. I hypothesized that this issue could potentially be solved by adding the tissue curvature to the model.

Another feature of real data acquisition investigated in this work was the effect of tissue curvature on optical estimations. In the absence of an analytical model that deals with this issue, I used a numerical model, lookup-table-based, to perform this study. I concluded that incorporating tissue curvature into the model of data analysis improved the accuracy of optical estimations in surfaces with nonzero curvature. On top of that, it is more important to consider this feature in the model than adjust it for the actual curvature of the data acquisition interface in the investigated range (from 5 to 20 cm). Moreover, the addition of the curvature also increases the optical estimations in real data.

The COVID-19 pandemic highlighted the need for more accurate StO_2 measurements across diverse populations, especially for non-white individuals. In this sense, I investigated the influence of skin tissue on FD-DOS estimations. I concluded that skin absorption is around 10 times higher than the absorption of deep tissue for darker tones. This influence could lead to an error up to 5% in StO_2, enough to cause the occult hypoxemia problem. I also propose a method for removing the bias of skin influence over optical estimations. This method decreases the upper boundary of the 95th MAPE StO_2 percentile from 4.3 to 3.4%. In real data, this approach introduces percentage changes up to 6% on estimations. It suggests that, although preliminary, this method is promising in terms of increasing the accuracy of optical estimations facing darker skin tones.

Based on the investigations exhibited in this work, I concluded that accounting for tissue heterogeneity increases the accuracy of optical estimations, just as considering the tissue curvature does. In order to improve the reliability even more, I tried to perform both corrections simultaneously in DO data. To this end, I acquired FD-DOS and DCS data simultaneously, which allowed me also to calculate CrCP. As I had no prior knowledge of ℓ since the participants did not have a Magnetic Resonance image, I tried to estimate it through FD-DOS data or fixed it at a reasonable value. I concluded that the fine-tuning of the heterogeneity through an accurate estimation of ℓ is more relevant to optical estimations than accounting for tissue curvature. Moreover, CrCP values estimated through heterogeneous models aligned better with values available in the literature.

8.3 Future Directions

The methods I propose in this work aim to increase the accuracy of estimations using DO techniques. However, I failed to combine those methodologies to improve even further the model to analyze data. I found out that fine-tuning the architecture of the layered model through a precise ℓ value impacts the estimations more than adjusting for the curvature. Thus, it is crucial to develop more accurate methods for estimating this parameter. However, it is not easily assessable information since not always a participant has magnetic resonance imaging available. In this sense, novel approaches to estimate ℓ must be explored. I proposed an approach using FD-DOS data, but the results suggest that estimations were not ideal. In this sense, machine learning algorithms could be trained on large datasets with known ℓ or simulations to improve the accuracy when predicting this parameter. Another alternative is to try to use anatomical atlases to estimate ℓ based on participant demographics and anatomical characteristics. The ability to accurately estimate the first layer thickness without a magnetic resonance image would reduce costs and complexity in clinical applications.

Additionally, improvements in the methods of generating FD-DOS data in skin presence are needed. While the method I presented has shed light on the impact this feature has on physiological estimations through FD-DOS, it has some limitations. Of note, it assumes homogeneous scattering between the skin and the underneath tissue, and it also assumes that the point-source is deeper than the first layer in some approaches. Although the results I discussed have the right trend, more accurate approaches are needed. Future simulations should rely on more precise methods (e.g., using NIRFASTer with meshes with small node sizes). Once the method is set, investigations of this effect over other techniques, such as using continuous light as pulse oxymeters, must also be conducted. This will be crucial in addressing disparities in healthcare outcomes.

REFERENCES

[1] Jain, K. *Role of Biomarkers in Healthcare* (Humana Press, 2017).

[2] Zhang, B., Zhang, B. J., Zhou, Z. L., Guo, Y. T. & Wang, D. The value of glycosylated hemoglobin in the diagnosis of diabetic retinopathy: a systematic review and meta-analysis. *Bmc Endocrine Disorders* **21**, 11 (2021).

[3] Stanciulescu, L. A., Scafa-Udriste, A. & Dorobantu, M. Exploring the association between low-density lipoprotein subfractions and major adverse cardiovascular outcomes-a comprehensive review. *International Journal of Molecular Sciences* **24**, 12 (2023).

[4] Chary, A., Tohidi, M. & Hedayati, M. Association of ldl-cholesterol subfractions with cardiovascular disorders: a systematic review. *Bmc Cardiovascular Disorders* **23**, 10 (2023).

[5] Samson, C. & Koh, A. Stress monitoring and recent advancements in wearable biosensors. *Frontiers in Bioengineering and Biotechnology* **8**, 8 (2020).

[6] Akiyoshi, J. *Acute Stress in Patients with Panic Disorders Produces Effects on Salivary Amylase and Cortisol* (IntechOpen, 2011).

[7] Dochez, V. *et al.* Biomarkers and algorithms for diagnosis of ovarian cancer: Ca125, he4, rmi and roma, a review. *Journal of Ovarian Research* **12**, 9 (2019).

[8] Saini, S. Psa and beyond: alternative prostate cancer biomarkers. *Cellular Oncology* **39**, 97–106 (2016).

[9] O'Neill, B. J., Rana, S. N. & Bowman, V. An integrated approach for vascular health: A call to action. *Canadian Journal of Cardiology* **31**, 99–102 (2015).

[10] Durduran, T., Choe, R., Baker, W. B. & Yodh, A. G. Diffuse optics for tissue monitoring and tomography. *Reports on Progress in Physics* **73**, 43 (2010).

[11] Bruns, D. E. & Boyd, J. C. Assessing the impact of biomarkers on patient outcome: An obligatory step. *Scandinavian Journal of Clinical I& Laboratory Investigation* **70**, 85–89 (2010).

[12] Hallacoglu, B. *et al.* Absolute measurement of cerebral optical coefficients, hemoglobin concentration and oxygen saturation in old and young adults with near-infrared spectroscopy. *Journal of Biomedical Optics* **17**, 8 (2012).

[13] Hallacoglu, B., Sassaroli, A. & Fantini, S. Optical characterization of two-layered turbid media for non-invasive, absolute oximetry in cerebral and extracerebral tissue. *Plos One* **8**, 15 (2013).

[14] Gagnon, L., Desjardins, M., Jehanne-Lacasse, J., Bherer, L. & Lesage, F. Investigation of diffuse correlation spectroscopy in multi-layered media including the human head. *Optics Express* **16**, 15514–15530 (2008).

[15] Forti, R. M., Martins, G. G., Baker, W. B. & Mesquita, R. C. Optimizing a two-layer method for hybrid diffuse correlation spectroscopy and frequency-domain diffuse optical spectroscopy cerebral measurements in adults. *Neurophotonics* **10**, 26 (2023).

[16] Vidal-Rosas, E. E., von Luhmann, A., Pinti, P. & Cooper, R. J. Wearable, high-density fnirs and diffuse optical tomography technologies: a perspective. *Neurophotonics* **10**, 18 (2023).

[17] Wheelock, M. D., Culver, J. P. & Eggebrecht, A. T. High-density diffuse optical tomography for imaging human brain function. *Review of Scientific Instruments* **90**, 24 (2019).

[18] Zhao, H. B. & Cooper, R. J. Review of recent progress toward a fiberless, whole-scalp diffuse optical tomography system. *Neurophotonics* **5**, 11 (2018).

[19] Boas, D. A., Dale, A. M. & Franceschini, M. A. Diffuse optical imaging of brain activation: approaches to optimizing image sensitivity, resolution, and accuracy. *Neuroimage* **23**, S275–S288 (2004).

[20] Li, S. Y., Huang, K. X., Zhang, M. H., Uddin, K. M. S. & Zhu, Q. Effect and correction of optode coupling errors in breast imaging using diffuse optical tomography. *Biomedical Optics Express* **12**, 689–704 (2021).

[21] Sassaroli, A., Martelli, F., Zaccanti, G. & Yamada, Y. Performance of fitting procedures in curved geometry for retrieval of the optical properties of tissue from time-resolved measurements. *Applied Optics* **40**, 185–197 (2001).

[22] Zhang, S., Chen, S. Y., Liu, Y. X., Liu, Y. H. & Tan, Z. J. Effects of tissue surface curvature and incident light angle on diffuse correlation spectroscopy. *Journal of Modern Optics* **66**, 93–99 (2019).

[23] Berberansantos, M. N. Beer law revisited. *Journal of Chemical Education* **67**, 757–759 (1990).

[24] Baker, W. B. *Optical Cerebral Blood Flow Monitoring of Mice to Men*. Thesis, University of Pennsylvania (2015).

[25] Cheong, W. F., Prahl, S. A. & Welch, A. J. A review of the optical-properties of biological tissues. *Ieee Journal of Quantum Electronics* **26**, 2166–2185 (1990).

[26] Jacques, S. L. & Pogue, B. W. Tutorial on diffuse light transport. *Journal of Biomedical Optics* **13**, 19 (2008).

[27] Kaplan, P. D., Kao, M. H., Yodh, A. G. & Pine, D. J. Geometric constraints for the design of diffusing-wave spectroscopy experiments. *Applied Optics* **32**, 3828–3836 (1993).

[28] Arridge, S. R., Cope, M. & Delpy, D. T. The theoretical basis for the determination of optical pathlengths in tissue - temporal and frequency-analysis. *Physics in Medicine and Biology* **37**, 1531–1560 (1992).

[29] Liemert, A. & Kienle, A. Light diffusion in a turbid cylinder. ii. layered case. *Optics Express* **18**, 9266–9279 (2010).

[30] Zhao, H. T., Sathialingam, E. & Buckley, E. M. Accuracy of diffuse correlation spectroscopy measurements of cerebral blood flow when using a three-layer analytical model. *Biomedical Optics Express* **12**, 7149–7161 (2021).

[31] Zhao, H. T. *et al.* Comparison of diffuse correlation spectroscopy analytical models for measuring cerebral blood flow in adults. *Journal of Biomedical Optics* **28**, 13 (2023).

[32] Liao, Y. K. & Tseng, S. H. Reliable recovery of the optical properties of multi-layer turbid media by iteratively using a layered diffusion model at multiple source-detector separations. *Biomedical Optics Express* **5**, 975–989 (2014).

[33] Arridge, S. R. & Lionheart, W. R. B. Nonuniqueness in diffusion-based optical tomography. *Optics Letters* **23**, 882–884 (1998).

[34] Vanstaveren, H. J., Moes, C. J. M., Vanmarle, J., Prahl, S. A. & Vangemert, M. J. C. Light-scattering in intralipid-10-percent in the wavelength range of 400-1100 nm. *Applied Optics* **30**, 4507–4514 (1991).

[35] Yalavarthy, P. K., Pogue, B. W., Dehghani, H. & Paulsen, K. D. Weight-matrix structured regularization provides optimal generalized least-squares estimate in diffuse optical tomography. *Medical Physics* **34**, 2085–2098 (2007).

[36] Suzuki, S., Takasaki, S., Ozaki, T. & Kobayashi, Y. A tissue oxygenation monitor using nir spatially resolved spectroscopy. In *Conference on Optical Tomography and Spectroscopy of Tissue III*, vol. 3597 of *Proceedings of the Society of Photo-Optical Instrumentation Engineers (Spie)*, 582–592 (Spie-Int Soc Optical Engineering, BELLINGHAM, 1999).

[37] Matcher, S. J., Kirkpatrick, P., Nahid, K., Cope, M. & Delpy, D. T. Absolute quantification methods in tissue near infrared spectroscopy. In *Conference on Optical Tomography, Photon Migration, and Spectroscopy of Tissue and Model Media - Theory, Human Studies and Instrumentation*, vol. 2359 of *Proceedings of the Society of Photo-Optical Instrumentation Engineers (Spie)*, 486–495 (Spie - Int Soc Optical Engineering, BELLINGHAM, 1995).

[38] Liu, W. K., Li, S. F. & Park, H. S. Eighty years of the finite element method: Birth, evolution, and future. *Archives of Computational Methods in Engineering* **29**, 4431–4453 (2022).

[39] Dehghani, H. *et al.* Near infrared optical tomography using nirfast: Algorithm for numerical model and image reconstruction. *Communications in Numerical Methods in Engineering* **25**, 711–732 (2009).

[40] Arridge, S. R., Schweiger, M., Hiraoka, M. & Delpy, D. T. A finite-element approach for modeling photon transport in tissue. *Medical Physics* **20**, 299–309 (1993).

[41] Paulsen, K. D. & Jiang, H. B. Spatially varying optical property reconstruction using a finite-element diffusion equation approximation. *Medical Physics* **22**, 691–701 (1995).

[42] Jermyn, M. *et al.* Fast segmentation and high-quality three-dimensional volume mesh creation from medical images for diffuse optical tomography. *Journal of Biomedical Optics* **18**, 10 (2013).

[43] Bargo, P. R., Prahl, S. A. & Jacques, S. L. Collection efficiency of a single optical fiber in turbid media. *Applied Optics* **42**, 3187–3197 (2003).

[44] Bargo, P. R., Prahl, S. A. & Jacques, S. L. Optical properties effects upon the collection efficiency of optical fibers in different probe configurations. *Ieee Journal of Selected Topics in Quantum Electronics* **9**, 314–321 (2003).

[45] Papaioannou, T. *et al.* Effects of fiber-optic probe design and probe-to-target distance on diffuse reflectance measurements of turbid media: an experimental and computational study at 337 nm. *Applied Optics* **43**, 2846–2860 (2004).

[46] Brown, W. *Dynamic Light Scattering: The Method and Some Applications* (Clarendon Press, 1993).

[47] Lemieux, P. A. & Durian, D. J. Investigating non-gaussian scattering processes by using nth-order intensity correlation functions. *Journal of the Optical Society of America a-Optics Image Science and Vision* **16**, 1651–1664 (1999).

[48] Ackerson, B. J., Dougherty, R. L., Reguigui, N. M. & Nobbmann, U. Correlation transfer - application of radiative-transfer solution methods to photon-correlation problems. *Journal of Thermophysics and Heat Transfer* **6**, 577–588 (1992).

[49] Boas, D. A., Campbell, L. E. & Yodh, A. G. Scattering and imaging with diffusing temporal field correlations. *Physical Review Letters* **75**, 1855–1858 (1995).

[50] Farzam, P. & Durduran, T. Multidistance diffuse correlation spectroscopy for simultaneous estimation of blood flow index and optical properties. *Journal of Biomedical Optics* **20**, 10 (2015).

[51] Shang, Y. *et al.* Portable optical tissue flow oximeter based on diffuse correlation spectroscopy. *Optics Letters* **34**, 3556–3558 (2009).

[52] Boas, D. A. & Yodh, A. G. Spatially varying dynamical properties of turbid media probed with diffusing temporal light correlation. *Journal of the Optical Society of America a-Optics Image Science and Vision* **14**, 192–215 (1997).

[53] Yu, G. Q. *et al.* Noninvasive monitoring of murine tumor blood flow during and after photodynamic therapy provides early assessment of therapeutic efficacy. *Clinical Cancer Research* **11**, 3543–3552 (2005).

[54] Buckley, E. M. *et al.* Cerebral hemodynamics in preterm infants during positional intervention measured with diffuse correlation spectroscopy and transcranial doppler ultrasound. *Optics Express* **17**, 12571–12581 (2009).

[55] Byrd, R. H., Gilbert, J. C. & Nocedal, J. A trust region method based on interior point techniques for nonlinear programming. *Mathematical Programming* **89**, 149–185 (2000).

[56] Jacques, S. L. Optical properties of biological tissues: a review. *Physics in Medicine and Biology* **58**, R37–R61 (2013).

[57] Mosca, S. *et al.* Optical characterization of porcine tissues from various organs in the 650-1100 nm range using time-domain diffuse spectroscopy. *Biomedical Optics Express* **11**, 1697–1706 (2020).

[58] Farina, A. *et al.* In-vivo multilaboratory investigation of the optical properties of the human head. *Biomedical Optics Express* **6**, 2609–2623 (2015).

[59] Heino, J., Arridge, S., Sikora, J. & Somersalo, E. Anisotropic effects in highly scattering media. *Physical Review E* **68**, 8 (2003).

[60] Mohlenhoff, B., Romeo, M., Diem, M. & Woody, B. R. Mie-type scattering and non-beer-lambert absorption behavior of human cells in infrared microspectroscopy. *Biophysical Journal* **88**, 3635–3640 (2005).

[61] Bonner, R. & Nossal, R. Model for laser doppler measurements of blood-flow in tissue. *Applied Optics* **20**, 2097–2107 (1981).

[62] Ninck, M., Untenberger, M. & Gisler, T. Diffusing-wave spectroscopy with dynamic contrast variation: disentangling the effects of blood flow and extravascular tissue shearing on signals from deep tissue. *Biomedical Optics Express* **1**, 1502–1513 (2010).

[63] Durduran, T. *et al.* Diffuse optical measurement of blood flow, blood oxygenation, and metabolism in a human brain during sensorimotor cortex activation. *Optics Letters* **29**, 1766–1768 (2004).

[64] Mesquita, R. C. *et al.* Direct measurement of tissue blood flow and metabolism with diffuse optics. *Philosophical Transactions of the Royal Society a-Mathematical Physical and Engineering Sciences* **369**, 4390–4406 (2011).

[65] Fantini, S., Franceschini, M. A. & Gratton, E. Semi-infinite-geometry boundary-problem for light migration in highly scattering media - a frequency-domain study in the diffusion-approximation. *Journal of the Optical Society of America B-Optical Physics* **11**, 2128–2138 (1994).

[66] Liu, X. *Linear mixed-effects models* (Academic Press, 2016).

[67] Forti, R. M. *Determination of the dynamical properties in turbid media using diffuse correlation spectroscopy: applications to biological tissues.* Thesis, University of Campinas (2015).

[68] Lu, R. J. *et al.* Genomic characterisation and epidemiology of 2019 novel coronavirus: implications for virus origins and receptor binding. *Lancet* **395**, 565–574 (2020).

[69] Richardson, S. *et al.* Presenting characteristics, comorbidities, and outcomes among 5700 patients hospitalized with covid-19 in the new york city area. *Jama-Journal of the American Medical Association* **323**, 2052–2059 (2020).

[70] Wu, C. M. *et al.* Risk factors associated with acute respiratory distress syndrome and death in patients with coronavirus disease 2019 pneumonia in wuhan, china. *Jama Internal Medicine* **180**, 934–943 (2020).

[71] Ranieri, V. M. *et al.* Acute respiratory distress syndrome the berlin definition. *Jama-Journal of the American Medical Association* **307**, 2526–2533 (2012).

[72] Huang, C. L. *et al.* Clinical features of patients infected with 2019 novel coronavirus in wuhan, china. *Lancet* **395**, 497–506 (2020).

[73] Mutlu, G. M. & Budinger, G. R. S. Incidence and outcomes of acute lung injury. *New England Journal of Medicine* **354**, 416–416 (2006).

[74] Mikkelsen, M. E. *et al.* The epidemiology of acute respiratory distress syndrome in patients presenting to the emergency department with severe sepsis. *Shock* **40**, 375–381 (2013).

[75] Bienvenu, O. J. *et al.* Depressive symptoms and impaired physical function after acute lung injury a 2-year longitudinal study. *American Journal of Respiratory and Critical Care Medicine* **185**, 517–524 (2012).

[76] Linko, R. *et al.* One-year mortality, quality of life and predicted life-time cost-utility in critically ill patients with acute respiratory failure. *Critical Care* **14**, 9 (2010).

[77] Orfanos, S. E., Mavrommati, I., Korovesi, I. & Roussos, C. Pulmonary endothelium in acute lung injury: from basic science to the critically ill. *Intensive Care Medicine* **30**, 1702–1714 (2004).

[78] Cross, L. J. M. & Matthay, M. A. Biomarkers in acute lung injury: Insights into the pathogenesis of acute lung injury. *Critical Care Clinics* **27**, 355–+ (2011).

[79] Moussa, M. D. *et al.* Evaluation of endothelial damage in sepsis-related ards using circulating endothelial cells. *Intensive Care Medicine* **41**, 231–238 (2015).

[80] Pareznik, R., Knezevic, R., Voga, G. & Podbregar, M. Changes in muscle tissue oxygenation during stagnant ischemia in septic patients. *Intensive Care Medicine* **32**, 87–92 (2006).

[81] Gomez, H. *et al.* Use of non-invasive nirs during a vascular occlusion test to assess dynamic tissue o₂ saturation response. *Intensive Care Medicine* **34**, 1600–1607 (2008).

[82] Bezemer, R. *et al.* Assessment of tissue oxygen saturation during a vascular occlusion test using near-infrared spectroscopy: the role of probe spacing and measurement site studied in healthy volunteers. *Critical Care* **13**, 7 (2009).

[83] Cortes, D. O. *et al.* Microvascular reactivity is altered early in patients with acute respiratory distress syndrome. *Respiratory Research* **17**, 7 (2016).

[84] De Backer, D., Donadello, K. & Cortes, D. O. Monitoring the microcirculation. *Journal of Clinical Monitoring and Computing* **26**, 361–366 (2012).

[85] van Beekvelt, M. C. P., Colier, W., Wevers, R. A. & van Engelen, B. G. M. Performance of near-infrared spectroscopy in measuring local o₂ consumption and blood flow in skeletal muscle. *Journal of Applied Physiology* **90**, 511–519 (2001).

[86] Bopp, C. M., Townsend, D. K. & Barstow, T. J. Characterizing near-infrared spectroscopy responses to forearm post- occlusive reactive hyperemia in healthy subjects. *European Journal of Applied Physiology* **111**, 2753–2761 (2011).

[87] Leo, F. B., Wormanns, D. & Grohe, C. Covid-19 from the perspective of pneumology long-term consequences and implications for pneumological aftercare. *Deutsche Medizinische Wochenschrift* **145**, 1086–1092 (2020).

[88] Schelling, G. *et al.* Pulmonary function and health-related quality of life in a sample of long-term survivors of the acute respiratory distress syndrome. *Intensive Care Medicine* **26**, 1304–1311 (2000).

[89] Herridge, M. S. *et al.* Functional disability 5 years after acute respiratory distress syndrome. *New England Journal of Medicine* **364**, 1293–1304 (2011).

[90] Bein, T., Weber-Carstens, S. & Apfelbacher, C. Long-term outcome after the acute respiratory distress syndrome: different from general critical illness? *Current Opinion in Critical Care* **24**, 35–40 (2018).

[91] Chiumello, D., Coppola, S., Froio, S. & Gotti, M. What's next after ards: Long-term outcomes. *Respiratory Care* **61**, 689–699 (2016).

[92] Enright, P. L. & Sherrill, D. L. Reference equations for the six-minute walk in healthy adults. *American Journal of Respiratory and Critical Care Medicine* **158**, 1384–1387 (1998).

[93] Kato, B. S. *et al.* Application of multilevel models to structured repeated measurements. *Quality I& Quantity* **39**, 711–732 (2005).

[94] Gurka, M. J. & Edwards, L. J. *Mixed Models* (2007).

[95] Koerner, T. K. & Zhang, Y. Application of linear mixed-effects models in human neuroscience research: A comparison with pearson correlation in two auditory electrophysiology studies. *Brain Sciences* **7**, 11 (2017).

[96] Venables, W. N. & Ripley, B. D. *Regression and Correlation*, book section 11 (Springer, 2002).

[97] Burnham, K. P. & Anderson, D. R. *Practical Use of the Information-Theoretic Approach* (Springer, 2002).

[98] Burnham, K. P. & Anderson, D. R. *Information and Likelihood Theory*, book section 2 (Springer, 2002).

[99] Andel, J., Perez, M. G. & Negrao, A. I. Estimating the dimension of a linear-model. *Kybernetika* **17**, 514–525 (1981).

[100] Akaike, H. Citation classic - a new look at the statistical-model identification. *Current Contents/Engineering Technology I& Applied Sciences* 22–22 (1981).

[101] Giacalone, G. *et al.* Cerebral time domain-nirs: reproducibility analysis, optical properties, hemoglobin species and tissue oxygen saturation in a cohort of adult subjects. *Biomedical Optics Express* **8**, 4987–5000 (2017).

[102] Gatto, R., Hoffman, W. E., Mueller, M., Paisansathan, C. & Charbel, F. Age effects on brain oxygenation during hypercapnia. *Journal of Biomedical Optics* **12**, 4 (2007).

[103] Mesquida, J. *et al.* Peripheral microcirculatory alterations are associated with the severity of acute respiratory distress syndrome in covid-19 patients admitted to intermediate respiratory and intensive care units. *Critical Care* **25**, 10 (2021).

[104] Varga, Z. *et al.* Endothelial cell infection and endotheliitis in covid-19. *Lancet* **395**, 1417–1418 (2020).

[105] Fernandez, S. *et al.* Distinctive biomarker features in the endotheliopathy of covid-19 and septic syndromes. *Shock* **57**, 95–105 (2022).

[106] Ostergaard, L. Sars cov-2 related microvascular damage and symptoms during and after covid-19: Consequences of capillary transit-time changes, tissue hypoxia and inflammation. *Physiological Reports* **9**, 12 (2021).

[107] Bateman, R. M., Sharpe, M. D., Jagger, J. E. & Ellis, C. G. Sepsis impairs microvascular autoregulation and delays capillary response within hypoxic capillaries. *Critical Care* **19**, 14 (2015).

[108] Cusack, R., Leone, M., Rodriguez, A. H. & Martin-Loeches, I. Endothelial damage and the microcirculation in critical illness. *Biomedicines* **10**, 20 (2022).

[109] Jacob, M., Chappell, D. & Becker, B. F. Regulation of blood flow and volume exchange across the microcirculation. *Critical Care* **20**, 13 (2016).

[110] Skarda, D. E., Mulier, K. E., Myers, D. E., Taylor, J. H. & Beilman, G. J. Dynamic near-infrared spectroscopy measurements in patients with severe sepsis. *Shock* **27**, 348–353 (2007).

[111] Ikonomidis, I. *et al.* Impaired endothelial glycocalyx predicts adverse outcome in subjects without overt cardiovascular disease: a 6-year follow-up study. *Journal of Cardiovascular Translational Research* **15**, 890–902 (2022).

[112] Ikonomidis, I. *et al.* Association of impaired endothelial glycocalyx with arterial stiffness, coronary microcirculatory dysfunction, and abnormal myocardial deformation in untreated hypertensives. *Journal of Clinical Hypertension* **20**, 672–679 (2018).

[113] Zhang, C. E., Staals, J., van Oostenbrugge, R. J. & Vink, H. Uncoupling of microvascular blood flow and capillary density in vascular cognitive impairment. *Frontiers in Neurology* **10**, 6 (2019).

[114] Mitsides, N. *et al.* Extracellular overhydration linked with endothelial dysfunction in the context of inflammation in haemodialysis dependent chronic kidney disease. *Plos One* **12**, 15 (2017).

[115] Ayaz, H. *et al.* Optical imaging and spectroscopy for the study of the human brain: status report. *Neurophotonics* **9**, 65 (2022).

[116] Giovannella, M. *et al.* Validation of diffuse correlation spectroscopy against ¹⁵o-water pet for regional cerebral blood flow measurement in neonatal piglets. *Journal of Cerebral Blood Flow and Metabolism* **40**, 2055–2065 (2020).

[117] Mesquita, R. C. *et al.* Influence of probe pressure on the diffuse correlation spectroscopy blood flow signal: extra-cerebral contributions. *Biomedical Optics Express* **4**, 978–994 (2013).

[118] Baker, W. B. *et al.* Pressure modulation algorithm to separate cerebral hemodynamic signals from extracerebral artifacts. *Neurophotonics* **2**, 20 (2015).

[119] Choi, J. *et al.* Noninvasive determination of the optical properties of adult brain: near-infrared spectroscopy approach. *Journal of Biomedical Optics* **9**, 221–229 (2004).

[120] Verdecchia, K. *et al.* Assessment of a multi-layered diffuse correlation spectroscopy method for monitoring cerebral blood flow in adults. *Biomedical Optics Express* **7**, 3659–3674 (2016).

[121] Wu, J. Y. *et al.* Two-layer analytical model for estimation of layer thickness and flow using diffuse correlation spectroscopy. *Plos One* **17**, 20 (2022).

[122] Hori, H., Moretti, G., Rebora, A. & Crovato, F. Thickness of human scalp - normal and bald. *Journal of Investigative Dermatology* **58**, 396– (1972).

[123] Milej, D. *et al.* Quantification of cerebral blood flow in adults by contrast-enhanced near-infrared spectroscopy: Validation against mri. *Journal of Cerebral Blood Flow and Metabolism* **40**, 1672–1684 (2020).

[124] Doulgerakis, M., Eggebrecht, A. T. & Dehghani, H. High-density functional diffuse optical tomography based on frequency-domain measurements improves image quality and spatial resolution. *Neurophotonics* **6**, 14 (2019).

[125] Schatzel, K. Correlation techniques in dynamic light-scattering. *Applied Physics B-Photophysics and Laser Chemistry* **42**, 193–213 (1987).

[126] Zhou, C. *et al.* Diffuse optical correlation tomography of cerebral blood flow during cortical spreading depression in rat brain. *Optics Express* **14**, 1125–1144 (2006).

[127] Baker, W. B. *et al.* Noninvasive optical monitoring of critical closing pressure and arteriole compliance in human subjects. *Journal of Cerebral Blood Flow and Metabolism* **37**, 2691–2705 (2017).

[128] Tran, A. P., Yan, S. & Fang, Q. Improving model-based functional near-infrared spectroscopy analysis using mesh-based anatomical and light-transport models. *Neurophotonics* **7**, 015008 (2020).

[129] Selb, J. *et al.* Sensitivity of near-infrared spectroscopy and diffuse correlation spectroscopy to brain hemodynamics: simulations and experimental findings during hypercapnia. *Neurophotonics* **1**, 15 (2014).

[130] Brigadoi, S. & Cooper, R. J. How short is short? optimum source-detector distance for short-separation channels in functional near-infrared spectroscopy. *Neurophotonics* **2**, 9 (2015).

[131] Middleton, A. A. & Fisher, D. S. Discrete scatterers and autocorrelations of multiply scattered-light. *Physical Review B* **43**, 5934–5938 (1991).

[132] Ohmae, E. *et al.* Cerebral hemodynamics evaluation by near-infrared time-resolved spectroscopy: Correlation with simultaneous positron emission tomography measurements. *Neuroimage* **29**, 697–705 (2006).

[133] Selb, J., Ogden, T. M., Dubb, J., Fang, Q. Q. & Boas, D. A. Comparison of a layered slab and an atlas head model for monte carlo fitting of time-domain near-infrared spectroscopy data of the adult head. *Journal of Biomedical Optics* **19**, 10 (2014).

[134] Wu, M. M. *et al.* Improved accuracy of cerebral blood flow quantification in the presence of systemic physiology cross-talk using multi-layer monte carlo modeling. *Neurophotonics* **8**, 24 (2021).

[135] Wu, M. M. *et al.* Complete head cerebral sensitivity mapping for diffuse correlation spectroscopy using subject-specific magnetic resonance imaging models. *Biomedical Optics Express* **13**, 1131–1151 (2022).

[136] Ferrari, M. & Quaresima, V. A brief review on the history of human functional near-infrared spectroscopy (fnirs) development and fields of application. *Neuroimage* **63**, 921–935 (2012).

[137] Fantini, S. & Sassaroli, A. Frequency-domain techniques for cerebral and functional near-infrared spectroscopy. *Frontiers in Neuroscience* **14**, 18 (2020).

[138] Fantini, S., Frederick, B. & Sassaroli, A. Perspective: Prospects of non-invasive sensing of the human brain witn diffuse optical imaging. *Apl Photonics* **3**, 15 (2018).

[139] Kienle, A., Glanzmann, T., Wagnieres, G. & van den Bergh, H. Investigation of two-layered turbid media with time-resolved reflectance. *Applied Optics* **37**, 6852–6862 (1998).

[140] Kienle, A. *et al.* Noninvasive determination of the optical properties of two-layered turbid media. *Applied Optics* **37**, 779–791 (1998).

[141] Ripoll, J. *et al.* Recovery of optical parameters in multiple-layered diffusive media: theory and experiments. *Journal of the Optical Society of America a-Optics Image Science and Vision* **18**, 821–830 (2001).

[142] Alexandrakis, G., Farrell, T. J. & Patterson, M. S. Accuracy of the diffusion approximation in determining the optical properties of a two-layer turbid medium. *Applied Optics* **37**, 7401–7409 (1998).

[143] Hielscher, A. H., Liu, H. L., Chance, B., Tittel, F. K. & Jacques, S. L. Time-resolved photon emission from layered turbid media. *Applied Optics* **35**, 719–728 (1996).

[144] Rodriguez, R. C. *Utilizacao da fase para estimativa das propriedades opticas absolutas do tecido biologico com espectroscopia optica de difusao.* Thesis, University of Campinas (2014).

[145] Lee, S. Y., Zheng, C., Brothers, R. & Buckley, E. M. Small separation frequency-domain near-infrared spectroscopy for the recovery of tissue optical properties at millimeter depths. *Biomedical Optics Express* **10**, 5362–5377 (2019).

[146] Sutin, J. *Development of a novel diffuse correlation spectroscopy platform for monitoring cerebral blood flow and oxygen metabolism: from novel concepts and devices to preclinical live animal studies.* Ph. d. thesis, Boston University (2017).

[147] Jonasson, H. *et al.* In vivo characterization of light scattering properties of human skin in the 475-to 850-nm wavelength range in a swedish cohort. *Journal of Biomedical Optics* **23**, 6 (2018).

[148] Auger, H. *et al.* Quantification of extra-cerebral and cerebral hemoglobin concentrations during physical exercise using time-domain near infrared spectroscopy. *Biomedical Optics Express* **7**, 3826–3842 (2016).

[149] Farzam, P. *et al.* Shedding light on the neonatal brain: probing cerebral hemodynamics by diffuse optical spectroscopic methods. *Scientific Reports* **7**, 10 (2017).

[150] Moreau, F., Yang, R., Nambiar, V., Demchuk, A. M. & Dunn, J. F. Near-infrared measurements of brain oxygenation in stroke. *Neurophotonics* **3**, 8 (2016).

[151] Kainerstorfer, J. M., Sassaroli, A., Tgavalekos, K. T. & Fantini, S. Cerebral autoregulation in the microvasculature measured with near-infrared spectroscopy. *Journal of Cerebral Blood Flow and Metabolism* **35**, 959–966 (2015).

[152] Yang, R. Z. & Dunn, J. F. Reduced cortical microvascular oxygenation in multiple sclerosis: a blinded, case-controlled study using a novel quantitative near-infrared spectroscopy method. *Scientific Reports* **5**, 9 (2015).

[153] Milej, D., Abdalmalak, A., Rajaram, A. & St Lawrencea, K. Direct assessment of extracerebral signal contamination on optical measurements of cerebral blood flow, oxygenation, and metabolism. *Neurophotonics* **7**, 17 (2020).

[154] Afshari, A. *et al.* Evaluation of the robustness of cerebral oximetry to variations in skin pigmentation using a tissue-simulating phantom. *Biomedical Optics Express* **13**, 2909–2928 (2022).

[155] Shi, C. H. *et al.* The accuracy of pulse oximetry in measuring oxygen saturation by levels of skin pigmentation: a systematic review and meta-analysis. *Bmc Medicine* **20**, 14 (2022).

[156] Al-Halawani, R., Charlton, P. H., Qassem, M. & Kyriacou, P. A. A review of the effect of skin pigmentation on pulse oximeter accuracy. *Physiological Measurement* **44**, 22 (2023).

[157] Wassenaar, E. B. & Van den Brand, J. G. Reliability of near-infrared spectroscopy in people with dark skin pigmentation. *J Clin Monit Comput* **19**, 195–9 (2005).

[158] Zeballos, R. J. & Weisman, I. M. Reliability of noninvasive oximetry in black subjects during exercise and hypoxia. *American Review of Respiratory Disease* **144**, 1240–1244 (1991).

[159] Barrot, L. *et al.* Liberal or conservative oxygen therapy for acute respiratory distress syndrome. *New England Journal of Medicine* **382**, 999–1008 (2020).

[160] Chu, D. K. *et al.* Mortality and morbidity in acutely ill adults treated with liberal versus conservative oxygen therapy (iota): a systematic review and meta-analysis. *Lancet* **391**, 1693–1705 (2018).

[161] Fawzy, A. *et al.* Racial and ethnic discrepancy in pulse oximetry and delayed identification of treatment eligibility among patients with covid-19. *Jama Internal Medicine* **182**, 730–738 (2022).

[162] Valbuena, V. S. M. *et al.* Racial bias and reproducibility in pulse oximetry among medical and surgical inpatients in general care in the veterans health administration 2013-19: multicenter, retrospective cohort study. *Bmj-British Medical Journal* **378**, 9 (2022).

[163] Mandeville, J. B. *et al.* Evidence of a cerebrovascular postarteriole windkessel with delayed compliance. *Journal of Cerebral Blood Flow and Metabolism* **19**, 679–689 (1999).

[164] Baumbach, G. L. & Heistad, D. D. Remodeling of cerebral arterioles in chronic hypertension. *Hypertension* **13**, 968–972 (1989).

[165] Caughey, A. B. Hidden in plain sight-reconsidering the use of race correction in clinical algorithms. *Obstetrical I& Gynecological Survey* **76**, 5–7 (2021).

[166] Okunlola, O. E. *et al.* Pulse oximeter performance, racial inequity, and the work ahead. *Respiratory Care* **67**, 252–257 (2022).

[167] Ly, B. C. K., Dyer, E. B., Feig, J. L., Chien, A. L. & Del Bino, S. Research techniques made simple: Cutaneous colorimetry: A reliable technique for objective skin color measurement. *Journal of Investigative Dermatology* **140**, 3–+ (2020).

[168] Dognitz, N. & Wagnieres, G. Determination of tissue optical properties by steady-state spatial frequency-domain reflectometry. *Lasers in Medical Science* **13**, 55–65 (1998).

[169] Dognitz, N., Wagnieres, G., Kienle, A. & van den Bergh, H. Determination of the absorption and reduced scattering coefficients of human skin and bladder by spatial frequency domain reflectometry. In *Laser-Tissue Interaction, Tissue Optics, and Laser Welding III Conference*, vol. 3195 of *Proceedings of the Society of Photo-Optical Instrumentation Engineers (Spie)*, 102–109 (Spie-Int Soc Optical Engineering, BELLINGHAM, 1998).

[170] Gioux, S., Mazhar, A. & Cuccia, D. J. Spatial frequency domain imaging in 2019: principles, applications, and perspectives. *Journal of Biomedical Optics* **24**, 18 (2019).

[171] Phan, T. *et al.* Quantifying the confounding effect of pigmentation on measured skin tissue optical properties: a comparison of colorimetry with spatial frequency domain imaging. *Journal of Biomedical Optics* **27**, 14 (2022).

[172] Phan, T. *et al.* Characterizing reduced scattering coefficient of normal human skin across different anatomic locations and fitzpatrick skin types using spatial frequency domain imaging. *Journal of Biomedical Optics* **26**, 11 (2021).

[173] Junior, L. B. d. C. *Optical Characterization of Highly Turbid Samples in the Visible and Near Infrared Spectra.* Thesis, University of Sao Paulo (2023).

[174] Cruz, J., L. B., Girasol, C. E., Coltro, P. S., Guirro, R. R. J. & Bachmann, L. Absorption and reduced scattering coefficient estimation in pigmented human skin tissue by experimental colorimetric fitting. *Journal of the Optical Society of America a-Optics Image Science and Vision* **40**, 1680–1685 (2023).

[175] Modules, S. T. Layers of the skin.

[176] Goldsmith, L. A. *et al. Biology of Pigment Cells*, book section 7 (McGraw-Hill Education, 2019).

[177] Betts, J. G. *et al. The Integumentary System*, book section 5 (OpenStax, Rice University, 2013).

[178] Joly-Tonetti, N., Wibawa, J. I. D., Bell, M. & Tobin, D. J. An explanation for the mysterious distribution of melanin in human skin: a rare example of asymmetric (melanin) organelle distribution during mitosis of basal layer progenitor keratinocytes. *British Journal of Dermatology* **179**, 1115–1126 (2018).

[179] Le Roux, P. Physiological monitoring of the severe traumatic brain injury patient in the intensive care unit. *Current Neurology and Neuroscience Reports* **13**, 16 (2013).

[180] Tzeng, Y. C. & Ainslie, P. N. Blood pressure regulation ix: cerebral autoregulation under blood pressure challenges. *European Journal of Applied Physiology* **114**, 545–559 (2014).

[181] Jones-Muhammad, M. & Warrington, J. P. Cerebral blood flow regulation in pregnancy, hypertension, and hypertensive disorders of pregnancy. *Brain Sciences* **9**, 15 (2019).

[182] Donnelly, J., Budohoski, K. P., Smielewski, P. & Czosnyka, M. Regulation of the cerebral circulation: bedside assessment and clinical implications. *Critical Care* **20**, 17 (2016).

[183] Schmidt, J. M. *et al.* Cerebral perfusion pressure thresholds for brain tissue hypoxia and metabolic crisis after poor-grade subarachnoid hemorrhage. *Stroke* **42**, 1351–1356 (2011).

[184] Samria, R. *et al.* Noninvasive cuffless estimation of blood pressure using photoplethysmography without electrocardiograph measurement. *2014 Ieee Region 10 Symposium* 254–257 (2014).

[185] Kirkman, M. A. & Smith, M. Intracranial pressure monitoring, cerebral perfusion pressure estimation, and icp/cpp-guided therapy: a standard of care or optional extra after brain injury? *British Journal of Anaesthesia* **112**, 35–46 (2014).

[186] Canac, N., Jalaleddini, K., Thorpe, S. G., Thibeault, C. M. & Hamilton, R. B. Review: pathophysiology of intracranial hypertension and noninvasive intracranial pressure monitoring. *Fluids and Barriers of the Cns* **17**, 21 (2020).

[187] Dewey, R. C., Pieper, H. P. & Hunt, W. E. Experimental cerebral hemodynamics - vasomotor tone, critical closing pressure, and vascular bed resistance. *Journal of Neurosurgery* **41**, 597–606 (1974).

[188] Weyland, A. *et al.* Cerebrovascular tone rather than intracranial pressure determines the effective downstream pressure of the cerebral circulation in the absence of intracranial hypertension. *Journal of Neurosurgical Anesthesiology* **12**, 210–216 (2000).

[189] Maas, J. J., de Wilde, R. B., Aarts, L. P., Pinsky, M. R. & Jansen, J. R. Determination of vascular waterfall phenomenon by bedside measurement of mean systemic filling pressure and critical closing pressure in the intensive care unit. *Anesthesia and Analgesia* **114**, 803–810 (2012).

[190] Yonas, H. & Pindzola, R. R. Physiological determination of cerebrovascular reserves and its use in clinical management. *Cerebrovascular and Brain Metabolism Reviews* **6**, 325–340 (1994).

[191] Kaczmarska, K. *et al.* Critical closing pressure during controlled increase in intracranial pressure-comparison of three methods. *Ieee Transactions on Biomedical Engineering* **65**, 619–624 (2018).

[192] Varsos, G. V. *et al.* A noninvasive estimation of cerebral perfusion pressure using critical closing pressure. *Journal of Neurosurgery* **123**, 638–648 (2015).

[193] Lopez-Magana, J. A. *et al.* Critical closing pressure: comparison of three methods. *Journal of Cerebral Blood Flow and Metabolism* **29**, 987–993 (2009).

[194] Elizondo, L. *Critical Closing Pressure by Diffuse Correlation Spectroscopy in a Neonatal Piglet Model* (Springer, Cham, 2021).

[195] Lafontant, A. *et al.* Comparison of optical measurements of critical closing pressure acquired before and during induced ventricular arrhythmia in adults. *Neurophotonics* **9**, 11 (2022).

[196] Westerhof, N., Lankhaar, J. W. & Westerhof, B. E. The arterial windkessel. *Medical I& Biological Engineering I& Computing* **47**, 131–141 (2009).

[197] Varsos, G. V. *et al.* Critical closing pressure determined with a model of cerebrovascular impedance. *Journal of Cerebral Blood Flow and Metabolism* **33**, 235–243 (2013).

APPENDIX A

AUXILIARY STEPS FOR CHAPTER 2

A.1 Section 1

Since L is a function of $\hat{\Omega}$, t, and $\vec{r} = (r_1, r_2, r_3)$, where r_n are the components of $\vec{r}$ in a coordinate system, the infinitesimal change over the radiance when it travels a distance dr at a specific (and fixed) direction $\hat{\Omega}$ is:

$$dL = \frac{\partial L}{\partial t}dt + \sum_i \frac{\partial L}{\partial r_i}dr_i = \frac{\partial L}{\partial t}dt + \vec{\nabla}L \cdot d\vec{r} = \frac{\partial L}{\partial t}dt + v\,dt\,\hat{\Omega}\cdot\vec{\nabla}L. \tag{A.1}$$

Here, $d\vec{r} = dr\hat{r} = v\,dt\hat{\Omega}$, where $v = c/n$ is the speed of light in the medium with refractive index n. From now on, we will omit the redundant dependences over the variables. We will also assume v as a constant to avoid writing $v = v(\vec{r}, t)$. However, this is not a significant restrictive condition since the RTE is still valid if v is constant between two scattering events and independent of $\hat{\Omega}$.

In the medium, radiance may decrease by absorption and scattering events through dr, and it may also increase due to scatterings resulting in a photon traveling at $\hat{\Omega}$. Also, let's denote $Q(\vec{r}, \hat{\Omega}, t)$ as the power emitted per unit of volume by the sources at $\vec{r}$ in the $\hat{\Omega}$ direction at time t. Numerically speaking:

$$dL = -\mu_a L(\hat{\Omega})\,dr - \mu_s \int_{\hat{\Omega}^*} L(\hat{\Omega}) f(\hat{\Omega}, \hat{\Omega}')d\Omega' dr + \mu_s \int_{\hat{\Omega}^*} f(\hat{\Omega}', \hat{\Omega}) L(\hat{\Omega}')d\Omega' dr + Q(\vec{r}, \hat{\Omega}, t)dr,$$

where $f(\hat{\Omega}, \hat{\Omega}')$ is the normalized differential cross-section, i.e., the probability of a certain photon traveling at the $\hat{\Omega}'$, ends up traveling at the $\hat{\Omega}$ direction after a scattering event. $\hat{\Omega}^*$ denotes that the integral is over all $\hat{\Omega}'$ except $\hat{\Omega}$. Now, let's sum and subtract the term $\mu_s L(\hat{\Omega}) f(\hat{\Omega}, \hat{\Omega}) d\Omega dr$ to the right side of the previous equation. Grouping the negative term with the second term on the right side, we have:

$$-\mu_s \int_{\hat{\Omega}^*} L(\hat{\Omega}) f(\hat{\Omega},\hat{\Omega}^{'}) d\Omega^{'} dr - \mu_s L(\hat{\Omega}) f(\hat{\Omega},\hat{\Omega}) d\hat{\Omega} dr =$$
$$-\mu_s L(\hat{\Omega}) \left(\int_{\hat{\Omega}^*} f(\hat{\Omega},\hat{\Omega}^{'}) d\Omega^{'} dr + f(\hat{\Omega},\hat{\Omega}) d\hat{\Omega} dr \right) =$$
$$-\mu_s L(\hat{\Omega}) \left(\int_{4\pi} f(\hat{\Omega},\hat{\Omega}^{'}) d\Omega^{'} dr \right) = -\mu_s L(\hat{\Omega})\, v\, dt.$$

Using the same logic, grouping the positive term with the third term makes the integral sum over all 4π steradians. Thus:

$$dL = -(\mu_a + \mu_s) L(\hat{\Omega})\, v\, dt + \mu_s \int_{4\pi} L(\vec{r},\hat{\Omega}^{'},t) f(\hat{\Omega},\hat{\Omega}^{'}) d\Omega^{'}\, v\, dt + Q(\vec{r},\hat{\Omega},t) dr. \tag{A.2}$$

By making Equation A.1 equal to Equation A.2 and dividing all terms by $dr = v\, dt$, we obtain the RTE:

$$\frac{1}{v}\frac{\partial L}{\partial t} + \hat{\Omega}\cdot\vec{\nabla} L = -(\mu_a + \mu_s) L + Q(\vec{r},\hat{\Omega},t) + \mu_s \int_{4\pi} L(\vec{r},\hat{\Omega}^{'},t) f(\hat{\Omega},\hat{\Omega}^{'}) d\Omega^{'}. \tag{A.3}$$

A.2 Section 2

For biological tissue, the radiance is nearly isotropic, so we can expand L using a spherical harmonics basis:

$$L(\vec{r},\hat{\Omega},t) = \sum_{l=0}^{N} \sum_{m=-l}^{l} \sqrt{\frac{2l+1}{4\pi}} \phi_{lm}(\vec{r},t)\, Y_{lm}(\hat{\Omega}),$$

and keep only the terms up to $N = 1$, obtaining:

$$L(\vec{r},\hat{\Omega},t) = \frac{1}{\sqrt{4\pi}} \phi_{00} Y_{00} + \sqrt{\frac{3}{4\pi}} \left(\phi_{1-1} Y_{1-1} + \phi_{10} Y_{10} + \phi_{11} Y_{11} \right).$$

Using the definition of Y_{lm}, the equation above becomes:

$$L(\vec{r},\hat{\Omega},t) = \frac{1}{4\pi}\phi_{00} + \frac{3}{4\pi}\left(\frac{1}{\sqrt{2}} \phi_{1-1} sin\theta e^{-i\varphi} + \phi_{10} cos\theta - \frac{1}{\sqrt{2}} \phi_{11} sin\theta e^{i\varphi} \right).$$

Defining $\phi_{00} \equiv \phi(\vec{r},t)$ as a quantity independent of orientation, and writing the complex exponentials as trigonometric functions:

$$L(\vec{r},\hat{\Omega},t) = \frac{1}{4\pi}\phi(\vec{r},t) + \frac{3}{4\pi}\left(\frac{1}{\sqrt{2}}sin\theta cos\varphi(\phi_{1-1}-\phi_{11}) - \frac{i}{\sqrt{2}}sin\theta sin\varphi(\phi_{1-1}+\phi_{11}) + cos\theta\phi_{10}\right).$$

Now, writing that $sin\theta cos\varphi = \hat{\Omega}\cdot\hat{x}$, $sin\theta sin\varphi = \hat{\Omega}\cdot\hat{y}$ e $cos\theta = \hat{\Omega}\cdot\hat{z}$, the equation becomes:

$$L(\vec{r},\hat{\Omega},t) = \frac{1}{4\pi}\phi(\vec{r},t) + \frac{3}{4\pi}\left(\frac{1}{\sqrt{2}}(\phi_{1-1}-\phi_{11})\hat{x} - \frac{i}{\sqrt{2}}(\phi_{1-1}+\phi_{11})\hat{y} + \phi_{10}\hat{z}\right)\cdot\hat{\Omega}.$$

Defining $\vec{J}(\vec{r},t) \equiv \frac{1}{\sqrt{2}}(\phi_{1-1}-\phi_{11})\hat{x} - \frac{i}{\sqrt{2}}(\phi_{1-1}+\phi_{11})\hat{y} + \phi_{10}\hat{z}$, finally:

$$L(\vec{r},\hat{\Omega},t) = \frac{1}{4\pi}\phi(\vec{r},t) + \frac{3}{4\pi}\vec{J}(\vec{r},t)\cdot\hat{\Omega} \equiv L_1(\vec{r},\hat{\Omega},t). \tag{A.4}$$

A.3 Section 3

As $\vec{J}(\vec{r},t)$ and $\phi(\vec{r},t)$ come from L, there must be a relation between them. By integrating Equation 2.2 over all solid angles, we have:

$$\frac{1}{v}\frac{\partial}{\partial t}\int L\,d\Omega + \int \hat{\Omega}\cdot\vec{\nabla}L\,d\Omega = -\int(\mu_a+\mu_s)L d\Omega + \int Q(\vec{r},\hat{\Omega},t)\,d\Omega + \int\mu_s\int L(\vec{r},\hat{\Omega},t)f(\hat{\Omega},\hat{\Omega}')\,d\Omega' d\Omega.$$

We can now make two assumptions. The first one is that μ_a and μ_s are independent of $\hat{\Omega}$. The second is that $f(\hat{\Omega},\hat{\Omega}') = f(\hat{\Omega}\cdot\hat{\Omega}')$, i.e., $f(\hat{\Omega},\hat{\Omega}')$ depends only on the angle between $\hat{\Omega}$ and $\hat{\Omega}'$. In practice, these approximations hold for cases where the medium is symmetrical by rotations at a length of $\sim \ell_s, \ell_a$, where the next interaction will occur. Note that both assumptions are similar and usually work well for biological tissue.

To continue, let's assume that $\hat{\Omega} = \hat{z}$, so we can solve the previous equation using spherical coordinates. This is a reasonable approach since the equation is integrated over all $\hat{\Omega}'$. Thus, $\hat{\Omega}\cdot\hat{\Omega}' = cos\theta'$ and $\int f(\hat{\Omega}\cdot\hat{\Omega}')\,d\Omega' = \int f(cos\theta')\,d\Omega' = 1$, since f is a normalized function. Therefore:

$$\int L(\vec{r},\hat{\Omega},t)\left(\int f(\hat{\Omega}\cdot\hat{\Omega}')\,d\Omega'\right)d\Omega = \int L(\vec{r},\hat{\Omega},t)\,d\Omega = \phi(\vec{r},t).$$

The integral of the *RTE* over all solid angles results in:

$$\frac{1}{v}\frac{\partial\phi}{\partial t} + \int\hat{\Omega}\cdot\vec{\nabla}L\,d\Omega = -(\mu_a+\mu_s)\phi + \int Q(\vec{r},\hat{\Omega},t)\,d\Omega + \mu_s\phi.$$

Defining the power per unit of volume emitted radially outside the infinitesimal volume in $\vec{r}$ at time t as $\int Q(\vec{r},\hat{\Omega},t)\,d\Omega \equiv S(\vec{r},t)$:

$$S(\vec{r},t) = \frac{1}{v}\frac{\partial\phi}{\partial t} + \mu_a\phi + \int \hat{\Omega}\cdot\vec{\nabla}L\,d\Omega.$$

On the other hand, the divergence of $\vec{J}$ is:

$$\vec{\nabla}\cdot\vec{J} = \vec{\nabla}\cdot\int L\hat{\Omega}\,d\Omega = \int\left(\vec{\nabla}L\cdot\hat{\Omega} + L\vec{\nabla}\cdot\hat{\Omega}\right)d\Omega = \int \vec{\nabla}L\cdot\hat{\Omega}\,d\Omega,$$

since $\vec{\nabla}\cdot\hat{\Omega} = 0$. Finally:

$$S(\vec{r},t) = \frac{1}{v}\frac{\partial\phi}{\partial t} + \mu_a\phi + \vec{\nabla}\cdot\vec{J}. \tag{A.5}$$

Taking L as L_1 in the *RTE*, i.e., using Equation 2.3 in Equation 2.2, results in

$$\frac{1}{v}\frac{\partial}{\partial t}\left(\frac{1}{4\pi}\phi + \frac{3}{4\pi}\vec{J}\cdot\hat{\Omega}\right) + \hat{\Omega}\cdot\vec{\nabla}\left(\frac{1}{4\pi}\phi + \frac{3}{4\pi}\vec{J}\cdot\hat{\Omega}\right) =$$
$$-(\mu_a+\mu_s)\left(\frac{1}{4\pi}\phi + \frac{3}{4\pi}\vec{J}\cdot\hat{\Omega}\right) + Q(\vec{r},\hat{\Omega},t) + \mu_s\int_{4\pi}\left(\frac{1}{4\pi}\phi + \frac{3}{4\pi}\vec{J}\cdot\hat{\Omega}'\right)f(\hat{\Omega},\hat{\Omega}')\,d\Omega'.$$

Multiplying both sides by $\hat{\Omega}$, integrating over all solid angles, and using the fact that, for any vector $\vec{V}$,

i) $\int \hat{\Omega}\,d\Omega = \vec{0}$,

ii) $\int(\vec{V}\cdot\hat{\Omega})\hat{\Omega}\,d\Omega = \frac{4\pi}{3}\vec{V}$, and

iii) $\int \hat{\Omega}[\hat{\Omega}\cdot\left(\vec{\nabla}(\vec{V}\cdot\hat{\Omega})\right)]\,d\Omega = \vec{0}$,

the approximation becomes:

$$\frac{1}{v}\frac{\partial\vec{J}}{\partial t} + \frac{1}{3}\vec{\nabla}\phi = -(\mu_a+\mu_s)\vec{J} + \int Q(\vec{r},\hat{\Omega},t)\hat{\Omega}\,d\Omega$$
$$+\frac{\mu_s}{4\pi}\left[\phi\int\left(\int f(\hat{\Omega}\cdot\hat{\Omega}')\,d\Omega'\right)\hat{\Omega}\,d\Omega + 3\int\left(\int(\vec{J}\cdot\hat{\Omega}')f(\hat{\Omega}\cdot\hat{\Omega}')\,d\Omega'\right)\hat{\Omega}\,d\Omega\right].$$

Since f is normalized, the second to last term on the right side vanishes. For the last one, we again take $\hat{\Omega} = \hat{z}$ to solve it in spherical coordinates. Thus:

$$\int(\vec{J}\cdot\hat{\Omega}')f(\hat{\Omega}\cdot\hat{\Omega}')\,d\Omega' =$$
$$\int f(cos\theta')[sin\theta' cos\phi' J_x + sin\theta' sin\phi' J_y + cos\theta' J_z]sin\theta' d\theta' d\phi' =$$
$$\int f(cos\theta')cos\theta' J_z\,d\Omega' = J_z\int f(cos\theta')cos\theta'\,d\Omega' \equiv g J_z,$$

where $g \equiv \int f(cos\theta')cos\theta' d\Omega' = \langle cos\theta \rangle$ is the *anisotropic factor*. The closer g is to 1, the greater the probability that the photon will travel in a direction close to the incident one after a scattering event. However, since $\hat{z}$ is an arbitrary direction, the previous calculations show that the component of $\vec{J}$ that survives the integration is the one parallel to $\hat{\Omega}$, $\vec{J} \cdot \hat{\Omega}$. Therefore, the last term is $3g \int (\vec{J} \cdot \hat{\Omega})\hat{\Omega} d\Omega = 4\pi g \vec{J}$, and approximating L by L_1 results in:

$$\frac{1}{v}\frac{\partial \vec{J}}{\partial t} + \frac{1}{3}\vec{\nabla}\phi = -(\mu_a + \mu_s)\vec{J} + \int Q(\vec{r}, \hat{\Omega}, t)\hat{\Omega}\, d\Omega + \frac{\mu_s}{4\pi}[4\pi g \vec{J}] \Rightarrow$$

$$\vec{\nabla}\phi = -\frac{3}{v}\frac{\partial \vec{J}}{\partial t} - 3(\mu_a + \mu_s)\vec{J} + 3\int Q(\vec{r}, \hat{\Omega}, t)\hat{\Omega}\, d\Omega + 3\mu_s g \vec{J}.$$

At this point, we will assume isotropic sources, $Q(\vec{r}, \hat{\Omega}, t) = Q(\vec{r}, t)$, and slow temporal variation, $\frac{3\partial \vec{J}}{v\partial t} << 3(\mu_a + \mu_s - g\mu_s)\vec{J}$:

$$\vec{\nabla}\phi = -3(\mu_a + \mu_s)\vec{J} + 3\mu_s g \vec{J}.$$

APPENDIX B

EXTRAPOLATED-ZERO BOUNDARY CONDITION

Usually, we assume that a non-scattering medium, usually air, involves the turbid medium under study. Thus, rarely do photons that leave the medium enter again since their direction of propagation remains approximately constant. As DOS assumes sources at a distance ℓ_{tr} inside the medium, the radiance that enters at some specific location on the interface must be due to reflections of the light trying to escape (see Figure B.1). For simplicity, we will assume the refraction index of the outside medium as $n_{out} = 1$ and let n be the index of the turbid media. If this is not the case, assume n as the ratio between the refraction indexes.

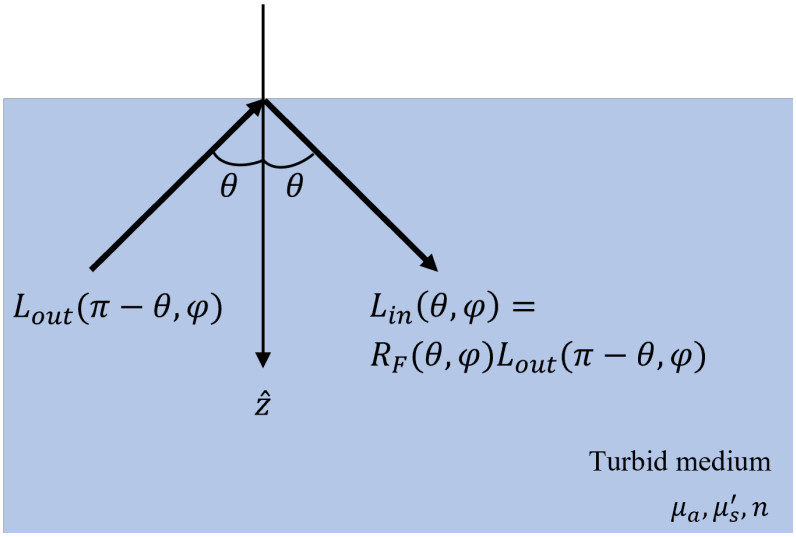

Figure B.1: Illustration of internal reflection of the radiance in an interface.

In terms of the flux, the radiance entering the medium in a given interface position is:

$$J = \int L_{in}(\hat{\Omega}) \hat{\Omega} d\Omega \cdot \hat{z} = \int R_F(\hat{\Omega}) L_{out}(\hat{\Omega}) \hat{\Omega} d\Omega \cdot (-\hat{z}),$$

where $R_F(\hat{\Omega})$ is the Fresnel reflection coefficient. Using Equation 2.3 on the left side of the previous equation:

$$J = \int_0^{\frac{\pi}{2}} \int_0^{\frac{\pi}{2}} \left(\frac{\phi}{4\pi} + \frac{3\vec{J}}{4\pi} \cdot \hat{\Omega} \right) \hat{\Omega} \cdot \hat{z} \, sin\theta d\varphi d\theta =$$

$$\int_0^{\frac{\pi}{2}}\int_0^{\frac{\pi}{2}}\left(\frac{\phi}{4\pi}+\frac{3\vec{J}}{4\pi}\cdot(sin\theta cos\varphi\hat{x}+sin\theta sin\varphi\hat{y}+cos\theta\hat{z})\right)cos\theta sin\theta d\varphi d\theta \Rightarrow$$

$$J=\frac{\phi}{4}+\frac{J_z}{2}, \tag{B.1}$$

where $J_z=\vec{J}\cdot\hat{z}$. Similarly, using the right side:

$$J=\int_0^{\frac{\pi}{2}}\int_0^{\frac{\pi}{2}}R_F(\theta)L(\pi-\theta,\varphi)(-cos(\pi-\theta))sin(\phi-\theta)d\varphi d\theta =$$

$$\int_0^{\frac{\pi}{2}}\int_0^{\frac{\pi}{2}}R_F(\theta)\left(\frac{\phi}{4\pi}-\frac{3J_z}{4\pi}cos\theta\right)cos\theta sin\theta d\varphi d\theta \Rightarrow$$

$$J=R_\phi\frac{\phi}{4}-R_J\frac{J_z}{2}, \tag{B.2}$$

where:

$$R_\phi\equiv\int_0^{\frac{\pi}{2}}2sin\theta cos\theta R_F(\theta)d\theta;$$

$$R_J\equiv\int_0^{\frac{\pi}{2}}3sin\theta cos^2\theta R_F(\theta)d\theta.$$

To remember, for unpolarized light where the medium has a higher refraction index than the outside, $R_F(\theta)=1$ if $\theta_c\leq\theta\leq\pi/2$, where θ_c is the critical angle ($nsin\theta_c=1$), and:

$$R_F(\theta)=\frac{1}{2}\left(\frac{ncos\theta^{'}-cos\theta}{ncos\theta^{'}+cos\theta}\right)^2+\frac{1}{2}\left(\frac{ncos\theta-cos\theta^{'}}{ncos\theta+cos\theta^{'}}\right)^2,$$

if $0\leq\theta\leq\theta_c$. Here, $\theta^{'}$ is such that $nsin\theta=sin\theta^{'}$. Merging Equation B.1 and Equation B.2:

$$\phi=-2\frac{1+R_{eff}}{1-R_{eff}}J_z,$$

where $R_{eff}\equiv(R_\phi+R_J)/(2-R_\phi+R_J)$. Using 2.6 in the previous equation, we obtain:

$$\phi=\frac{2}{3\ell_{tr}}\frac{1+R_{eff}}{1-R_{eff}}\frac{\partial\phi}{\partial z}\equiv z_b\frac{\partial\phi}{\partial z}, \tag{B.3}$$

since $\partial\phi/\partial z=(\vec{\nabla}\phi)_z$. Here,

$$z_b=\frac{2}{3}\frac{1}{\ell_{tr}}\frac{1+R_{eff}}{1-R_{eff}}. \tag{B.4}$$

As the integral evaluated so far was over 2π steradians instead of 4π, the boundary condition described in Equation B.3 is known as *partial-flux boundary condition.* However, it is hard to obtain analytical solutions for Equation 2.9 using this condition. An alternative to this condition involves expanding ϕ at the interface. Assuming a linear approximation as the outside medium is not as scattering as the inside:

$$\phi(z) \approx \phi(0) + \left.\frac{\partial \phi}{\partial z}\right|_{z=0} z.$$

Using B.3:

$$\phi(z) = \phi(0) + \frac{\phi(0)}{z_b} z,$$

which means that:

$$\phi(-z_b) = 0. \tag{B.5}$$

This condition is known as *extrapolated-zero boundary condition*.

APPENDIX C

OBTAINING THE $G_1(s_n, z, \omega)$ FUNCTION FOR THE LAYERED MODEL

Now, our problem is illustrated in Figure C.1 based on Liemert's paper [29]. As data acquisition is performed on the first layer (surface), we want to solve the Photon Diffusion Model in the region $0 \leq z \leq l_1$, finding ϕ_1. The steps shown in the paper lead to the solution of layer k:

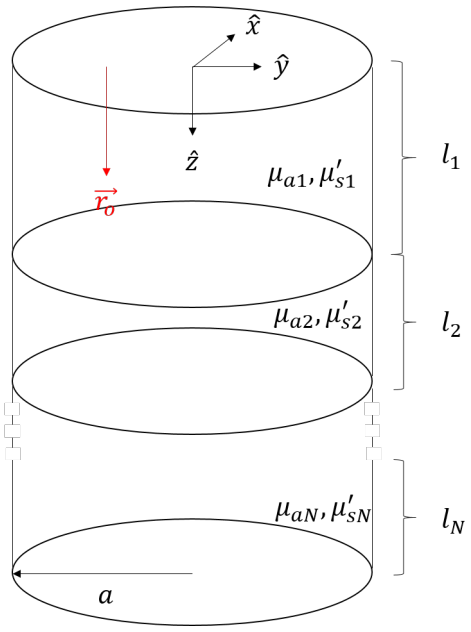

Figure C.1: Scheme of the layered cylinder geometry

$$\phi_k(\varphi, \rho) = \frac{1}{\pi(a')^2} \sum_{n=1}^{\infty} G_k(s_n, z, \omega) \frac{J_0(s_n \rho)}{J^2_{m+1}(a' s_n)}, L_{k-1} \leq z \leq L_k,$$

where $L_k = l_1 + l_2 + \cdots + l_k$, $a' = a + z_{bk}$, J is the Bessel function and $a' s_n$ is the nth root of J. As there are only sources in the first layer, the paper discuss that we can write that G is the solution of:

$$\frac{\partial^2 G_1(s_n, z, \omega)}{\partial z^2} - \alpha_1^2 G_1(s_n, z, \omega) = -\frac{1}{D_1} \delta(z - z_o), 0 \leq z \leq l_1 \tag{C.1}$$

$$\frac{\partial^2 G_k(s_n, z, \omega)}{\partial z^2} - \alpha_k^2 G_k(s_n, z, \omega) = 0, k \neq 1, L_{k_1} \leq z \leq L_k \tag{C.2}$$

where $D_k = \frac{1}{3\mu'_{sk}}$ and

$$\alpha_k^2 \equiv s_n^2 + \frac{\mu_{ak}}{D_k} + \frac{i\omega}{D_k c}.$$

Let's solve equation C.1 first. We know that a G_1 solution is a linear combination of a homogeneous and a particular solution. I will first find the particular solution. In other words, let's solve:

$$\frac{\partial^2 G(s_n, z, \omega)}{\partial z^2} - \alpha^2 G(s_n, z, \omega) = -\frac{1}{D}\delta(z - z_o)$$

where we omit the subindex 1. Performing a Fourier transformation:

$$\int_{-\infty}^{\infty} \frac{\partial^2 G(s_n, z, \omega)}{\partial z^2} e^{-ikz} dz - \alpha^2 \int_{-\infty}^{\infty} G(s_n, z, \omega) e^{-ikz} dz =$$

$$-\frac{1}{D}\int_{-\infty}^{\infty} \delta(z - z_o) e^{-ikz} dz \Rightarrow$$

$$-\int_{-\infty}^{\infty} (-ik) \frac{\partial G(s_n, z, \omega)}{\partial z} e^{-ikz} dz - \alpha^2 \tilde{G} = -\frac{1}{D} e^{-ikz_o} \Rightarrow$$

$$-ik\int_{-\infty}^{\infty} (-ik) G e^{ikz} dz - \alpha^2 \tilde{G} = -\frac{e^{-ikz_o}}{D} \Rightarrow$$

$$-k^2 \tilde{G} - \alpha^2 \tilde{G} = -\frac{e^{-ikz_o}}{D} \Rightarrow$$

$$\tilde{G} = \frac{1}{D}\frac{e^{-ikz_o}}{\alpha^2 + k^2} \tag{C.3}$$

where we can find G through the inverse Fourier transform of C.3:

$$G(z) = \frac{1}{2\pi D}\int_{-\infty}^{\infty} \frac{e^{-ikz_o}}{\alpha^2 + k^2} e^{ikz} dk \Rightarrow$$

$$G^p(z) = \frac{1}{2\pi D}\int_{-\infty}^{\infty} \frac{e^{ik(z - z_o)}}{\alpha^2 + k^2} dk \tag{C.4}$$

where p denotes that it is a particular solution. Now, let's evaluate:

$$I = \int_{-\infty}^{\infty} \frac{e^{ik(z - z_o)}}{\alpha^2 + k^2} dk = \int_{-\infty}^{\infty} \frac{e^{ik(z - z_o)}}{(k + i\alpha)(k - i\alpha)} dk$$

To this end, we must use the complex plane, as illustrated in Figure C.2, writing $k = Re_k + iIm_k$ as a complex number. The poles are located at $k = \pm i\alpha$. We must split the solution into two cases to properly solve the problem.

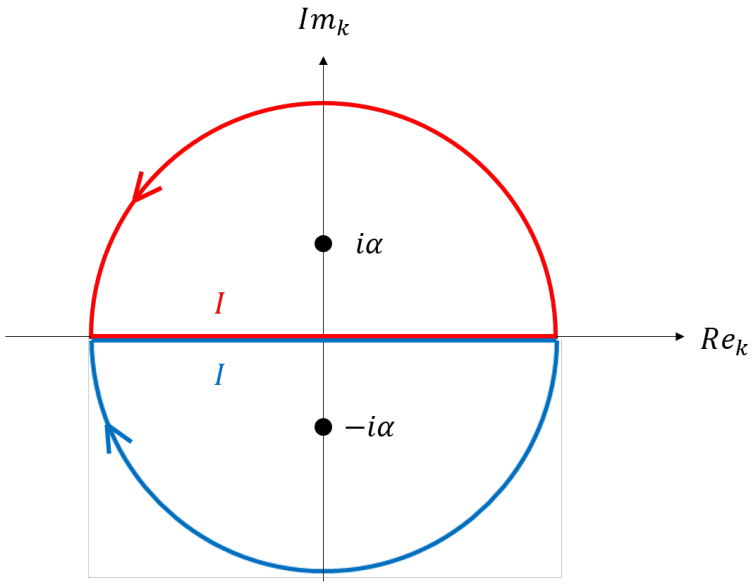

Figure C.2: Complex plane used for integral evaluation. Note the presence of poles and paths used.

i) $z > z_o$

The exponential on integrating becomes:

$$e^{((z-z_o)i(Re_k+iIm_k)} = e^{((z-z_o)(iRe_k-Im_k))}.$$

The absolute value of this term is $exp(-(z-z_o)Im_k)$. As $z-z_o > 0$ in this case, we must have $Im_k > 0$, so the integral does not diverge for large Im_k. Thus, I will use the residue theorem over the red (r) path in Figure C.2. This path can be separated into the original integral I and the red semicircle (scr). So:

$$\oint_r = I + \int_{scr} = 2\pi i \sum_j Res_j,$$

where Res_j is the j-th residue of the integrating inside the red path. To properly evaluate I, I must let $Im_k \to \infty$, i.e., assume the radius of scr goes to ∞. In this limit, the integral over scr goes to zero according to Jordan's theorem.

The general expression to evaluate a n-th order residue at the pole x_o is:

$$Res^{(n)}_{x_o} f(x) = \lim_{x \to x_o} \frac{1}{(n-1)!} \frac{d^{n-1}}{dx^{n-1}} \{(x-x_o)^n f(x)\}.$$

So, the residue at $k = i\alpha$ is:

$$Res = \lim_{k \to i\alpha} (k - i\alpha) \frac{e^{ik(z-z_o)}}{(k+i\alpha)(k-i\alpha)} = \frac{e^{-\alpha(z-z_o)}}{2i\alpha},$$

thus:

$$I = \frac{2\pi i}{2i\alpha} e^{-\alpha(z-z_o)} \Rightarrow$$

$$I = \frac{\pi}{\alpha} e^{-\alpha|z-z_o|}, \tag{C.5}$$

as $|z - z_o| = (z - z_o)$.

ii) $z < z_o$

The integrating exponential becomes:

$$e^{((z-z_o)i(Re_k+iIm_k))} = e^{((z-z_o)(iRe_k-Im_k))}.$$

The absolute value is $exp(-(z-z_o)Im_k)$. As $z - z_o < 0$, we must have $Im_k < 0$, so the integral does not diverge for a large Im_k limit. Thus, I will use the residue theorem over the blue (b) path in Figure C.2. This path can be split into the original integral I and the blue semicircle (scb). So:

$$\oint_b = I + \int_{scb} = -2\pi i \sum_j Res_j,$$

since now the integration is clockwise. To recover I properly, I must once more let $Im_k \to \infty$, which makes the semicircle radius large enough so that the integral over scb goes to zero according to Jordan's theorem. The residue at $k = -i\alpha$ is:

$$Res = \lim_{k \to -i\alpha} (k + i\alpha) \frac{e^{ik(z-z_o)}}{(k+i\alpha)(k-i\alpha)} = -\frac{e^{\alpha(z-z_o)}}{2i\alpha},$$

so:

$$I = \frac{2\pi i}{2i\alpha} e^{\alpha(z-z_o)} \Rightarrow$$
$$I = \frac{\pi}{\alpha} e^{-\alpha|z-z_o|} \tag{C.6}$$

as $|z - z_o| = -(z - z_o)$.

As I on both conditions are the same, we can use C.5 or C.6 to write:

$$G_1^p = \frac{e^{-\alpha_1|z-z_o|}}{2D_1\alpha_1}, \tag{C.7}$$

where I put back the subindex 1.

The next step is to find the homogeneous contribution of the solution. All homogeneous equations for G are essentially the same regardless of the layer:

$$\frac{\partial^2 G_k^h}{\partial z^2} - \alpha_k^2 G_k^h = 0 \Rightarrow$$

$$G_k^h = A_k e^{\alpha_k z} + B_k e^{-\alpha_k z}, \tag{C.8}$$

where h denotes a homogeneous solution. Finally, using C.7 and C.8, we can write all solutions for each layer:

$$G_1(s_n, \omega, z) = A_1 e^{\alpha_1 z} + B_1 e^{-\alpha_1 z} + \frac{e^{-\alpha_1 |z - z_o|}}{2D_1 \alpha_1}, 0 \leq z \leq l_1 \tag{C.9}$$

$$G_k(s_n, \omega, z) = A_k e^{\alpha_k z} + B_k e^{-\alpha_k z}, k > 1, L_{k-1} \leq z \leq L_k \tag{C.10}$$

The constants A_k and B_k are yet to be determined. There are four kinds of boundary conditions to find all free constants. The first two are related to the extrapolated-zero fluency boundary condition of the first and last layer:

1) $G_1(z = -zb_1) = 0$**;**

2) $G_N(z = L_k + zb_N) = 0$**;**

The third is related to the flux continuity at the interface between two layers:

3) $D_k \frac{\partial G_k}{\partial z}(z = L_k) = D_{k+1} \frac{\partial G_{k+1}}{\partial z}(z = L_k)$;

And the last is related to the fluency continuity at the interface between two layers:

4) $n_{k+1}^2 G_k(z = L_k) = n_k^2 G_{k+1}(z = L_k)$

With Equations C.7, C.8 and these four boundary conditions, the constants provided in the paper can be determined. For the two-layer model, k ranges up to 2, so there are only four constants to be found (A_1, B_1, A_2, and B_2), yet only two constants are of interest (A_1 and B_1).

APPENDIX D

ALTERNATIVE GEOMETRIES WHERE I SOLVED THE PHOTON DIFFUSION MODEL

In this appendix, I aim to exhibit the highlights of the alternative solutions I developed for the Photon Diffusion Model. Figure D.1 illustrates the two geometries I approached. In this figure, variables with subindex *o* are related to source location, while the superindex * refers to the extrapolated-zero boundary condition surfaces (refer to Appendix B). The first one (Figure D.1a) is a homogeneous sphere, where I aimed to obtain an analytical equation that takes into account the curvature at the acquisition interface. The second (Figure D.1b) is a composition of a cylinder and a cylinder shell. Here, my goal was to obtain a model that simultaneously accounts for tissue heterogeneity and curvature. For this second solution, I thank a lot Professor Jayme Vaz for the help and meaningful discussions. Unfortunately, both solutions I achieved are not numerically robust, which makes me use a numerical model to solve the forward/inverse problem.

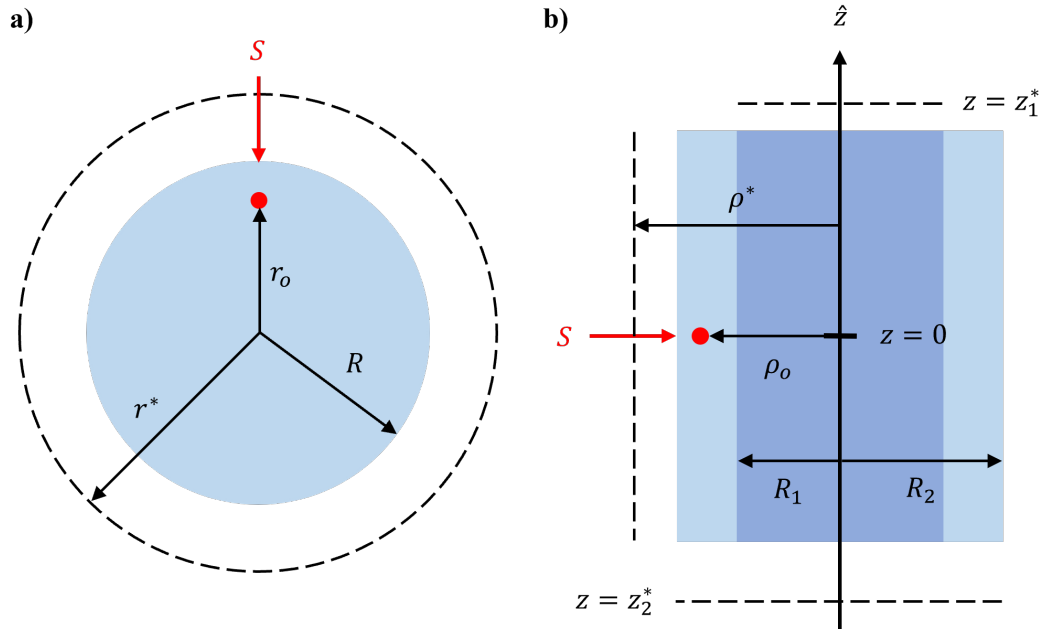

Figure D.1: Alternative geometries in which I solved the Photon Diffusion Model. a) Homogeneous sphere. b) Two-layered concentric cylinders.

D.1 Homogeneous Sphere

In spherical coordinates, the Photon Diffusion Model becomes:

$$\frac{1}{r^2}\frac{\partial}{\partial r}\left(r^2\frac{\partial\phi}{\partial r}\right)+\frac{1}{r^2 sin\theta}\frac{\partial}{\partial\theta}\left(sin\theta\frac{\partial\phi}{\partial\theta}\right)+\frac{1}{r^2 sin^2\theta}\frac{\partial^2\phi}{\partial\varphi}-k^2\phi = -\frac{1}{Dr^2}\delta(r-r_o)\delta(cos\theta-cos\theta_o)\delta(\varphi-\varphi_o),$$

where the source is located at the position (r_o,θ_o,φ_o). It is easier to solve this problem by expanding ϕ in terms of the spherical harmonics Y_{lm}:

$$\phi=\sum_{l=0}^{\infty}\sum_{m=-l}^{l}Y_{lm}^*(\theta_o,\varphi_o)Y_{lm}(\theta,\varphi)G_l(r,r_o),$$

where:

$$Y_{lm}=(-1)^m\sqrt{\frac{2l+1}{4\pi}\frac{(l-m)!}{(l+m)!}}e^{im\varphi}P_l^m(cos\theta),$$

where P_l^m are the Legendre polynomials. This is a useful expansion since:

$$\left(\frac{1}{sin^2\theta}\frac{\partial^2}{\partial\varphi^2}+\frac{1}{sin\theta}\frac{\partial}{\partial\theta}\left(sin\theta\frac{\partial}{\partial\theta}\right)\right)Y_{lm}=-l(l+1)Y_{lm},$$

$$\frac{\partial}{\partial\varphi}Y_{lm}=imY_{lm},$$

$$\sum_{l=0}^{\infty}\sum_{m=-l}^{l}Y_{lm}^*(\theta_o,\varphi_o)Y_{lm}(\theta,\varphi)=\sum_{l=0}^{\infty}\sum_{m=-l}^{l}\theta(cos\theta-cos\theta_o)\delta(\varphi-\varphi_o).$$

Thus, the equation becomes:

$$\frac{\partial}{\partial r}\left(r^2\frac{\partial G_l}{\partial r}\right)-l(l+1)G_l-k^2r^2G_l=-\frac{1}{D}\delta(r-r_o)\Rightarrow$$

$$r^2\frac{d^2G_l}{dr^2}+2r\frac{dG_l}{dr}-(l(l+1)+k^2r^2)G_l=\delta(r-r_o). \tag{D.1}$$

Let $u\equiv kr$. Thus, $d/dr=k\cdot d/du$ and $d^2/dr^2=k^2\cdot d^2/du^2$. Thus:

$$u^2\frac{d^2G_l}{du^2}+2u\frac{dG}{du}+(u^2+l(l+1))G_l=0$$

for $r\neq r_o$. Now let $v=-iu$, $d/du=-i\cdot d/dv$, and $d^2/du^2=-d^2/dv^2$. Thus:

$$v^2\frac{d^2G}{dv^2}+2v\frac{dG}{dv}+(v^2-l(l+1))G=0.$$

This equation is the so-called spherical Bessel equation, whose solution is:

$$G_l = Aj_l(v) + By_l(v) = Aj_l(-ikr) + By_l(-ikr) \Rightarrow$$

$$G_l = A\sqrt{\frac{\pi}{-2ikr}}J_{l+1/2}(-ikr) + B\sqrt{\frac{\pi}{-2ikr}}Y_{l+1/2}(-ikr), \tag{D.2}$$

where j_l and y_l are the spherical Bessel functions of the first and second kinds, while J_l and Y_l are the Bessel functions of the first and second kinds.

Now, let's split this solution into two regions. In $r \leq r_o$, we must have $G_l^i = Aj_l(-ikr)$ as y_l diverges at $r = 0$. In the region $r \geq r_o$, $G_l^{ii} = Bj_l(-ikr) + Cy_l(-ikr)$. Here, using the extrapolated-zero boundary condition, we must have $G_l^{ii}(r^*) = 0$, where $r^* = R + z_b$, being R the sphere radius. Thus:

$$B = \frac{-Cy_l(-ikr^*)}{j_l(-ikr^*)} \Rightarrow$$

$$G_l^{ii} = -C\left(\frac{y_l(-ikr^*)j_l(-ikr)}{j_l(-ikr^*)} - \frac{y_l(-ikr)j_l(-ikr^*)}{j_l(-ikr^*)}\right) \equiv \frac{-C}{j_l(-ikr^*)}F_l(kr^*;kr)$$

To find the constants A and C, we must deal with the continuity of G at $r = r_o$. There are two conditions. The first one is:

$$G_l^i(r_o) = G_l^{ii}(r_o) \Rightarrow Aj_l(-ikr_o) = \frac{-C}{j_l(-ikr^*)}F_l(kr^*;kr_o) \Rightarrow$$

$$A = \frac{-CF_l(kr^*;kr_o)}{j_l(-ikr^*)j_l(-ikr_o)}.$$

The second one comes from integrating the remaining radial equation from $r = r_o - \varepsilon$ to $r = r_o + \varepsilon$ with $\varepsilon \to 0$:

$$\int_{r_o-\varepsilon}^{r_o+\varepsilon}\left(\frac{d}{dr}\left(r^2\frac{dG_l}{dr}\right) - (k^2r^2 + l(l+1))G_l\right)dr = \int_{r_o-\varepsilon}^{r_o+\varepsilon} -\frac{\delta(r-r_o)}{D}dr.$$

As G_l is continuous at r_o, the equation becomes:

$$r_o^2\left(\frac{dG_l^{ii}(r_o)}{dr} - \frac{dG_l^i(r_o)}{dr}\right) = -\frac{1}{D}.$$

Using the relationship between A and C:

$$\frac{ikCF_l^{'}(kr^*;kr_o)}{j_l(-ikr^*)} - ik\frac{CF_l(kr^*;kr_o)}{j_l(-ikr^*)j_l(-ikr_o)}j_l^{'}(-ikr_o) = -\frac{1}{r_o^2D} \Rightarrow$$

$$C = -\frac{1}{ikr_o^2 D}\frac{j_l(-ikr^*)j_l(-ikr_o)}{F_l^{'}(kr^*;kr_o)j_l(-ikr_o) - F_l(kr^*;kr_o)j_l^{'}(-ikr_o)}.$$

Thus:

$$G_l^{ii}(r,r_o) = -\frac{C}{j_l(-ikr^*)}F_l(kr^*;kr),$$

and, finally:

$$\phi(r \geq r_o) = \sum_{l=0}^{\infty}\sum_{m=-l}^{l} Y_{lm}^*(\theta_o,\varphi_o)Y_{lm}(\theta,\varphi)G_l^{ii}(r,r_o).$$

To use this equation in the forward problem, one must evaluate $\phi(r = R, \theta = \theta_D, \varphi = \varphi_D)$, where θ_D and φ_D are the angular positions of the detectors.

D.2 Two-layered Concentric Cylinders

Let's start splitting the problem into two regions, $\rho \leq R_1$ and $\rho \geq R_1$. In the inner cylinder, the Photon Diffusion Model in cylindrical coordinates is:

$$\frac{\partial^2\phi_1}{\partial\rho^2} + \frac{1}{\rho}\frac{\partial\phi_1}{\partial\rho} + \frac{1}{\rho^2}\frac{\partial^2\phi_1}{\partial\theta^2} + \frac{\partial^2\phi_1}{\partial z^2} - k_1^2\phi_1 = 0.$$

Dealing with the variables θ and z with Fourier transforms, i.e.:

$$\tilde{\phi}_1(\rho,m,n) \equiv \frac{1}{2\pi z_1^*}\int_{-\pi}^{\pi}\int_{-z_1^*}^{z_1^*}\phi_1(\rho,\theta,z)e^{-im\theta}sin(M_n(z+z_1^*))\,dz\,d\theta,$$

$$\phi_1(\rho,\theta,z) = \sum_{m=-\infty}^{\infty}\sum_{n=1}^{\infty}\tilde{\phi}_1(\rho,m,n)e^{im\theta}sin(M_n(z+z_1^*)),$$

where $M_n = n\pi/(2z_1^*)$, $z_1^* = h + z_{b1}$ where the cylinder high is $2h$, $n = 0,1,2,...$, $m \in \mathbb{Z}$, we have, by applying a Fourier transform in the Photon Diffusion Model:

$$\frac{\partial^2\tilde{\phi}_1(\rho,m,n)}{\partial\rho^2} + \frac{1}{\rho}\frac{\partial\tilde{\phi}_1(\rho,m,n)}{\partial\rho} - \frac{m^2}{\rho^2}\tilde{\phi}_1(\rho,m,n) - (M_n^2 + k_1^2)\tilde{\phi}_1(\rho,m,n) = 0.$$

The previous equation is a modified Bessel equation of order m, whose general solution is:

$$\tilde{\phi}_1 = A_{mn}I_m(\alpha_n\rho) + B_{mn}K_m(\alpha_n\rho),$$

where $\alpha_n^2 = M_n^2 + k_1^2$ and I_m and K_m are the modified Bessel functions. As K_m diverges when $\rho \to 0$, $B_{mn} = 0$ and:

$$\tilde{\phi}_1 = A_{mn} I_m(\alpha_n \rho) \Rightarrow$$

$$\phi_1(\rho,\theta,z) = \sum_{m=-\infty}^{\infty} \sum_{n=1}^{\infty} A_{mn} I_m(\alpha_n \rho) e^{im\theta} sin(M_n(z+z_1^*)). \tag{D.3}$$

For $\rho \geq R_1$, the equation becomes:

$$\frac{\partial^2 \phi_1}{\partial \rho^2} + \frac{1}{\rho}\frac{\partial \phi_1}{\partial \rho} + \frac{1}{\rho^2}\frac{\partial^2 \phi_1}{\partial \theta^2} + \frac{\partial^2 \phi_1}{\partial z^2} - k_2^2 \phi_1 = -\frac{1}{D_2}\frac{1}{\rho}\delta(\rho-\rho_o)\delta(\theta-\theta_o)\delta(z-z_o).$$

Similar to the previous approach, I will use Fourier transforms to solve the problem in θ and z with $z_1^* \rightarrow z_2^*$ and $M_n \rightarrow \tilde{M}_n = n\pi/(2z_2^*)$. Thus:

$$\rho\frac{\partial^2 \tilde{\phi}_2(\rho,m,n)}{\partial \rho^2} + \frac{\partial \tilde{\phi}_2(\rho,m,n)}{\partial \rho} - \frac{m^2}{\rho}\tilde{\phi}_2(\rho,m,n) - (\tilde{M}_n^2 + k_2^2)\rho\tilde{\phi}_1(\rho,m,n)$$
$$= -\frac{1}{D_2}\delta(\rho-\rho_o)e^{-im\theta_o} sin(\tilde{M}_n(z_o+z_2^*)) \equiv -F\delta(\rho-\rho_o). \tag{D.4}$$

As is the homogeneous spherical case, I will split this region ($\rho \geq R_1$) into two subregions. For $R_1 \leq \rho < \rho_o$, the right-hand side of the previous equation is 0, and the solution is:

$$\tilde{\phi}_2^i = AI_m(\kappa\rho) + BK_m(\kappa\rho),$$

where $\kappa^2 = \tilde{M}_n^2 + k_2^2$. For $\rho_o < \rho \leq \rho^* = R_2 + z_{b2}$, the solution is:

$$\tilde{\phi}_2^{ii} = C^{'} I_m(\kappa\rho) + D^{'} K_m(\kappa\rho).$$

using that $\tilde{\phi}_2(\rho^*) = 0$, we obtain that $C^{'} = -D^{'} K_m(\kappa\rho^*)/I_m(\kappa\rho^*)$. Defining $D \equiv -D^{'}/I_m(\kappa\rho^*)$:

$$\tilde{\phi}_2^{ii} = D(K_m(\kappa\rho^*)I_m(\kappa\rho) - I_m(\kappa\rho^*)K_m(\kappa\rho)) \equiv D\Upsilon_m(\kappa\rho^*;\kappa\rho).$$

Constants A, B, and D might be related by analyzing $\tilde{\phi}_2$ at $\rho = \rho_o$. Since it is a continuous function:

$$\tilde{\phi}_2^i(\rho_o) = \tilde{\phi}_2^{ii}(\rho_o) \Rightarrow$$

$$D\Upsilon_m(\kappa\rho^*;\kappa\rho_o) = AI_m(\kappa\rho_o) + BK_m(\kappa\rho_o). \tag{D.5}$$

Equation D.4 may be written as:

$$\frac{\partial}{\partial\rho}\left(\rho\frac{\partial\tilde{\phi}_2}{\partial\rho}\right)-\left(\frac{m^2}{\rho}+(\tilde{M}_n^2+k_2^2)\rho\right)\tilde{\phi}_2=-F\delta(\rho-\rho_o).$$

Using the same strategy as in the spherical homogeneous case (i.e., integrating from $\rho=\rho_o-\varepsilon$ to $\rho=\rho_o+\varepsilon$ and letting $\varepsilon\to 0$):

$$\frac{\partial\tilde{\phi}_2^{ii}(\rho_o)}{\partial\rho}-\frac{\partial\tilde{\phi}_2^{i}(\rho_o)}{\partial\rho}=\frac{-F}{\rho_o}\Rightarrow$$

$$D\Upsilon_m^{'}(\kappa\rho^*;\kappa\rho_o)-\left(AI_m^{'}(\kappa\rho_o)+BK_m^{'}(\kappa\rho_o)\right)=\frac{-F}{\kappa\rho_o}. \tag{D.6}$$

Using Equation D.5 into Equation D.6:

$$A\Big(I_m(\kappa\rho_o)K_m^{'}(\kappa\rho_o)-I_m^{'}(\kappa\rho_o)K_m(\kappa\rho_o)\Big)$$
$$-D\Big(\Upsilon_m(\kappa\rho^*;\kappa\rho_o)K_m^{'}(\kappa\rho_o)-\Upsilon_m^{'}(\kappa\rho^*;\kappa\rho_o)K_m(\kappa\rho_o)\Big)=\frac{-F}{\kappa\rho_o}$$

$$\Rightarrow A=D\frac{\Upsilon_m(\kappa\rho^*;\kappa\rho_o)K_m^{'}(\kappa\rho_o)-\Upsilon_m^{'}(\kappa\rho^*;\kappa\rho_o)K_m(\kappa\rho_o)}{W[I_m,K_m](\kappa\rho_o)}-\frac{F}{\kappa\rho_o}\frac{K_m(\kappa\rho_o)}{W[I_m,K_m](\kappa\rho_o)}, \tag{D.7}$$

where $W[I_m,K_m](x)$ is the Wronskian of I_m and K_m, i.e., $W[I_m,K_m](x)=I_m(x)K_m^{'}(x)-I_m^{'}(x)K_m(x)$. Thus:

$$A=DK_m(\kappa\rho^*)-\frac{F}{\kappa\rho_o}\frac{K_m(\kappa\rho_o)}{W[I_m,K_m](\kappa\rho_o)}.$$

Using it to solve for B in Equation D.5:

$$B=D\frac{\Upsilon_m(\kappa\rho^*)}{K_m(\kappa\rho_o)}-D\frac{K_m(\kappa\rho^*)I_m(\kappa\rho_o)}{K_m(\kappa\rho_o)}+\frac{F}{\kappa\rho_o}\frac{I_m(\kappa\rho_o)}{W[I_m,K_m](\kappa\rho_o)}\Rightarrow$$

$$B=-DI_m(\kappa\rho^*)+\frac{F}{\kappa\rho_o}\frac{I_m(\kappa\rho_o)}{W[I_m,K_m](\kappa\rho_o)}. \tag{D.8}$$

As $W[I_m,K_m](x)=1/x$, $\tilde{\phi}_2^i=AI_m(\kappa\rho)+BK_m(\kappa\rho)$ becomes, using Equations D.7 and D.8:

$$\phi_2^i=D\Upsilon_m(\kappa\rho^*;\kappa\rho)+F\Upsilon_m(\kappa\rho_o;\kappa\rho).$$

We finally can write:

$$\tilde{\phi}_2 = \begin{cases} D\Upsilon_m(\kappa\rho^*;\kappa\rho) + F\Upsilon_m(\kappa\rho_o;\kappa\rho), R_1 \leq \rho \leq \rho_o, \\ D\Upsilon_m(\kappa\rho^*;\kappa\rho), \rho_o \leq \rho \leq \rho^*. \end{cases}$$

To standardize the notation used in $\tilde{\phi}_1$, let's write:

$$\Theta_{mn}(\rho_o,\theta_o,z_o,\rho) = \frac{1}{D_2} e^{-im\theta_o} sin(\tilde{M}_n(z_o + z_2^*))\Upsilon_m(\beta_n\rho_o;\beta_n,\rho)$$

$$\beta_n = \kappa, D_{mn} = D.$$

Thus:

$$\tilde{\phi}_2 = \begin{cases} D_{mn}\Upsilon_m(\beta_n\rho^*;\beta_n\rho) + \Theta_{mn}(\rho), R_1 \leq \rho \leq \rho_o, \\ D_{mn}\Upsilon_m(\beta_n\rho^*;\beta_n\rho), \rho_o \leq \rho \leq \rho^*, \end{cases}$$

and to obtain the actual solution:

$$\phi_2(\rho,\theta,z) = \sum_{m=-\infty}^{\infty}\sum_{n=0}^{\infty} \tilde{\phi}_2(\rho,m,n)e^{im\theta} sin(\tilde{M}_n(z + z_2^*)).$$

ϕ_2 for $\rho \geq R_1$ is the expression we aim to use since it is related to the acquisition data interface. Still, there is the D_{mn} constant to be determined. Recalling that:

$$\tilde{\phi}_1 = A_{mn} I_m(\alpha_n\rho),$$

there is two conditions that $\tilde{\phi}$ must attend at $\rho = R_1$. From now on, I will assume $z = 0$ without loss of generality. The first one is:

$$n_2^2\tilde{\phi}_1(R_1) = n_1^2\tilde{\phi}_2(R_1),$$

where n_i is the refractive index of the region i. Thus:

$$A_{mn} = \left(\frac{D_{mn}\Upsilon_m(\beta_n\rho^*;\beta_n R_1)}{I_m(\alpha_n R_1)} + \frac{\Theta_{mn}(R_1)}{I_m(\alpha_n R_1)}\right)\left(\frac{n_1}{n_2}\right)^2. \tag{D.9}$$

The second one is:

$$D_1\frac{\partial\tilde{\phi}_1(R_1)}{\partial\rho} = D_2\frac{\partial\tilde{\phi}_2(R_1)}{\partial\rho} \Rightarrow$$

$$D_1 A_{mn}\alpha_n I_m^{'}(\alpha_n R_1) = D_2 D_{mn}\beta_n \Upsilon_m^{'}(\beta_n\rho^*;\beta_n\rho) + D_2\beta_n\Theta_{mn}^{'}(R_1). \tag{D.10}$$

Putting Equation D.9 into Equation D.10:

$$D_{mn} = \frac{n_2^2 D_2 \beta_n \Theta'_{mn}(R_1) I_m(\alpha_n R_1) - n_1^2 D_1 \alpha_n \Theta_{mn}(R_1) I'_m(\alpha_n R_1)}{n_1^2 D_1 \alpha_n \Upsilon_m(\beta_n \rho^*; \beta_n R_1) I'_m(\alpha_n R_1) - n_2^2 D_2 \beta_n \Upsilon'_m(\beta_n \rho^*; \beta_n R_1) I_m(\alpha_n R_1)}.$$

APPENDIX E

COUPLING FACTOR FROM A SINGLE FIBER

To illustrate the problem, let's consider the detection procedure using an optical fiber (Figure E.1). The recorded intensity is the integral of the radiance:

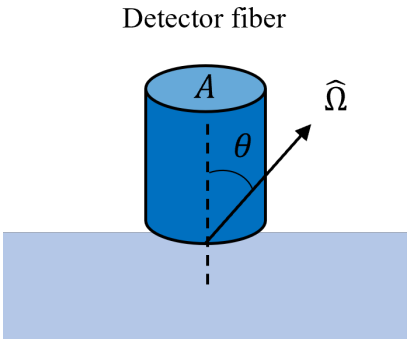

Figure E.1: Illustration of an optical fiber used as a detector to measure the emerging radiance from a turbid medium.

$$I = \int_A \int_0^{\theta_c} sin\theta D(\theta) \int_0^{2\pi} \frac{1}{4\pi}(\phi + 3\vec{J}\cdot\hat{\Omega}) d\varphi d\theta dA,$$

where D is the probability of the detector successfully detects a photon and θ_c is the maximum cone angle that light can propagate through the fiber. Since $\hat{\Omega} = sin\theta cos\varphi\hat{x} + sin\theta cos\varphi\hat{y} - cos\varphi\hat{z}$,

$$I = \int_A \int_0^{\theta_c} D(\theta)\frac{1}{2}\Big(\phi - 3J_z cos\theta\Big) sin\theta d\theta dA.$$

Using B.3:

$$I = \int_A \phi dA \int_0^{\theta_c} D(\theta)\frac{1}{2}\left(1 + \frac{3}{2}\frac{1-R_{eff}}{1+R_{eff}}\right) d\theta \equiv C' \int_A \phi dA$$

If ϕ is constant over the detection area, the integral over A results in $A\phi$ and the equation becomes:

$$I = C\phi,$$

where $C = AC'$ is the *coupling factor* between the optical fiber and the turbid medium.

APPENDIX F

SIEGERT'S RELATION

This appendix discusses the highlights of [47] applied for our case. The most simple scenario is to assume that the electric field $\vec{E}(t)$ is linearly polarized, which means it can be assumed as linear in one dimension. Thus, the intensity is $I(t) = E^*(t)E(t)$. By letting the medium be a set of N volumes, the scattered electric field is:

$$E(t) = \sum_{i=1}^{N} E_j(t).$$

Even in cases where the subregions inside the medium are not correlated, it is acceptable since we can assume large N anytime. Additionally, if $N \to \infty$ and each E_j are statistically independent ($\langle E_j E_k \rangle = \langle E_j \rangle \langle E_k \rangle$), $E(t)$ and $E^*(t)$ are Gaussian variables of zero mean according to the limit central theorem. The intensity autocorrelation is $\langle I(t)I(t+\tau)\rangle = \langle E^*(t)E(t)E^*(t+\tau)E(t+\tau)\rangle$. Since Gaussian variables of zero mean are described by their second moment (variance), the previous equation, which ranges up to the 4th order in the electric field, may be written as the sum of the second moments:

$$\langle I(t)I(t+\tau)\rangle = \langle E^*(t)E(t)\rangle\langle E^*(t+\tau)E(t+\tau)\rangle + \langle E(t)E(t+\tau)\rangle\langle E^*(t)E^*(t+\tau)\rangle$$

$$+\langle E^*(t+\tau)E(t)\rangle\langle E^*(t)E^*(t+\tau)\rangle \Rightarrow$$

$$\langle I(t)I(t+\tau)\rangle = \langle I\rangle^2 + \left|\langle E(t)E(t+\tau)\rangle\right|^2 + \left|\langle E^*(t)E(t+\tau)\rangle\right|^2,$$

since $\langle E^*(t)E(t)\rangle = \langle E^*(t+\tau)E(t+\tau)\rangle = \langle E^*(0)E(0)\rangle$. Moreover, $E(t)$ typically has a $exp(-i\omega_0 t)$ dependence, where $\omega_0 = 2\pi f$, f the light frequency. Thus, $E(t)E(t+\tau)$ depends on $exp(-2i\omega_0 t)$, making its time average neglectable compared to $E(t)E^*(t+\tau)$. Therefore:

$$g_2(\tau) = 1 + \frac{\left|\langle E^*(t)E(t+\tau)\rangle\right|^2}{\left|\langle E^*(t)E(t)\rangle\right|^2},$$

where $g_2(\tau)$ is the intensity autocorrelation function. However, the detection of the scattered light does not occur at a single point, but in a detection area A. Indeed, if there are several scatterers on the medium, the scattered intensity forms a speckle pattern. The typical size

of the speckles is $d \sim \lambda\rho/\ell$, where λ is the light wavelength, ρ is the distance between the medium and the detector, and ℓ is the size of the scattering volume. Thus, a detector of area A measures $M = A/d^2$ speckles with Gaussian statistics (as the electric field, $\langle I_j(t)I_k(t+\tau)\rangle = \langle I_j\rangle\langle I_k\rangle$, $j \neq k$):

$$I(t) = \sum_{i=1}^{M} I_j(t),$$

$$\langle I_j(t)I_k(t+\tau)\rangle = \langle I_j\rangle^2\Big(1+|g_1(\tau)|^2\Big), j = k,$$

$$g_1(\tau) \equiv \frac{\langle E^*(t)E(t+\tau)\rangle^2}{\langle E^*(t)E(t)\rangle^2}$$

where we use the expression for $g_2(\tau)$ to obtain the second equation. We now can compute the intensity autocorrelation function, $g_2(\tau)$, for real light detection:

$$\langle I(t)I(t+\tau)\rangle = \langle \sum_{j,k=1}^{M} I_j(t)I_k(t+\tau)\rangle = \langle \sum_{j\neq k} I_j(t)I_k(t+\tau)\rangle + \langle \sum_{j=k} I_J(t)I_k(t+\tau)\rangle;$$

$$g_2(\tau) = \frac{\langle\sum_{j\neq k} I_j(t)I_k(t+\tau)\rangle + \langle\sum_j \langle I_j\rangle^2\big(1+|g_1(\tau)|^2\big)\rangle}{\langle I\rangle^2}$$

$$= \frac{\sum_{j\neq k}\langle I_j\rangle\langle I_k\rangle + \sum_j \langle I_j\rangle^2}{\Big(\sum_j \langle I_j\rangle\Big)^2} + \frac{\sum_j \langle I_j\rangle^2|g_1(\tau)|^2}{\Big(\sum_j \langle I_j\rangle\Big)^2}.$$

Let's look at the first ratio on the right side of the previous equation for $g_2(\tau)$. If we sum over all values on the first sum, the values *missing* ($j \neq k$) are exactly the second sum over j. Thus:

$$g_2(\tau) = \frac{\Big(\sum_j \langle I_j\rangle\Big)^2}{\Big(\sum_j \langle I_j\rangle\Big)^2} + \frac{\sum_j \langle I_j\rangle^2|g_1(\tau)|^2}{\Big(\sum_j \langle I_j\rangle\Big)^2} = 1 + \frac{\sum_j \langle I_j\rangle^2|g_1(\tau)|^2}{\Big(\sum_j \langle I_j\rangle\Big)^2} \Rightarrow$$

$$g_2(\tau) \equiv 1 + \beta|g_1(\tau)|^2,$$

$$\beta = \frac{\sum_j \langle I_j\rangle^2}{\Big(\sum_j \langle I_j\rangle\Big)^2}.$$

Note that β, in summary, is an experimental parameter that depends on the light detection setup.

However, the electric field is typically unpolarized. Thus, we can say that the light is a composition of two polarized light and the recorded intensity is a superposition of two independent speckle patterns with an average intensity ratio of $p = \langle I_1\rangle/\langle I_2\rangle$. Assuming the

detector is a single-mode optical fiber (i.e., only one speckle is recorded), we can neglect the spatial average we just performed and assume the detected intensity is $I(t) = I_1(t) + I_2(t)$ from both polarizations. Thus:

$$\beta = \frac{\sum_{j=1}^{2} \langle I_j \rangle^2}{\left(\sum_{j=1}^{2} \langle I_j \rangle\right)^2} = \frac{\langle I_1 \rangle^2 + \langle I_2 \rangle^2}{\langle I_1 \rangle^2 + 2\langle I_1 \rangle \langle I_2 \rangle + \langle I_2 \rangle^2} = \frac{p^2 + 1}{p^2 + 2p + 1} \Rightarrow$$

$$\beta = \frac{1 + p^2}{(1 + p)^2}.$$

In case the light is unpolarized, $p = 1$ and $\beta = 0.5$. However, as there are several experimental phenomena that may compromise all these assumptions, it is useful not to predict β theoretically, but to adjust around 0.5 based on the acquired data.

APPENDIX G

CRITICAL CLOSING PRESSURE EQUATION

In this appendix, I exhibit the highlights of the deduction of Equation 7.1. A more detailed description and exploration may be found in [163]. Briefly, the arteriole compartment is modeled through an RC parallel circuit (Figure G.1), in which the capacitor models the vascular compliance. In this analogy, F plays the role of the electric current, while the pressure gradient is the driving force (i.e., similar to the electromotive force). Assuming that the incoming pressure at the arteriole compartment is a fraction of the arterial pressure, $P_A = \gamma ABP$ (usually $\gamma = 0.6$), and the opposing pressure to the blood flows to the precapillary sphincter is CrCP, Ohm's law for this circuit is:

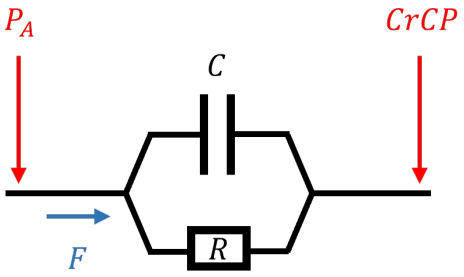

Figure G.1: RC circuit used to model the arteriole compartment.

$$\frac{P_A - CrCP}{F} = Z, \tag{G.1}$$

where Z is the impedance. Since the resistor impedance is $X_R = R$ and the capacitor impedance is $X_C = 1/i\omega C$, where ω is the angular oscillation frequency of F:

$$Z = \frac{R/i\omega C}{R + 1/i\omega C} = R\frac{1 - i\omega CR}{1 + \omega^2 R^2 C^2} \equiv \frac{R(1 - 2\pi f\tau)}{1 + (2\pi f\tau)^2}, \tag{G.2}$$

where $\tau = RC$. As P_A, CrCP and F oscillate, we can write their Fourier transforms as $P_A(f) = |P_A(f)|cos(2\pi ft)$, $CrCP(f) = |CrCP(f)|cos(2\pi ft)$, and $F(f) = |F(f)|cos(2\pi ft - \varphi(f))$, where $\varphi(f)$ is the phase shift between the pressure quantities and the blood flow. Thus, Equation G.1 in the frequency-domain is:

$$\frac{|P_A(f)| - |CrCP(f)|}{|F(f)|} e^{i\varphi(f)} = \frac{R}{1 + (2\pi f\tau)^2}(1 - i2\pi f\tau). \tag{G.3}$$

Since CrCP is constant at the heartbeat frequency (f_c), $|CrCP(f_c)| = 0$ and the previous equation becomes:

$$\frac{|P_A(f_c)|}{|F(f_c)|}e^{i\varphi(f_c)} = \frac{R}{\sqrt{1+(2\pi f_c\tau)^2}}e^{i\,atan(-2\pi f_c\tau)}. \tag{G.4}$$

By matching the phases of Equation G.4:

$$\tau = \frac{-tan(f_c)}{2\pi f_c}, \tag{G.5}$$

and by matching the amplitudes:

$$R = \frac{|P_A(f_c)|}{|F(f_c)|}\sqrt{1+(2\pi f_c\tau)^2}. \tag{G.6}$$

Taking $f = 0$ in Equation 2.8:

$$\frac{|P_A(0)| - |CrCP(0)|}{|F(0)|}e^{i\varphi(0)} = R \Rightarrow \frac{\langle P_A\rangle - CrCP}{\langle F\rangle} = R, \tag{G.7}$$

since $f = 0$ is the frequency related to the temporal average, denoted by $\langle\cdot\rangle$. As $\langle P_A\rangle = \gamma\langle ABP\rangle$ and using G.6 in G.7:

$$\frac{\gamma\langle ABP\rangle - CrCP}{\langle F\rangle} = \frac{|P_A(f_c)|}{|F(f_c)|}\sqrt{1+(2\pi f_c\tau)^2} \Rightarrow$$

$$CrCP = \gamma\langle ABP\rangle\left(1 - \frac{|ABP(f_c)|/\langle ABP\rangle}{|F(f_c)|/\langle F\rangle}\sqrt{1+(2\pi f_c\tau)^2}\right),$$

where τ is given by Equation G.5.

APPENDIX H

INFORMED CONSENT FORM FOR COVID-19 CONTROL PARTICIPANTS

TERMO DE CONSENTIMENTO LIVRE E ESCLARECIDO

Projeto: Caracterização não invasiva da reatividade microvascular em pacientes com COVID-19 e outras doenças respiratórias graves com a espectroscopia do infravermelho próximo

CAAE: 34454920.7.0000.5404

Pesquisadores: Rickson C. Mesquita, Rodrigo M. Forti, Andrés F. Q. Soto, Italo K. Aventurato, Gabriela Lívio Emídio, Lígia dos Santos Roceto Ratti, Antonio L. E. Falcão

Você está sendo convidado a participar como voluntário de uma pesquisa clínica. A participação não é obrigatória, e não haverá nenhum tipo de penalização ou prejuízo se você não aceitar participar. Após aceitar, você poderá desistir durante qualquer etapa da pesquisa, também sem qualquer prejuízo. Para garantir seus direitos como participante, o pesquisador fornecerá todas as informações necessárias através deste documento chamado "Termo de Consentimento Livre e Esclarecido", o qual está elaborado em duas vias, ambas assinadas por você e pelo pesquisador. Ao finalizar os esclarecimentos, uma via assinada será entregue para cada parte.

Por favor, leia com atenção e calma, aproveitando para esclarecer suas dúvidas. Se houver perguntas antes ou mesmo depois de assiná-lo, você poderá esclarecê-las com o pesquisador. Se preferir, pode levar este Termo com você para consultar seus familiares ou outras pessoas antes de decidir participar.

Justificativa e objetivos:
O objetivo geral deste projeto de pesquisa é introduzir e testar clinicamente um sistema não invasivo para monitorar pacientes internados em unidades de terapia intensiva (UTI) devido a síndrome respiratória aguda. O estudo poderá fornecer novas informações com grande potencial para melhorar os procedimentos clínicos, e os resultados obtidos poderão ajudar os médicos a entenderem melhor os efeitos da COVID-19 e outras doenças respiratórias agudas. A técnica utilizada neste estudo é conhecida como NIRS (Espectroscopia do infravermelho próximo), e ela usa luz infravermelha de baixa potência para medir a oxigenação no músculo.

Procedimentos:
Aceitando a participação no estudo, usaremos suas informações para termos controles sobre as variáveis que podem afetar os resultados deste estudo. Deste modo, os pesquisadores responsáveis por esse estudo farão perguntas sobre seu histórico clínico. Mais especificamente, antes do início do teste os pesquisadores poderão coletar seus dados demográficos e os valores dos seus sinais vitais. Caso necessário, algumas informações serão confirmadas diretamente com você.

Um sensor de NIRS será posicionado no seu antebraço, juntamente com uma braçadeira inflável para realização de um teste de oclusão vascular. O teste de oclusão vascular consiste em inflarmos a braçadeira

para temporariamente obstruir o fluxo sanguíneo do braço. O protocolo consiste em um período de repouso inicial de 5 minutos, seguido por um período de 3 minutos onde inflaremos a braçadeira com uma pressão de até 50mmHg acima da sua pressão arterial. O período de oclusão será seguido por um segundo período de repouso de 5 minutos. Durante o teste o você não precisará realizar nenhuma ação, e terá apenas de ficar em repouso enquanto realizamos o teste, que durará cerca de 10 a 15 minutos.

Desconfortos e riscos:
NIRS tem sido usado em diferentes situações de pesquisa desde 1990, desde recém-nascidos até idosos, incluindo voluntários sadios e pacientes com distúrbios e doenças neurológicas. Não há nenhum risco previsto da técnica, pois a potência da luz utilizada é muito baixa para produzir algum dano ao tecido. Durante o teste, você poderá sentir algum desconforto temporário devido a pressão do manguito. Se o desconforto for excessivo, pararemos o teste instantaneamente. Todos os testes serão realizados por profissionais da saúde, e todos os cuidados necessários para evitar a transmissão da COVID-19 serão tomados. Isto é, os profissionais da saúde estarão sempre com todos os equipamentos de proteção necessários e todos os equipamentos utilizados durante o estudo serão sempre desinfectados antes e depois de todos os testes realizados. Em caso de qualquer evento adverso relacionado à pesquisa, você terá direito a assistência médica imediata, gratuita e pelo tempo necessário.

Benefícios:
Você não obterá nenhuma vantagem direta com a sua participação nesse estudo. Contudo, os resultados da pesquisa podem, a longo prazo, trazer melhorias nos diagnósticos e tratamentos clínicos para pacientes com síndrome respiratórias aguda graves causada pelo COVID-19 e outras doenças. Os resultados do exame ficarão à disposição caso você e/ou seu médico tenham interesse no futuro.

Sigilo e privacidade:
Você tem a garantia de que sua identidade será mantida em sigilo e nenhuma informação pessoal será dada a outras pessoas que não façam parte da equipe de pesquisadores. Na divulgação dos resultados desse estudo, seu nome não será citado. Este estudo faz parte de uma colaboração internacional, e os dados coletados e analisados serão adicionados a um banco de dados compartilhado com os outros parceiros, porém sempre garantindo a sua privacidade.

Ressarcimento e Indenização:
Você não será reembolsado pela sua participação na pesquisa, uma vez que a mesma não vai gerar nenhum gasto. Embora seja muito pouco provável que algum dano seja causado no decorrer da pesquisa, caso algo aconteça você terá a garantia ao direito a uma indenização diante de eventuais danos.

Contato:
Em caso de dúvidas sobre a pesquisa, você poderá entrar em contato com o pesquisador Rickson Coelho Mesquita no Laboratório de Física Médica do Hospital das Clínicas da UNICAMP, localizado na Rua Tessália Vieira de Camargo, 126, telefone (19) 3521-0137, e-mail: rickson@ifi.unicamp.br.

Em caso de denúncias ou reclamações sobre sua participação e sobre questões éticas do estudo, você poderá entrar em contato com a secretaria do Comitê de Ética em Pesquisa (CEP) da UNICAMP das

08:30hs às 11:30hs e das 13:00hs as 17:00hs na Rua: Tessália Vieira de Camargo, 126; CEP 13083-887 Campinas – SP; telefone (19) 3521-8936 ou (19) 3521-7187; e-mail: cep@fcm.unicamp.br.

O Comitê de Ética em Pesquisa (CEP):
O papel do CEP é avaliar e acompanhar os aspectos éticos de todas as pesquisas envolvendo seres humanos. A Comissão Nacional de Ética em Pesquisa (CONEP), tem por objetivo desenvolver a regulamentação sobre proteção dos seres humanos envolvidos nas pesquisas. Desempenha um papel coordenador da rede de Comitês de Ética em Pesquisa (CEPs) das instituições, além de assumir a função de órgão consultor na área de ética em pesquisas.

Consentimento livre e esclarecido:
Após ter recebido esclarecimentos sobre a natureza da pesquisa, seus objetivos, métodos, benefícios previstos, potenciais riscos e o incômodo que esta possa acarretar, aceito participar e declaro estar recebendo uma via original deste documento assinada pelo pesquisador e por mim, tendo todas as folhas por nós rubricadas:

Nome do (a) participante: _____

Contato telefônico: _____

E-mail (opcional): _____

_____ Data: ____/_____/_____.

(Assinatura do participante ou nome e assinatura do seu RESPONSÁVEL LEGAL)

Responsabilidade do Pesquisador:
Asseguro ter cumprido as exigências da resolução 466/2012 CNS/MS e complementares na elaboração do protocolo e na obtenção deste Termo de Consentimento Livre e Esclarecido. Asseguro, também, ter explicado e fornecido uma via deste documento ao participante. Informo que o estudo foi aprovado pelo CEP perante o qual o projeto foi apresentado. Comprometo-me a utilizar o material e os dados obtidos nesta pesquisa exclusivamente para as finalidades previstas neste documento ou conforme o consentimento dado pelo participante.

_____ Data: ____/_____/_____.

(Assinatura do pesquisador)

Rubrica do pesquisador: _____ Rubrica do participante: _____

APPENDIX I

INFORMED CONSENT FORM FOR COVID-19 PATIENT PARTICIPANTS

TERMO DE CONSENTIMENTO LIVRE E ESCLARECIDO

Projeto: Caracterização não invasiva da reatividade microvascular em pacientes com COVID-19 e outras doenças respiratórias graves com a espectroscopia do infravermelho próximo

CAAE: 34454920.7.0000.5404

Pesquisadores: Rickson C. Mesquita, Rodrigo M. Forti, Andrés F. Q. Soto, Italo K. Aventurato, Gabriela Lívio Emídio, Lígia dos Santos Roceto Ratti, Antonio L. E. Falcão

Você está sendo convidado a participar como voluntário de uma pesquisa clínica. A participação não é obrigatória, e não haverá nenhum tipo de penalização ou prejuízo no tratamento se você não aceitar participar. Após aceitar, você poderá desistir durante qualquer etapa da pesquisa, também sem qualquer prejuízo. Para garantir seus direitos como participante, o pesquisador fornecerá todas as informações necessárias através deste documento chamado "Termo de Consentimento Livre e Esclarecido", o qual está elaborado em duas vias, ambas assinadas por você e pelo pesquisador. Ao finalizar os esclarecimentos, uma via assinada será entregue para cada parte. Nos casos onde houver dificuldade na obtenção da assinatura em uma cópia de papel deste termo devido à pandemia da COVID-19, este termo poderá também ser assinado digitalmente. Nos casos em que houver necessidade da assinatura digital deste termo de consentimento, ambas as partes devem salvar uma cópia impressa ou digital da versão assinada deste documento.

Por favor, leia com atenção e calma, aproveitando para esclarecer suas dúvidas. Se houver perguntas antes ou mesmo depois de assiná-lo, você poderá esclarecê-las com o pesquisador. Se preferir, pode levar este Termo com você para consultar seus familiares ou outras pessoas antes de decidir participar.

Justificativa e objetivos:
O objetivo geral deste projeto de pesquisa é introduzir e testar clinicamente um sistema não invasivo para monitorar pacientes internados em unidades de terapia intensiva (UTI) devido a síndrome respiratória aguda. O estudo poderá fornecer novas informações com grande potencial para melhorar os procedimentos clínicos, e os resultados obtidos poderão ajudar os médicos a entenderem melhor os efeitos da COVID-19 e outras doenças respiratórias agudas. A técnica utilizada neste estudo é conhecida como NIRS (Espectroscopia do infravermelho próximo), e ela usa luz infravermelha de baixa potência para medir a oxigenação no músculo.

Procedimentos:
Aceitando a participação no estudo, usaremos suas informações para termos controles sobre as variáveis que podem afetar os resultados deste estudo. Deste modo, os pesquisadores responsáveis por esse estudo terão acesso ao seu histórico clínico através do prontuário fornecido pelo hospital. Mais especificamente, antes do início de todos os testes coletaremos seus dados demográficos, os valores dos seus sinais vitais, os dados do ventilador mecânico, entre outros parâmetros clínicos. Caso necessário, algumas informações serão confirmadas diretamente com você ou seu responsável legal. Dependendo da

sua condição clínica, você poderá ser convocado para realizar o teste óptico mais de uma vez durante a sua internação. Repetiremos o teste no máximo duas vezes por dia durante o tempo que você estiver internado no hospital.

Um sensor de NIRS será posicionado no seu antebraço, juntamente com uma braçadeira para realização de um teste de oclusão vascular. O teste de oclusão vascular consiste em inflarmos a braçadeira para temporariamente obstruir o fluxo sanguíneo do braço (similar a uma medida de pressão arterial). O protocolo consiste em um período de repouso inicial de 5 minutos, seguido por um período de 3 minutos onde inflaremos a braçadeira com uma pressão acima da sua pressão arterial. O período de oclusão será seguido por um segundo período de repouso de 5 minutos. Durante o teste o você não precisará realizar nenhuma ação, e terá apenas de ficar em repouso enquanto realizamos o teste, que durará cerca de 10 a 15 minutos.

Desconfortos e riscos:
NIRS tem sido usado em diferentes situações de pesquisa desde 1990, desde recém-nascidos até idosos, incluindo voluntários sadios e pacientes com distúrbios e doenças neurológicas. Não há nenhum risco previsto da técnica, pois a potência da luz utilizada é muito baixa para produzir algum dano ao tecido. Durante o teste, você poderá sentir algum desconforto temporário devido a pressão da braçadeira. Se o desconforto for excessivo, pararemos o teste instantaneamente. Todos os testes serão realizados por profissionais da saúde, e todos os cuidados necessários para evitar a transmissão da COVID-19 serão tomados. Isto é, os profissionais da saúde estarão sempre com todos os equipamentos de proteção necessários e todos os equipamentos utilizados durante o estudo serão sempre desinfectados antes e depois de todos os testes realizados. Em caso de qualquer evento adverso relacionado à pesquisa, você terá direito a assistência médica imediata, gratuita e pelo tempo necessário.

Benefícios:
Você não obterá nenhuma vantagem direta com a sua participação nesse estudo. Contudo, os resultados da pesquisa podem, a longo prazo, trazer melhorias nos diagnósticos e tratamentos clínicos para pacientes com síndrome respiratórias aguda graves causada pelo COVID-19 e outras doenças. Os resultados do exame ficarão à disposição caso você e/ou seu médico tenham interesse no futuro.

Sigilo e privacidade:
Você tem a garantia de que sua identidade será mantida em sigilo e nenhuma informação pessoal será dada a outras pessoas que não façam parte da equipe de pesquisadores. Na divulgação dos resultados desse estudo, seu nome não será citado. Os resultados do estudo poderão fazer parte do prontuário médico, mesmo que retrospetivamente. Este estudo faz parte de uma colaboração internacional, e os dados coletados e analisados serão compartilhados com os outros parceiros, porém sempre garantindo a sua privacidade.

Ressarcimento e Indenização:
Você não será reembolsado pela sua participação na pesquisa, uma vez que a mesma não vai gerar nenhum gasto. Embora seja muito pouco provável que algum dano seja causado no decorrer da pesquisa, caso algo aconteça você terá a garantia ao direito a uma indenização diante de eventuais danos.

Rubrica do pesquisador: _____ Rubrica do participante: _____

Contato:
Em caso de dúvidas sobre a pesquisa, você poderá entrar em contato com o pesquisador Rickson Coelho Mesquita no Laboratório de Física Médica do Hospital das Clínicas da UNICAMP, localizado na Rua Tessália Vieira de Camargo, 126, telefone (19) 3521-0137, e-mail: rickson@ifi.unicamp.br.
Em caso de denúncias ou reclamações sobre sua participação e sobre questões éticas do estudo, você poderá entrar em contato com a secretaria do Comitê de Ética em Pesquisa (CEP) da UNICAMP das 08:30hs às 11:30hs e das 13:00hs as 17:00hs na Rua: Tessália Vieira de Camargo, 126; CEP 13083-887 Campinas – SP; telefone (19) 3521-8936 ou (19) 3521-7187; e-mail: cep@fcm.unicamp.br.

O Comitê de Ética em Pesquisa (CEP):
O papel do CEP é avaliar e acompanhar os aspectos éticos de todas as pesquisas envolvendo seres humanos. A Comissão Nacional de Ética em Pesquisa (CONEP), tem por objetivo desenvolver a regulamentação sobre proteção dos seres humanos envolvidos nas pesquisas. Desempenha um papel coordenador da rede de Comitês de Ética em Pesquisa (CEPs) das instituições, além de assumir a função de órgão consultor na área de ética em pesquisas.

Consentimento livre e esclarecido:
Após ter recebido esclarecimentos sobre a natureza da pesquisa, seus objetivos, métodos, benefícios previstos, potenciais riscos e o incômodo que esta possa acarretar, aceito participar e declaro estar recebendo uma via original deste documento assinada pelo pesquisador e por mim, tendo todas as folhas por nós rubricadas:

Nome do (a) participante: _____

Contato telefônico: _____

E-mail (opcional): _____

_____ Data: ____/_____/_____.

(Assinatura do participante ou nome e assinatura do seu RESPONSÁVEL LEGAL)

Responsabilidade do Pesquisador:
Asseguro ter cumprido as exigências da resolução 466/2012 CNS/MS e complementares na elaboração do protocolo e na obtenção deste Termo de Consentimento Livre e Esclarecido. Asseguro, também, ter explicado e fornecido uma via deste documento ao participante. Informo que o estudo foi aprovado pelo CEP perante o qual o projeto foi apresentado. Comprometo-me a utilizar o material e os dados obtidos nesta pesquisa exclusivamente para as finalidades previstas neste documento ou conforme o consentimento dado pelo participante.

_____ Data: ____/_____/_____.

(Assinatura do pesquisador)

Rubrica do pesquisador: _____ Rubrica do participante: _____

APPENDIX J

INFORMED CONSENT FORM FOR FD-DOS AND DCS ACQUISITIONS

Laboratório de Óptica Biomédica

TERMO DE CONSENTIMENTO LIVRE ESCLARECIDO

Obtenção de propriedades ópticas e dinâmicas de tecidos biológicos com espectroscopias ópticas de difusão

Giovani Grisotti Martins, Andrés Fabián Quiroga Soto, Antonio Luis Eiras Falcão, Rickson Coelho Mesquita

Protocolo CAAE: 50436921.3.0000.5404

Você está sendo convidado a participar de uma pesquisa. Este documento, chamado Termo de Consentimento Livre e Esclarecido, visa assegurar os seus direitos como participante e é elaborado em duas vias, uma que deverá ficar com você e outra com o pesquisador.

Por favor, leia com atenção e calma, aproveitando para esclarecer suas dúvidas. Se houver perguntas antes ou depois de assiná-lo, você pode esclarecê-las com o pesquisador. Se preferir, pode levar para casa e consultar seus familiares ou outras pessoas antes de decidir participar. Se você não quiser participar, ou quiser retirar sua autorização para participar, você poderá fazer isso a qualquer momento. Não haverá nenhum tipo de penalização ou prejuízo.

Justificativa e Objetivos:

O objetivo deste estudo é usar uma técnica nova, chamada espectroscopia óptica de difusão (ou DOS), para estimar algumas características fisiológicas do seu corpo (isto é, características que estão relacionadas com o funcionamento do corpo). A DOS usa luz na região do infravermelho próximo, que se parece com o vermelho, mas é invisível aos nossos olhos. Nosso grupo de pesquisa na UNICAMP desenvolve esta tecnologia no Brasil construindo equipamentos nacionais para serem utilizados no hospital. Como esta técnica é nova e ainda pouco conhecida, ela precisa ser melhorada – e este estudo é uma parte deste esforço, que visa especificamente testar modelos mais detalhados na análise de dados visando aumentar a acurácia das características que estimamos com esta técnica. A DOS é uma técnica inofensiva, e as características que ela mede são a oxigenação e o fluxo de sangue no tecido biológico, como, por exemplo, o cérebro. Por isto, a DOS apresenta um alto potencial para o acompanhamento de diversos distúrbios neurológicos. Ou seja, a participação nesta pesquisa poderá ajudar indiretamente diversas pessoas portadoras de doenças e/ou distúrbios neurológicos no futuro como, por exemplo, epilepsia, traumatismo craniano, AVC e Alzheimer, além possibilitar melhorias em outras áreas de pesquisa como o esporte e o ensino.

Procedimentos

Ao concordar em participar deste estudo, primeiramente você vai responder algumas perguntas a respeito da sua saúde, do seu histórico clínico e dos seus hábitos usuais. Não há nenhum julgamento nestas perguntas, mas precisamos ter estas informações para melhor interpretar os dados que vamos coletar com o nosso equipamento. A seguir, os pesquisadores

Rubrica do pesquisador: _____ Rubrica do participante: _____

colocarão um arranjo de fibras ópticas que agem como fontes e detectores de luz na sua cabeça. Fique tranquilo porque essas fontes de luz são LEDs ou lasers que operam com baixíssima energia e potência, e não têm riscos de machucá-lo ou afetá-lo de qualquer forma. Você poderá apenas sentir um desconforto se o arranjo ficar muito apertado na sua cabeça. Se isso acontecer, nos avise imediatamente para que possamos afrouxar o arranjo com as fontes e detectores, de forma que ocorra tudo bem durante o experimento. Além disso, um outro sensor será colocado no seu dedo indicador esquerdo. Este sensor vai monitorar sua pressão sanguínea, o batimento do seu coração e saturação de oxigênio no seu pulso. Novamente, este sensor funciona por pressão e radiação de baixa potência, sendo incapaz de oferecer algum risco.

Durante o experimento, você vai precisar ficar sentado, quieto e em silêncio enquanto coletamos os dados. Em alguns momentos, o pesquisador vai pedir para você prender a respiração até quando você conseguir, ou até um máximo de 30 segundos (o que acontecer primeiro). Nesta etapa, utilizaremos um capnógrafo para medir a quantidade de CO_2 expirada pelo seu nariz e boca. Este equipamento também não oferece riscos, visto que sua função é apenas analisar o ar expirado por você. Existe a possibilidade de, nesta etapa, usarmos um outro equipamento, chamado de Doppler transcraniano ou TCD, que usa sons fora da faixa audível para medir o fluxo de sangue nas grandes artérias cerebrais. Este equipamento é comumente utilizado no hospital e não oferece riscos. No total, a coleta dos dados terá duração de 10 a 40 minutos, incluindo a montagem do aparato. Dependendo da sua disponibilidade, os pesquisadores irão pedir para que você retorne em outras datas para repetir a aquisição de dados. Este retorno é importante porque queremos verificar a variabilidade da técnica utilizada. Entretanto, você pode optar por não retornar, sem qualquer prejuízo.

Durante todo o tempo do exame, você estará acompanhado pelos pesquisadores. Caso queira ou se sinta mal, você poderá solicitar que o estudo seja interrompido, sem prejuízos para você. Além disto, os pesquisadores lhe passarão informações detalhadas e esclarecerão as suas dúvidas a respeito de cada etapa do procedimento de aquisição de dados. É importante que você esclareça todas as suas dúvidas, então não hesite em perguntar. Os pesquisadores estarão sempre dispostos a responder todas as suas perguntas.

Desconfortos e riscos:

Não há nenhum risco previsível das técnicas de coleta de dados. Estas técnicas têm sido utilizadas em pesquisas clínicas no mundo inteiro há vários anos e nunca um dano, problema ou risco foi reportado, nem a curto nem a longo prazo. Entretanto, é possível que você sinta alguns desconfortos devido à colocação dos sensores dos equipamentos. Caso o desconforto seja grande, por favor avise imediatamente os pesquisadores e o procedimento de coleta de dados será interrompido para que os ajustes sejam feitos. Caso necessário, pararemos toda a coleta sem qualquer prejuízo para você.

Benefícios:

Você não obterá nenhum benefício direto com a sua participação nesse estudo. Contudo, muitas pessoas poderão ser ajudadas de forma indireta com a sua participação a partir dos resultados que obtivermos ao final desta pesquisa.

Rubrica do pesquisador: _____ Rubrica do participante: _____

Acompanhamento e assistências:

Durante toda a coleta de dados, os pesquisadores estarão presentes no local com você. Qualquer dúvida e/ou problema, você poderá questioná-los a qualquer momento da pesquisa.

Sigilo e privacidade:

Você tem a garantia de que sua identidade será mantida em sigilo e nenhuma informação será dada a outras pessoas que não façam parte da equipe de pesquisadores cadastrados nesta pesquisa. Na divulgação dos resultados desse estudo, seu nome não será citado.

Ressarcimento:

Embora improvável, no caso de qualquer dano decorrente direta ou indiretamente da participação na pesquisa está garantida a assistência integral e imediata, de forma gratuita, sem ônus de qualquer espécie pelo tempo que for necessário. Você também tem direito a indenização em caso de danos.

Contato:

Em caso de dúvidas sobre o estudo, você poderá entrar em contato com os pesquisadores:

- Giovani Grisotti Martins, telefone (11) 9 9591 3360 e e-mail ggrisoti@ifi.unicamp.br;
- Andrés Fabián Quiroga Soto, telefone (19) 9 8380 1835 e e-mail a153906@dac.unicamp.br ou;
- Rickson Coelho Mesquita, telefone (19) 3251 0137 e e-mail rickson@ifi.unicamp.br.

Em caso de denúncias ou reclamações sobre sua participação e sobre questões éticas do estudo, você pode entrar em contato com a secretaria do Comitê de Ética em Pesquisa (CEP) da UNICAMP: Rua: Tessália Vieira de Camargo, 126; CEP 13083-887, Campinas - SP; telefone (19) 3521 8936; fax (19) 3521 7187; e-mail: cep@unicamp.br.

Rubrica do pesquisador: _____ Rubrica do participante: _____

Consentimento livre esclarecido:

Após ter sido esclarecido sobre a natureza da pesquisa, seus objetivos, métodos, benefícios previstos, potenciais riscos e o incômodo que esta possa acarretar, aceito participar:

Nome do(a) participante_____

_____ Data:___/_____/_____.
(Assinatura do participante ou nome e assinatura do seu responsável LEGAL)

Responsabilidade do Pesquisador:

Asseguro ter cumprido as exigências da resolução 466/2012 CNS/MS e complementares na elaboração do protocolo e na obtenção deste Termo de Consentimento Livre e Esclarecido. Asseguro, também, ter explicado e fornecido uma das vias deste documento ao participante. Informo que o estudo foi aprovado pelo CEP perante o qual o projeto foi apresentado. Comprometo-me a utilizar o material e os dados obtidos nesta pesquisa exclusivamente para as finalidades previstas neste documento ou conforme o consentimento dado pelo participante.

_____ Data:___/_____/_____.
(Assinatura do pesquisador)

Rubrica do pesquisador: _____ Rubrica do participante: _____